Praseodymium- and Holmium-Doped Crystals for Lasers Emitting in the Visible Spectral Region

Dissertation

zur Erlangung des Doktorgrades
des Department Physik
der Universität Hamburg

vorgelegt von

Fabian Reichert

aus Hamburg

Hamburg
2013

Gutachter der Dissertation:	Prof. Dr. G. Huber Prof. Dr. M. Tonelli
Gutachter der Disputation:	Prof. Dr. G. Huber Prof. Dr. K. Sengstock
Datum der Disputation:	08. August 2013
Vorsitzender des Prüfungsausschusses:	Prof. Dr. P. Schmelcher
Vorsitzender des Promotionsausschusses:	Prof. Dr. P. Hauschildt
Dekan der Fakultät für Mathematik, Informatik und Naturwissenschaften:	Prof. Dr. H. Graener

Abstract

F. Reichert: *Praseodymium- and Holmium-Doped Crystals for Lasers Emitting in the Visible Spectral Region*

The topic of this work is the investigation of novel gain media for the realization of solid state lasers directly emitting in the visible spectral region. For this purpose, the rare-earth ions Pr^{3+} and Ho^{3+} were chosen due to their favorable energy level structure which results in absorption and emission lines in the visible spectral range.

For the Pr^{3+}-ion the oxide host materials $SrAl_{12}O_{19}$ (SRA), $CaAl_{12}O_{19}$ (CAlO), and $LaMgAl_{11}O_{19}$ (LMA) were chosen. These host lattices offer an advantageous site symmetry for the Pr^{3+}-ion as well as favorable thermomechanical properties. Additionally the low-phonon fluoride material LaF_3 was employed. For the Ho^{3+}-ion, $LiLuF_4$ (LLF) and LaF_3 were used as host systems. SRA, CAlO, LMA as well as LLF crystals were fabricated by means of the Czochralski method while LaF_3 was grown by the seedless cooling down method.

The active media were characterized in terms of ground state absorption (GSA), emission, and excited state absorption (ESA). For the Pr^{3+}- as well as for the Ho^{3+}-doped systems absorption bands in the blue spectral range suitable for pumping by InGaN laser diodes or frequency doubled optically pumped semiconductor lasers were found. Emission measurements showed that the Pr^{3+}-doped systems exhibit distinct emission peaks in the blue to deep red spectral region which were not influenced by ESA. The Ho^{3+}-doped materials exhibit emission peaks in the green spectral range where GSA is also present. Therefore gain spectra were derived and revealed that for both Ho^{3+}-doped systems inversion levels of at least 20 % are required to achieve gain. The wavelength region in which gain can be expected is not influenced by ESA. In addition, measurements of the decay dynamics revealed maximum quantum efficiencies of less than 40 % (Ho:LLF) and approximately 75 % (Ho:LaF_3).

Laser experiments were carried out with all active media. With Ho:LLF it was not possible to achieve green laser emission. However, with Ho:LaF_3 room temperature laser operation in the green spectral region was demonstrated for the first time with a Ho^{3+}-doped crystalline system. The laser operated in a self pulsed regime with a repetition rate of approximately 5.4 kHz, a pulse duration of 1.6 µs, and a peak pulse power of 0.9 W.

Laser operation was demonstrated with all Pr^{3+}-doped host materials. Best results were obtained with Pr:SRA where more than 1 W of output power and slope efficiencies of almost 60 % were realized in the red and deep red spectral region. Furthermore it was possible to demonstrate cw laser operation of a Pr^{3+}-doped oxide in the green spectral range for the first time at room temperature. In addition, experiments were carried out in a thin disk setup and it was possible to realize first laser operation in this geometry of a Pr^{3+}-doped gain medium. Waveguiding structures in Pr:SRA were fabricated by fs-laser inscription. With these waveguides laser operation was demonstrated in the red spectral region with an output power of more than 1 W at almost 40 % slope efficiency. These structures also allowed for the first time laser emission in the green spectral range from a Pr^{3+}-doped crystalline waveguide.

Kurzfassung

F. Reichert: *Praseodym- und Holmium-dotierte Kristalle für Laser im sichtbaren Spektralbereich*

Ziel dieser Arbeit war es, neue aktive Materialien zur Realisierung von Festkörperlasern mit direkter Emission im sichtbaren Spektralbereich zu untersuchen. Hierfür wurden die beiden Seltenerd-Ionen Pr^{3+} und Ho^{3+} ausgewählt, da die Struktur ihrer Energieniveaus sowohl Anregung als auch Emission im sichtbaren Spektralbereich ermöglicht.

Für das Pr^{3+}-Ion wurden die oxidischen Wirtskristalle $SrAl_{12}O_{19}$ (SRA), $CaAl_{12}O_{19}$ (CAlO), und $LaMgAl_{11}O_{19}$ (LMA) ausgesucht, da sie gute thermomechanische Eigenschaften aufweisen und dem Pr^{3+} einen Gitterplatz mit vorteilhafter Symmetrie bieten. Zusätzlich wurde das fluoridische Material Pr:LaF_3 untersucht. Für Ho^{3+} wurden $LiLuF_4$ (LLF) sowie ebenfalls LaF_3 eingesetzt. SRA, CAlO, LMA und LLF Kristalle wurden nach dem Czochralski-Verfahren gezüchtet, während LaF_3 durch langsames Abkühlen hergestellt wurde.

Alle aktiven Materialien wurden hinsichtlich ihrer Grundzustandsabsorption (GSA), Emission und der Absorption aus angeregten Zuständen (ESA) untersucht. Mögliche Anregungslinien für Pr^{3+} sowie für Ho^{3+} zeigten sich hierbei im blauen Spektralbereich. Diese können mit InGaN Laserdioden oder frequenzverdoppelten optisch gepumpten Halbleiterlasern adressiert werden. Spektroskopische Untersuchungen an den Pr^{3+}-dotierten Systemen zeigten Emissionslinien im blauen bis tiefroten Spektralbereich welche nicht durch ESA-Prozesse beeinträchtigt sind. Die Ho^{3+}-dotierten Materialien zeigten Emission im grünen Spektralbereich, in dem zusätzlich GSA vorhanden ist. Die Verstärkungsspektren wurden bestimmt und es folgte, dass für beide Ho^{3+}-dotierte Systeme Anregungsdichten von mindesten 20 % notwendig sind, um Verstärkung zu erzielen. In den Bereichen in denen Verstärkung erwartet wird, tritt keine ESA auf. Zusätzlich wurden Messungen der Zerfallsdynamik durchgeführt, mit deren Hilfe die Quanteneffizienzen auf maximal 40 % in Ho:LLF sowie ungefähr 75 % in Ho:LaF_3 abgeschätzt wurde.

Mit allen aktiven Materialien wurden Laserexperimente durchgeführt. Mit Ho:LLF konnte keine grüne Laseremission erreicht werden. Jedoch konnte mit Ho:LaF_3 erstmals bei Raumtemperatur Lasertätigkeit eines Ho^{3+}-dotierten kristallinen Materials im grünen Spektralbereich erzielt werden. Der Laser arbeitete in einem selbst-gepulsten Regime mit einer Repetitionsrate von ungefähr 5,4 kHz, einer Pulslänge von 1,6 µs und einer Pulsspitzenleistung von 0,9 W.

Mit allen Pr^{3+}-dotierten Materialien konnte Lasertätigkeit demonstriert werden. Die besten Ergebnisse wurden mit Pr:SRA erreicht. Hierbei konnten Ausgangsleistungen von über 1 W und differentielle Wirkungsgrade von fast 60 % im roten und tiefroten Spektralbereich erzielt werden. Zusätzlich wurde erstmals Dauerstrich Laseremission mit einem Pr^{3+}-dotierten Oxidkristall im grünen Spektralbereich bei Raumtemperatur realisiert. In der Scheibenlasergeometrie konnte erstmalig Lasertätigkeit eines Pr^{3+}-dotierten Systems realisiert werden. In weiteren Experimenten wurden mittels fs-Laserstrukturierung wellenleitende Strukturen in Pr:SRA Volumenkristallen erzeugt. Diese erlaubten Lasertätigkeit mit Ausgangsleistungen von mehr als 1 W und differentiellen Wirkungsgraden von fast 40 % im roten Spektralbereich. Mit diesen Strukturen konnten erstmals grün emittierende Pr^{3+}-dotierte kristalline Wellenleiterlaser realisiert werden.

Contents

List of Figures **IX**

List of Tables **XIII**

1 Introduction **1**

2 Fundamentals **3**
2.1 The Rare Earth Ion . . . 3
2.1.1 The Free Ion . . . 3
2.1.2 The Ion in the Crystal Field . . . 5
2.1.3 Effect of the Crystal Field on the $4f^n5d^1$ Manifold . . . 6
2.2 Interaction of Light and Matter . . . 7
2.2.1 Intraionic Processes . . . 8
2.2.2 Interionic Processes . . . 10
2.3 The Laser Concept . . . 12
2.3.1 Four-Level-Systems . . . 12
2.3.2 Quasi-Three-Level-Systems . . . 14
2.4 Active Ions . . . 15
2.4.1 The Pr^{3+}-ion . . . 15
2.4.2 The Ho^{3+}-ion . . . 17

3 Host Materials **21**
3.1 Hexaaluminates $SrAl_{12}O_{19}$, $CaAl_{12}O_{19}$, and $LaMgAl_{11}O_{19}$ . . . 21
3.2 Fluoride Materials . . . 26
3.2.1 $LiLuF_4$ . . . 27
3.2.2 LaF_3 . . . 28

4 Crystal Growth **33**
4.1 Growth Techniques . . . 33
4.1.1 Czochralski Technique . . . 33
4.1.2 Seedless Cooling Down Method . . . 36
4.2 Growth Facilities . . . 37
4.3 Growth Results . . . 39
4.3.1 $SrAl_{12}O_{19}$ . . . 39
4.3.2 $CaAl_{12}O_{19}$ . . . 40
4.3.3 $LaMgAl_{11}O_{19}$ . . . 42
4.3.4 $LiLuF_4$ . . . 45
4.3.5 LaF_3 . . . 46

5 Waveguide Fabrication and Characterization **49**
5.1 Principles . . . 49
5.2 Fabrication . . . 51
5.2.1 Setup . . . 51
5.2.2 Parameters . . . 52
5.3 Characterization . . . 53
5.3.1 Microscopy . . . 53
5.3.2 Guiding Losses . . . 55
5.3.3 Mode Field Diameter and M^2 . . . 56
5.3.4 Numerical Aperture and Refractive Index Change . . . 58

6 Spectroscopy **61**
6.1 Measurement Techniques . . . 61
6.1.1 Ground State Absorption . . . 61
6.1.2 Fluorescence Dynamics . . . 62
6.1.3 Excitation Spectra . . . 63
6.1.4 Emission Spectra . . . 65
6.1.5 Determination of Stark Level Positions . . . 67
6.1.6 Gain Spectra . . . 68
6.1.7 Excited State Absorption . . . 69
6.2 Results: Praseodymium Doped Materials . . . 71
6.2.1 Ground State Absorption . . . 71
6.2.2 Decay Dynamics . . . 74
6.2.3 Site Selective Excitation and Emission Spectra . . . 77
6.2.4 Emission Spectra . . . 79
6.2.5 Excited State Absorption Spectra . . . 83
6.3 Results: Holmium Doped Materials . . . 86
6.3.1 Ground State Absorption . . . 86
6.3.2 Determination of the Stark Level Positions . . . 86
6.3.3 Emission Spectra . . . 88
6.3.4 Gain Spectra . . . 90
6.3.5 Decay Dynamics . . . 92
6.3.6 Excited State Absorption Spectra . . . 94
6.4 Summary: Spectroscopy . . . 97
6.4.1 Praseodymium Doped Materials . . . 97
6.4.2 Holmium Doped Materials . . . 98

7 Laser Experiments **99**
7.1 Pump Sources . . . 99
7.1.1 InGaN Based Laser Diodes . . . 99
7.1.2 Frequency Doubled Optically Pumped Semiconductor Lasers . . . 100
7.2 Lasers Based on Pr-Doped Materials . . . 102
7.2.1 State of the Art . . . 102
7.2.2 Pr,Mg:$SrAl_{12}O_{19}$ . . . 103
7.2.3 Pr,Mg:$CaAl_{12}O_{19}$ . . . 119

7.2.4 Pr:$LaMgAl_{11}O_{19}$ . . . 119
7.2.5 Pr:LaF_3 . . . 124
7.3 Lasers Based on Ho-Doped Materials . . . 129
7.3.1 State of the Art in the Visible Spectral Region . . . 129
7.3.2 Ho^{3+}:$LiLuF_4$ . . . 129
7.3.3 Ho^{3+}:LaF_3 . . . 130
7.4 Summary: Laser Experiments . . . 132
7.4.1 Praseodymium Doped Materials . . . 132
7.4.2 Holmium Doped Materials . . . 133

8 Conclusion **135**
8.1 Summary . . . 135
8.1.1 Pr-doped Materials . . . 135
8.1.2 Ho-doped Materials . . . 136
8.2 Outlook . . . 137

A References for Table 3.1 **139**

B Additional Spectroscopic Data **141**

C Additional Laser Parameters **143**

Bibliography **145**

List of Publications **159**

Acknowledgements **165**

List of Figures

2.1 Exemplary Pr^{3+} energy level scheme. 6
2.2 Possible intraionic processes. 8
2.3 Interionic processes 11
2.4 Schematic drawing of four- and quasi-three-level-system. 13
2.5 Schematic of the energy level positions of Pr^{3+}. 16
2.6 Exemplary Ho^{3+} energy level schemes. 18

3.1 Unit cell of $CaAl_{12}O_{19}$. 22
3.2 Phase diagrams of binary systems SrO - Al_2O_3 and CaO - Al_2O_3. 23
3.3 Infrared transmission spectra of $CaAl_{12}O_{19}$ and $LaMgAl_{11}O_{19}$ 24
3.4 Thermal conductivities of Pr^{3+}-doped hexaaluminates. 26
3.5 Unit cell of $LiLuF_4$. 27
3.6 Phase diagram of the binary system LiF - LuF_3 28
3.7 Unit cell of LaF_3. 29

4.1 Schematic setup for Czochralski crystal growth 34
4.2 Schematic setup for seedless cooling down growth runs. 37
4.3 Seedless cooling down method. 37
4.4 Pr,Mg:$SrAl_{12}O_{19}$ crystals. 40
4.5 Pr,Mg:$CaAl_{12}O_{19}$ crystals grown at the ILP. 41
4.6 Various Pr:$LaMgAl_{11}O_{19}$ crystals grown with the *Hereaus* facility. 43
4.7 Boules of Pr^{3+}-doped $LaMgAl_{11}O_{19}$. 44
4.8 As grown 0.5 at% Ho^{3+}:$LiLuF_4$ boule. 46
4.9 SCDM grown LaF_3 boules. 47

5.1 Nonlinear processes occuring in the focal region of a fs-laser beam. 50
5.2 Schematic of the setup used for the fs-laser inscription. 51
5.3 Schematic of the sample during the inscription process. 52
5.4 Microscope images of DTSs inscribed with different inscription parameters. 54
5.5 Schematic of the setup used for determining waveguiding losses and mode field diameters of the fabricated waveguides. 55
5.6 Guiding losses of waveguides inscribed in Pr,Mg:SRA. 56
5.7 Mode field diameters of waveguides inscribed in Pr,Mg:SRA and M^2 values. 57
5.8 Exemplary mode profiles for different inscription parameters. 57
5.9 NA and Δn of waveguides inscribed in Pr,Mg:SRA. 59

6.1 Schematic of the setup used to obtain fluorescence dynamics of the active media. 63

6.2 Schematic of the *Yobin Yvon* FL 321 Fluorolog-3. 64
6.3 Schematic of the setup employed for fluorescence measurements. 65
6.4 Schematic of the setup employed to transmission measurements at cryogenic temperatures. 68
6.5 Schematic of the setup employed to record excited state absorption spectra. 70
6.6 Polarization dependent ground state absorption spectra of Pr^{3+}-doped host systems. 72
6.7 Decay dynamics of the $^3P_0$ manifold in Pr,Mg:CAlO and Pr:LMA. 76
6.8 Excitation and emission spectra of 0.7 at% doped Pr:LMA. 78
6.9 Polarization dependent emission spectra of Pr^{3+}-doped host systems. . . . 80
6.10 Polarization dependent emission spectra of Pr^{3+}:LaF_3 at 10 K. 83
6.11 Polarization dependent excited state absorption spectra of Pr^{3+}-doped host systems. 84
6.12 Polarization dependent ground state absorption spectra of Ho^{3+}-doped host systems. 87
6.13 Transmission spectrum of Ho^{3+}:LaF_3 at 10 K. 88
6.14 Polarization dependent emission spectra of Ho^{3+}-doped host systems. . . . 89
6.15 Polarization dependent gain spectra derived for Ho^{3+}:$LiLuF_4$ and Ho^{3+}:LaF_3. 91
6.16 Temperature dependent decay dynamics of Ho^{3+}:$LiLuF_4$ and Ho^{3+}:LaF_3. . 93
6.17 Energy level schemes of Ho^{3+}. 95
6.18 Polarization dependent excited state absorption spectra of Ho^{3+}:$LiLuF_4$. . 96
6.19 Schematic energy level scheme of Ho^{3+} with ESA transitions. 96
6.20 Polarization dependent excited state absorption spectra of Ho^{3+}:LaF_3. . . . 97

7.1 Spectral characteristics of the InGaN laser diodes. 100
7.2 Spectral characteristics of the employed 2ωOPSLs. 102
7.3 Scheme for polarization coupling of InGaN laser diodes. 104
7.4 Schematic of the V-type resonator design used for the laser experiments. . 104
7.5 Input-output curves of InGaN LD pumped Pr,Mg:$SrAl_{12}O_{19}$ crystals with different dopant concentrations. 105
7.6 Laser characteristics of Pr,Mg:SRA lasers pumped by four InGaN laser diodes. 106
7.7 Caustics of diode pumped Pr,Mg:SRA lasers at various wavelengths. 108
7.8 Characteristics of Pr,Mg:$SrAl_{12}O_{19}$ lasers pumped by a 2ωOPSL. 110
7.9 Laser characteristics obtained with a sample of the Pr,Mg:SRA crystal provided by the IKZ Berlin. 112
7.10 Microscopy images of the laser sample prepared from the Pr,Mg:$SrAl_{12}O_{19}$ boule grown at the IKZ Berlin. 112
7.11 Schematic of the thin disk laser setup. 114
7.12 Characteristics of Pr,Mg:$SrAl_{12}O_{19}$ thin disk lasers for different output coupling rates. 115
7.13 Characteristics of Pr,Mg:$SrAl_{12}O_{19}$ thin disk lasers for different duty cycles. 115
7.14 Schematic of the setup used for the waveguide laser experiments. 116
7.15 Characteristics of Pr,Mg:$SrAl_{12}O_{19}$ waveguide lasers. 117
7.16 Laser characteristics of 2ωOPSL pumped Pr,Mg:CAlO lasers. 120

7.17 Schematic of the linear resonator design used for the laser experiments with Pr:LMA. 121
7.18 Laser characteristics of 2ωOPSL pumped Pr:LMA lasers. 122
7.19 Ratio of absorbed pump power and incident power with respect to the incident power for Pr:LMA in fluorescence mode under InGaN LD pumping. 123
7.20 Comparison of laser performance of Pr:LaF_3 at $\lambda_L = 719.8\,nm$ for different focal lengths of L and different dopant concentration. 125
7.21 Laser characteristics of 2ωOPSL pumped Pr:LaF_3 lasers 125
7.22 Schematic of the energy transfer process between a Pr^{3+} donor and an Eu^{3+} acceptor. 126
7.23 Laser performance of Pr^{3+},Eu^{3+}:LaF_3 under 2ωOPSL pumping. 127
7.24 Parameters of wavelength tunable laser operation of Pr:LaF_3. 128
7.25 Laser characteristics of the Ho^{3+}:$LiLuF_4$ laser operating on the $^5S_2 \rightarrow {}^5I_7$ transition. 130
7.26 Laser characteristics of the Ho^{3+}:LaF_3 laser operating at $\lambda_L = 549.4\,nm$. . . 131

B.1 Input. 141

C.1 Reflectivity of the Coating of the Pr,Mg:$SrAl_{12}O_{19}$ Waveguides. 143

List of Tables

3.1 Relevant properties of the investigated materials 31

4.1 Composition of the 2.5 at% doped Pr^{3+}:$LaMgAl_{11}O_{19}$ crystal determined by microprobe analysis. 44

5.1 Specification of the linear translation stages. 52

6.1 Specifications of gratings available in the *Fluorolog*. 64
6.2 Peak ground state absorption cross sections of Pr^{3+}-doped media. 73
6.3 Peak emission cross sections of Pr^{3+}-doped media. 82
6.4 Peak ground state absorption cross sections of the Ho^{3+}-doped systems. . . 87
6.5 Energetic positions of the five Stark levels composing the $^5S_2$ manifold in Ho^{3+}:LaF_3. 88
6.6 Peak emission cross sections of Ho^{3+}-doped media. 90

7.1 Laser characteristics of InGaN LD pumped Pr,Mg:$SrAl_{12}O_{19}$ lasers. 109
7.2 Laser characteristics of 2ωOPSL pumped Pr,Mg:$SrAl_{12}O_{19}$ lasers. 111
7.3 Laser characteristics Pr,Mg:$SrAl_{12}O_{19}$ TDL lasers. 116
7.4 Laser characteristics and mirror parameters of 2ωOPSL pumped Pr,Mg:$SrAl_{12}O_{19}$ waveguide lasers 118
7.5 Laser characteristics of 2ωOPSL pumped Pr,Mg:$CaAl_{12}O_{19}$ lasers. 121
7.6 Laser characteristics and mirror parameters of 2ωOPSL pumped Pr:$LaMgAl_{11}O_{19}$ lasers. 123
7.7 Laser characteristics of 2ωOPSL pumped Pr:LaF_3 lasers. 126

A.1 References for Table 3.1. 139

1 Introduction

Lasers with emission wavelengths in the visible spectral region have found applications in a great number of fields. In medicine they are used for example in ophthalmology for laser coagulation. Scientific applications include optical spectroscopy, fluorescence microscopes where such lasers can be employed as excitation sources for various dyes, and quantum optical experiments involving ytterbium or lithium. Another very interesting field is consumer electronics. Here lasers with emission wavelengths in the visible spectral region are employed for optical storage schemes or in projection devices where they enable to address a larger part of the color space than conventional techniques such as CRT screens or projectors based on high pressure lamps.

Today, lasers with emission wavelengths in the visible spectral region are often realized by nonlinear frequency conversion of near-infrared emitting lasers. Due to the conversion process, such systems are often complex, bulky, and their efficiency is lower than that of systems directly emitting in the visible spectral range. One way to achieve a high degree of efficiency and compactness is the use of laser diodes (LDs), and much progress has been made in past few years concerning LDs emitting in the blue to green spectral region [Nak09]. Unfortunately so far these sources yield only poor beam quality and their output power is low. Thus they are often unsuited for several of the aforementioned applications.

A very interesting approach to realize efficient laser operation with excellent beam quality, high output powers, and emission wavelengths in the visible spectral region is to employ rare earth (RE) doped crystalline active media. The energy level structure of several RE-ions allows transitions corresponding to wavelengths in the visible spectral range. Doped into crystalline host materials, cross sections in the order of $10^{-20}\,\mathrm{cm}^2$ are possible which therefore allows an efficient absorption of the pump radiation and low laser thresholds. Two very interesting ions are Pr^{3+} and Ho^{3+}. Both exhibit absorption bands in the blue spectral region which can be adressed with InGaN laser diodes (LDs) [Nic13a] or frequency doubled semiconductor lasers (2ωOPSLs) [McI03]. These ions also show emission in the green spectral range, and Pr^{3+} furthermore in the orange, red, and deep red.

By employing Pr^{3+}-doped fluorides as gain media it was already possible to demonstrate highly efficient laser operation in the visible spectral region [San94, Ric04, Ost08, Cor08, Bel10, Gün11c]. However, the standard Pr^{3+} hosts $LiYF_4$ and $LiLuF_4$ have several drawbacks and it is therefore reasonable to investigate other host systems with possibly more advantageous properties.

The major drawbacks of $LiYF_4$ and $LiLuF_4$ are their low mechanical stability as well as their comparatively low thermal conductivities [Agg05]. In addition, the growth of high quality crystals is challenging since the crystal quality is extremely sensitive to even trace amount of water vapor or oxygen in the growth chamber. In contrast, oxide crystals often have more advantageous thermomechanical properties and can be grown much more

easily. Unfortunately many Pr^{3+}-doped oxide gain media exhibit excited state absorption in the visible spectral region [Che94, Thi08] as well as strong multiphonon decay of the upper laser manifold [Mel95]. Nevertheless several systems have proven to be viable Pr^{3+} hosts for the generation of laser emission in the visible spectral region. Good results in the deep red spectral region have for example been obtained with Pr:$YAlO_3$ [Dan94b, Fib09]. A highly interesting system is the hexaaluminate Pr,Mg:$SrAl_{12}O_{19}$. Employed as gain medium it has already allowed efficient laser operation in bulk as well as in waveguide geometry [Fec11, Cal11]. One part of this thesis was therefore to further investigate, and if possible optimize this system in terms of dopant concentration and crystal quality as well as to employ other pump and resonator schemes to uncover the full potential of this material. In addition, several other crystals sharing the same lattice structure were explored since they might also exhibit comparable advantageous properties.

Another problem with the standard Pr^{3+} fluoride hosts $LiYF_4$ and $LiLuF_4$ is the unfavorable segregation coefficient which leads to a strong concentration gradient throughout the as-grown boules. Host systems where the subsituted ion is more similar to the Pr^{3+}-ion are likely to exhibit segreation coefficients closer to 1 and therefore smaller concentration gradients. Good candidates in this regard seem to be systems containing La^{3+} which can be attributed to the almost identical mass and ionic radius compared to Pr^{3+}. It was therefore also a topic of this work to investigate host systems which provide such a site.

Besides Pr^{3+} the trivalent holmium ion was also investigated in this thesis. Nowadays it is most often used to realize solid state lasers operating in the 2 µm region [Der07, Koo11, Lam12]. Nevertheless several lasers based on Ho^{3+}-doped gain media have been demonstrated in the deep red spectral range. Unfortunately, the choice of host lattices is limited. This is due to the fact that because of the close spacing of the energy levels in Ho^{3+}, this ion is prone for strong multiphonon decay, and therefore to low quantum efficiencies. For the realization of a laser based on Ho^{3+} that operates in the visible spectral region, a low cutoff frequency of the phonon spectrum is thus paramount. Laser operation was mostly realized by employing low phonon host crystals such as CaF_2, BaY_2F_8, or $LiYF_4$ [Vor65, Joh71, Pod76, Chi77]. The investigation of low-phonon host materials which may allow laser operation in the green spectral region was therefore also part of this work.

2 Fundamentals

In order to undestand the physics involved in the experiments which were conducted in this thesis a certain theoretical background is necessary. This chapter will provide an introduction to the utilized theory. It will start with deriving the energy level scheme of rare-earth ions in crystalline host materials by means of the time dependent Schrödinger equation and pertubation theory. The second part explains with the help of rate equations the processes that take place when light interacts with such ions. Lastly the basic properties of the laser process will be presented. For a deeper understanding of the topic the reader is referred to [CT99, Hen89, Sve98].

2.1 The Rare Earth Ion

The elements of the third group scandium (atomic number $Z = 21$), yttrium ($Z = 39$), as well as the lanthanoids (lanthanum ($Z = 57$) to lutetium ($Z = 71$)) belong to the rare earth (RE) elements. They are characterized by a similar chemical behaviour which is due to the comparable structure of their electron shell. In their atomic state all lanthanoids have fully occupied $5s$, $5p$, and $6s$ orbitals. Furthermore, with rising Z the $4f$ orbital is filled up, with the exception of the four elements Lanthanum, Cerium, Gadolinium, and Lutetium where the added electron occupies the $5d$ orbital. This leads to an electron configuration of $[\mathrm{Xe}]4f^{Z-56-n}\ 5d^{\mathrm{n}}$ with $n = 1$ for La, Ce, Ga, and Lu, and $n = 0$ for all others.

Doped into an ionic matrix, RE ions normally take up a threefold oxidized or trivalent state. In some cases divalent (Eu, Yb) and tetravalent (Ce, Pr, Tb) states are also possible and might affect the respective spectroscopic properties. In any instance the two $6s$ and one of the $4f$ electrons are lost to the surrounding ligands while the outer laying orbitals $5s$ and $5p$ stay fully occupied. This leads to a strong shielding of the $4f$ orbital against interaction with the crystal field caused by the ligands. These perturbations can therefore be treated as a perturbation to the Hamiltonian of the system.

Since the $4f$ orbitals are shielded, the energy level structure retains a discrete nature which is for the most part independent of the host system. Transitions between $4f$ energy levels in RE ions usually exhibit quite narrow linewidths especially compared to those in transition metal ions like titanium or chromium.

2.1.1 The Free Ion

The energy levels of an ion can be determined by solving the Schrödinger equation

$$\hat{H}\,|\Psi_n\rangle = E_n\,|\Psi_n\rangle\,, \tag{2.1}$$

for its energy eigenvalues E_n and the corresponding wavefunction $|\Psi_n\rangle$. All information about the system is given by the Hamiltonian $\hat{H}$, and the condition

$$\sum_{n=1}^{N} \langle \Psi_n \mid \Psi_n \rangle = 1 \tag{2.2}$$

allows $\langle \Psi_n \mid \Psi_n \rangle$ to be interpreted as the probability to measure the ion in the state n.

In a first approximation the ion can be considered to be a free ion for which the Hamiltonian takes the form

$$\hat{H} = \sum_{i=1} \left(-\frac{\hbar^2}{2m} \Delta_{\vec{r}_i} - \frac{Ze^2}{4\pi\epsilon_0 r_i} \right) + \sum_{i<j} \frac{e^2}{4\pi\epsilon_0 r_{ij}}. \tag{2.3}$$

It consists of three terms; the first being the kinetic energy of the ion, and the second and third the interaction between the nucleus and i^{th} electron, and i^{th} and j^{th} electron, respectively. In this first approximation, spin-orbit interactions are neglected. They will later be added as pertubations to the system. In this equation, m_e and e are the mass and charge of an electron, and ϵ_0 is the vacuum permittivity. The distance between the nucleus and electron i is given by r_i while r_{ij} signifies the distance between two electrons i and j.

Solving this equation analytically is impossible due to the coupling of i^{th} and j^{th} electron. Also, for large Z there are many terms of the r_{ij} nature. Combined these terms can have an effect in the same order of magnitude as the electron nucleus interaction. To resolve this problem the central field approximation as proposed by Hartree *et al.* is introduced [Bra03]. Here each electron moves in an effective potential $V(r_i)$. It consists of the attractive interaction between the nucleus and electron and the average repulsive interaction with the remaining $(N-1)$ electrons and can be assumed to be spherically symmetric. Interactions between single electrons are neglected and will later be added as petubations. This now allows the N single electron wavefunctions to be calculated which in turn can be used to obtain a more accurate effective potential. Successive iterations lead the potential to converge. The potential $V'(r_i)$ obtained in this way can be used to write down a Hamiltonian of this system that can be seperated:

$$\hat{H}_0 = \sum_{i=1} \left(-\frac{\hbar^2}{2m} \Delta_{\vec{r}_i} + V'(r_i) \right). \tag{2.4}$$

The time independent Schrödinger equation $\hat{H}_0 |\Psi_0\rangle = E_0 |\Psi_0\rangle$ now has as a solution the product of the N single electron wavefunctions

$$\Psi_0 = \prod_{i=1}^{N} |n_i l_i m_l\rangle \tag{2.5}$$

and the energy eigenvalues depend on the principal quantum number n_i, and the angular momentum l_i. The spherical nature of $V'(r_i)$ leads to a degeneracy towards the magnetic quantum number m_l.

Due to the fact that electrons are spin $\frac{1}{2}$ particles and therefore fermions, $|\Psi_0\rangle$ must fulfill the Pauli exclusion principle and thus has to be completely antisymmetric. This

can be achieved by writing it into a Slater determinant which adds a spin and therefore the spin quantum number $m_s = \pm\frac{1}{2}$ to each single electron wavefunction. Since the energy eigenvalues are also degenerate towards m_s, the total degeneracy of each individual electron energy is $2\,(2l+1)$.

As pointed out earlier the spin-orbit and electron-electron interactions were neglected so far. They can now be added as small perturbations to the system with the Hamiltonians

$$\hat{H}_{\mathrm{ee}} = \sum_{i<j}^{N} \frac{e^2}{4\pi\epsilon_0 r_{ij}} + \sum_{i=1}^{N} \left(-\frac{Ze^2}{4\pi\epsilon_0 r_i} + V(\vec{r}_i) \right) \tag{2.6}$$

and

$$\hat{H}_{\mathrm{ls}} = -\sum_{i=1}^{N} \frac{1}{2m_e^2 c^2 r_i} \cdot \frac{dV(r_i)}{dr_i} \cdot l_i \cdot s_i \tag{2.7}$$

where c is the speed of light. This leads to a new full Hamiltonian for the system

$$\hat{H} = \hat{H}_0 + \hat{H}_{\mathrm{ee}} + \hat{H}_{\mathrm{ls}}. \tag{2.8}$$

From this operator several different cases can be derived depending on the atomic number Z. For light elements with low values of Z the dominant perturbance is caused by $\hat{H}_{\mathrm{ee}}$. This means that first all spins couple to a total spin $\vec{S} = \sum_{i=1}^{N} \vec{s_i}$ and all orbital angular momenta to a total orbital angular momentum $\vec{L} = \sum_{i=1}^{N} \vec{l_i}$. The total angular momentum follows from the coupling of these two terms $\vec{J} = \vec{S} + \vec{L}$. This case is called LS- or Russell-Saunders coupling.

The second type occurs for heavy elements with large Z values where $\hat{H}_{\mathrm{ls}}$ causes the major perturbance. Here the spins and orbital angular momentum of each electron couple as $\vec{j_i} = \vec{s_i} + \vec{l_i}$ before the various angular momenta couple to a total angular momentum $\vec{J} = \sum_{i=1}^{N} \vec{j_i}$. This type is called jj-coupling.

For the elements of the group of the lanthanoids both terms, $\hat{H}_{\mathrm{ee}}$ and $\hat{H}_{\mathrm{ls}}$ are approximately of the same order. This leads to the so called intermediate coupling. The energy eigenstates in this case are linear combinations of LS-state with equal $\vec{J}$ values which are degenerate towards m_J leading to a total degeneracy of $(2J+1)$. The notation is ${}^{2S+1}L_J$ and thus follows that of the Russell-Saunders coupling.

2.1.2 The Ion in the Crystal Field

In order to account for the interaction between the electrons and the electrostatic field of the ligands, the Hamiltonian of the system must again be augmented. The strong shielding of the $4f$ orbitals enables to regard this interaction, denoted as the Stark effect, as another perturbation with the Hamiltonian

$$\hat{H}_{\mathrm{Stark}} = \frac{1}{4\pi\epsilon_0} \sum_i \sum_l \frac{Z_l e^2}{|\vec{R}_l - \vec{r}_i|}. \tag{2.9}$$

This term includes the atomic number Z_l and position $\vec{R}_l$ of each ligand. For lanthanoid ions it is approximately one order of magnitude smaller compared to $\hat{H}_{\mathrm{ee}}$ and $\hat{H}_{\mathrm{ls}}$. Adding

this term to equation 2.8 yields a Hamilton operator which now includes all perturbations to the system and leads to a breaking of the degeneracy of the $(2J+1)$ manifold. Again, two cases must be distinguished. Ions with an even number of electrons experience a $(2J+1)$-fold splitting. According to the Kramers theorem, an odd number leads to $\frac{(2J+1)}{2}$-sublevels and as such the levels retain a 2-fold degeneracy.

2.1.3 Effect of the Crystal Field on the $4f^n5d^1$ Manifold

In contrast to the shielded $4f$ orbitals, the crystal field has a strong effect on the $5d$ orbitals. In fact, for $5d$ energy levels the perturbation caused by the crystal field is much stronger compared to that caused by electron-electron or spin-orbit interactions ($\hat{H}_{\mathrm{Stark}} \geq \hat{H}_{\mathrm{ee}}, \hat{H}_{\mathrm{ls}}$). Assuming only ionic bonding, the ligand field theory [Sch67] can be employed to describe the splitting and centroid line shift caused by this interaction.

Group theory gives a splitting of the five $(2l+1)$ originally degenerate levels of a d^1 electron into two multiplets, the $T_{2,\mathrm{g}}$ consisting of three, and the E_{g} consisting of two degenerate levels. Neglecting electron-electron and spin-orbit interactions, the centroid line shift $\Delta\varepsilon$ of the two manifolds is given as

$$\begin{aligned} \Delta\varepsilon(E_{\mathrm{g}}) &= \varepsilon_{0,\mathrm{sym}} \pm 6Dq \qquad \text{and} \\ \Delta\varepsilon(T_{2,\mathrm{g}}) &= \varepsilon_{0,\mathrm{sym}} \mp 4Dq. \end{aligned} \tag{2.10}$$

It depends on two parameters: the shift of the center of gravity $\varepsilon_{0,\mathrm{sym}}$ of the $5d$ manifold, and the crystal field splitting parameter Dq (see figure 2.1), and is caused by two effects.

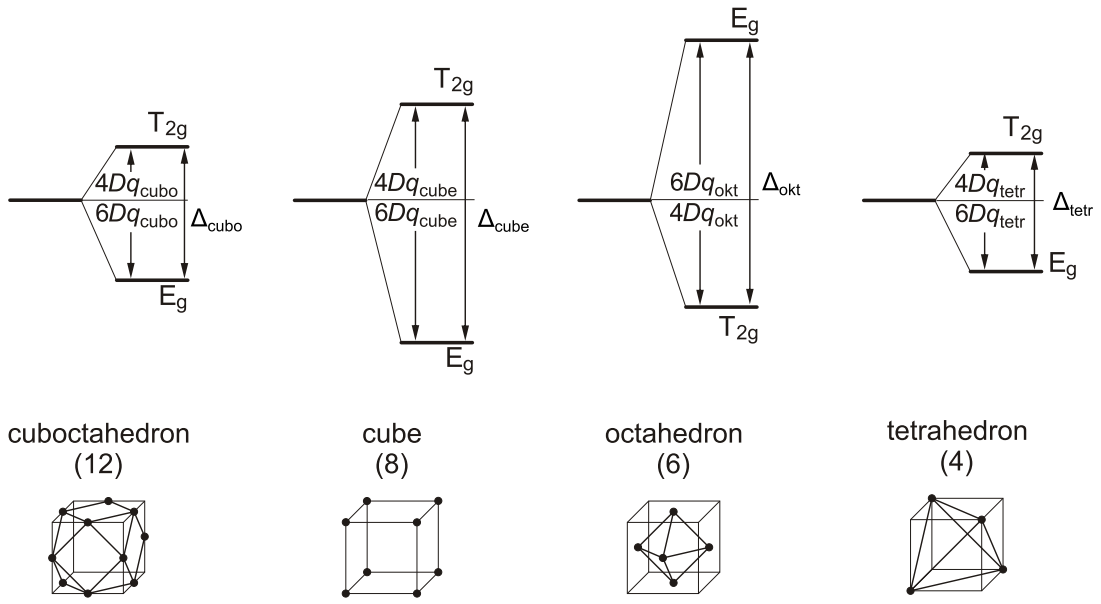

Figure 2.1: Crystal field splitting and centroid line shift caused by different symmetries of the coordination sphere [Sch67, Sch73]. The numer in parentheses indicates the number of ligands.

First, the radially symmetric part of the crystal field causes a downward[1] shift $\varepsilon_{0,\mathrm{sym}}$ of the barycenter of the $4f^n5d^1$ configuration compared to a free ion which increases with smaller ion-ligand distances. The angular dependent part determines the sign in equation 2.10 which is therefore dependent on the symmetry of the coordination sphere. For tetrahedral, cubic, and cuboctahedral spheres the E_g manifold is lowered and becomes the ground state of the $4f^n5d^1$ configuration, while the $T_{2,g}$ is raised. In an octahedral sphere the signs are reversed and the $T_{2,g}$ becomes the lowest $4f^n5d^1$ manifold.

Secondly the value of the crystal field splitting parameter Dq is determined by the symmetry of the coordination sphere. Assuming spheres which share the same value for their charge q and distance between ligand and coordinated ion, the splitting between the E_g and $T_{2,g}$ manifold compares as

$$\Delta_{\mathrm{cubo}} = \frac{9}{16}\Delta_{\mathrm{cube}} = -\frac{1}{2}\Delta_{\mathrm{oct}} = \frac{9}{8}\Delta_{\mathrm{tetr}}. \tag{2.11}$$

It has to be noted however that the distance between central ion and ligands generally decreases towards smaller numbers of ligand ions which leads to stronger crystal fields for lower order coordination spheres [Hen89].

Investigations by Dorenbos on the position of the lowest energy $5d^1$ band of numerous Ce^{3+} doped host system have shown that the two effects affecting $\Delta\varepsilon$ are independent of each other [Dor00a, Dor00b, Dor01, Dor02]. It was furthermore shown that the position of the $4f^n5d^1$ configuration of rare earth ions doped into a specific host lattice varies only marginally between different ions [Dor04]. Therefore the large amount of data that was gathered on the position of the $5d^1$ configuration of Ce^{3+} doped into various hosts can be used to draw conclusion for other RE ions.

The imperfectness of any real crystal furthermore leads to non perfect coordination spheres and gives rise to the Jahn-Teller effect [Hal71]. Taking this and the spin-orbit interactions into account the E_g and $T_{2,g}$ manifolds experience a further splitting and are thus no longer degenerate. A more detailed discription can be found in [Fec12]. In general it can be said that due to the strong electron-phonon coupling between the host lattice and the $4f^n5d^1$ manifolds, interconfigurational $4f^n \rightarrow 4f^{n-1}5d^1$ transitions exhibit broad linewidths.

2.2 Interaction of Light and Matter

This section deals with the processes that occur when light interacts with matter. They can in principle be devided into two classes. Depending whether they occur within a single ion or between two or more ions they are either intra- or interionic processes, respectively. To comprehend these processes is necessary to understand a laser.

[1] The model actually predicts an upward shift of $\varepsilon_{0,\mathrm{sym}}$. However, it assumes pure ionic bonds and neglects the covalent part. More details can be found in [Mor80, Aul86]

2.2.1 Intraionic Processes

Intraionic processes can be classified as radiative or nonradiative. The first case describes ions interacting with photons via absorption or emission processes, while the second deals with phonon assisted transitions.

Absorption and Stimulated Emission

Given a photon with an energy $E_{\text{phot}} = h\nu$ and an ion with two distinct energy levels (cf. figure 2.2a), absorption can take place if the condition $E_{\text{phot}} = E_2 - E_1$ is fulfilled. This leads to an excitation of the ion and is classified as ground state absorption (GSA). The change of the population N_1 is given by

$$\left(\frac{\mathrm{d}N_1}{\mathrm{d}t}\right)_{\text{abs}} = -W_{12}N_1 = -\sigma_{12}FN_1. \tag{2.12}$$

The transition probability between level 1 and 2 is given by W_{12}, while F is the photon flux, and σ_{12} the GSA cross section.

If the ion was already in an excited state it is furthermore possible that a second photon with identical direction, frequency, phase, and polarization is generated (see figure 2.2b). This process is called stimulated emission. The population N_2 of the excited state changes as

$$\left(\frac{\mathrm{d}N_2}{\mathrm{d}t}\right)_{\text{se}} = -W_{21}N_2 = -\sigma_{21}FN_2 \tag{2.13}$$

where W_{21} now gives the transition probability between level 2 and 1, and σ_{21} the cross section of the stimulated emission. For this model with only one ground and one excited state it follows from [Ein16] that $W_{12} = W_{21}$ and $\sigma_{12} = \sigma_{21}$. A photon flux through a medium with a length of z now changes according to

$$\frac{\mathrm{d}F}{\mathrm{d}z} = \sigma_{21}N_2F - \sigma_{12}N_1F = \sigma\left(N_2 - N_1\right)F. \tag{2.14}$$

From this equation it can be seen that the photon flux would experience an amplification for $N_2 > N_1$. However, due to the equal transition probabilities, this condition, which is called inversion, can not be achieved in this two level model. It is necessary to consider a system with at least three levels to create a situation in which inversion becomes possible.

If a third level is present and fulfills the condition $E_3 - E_2 = E_2 - E_1$ excited state absorption (ESA) transitions are possible. This means that a photon with the corresponding energy can lead to a further excitation of the ion.

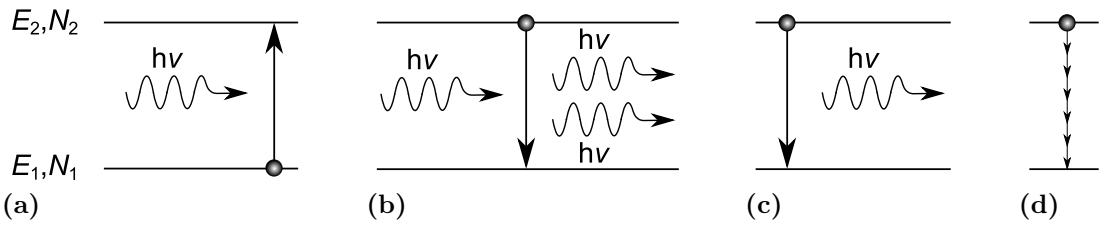

Figure 2.2: Possible intraionic processes. (a) absorption (b) stimulated and (c) spontaneous emission, and (d) multiphonon decay

Spontaneous Emission

If no photon is present to induce stimulated emission, an excited ion can decay via spontaneous emission of a photon (cf. figure 2.2c). This decay is characterized by a time constant τ_{rad} which is called the radiative lifetime of the respective excited state. The probability A of this decay is given by $A = \frac{1}{\tau_{\mathrm{rad}}}$. It allows the calculation the change of the population of N_2 caused by this process via

$$\left(\frac{\mathrm{d}N_2}{\mathrm{d}t}\right)_{\mathrm{sp}} = -A\ N_2. \tag{2.15}$$

Selection Rules

The radiative transitions of RE ions discussed in this thesis are mostly taking place within the $4f^{\mathrm{n}}$ orbital and thus between levels with equal parity. For electric dipole interactions this leads to vanishing transition matrix elements and the corresponding transitions are thus denoted as Laporte forbidden [Lap25]. In contrast, magnetic dipole interactions are possible but in general such processes are weaker than the electric kind by some orders of magnitude.

Rare earth ions that are doped into a crystalline matrix exhibit a weakening of the restraint imposed by the Laporte rule. For a non-inversion symmetric crystal field the $4f^{\mathrm{n}}$ levels experience an interconfigurational mixing with $5d$ states which carry a different parity. This leads to small but non vanishing matrix elements for the electric dipole operator. The resulting transitions obey a set of rules regarding the quantum numbers of initial and terminal state:

1. $\Delta l = \pm 1;\ \Delta P = 1$
2. $|\Delta S| = 0$
3. $|\Delta L| = 6 \leq 2l$
4. $|\Delta J| = 6 \leq 2l$ with $J = 0 \nRightarrow J' = 0$

The mixing ratio of levels with different parity can be calculated by employing the Judd-Ofelt-Theory [Jud62, Ofe62]. However, it is only valid for cases where the splitting caused by the spin-orbit interaction is small against the energetic distance between levels with varying parity.

In contrast to the forbidden intraconfigurational $4f^{\mathrm{n}} \rightarrow 4f^{\mathrm{n}}$ transitions, the interconfigurational $4f^{\mathrm{n}} \rightarrow 4f^{\mathrm{n\text{-}1}}5d^1$ transitions are not affected by the Laporte rule. This is caused by the different parity between $4f^{\mathrm{n}}$ and $4f^{\mathrm{n}}5d^1$ states. These transitions are thus parity allowed and can exhibit cross sections several order of magnitude larger than those of parity forbidden transitions.

Multiphonon Decay

The decay of an ion in an excited state can also take place via a coupling of this level to oscillation modes of the crystal lattice. This can be treated as the emission of quasi-particles

which are referred to as phonons and carry an energy $E_{\text{phon}} = \hbar\omega_{\text{eff}}$ (cf. figure 2.2d). The energy $\Delta E = E_2 - E_1$ which is stored in the ion can thus dissipate as heat by emitting p phonons with $\Delta E = p \cdot E_{\text{phon}}$ into the host matrix. Each host exhibits a characteristic phonon energy spectrum which depends on the mass of the lattice ions, their bonding strength, and on the lattice structure.

Since the population of the oscillator modes follows a Bose-Einstein distribution, the temperature dependent transfer rate for such a multiphonon decay can be given as [Ris68, Moo70]:

$$W_{\text{mp}}(T) = W_0 \cdot e^{-a\Delta E} \left(1 - e^{-\frac{\hbar\omega_{\text{eff}}}{kT}}\right)^{-p}. \tag{2.16}$$

The parameters W_0 and a are characteristic for each host with a describing the coupling strength between electrons and phonons. For RE ions this coupling is weakly pronounced, which can be attributed to the shielding of the $4f^{\text{n}}$ levels. From equation 2.16 it can be seen that the number of phonons p which are necessary to bridge the energy gap between two levels is crucial for the propability of such a process. The number of involved phonons at which the non-radiative decay rate is of the same order of magnitude as the radiative decay rate depends on the radiative lifetime of the respective energy level. For the rare earth ions investigated in this thesis, the critical number of phonons is $p \leq 4$ [Ris68, Moo70]. If this condition is fulfilled the excited level will suffer from strong population depletion by multiphonon relaxation. This effect is highly detrimental for laser operation and can even prevent it.

Like the spontaneous emission of photons, multiphonon transitions are characterized by a time constant τ_{mp} which is given by

$$\tau_{\text{mp}} = \frac{1}{W_{\text{mp}}}. \tag{2.17}$$

Since transitions between two levels often exhibit non vanishing values of W_{mp}, the effective lifetime of an excited state is given by

$$\frac{1}{\tau_{\text{eff}}} = \frac{1}{\tau_{\text{rad}}} + \frac{1}{\tau_{\text{mp}}}. \tag{2.18}$$

2.2.2 Interionic Processes

Processes between two or more ions are classified as interionic. In these interactions a donor ion D transfers at least part of its excitation energy to an acceptor ion A. The transfer follows the relation $D' + A = D + A' + \Delta E$ where primes indicate excited ions. If the energetic distances between the involved starting and terminal levels are not equal, the energy difference ΔE can be compensated by a phonon.

For ions of the same species several different types of interionic interactions are possible, for example upconversion, cross relaxation, energy migration, and reabsorption processes.

Energy Transfer Upconversion

An interionic interaction is classified as an energy transfer upconversion (ETU) if both ions are initially in an excited state. Furthermore, the terminal state of A must be

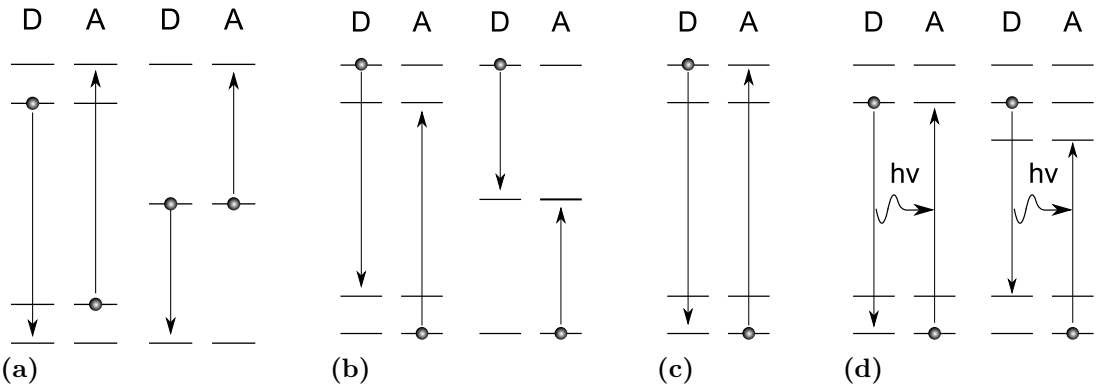

Figure 2.3: Possible interionic processes (a) energy transfer upconversion, (b) cross relaxation (c) energy migration, and (d) reabsorption.

energetically higher than the initial state of D (cf. figure 2.3 (a)). This process allows energetically higher levels to be populated without the need for a direct excitation.

Cross Relaxation

In a cross relaxation process only the donor is initially excited (cf. figure 2.3 (b)). It transfers part of its energy to the acceptor leaving both ions in an excited state. Considering a case where the final state of both ions is equal, two photons with the same energy can be generated from one pump photon which is referred to as a "two-for-one process".

Energy Migration

If the donor ion transfers its energy resonantly to the acceptor the process is referred to as energy migration (cf. figure 2.3 (c)). Since this is a resonant interaction, the energy can travel long distances within the lattice by successive steps. This increases the probability of a transfer to an impurity or defect site which leads to a dissipation of the excitation energy through heat.

Reabsorption

The emission and subsequent absorption of a photon by donor and acceptor respectively is denoted as reabsorption (cf. figure 2.3 (d)). Like energy migration it is a resonant process and can take place an arbitrary number of times before the photon leaves the crystal. This process can strongly affect spectroscopic properties such as the effective lifetime or fluorescence spectra and has to be taken into account when measuring these parameters.

Interaction Mechanisms in Interionic Processes

The interionic processes can be ascribed to two main mechanisms: multipolar and exchange interactions. Both types are strongly dependent on the interionic distance and exhibit different coupling strengths.

Multipolar Interaction

The interaction of the electric dipole d and/or quadrupole q fields of ions characterizes multipolar interactions. The coupling strength of these processes is proportional to the interionic distance with a factor of R^{-s}. The parameter s depends on the fields involved and can take values of 6 (dd), 8 (dq, qd), or 10 (qq). Multipolar interactions are therefore mainly governed by dd processes and exhibit a range of a few 10 Å [För48]. dq, qd and qq interations are only weakly pronounced and can be neglected. This also holds for the coupling strength between the magnetic fields which are thus disregarded too.

Exchange Interaction

Exchange interactions are caused by a direct overlap of the wavefunctions of the involved ions. This limits the range of this effect to a few Å [Lev69, Had99]. However, in this range the coupling strength can exceed that of the multipolar interaction. A special type of this process is the superexchange interaction [Mir96]. Here an energy transfer takes place via an intermediate ligand ion.

2.3 The Laser Concept

The basic concept of a laser[2] is the amplification of a light field in a gain medium. From equation 2.14 it is apparent that for such a process the active medium has to have at least three energy levels since inversion can not be achieved in a two level system (cf. section 2.2.1). Furthermore an array of mirrors around the medium is necessary to allow photons to pass it several times and create a feedback. Such a setup is denoted as an optical resonator. If the gain medium is excited, laser operation will start from spontaneously emitted photons which induce stimulated emission. After a certain number of passes, stimulated emission becomes the dominant process and, depending on the geometry of the setup, either a standing or running light wave is formed inside the resonator.

Independent of the actual energy level structure, active ions which support laser operation can be distinguished into two different regimes. They are either (quasi-)three- or four-level systems.

2.3.1 Four-Level-Systems

In a four-level-system four distinct Stark multiplets are involved in the laser process (cf. figure 2.4a). A pump transition transfers population from level 0 to 3 while the laser transition occurs from level 2 to 1. The levels 3 and 1 are depleted rapidly by decaying into level 2 and 0, respectively. The population of the four levels can therefore be assumed to be $N_3 = N_1 = 0$ and $N_2 + N_0 = N_{\mathrm{dop}}$ with N_{dop} as the number of active ions. Level 2 is denoted as the upper laser level while 1 is the lower laser level.

[2] **L**ight **A**mplification by **S**timulated **E**mission of **R**adiation

In an ideal four-level-system, inversion, as defined in section 2.2.1, is achieved for $N_2 \neq 0$. Assuming a uniform power density within pump and laser mode and a transversal single mode operation, the temporal evolution of N_2 can be calculated with

$$\frac{\mathrm{d}N_2}{\mathrm{d}t} = W_\mathrm{p} N_0 - \frac{q\,c}{A_\mathrm{l} L'} \cdot \sigma_\mathrm{em} N_2 - \frac{N_2}{\tau_\mathrm{eff}}. \tag{2.19}$$

The pump rate W_p can be determined from $W_\mathrm{p} = I_\mathrm{p} \frac{\sigma_\mathrm{p}(\lambda_\mathrm{p})}{h\nu_\mathrm{p}}$ with I_p as the intensity of the pump light, and σ_p and ν_p as the absorption cross section and frequency of the respective pump wavelength. The parameter q gives the number of photons in the laser mode with area A_l. The effective length L' of the resonator must be calculated via $L' = L + (n-1)\cdot l$ from the length l and refractive index n of the crystal, and the distance L between the mirrors. The first term in equation 2.19 accounts for the pump process which adds population to level 2. The second and third term describe the depopulation due to the laser process and the spontaneous emission, respectively. The evolution of the photon number with time within the cavity can further be determined by

$$\frac{\mathrm{d}q}{\mathrm{d}t} = q \cdot \left(\frac{N_2\, l\, c\, \sigma_\mathrm{em}}{L'} - \frac{1}{\tau_\mathrm{p}} \right) \tag{2.20}$$

with τ_p as the lifetime of photons within the cavity. The first term of the equation describes the adding of photons to the resonator mode by stimulated emission, and the second term the removal by loss processes. The lifetime is given as

$$\tau_\mathrm{p} = \frac{L'}{\gamma c}. \tag{2.21}$$

The losses per single pass γ are the sum of the losses γ_j introduced by the transmittance T_j of the j cavity mirrors and further resonator internal losses γ_i such that

$$2\gamma = \gamma_i + \sum_j \gamma_j \tag{2.22}$$

with

$$\gamma_j = -\ln\left(1 - T_j\right) \tag{2.23}$$

$$\gamma_i = -\ln\left(1 - L_i\right). \tag{2.24}$$

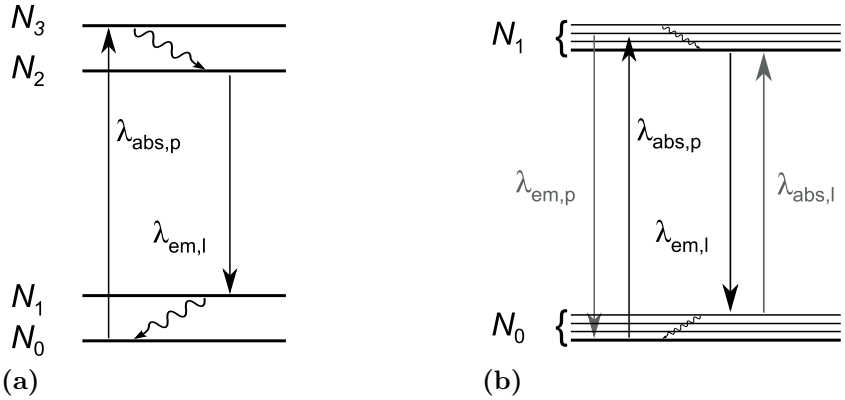

Figure 2.4: Schematic drawing of four- (a) and quasi-three-level-system (b).

The cavity internal losses γ_i can stem from various effects taking place in the gain medium or on the mirror surfaces. These can be, for example, scattering at impurities or defects of the crystal and mirror facets, and absorption effects caused by color centers or impurities.

Assuming a steady state ($\frac{\mathrm{d}N_2}{\mathrm{d}t} = 0$), the two terms in equation 2.20 must balance each other, i.e. the number of photons added through stimulated emission must equal the number of photons removed by loss processes so that $\frac{\mathrm{d}q}{\mathrm{d}t} = 0$. Above the laser threshold both terms are equal and it follows that $\frac{\mathrm{d}q}{\mathrm{d}t} = 0$ and $q = const.$ From equation 2.20 the critical population of the upper laser level can then be calculated to be

$$N_{2,\mathrm{c}} = \frac{\gamma}{\sigma_{\mathrm{em}} l}. \tag{2.25}$$

For a pumped area A_p the threshold pump power necessary to achieve this state follows as

$$P_{\mathrm{thr}} = \frac{h\ \nu_\mathrm{p}\, A_\mathrm{p}}{\tau_{\mathrm{eff}}} \cdot \frac{\gamma}{\sigma_{\mathrm{em}}}. \tag{2.26}$$

It allows for the calculation of the output power of a laser with

$$P_{\mathrm{out}} = \eta_{\mathrm{sl}} \left(P_{\mathrm{pump}} - P_{\mathrm{thr}}\right) \tag{2.27}$$

from the absorbed pump power P_{pump} and the slope efficiency η_{sl}. The parameter η_{sl} is given as

$$\eta_{\mathrm{sl}} = \eta_{\mathrm{pump}}\, \eta_{\mathrm{ol}}\, \eta_{\mathrm{OC}}\, \eta_{\mathrm{St}} \tag{2.28}$$

and thus incorporates several efficiencies influencing the laser such as the pump efficiency η_{pump}, the overlap efficiency between laser and pump mode η_{ol}, the output coupling rate through the j cavity mirrors $\eta_{\mathrm{OC}} = \frac{\gamma_{\mathrm{OC}}}{2\gamma}$ with $\gamma_{\mathrm{OC}} = \sum_j \gamma_j$, and the Stokes factor $\eta_{\mathrm{St}} = \frac{\nu_\mathrm{l}}{\nu_\mathrm{p}}$. For a given Stokes factor and slope efficiency, equation 2.28 can furthermore be used to estimate the maximum resonator internal losses. Assuming that all pump photons contribute to the laser process ($\eta_{\mathrm{pump}} = 1$) as well as a perfect overlap between pump and laser mode ($\eta_{\mathrm{ol}} = 1$) it follows together with equation 2.22 and 2.23 that

$$\gamma_\mathrm{i} = \left(\frac{\eta_{\mathrm{Stokes}}}{\eta_{\mathrm{sl}}} - 1\right) \cdot \gamma_{\mathrm{OC}}. \tag{2.29}$$

For small values of γ_{OC} it followes that

$$\gamma_{\mathrm{OC}} = \sum_j \gamma_j = \sum_j T_j. \tag{2.30}$$

2.3.2 Quasi-Three-Level-Systems

In a quasi-three-level-system the lower laser level belongs to the same Stark multiplet as the ground state (cf figure 2.4b). In this example, the same is true for the upper laser and terminal pump level although this is not a necessary condition. Since the lower laser level and ground state are now thermally coupled, their population follows a Boltzmann

distribution and can therefore no longer be assumed to be empty. As a result absorption occurs on the laser wavelength. Subsequently, the rate equations must be adapted to incorporate this effect. For the inversion density it follows that

$$\frac{\mathrm{d}N_1}{\mathrm{d}t} = W_\mathrm{p} N_0 - \frac{qc}{A_\mathrm{l} L'} \cdot (\sigma_\mathrm{em} N_1 - \sigma_\mathrm{abs} N_0) - \frac{N_1}{\tau_\mathrm{eff}} \tag{2.31}$$

while the temporal evolution of the photon number is given by

$$\frac{\mathrm{d}q}{\mathrm{d}t} = \frac{q\,c}{L'} \cdot \left[l \cdot (N_1\,\sigma_\mathrm{em} - N_0\,\sigma_\mathrm{abs}) - \gamma \right]. \tag{2.32}$$

The reabsorption of laser photons also results in an increase of the threshold pump power. Equation 2.26 transforms to

$$P_\mathrm{thr} = \frac{h\ \nu_\mathrm{p}\ A_\mathrm{p}}{\tau_\mathrm{eff}} \cdot \left(\frac{\gamma + \sigma_\mathrm{abs}\,N_\mathrm{tot}\,l}{\sigma_\mathrm{em} + \sigma_\mathrm{abs}} \right). \tag{2.33}$$

However, this does not affect the slope efficiency of a quasi-three-level-system.

2.4 Active Ions

2.4.1 The Pr^{3+}-ion

Praseodymium is the third element of the lanthanoids and carries the atomic number $Z = 59$. Doped into a crystalline host it mostly occurs trivalent with the electron configuration [Xe]$4f^2$, although the tetravalent ion with [Xe]$4f^1$ is also possible [Asp61, Hin95]. Following Hund's rules the two electrons that remain in the $4f^2$ orbital can assume 13 different states with the $^3\mathrm{H}_4$ as the ground state and the $^1\mathrm{S}_0$ at approximately $47 \cdot 10^3\,\mathrm{cm}^{-1}$ as the energetically highest manifold (see figure 2.5).

The $^3\mathrm{P}_J$ and $^1\mathrm{I}_6$ manifolds are superimposed and thermally coupled. Optical pumping into these manifolds is possible on any of the three transitions $^3\mathrm{H}_4 \rightarrow {}^3\mathrm{P}_0$,$^3\mathrm{P}_1$, and $^3\mathrm{P}_2$. The energetically lowest of these manifolds is the $^3\mathrm{P}_0$. Starting from this level, various transitions with emission wavelengths in the visible spectral range can occur. They range from the blue ($^3\mathrm{P}_1 \rightarrow {}^3\mathrm{H}_4$) through green ($^3\mathrm{P}_1 \rightarrow {}^3\mathrm{H}_5$), orange ($^3\mathrm{P}_0 \rightarrow {}^3\mathrm{H}_6$), and red ($^3\mathrm{P}_0 \rightarrow {}^3\mathrm{F}_2$), into the deep red region ($^3\mathrm{P}_0 \rightarrow {}^3\mathrm{F}_3$). These transitions typically show emission cross sections in the range of $10^{-20}\,\mathrm{cm}^2$. The small energetic distance between the $^3\mathrm{H}_J$ and $^3\mathrm{F}_J$ manifolds, which constitute as terminal levels for these transitions, allows a fast non-radiative decay into the $^3\mathrm{H}_4$ ground state. Depending on the pump transition, lasers based on Pr^{3+}-doped gain media constitute either four- ($^3\mathrm{H}_4 \rightarrow {}^3\mathrm{P}_1$, $^3\mathrm{P}_2$) or three-level lasers ($^3\mathrm{H}_4 \rightarrow {}^3\mathrm{P}_0$).

The energetic distance between the $^3\mathrm{P}_0$ and the $^1\mathrm{D}_2$ manifold is in the order of $3500\,\mathrm{cm}^{-1}$. This means that care has to be taken when selecting host materials. Depending on the exact energetic distance between $^3\mathrm{P}_0$ and $^1\mathrm{D}_2$ and the phonon spectrum of the host material a non-radiative decay $^3\mathrm{P}_0 \rightarrow {}^1\mathrm{D}_2$ can occur which leads to a depletion of the upper laser level (cf. equation 2.18, [Mel95]). Furthermore, Pr^{3+} doping concentrations above a critical value can lead to concentration quenching by cross relaxation processes (cf. figure 2.5 and [Heg82, Der03]).

Besides the intraconfigurational processes within the $4f$ orbitals, interconfigurational $4f^2 \rightarrow 4f^1 5d^1$ transitions can occur. As shown in section 2.1.3 the position of the lowest $4f^1 5d^1$ manifold strongly depends on the host lattice. In the case of hosts with weak crystal fields like fluorides, the lower edge of the transition band is usually located just above or below the $^1S_0$ state. For strong crystal fields, the splitting can lower the $4f^1 5d^1$ manifolds far below this point. The effect of this is twofold. The first problem that arises is that the $4f^1 5d^1$ manifolds can act as terminal levels for excited state absorption processes. Depending on the exact position of the lower edge of the $4f^1 5d^1$ band, ESA might occur either just for the high energy pump photons or also for some or all of the lower energy laser photons. Due to the fact that these $^3P_J \rightarrow 4f^1 5d^1$ transitions are parity allowed (cf. section 2.1.3), the associated cross sections are larger than those of the intraconfigurational transition thus rendering it unlikely that laser operation can be achieved.

The second issue that follows is due to the fact that the distance between the $^1S_0$ and the lowest $4f^1 5d^1$ manifold is small against the splitting caused by the spin-orbit interaction ($\approx 10^3\,\mathrm{cm}^{-1}$). The condition for applying the Judd-Ofelt theorem is therefore not fulfilled (cf. section 2.2.1) and results from such calculations can only be regarded as rough estimates.

The most common host materials for Pr^{3+} are fluoride materials. These host crystals exhibit low phonon energy thus minimizing the depletion if the $^3P_0$ manifold via non-radiative decay. Additionally the barycenter of the $4f^1 5d^1$ configuration in these materials experiences a comparably small shift ($\varepsilon_0 \leq 7500\,\mathrm{cm}^{-1}$) [Dor00a]. This means that even for a strong splitting between the E_g and $T_{2,g}$ manifold the lowest $4f^1 5d^1$ band is located

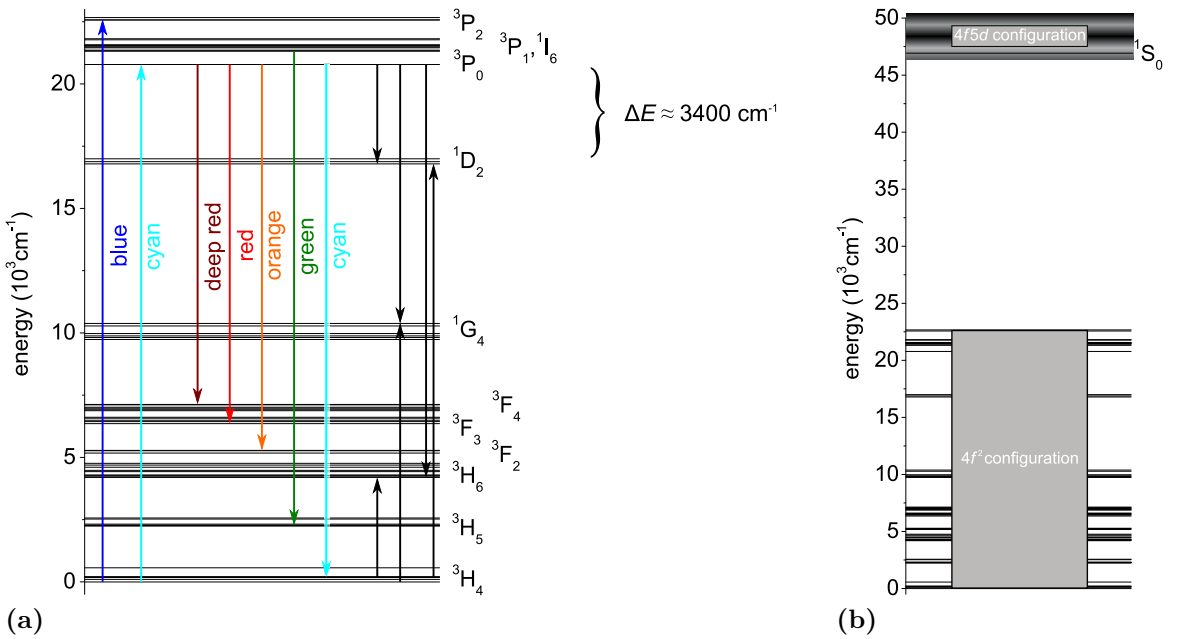

Figure 2.5: Schematic of the energy level positions of Pr^{3+}. (a) depicts the various manifolds of the $4f^2$ configuration. Relevant radiative transitions are indicated by colored arrows and non-radiative cross relaxation transitions by black arrows. (b) shows the two lowest $4f^1 5d^1$ bands in relation to the $4f^2$ manifolds.

just above or slightly below the $^1S_0$ manifold, thus rendering ESA transitions on pump or laser wavelengths impossible.

However, fluoride crystals also have drawbacks. They exhibit lower thermal conductivities and Mohs hardness than typical oxide materials for example [Agg05]. Besides this, the fabrication of high quality fluoride crystals is a challenging process as the presence of even small amounts of H_2O or O_2 can lead to the formation of oxyfluoride-compounds. These particles act as scattering centers in a gain medium and can introduce considerable losses into the cavity. To prevent the formation of such compounds it is necessary to create a high vacuum ($\leq 10^{-8}$ mbar) in the growth chamber or to perform the growth in an aggressive CF_4/HF athmosphere [Sob02]. Both techniques impose special requirements on the growth chamber.

Furthermore, the segregation coefficient (cf. section 4) of Pr^{3+} for these materials is often quite low. The most common host materials $LiYF_4$ and $LiLuF_4$ exhibit values of 0.22 and 0.15 [Ric07]. Pr^{3+}:$LiYF_4$ and Pr^{3+}:$LiLuF_4$ crystals can therefore exhibit strong dopant gradients along the growth direction.

In recent years the development of blue emitting InGaN laser diodes (LDs) and 2ωOPSL[3] has allowed efficient visible laser operation of such Pr^{3+}-doped fluoride crystals with compact resonator designs [Osi04, Ric04, Ric07, Gün11c]. A single step of intra cavity frequency doubling furthermore allows to obtain coherent radiation in the ultraviolet spectral region [Ric06, Gün11b].

In contrast, oxide crystals usually exhibit more advantageous thermomechanical properties and are easier to fabricate than fluoride hosts. However, their higher phonon energies often lead to a strong non-radiative depletion of the $^3P_0$ manifold. They also exhibit stronger redshifts of the barycenter and splitting between the E_g and $T_{2,g}$ manifolds of the $4f^15d^1$ configuration [Dor02, Rod02]. This enables ESA transitions which can prevent laser operation [Che94, Thi08].

Nevertheless several Pr^{3+}-doped oxide hosts support visible laser operation, for example the perovskites Pr^{3+}:$YAlO_3$ and Pr^{3+}:$LuAlO_3$ [Fib09, Fec09]. The most promising material so far is the hexaaluminate Pr,Mg:$SrAl_{12}O_{19}$. It was already investigated in some depth regarding its spectroscopic properties and also laser operation was shown in pulsed and cw regime [Mer96, Fec11, Fec12]. The results make the class of the hexaaluminates interesting candidates for doping with trivalent praseodymium and thus several of these materials will be investigated in this thesis.

2.4.2 The Ho^{3+}-ion

Holmium is the eleventh element of the lanthanoid group and carries the atomic number $Z = 67$. Doped into a crystalline host it occurs trivalent with the electron configuration [Xe]$4f^{11}$. The $4f^{11}$ configuration consists of 41 manifolds with the $^5I_8$ as the ground state (see figure 2.6).

Starting from the multiplet of the superimposed $^5S_2$ and $^5F_4$ manifolds, two transitions in the visible spectral range are present: $^5S_2 \rightarrow {}^5I_8$ in the green and $^5S_2 \rightarrow {}^5I_7$ in the deep red region. Due to the long lifetime of the $^5I_7$ multiplet [Wal98], this manifold can act as

[3]Frequency doubled **O**ptically **P**umped **S**emiconductor **L**asers

a population trap that can lead to self terminating behaviour of a laser operating on the transition $^5S_2 \rightarrow {}^5I_7$.

The $^5S_2$ manifold can be populated by pumping into the energetically higher lying multiplets $^5F_3$,$^5F_2$,$^3K_8$,$^5F_1$, and $^5G_5$, which are all thermally coupled. Strong absorption bands are often present in the 480 nm ($^5I_8 \rightarrow {}^5F_3$) and 450 nm range ($^5I_8 \rightarrow {}^5F_1$, $^5G_5$). Since the distance between the $^5S_2$ manifold and the $^5F_3$ is approximately 1900 cm^{-1}, sufficiently high phonon energies can cause a fast non-radiative decay and therefore an efficient population process for the $^5S_2$ manifold.

The energetic distance towards the $^5F_5$ multiplet, which is the next energetically lower level, is approximately 3000 cm^{-1}. This is a comparable situation as for the $^3P_0$ and $^1D_2$ manifolds in Pr^{3+}, and similarly the phonon spectrum of possible host systems has to be taken into account to prevent a pronounced non-radiative decay between the manifolds $^5F_5$ and $^5S_2$.

Unfortunately the large amount of manifolds at higher energies (cf. [Die63]) present a high number of possible terminal states for ESA transitions. Since these are intraconfigurational transitions they exhibit narrow linewidth with cross sections in the range of 10^{-21} cm^2. Therefore the presence of ESA processes on pump and laser wavelengths is highly sensitive to the exact position of the various Stark levels. In contrast to Pr^{3+}, the distance between the $4f^{11}$ and the $4f^{10}5d^1$ configuration is large enough to make interconfigurational ESA transitions in the relevant wavelength region impossible. The energetic distance between the two configurations also allows for the application of the Judd-Ofelt theory and thus the calculation of the energetic positions of the various Stark levels with reasonable results [Wal05].

Due to the small energetic gap between the $^5S_2$ and the $^5F_5$ manifold, the most promising host materials to obtain visible laser radiation with Ho^{3+} are low phonon fluoride hosts. So far, the only laser operation in the green spectral region was achieved in Ho^{3+}:CaF_2 at

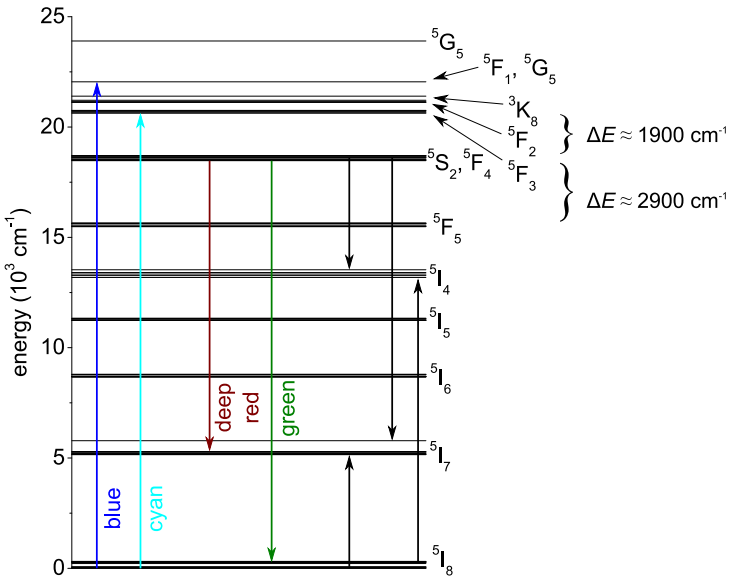

Figure 2.6: Exemplary Ho^{3+} energy level schemes. Radiative transitions are indicated by colored arrows and non-radiative transitions by black arrows.

a temperature of 77 K under Xe-flashlamp pumping [Vor65]. In the deep red region laser oscillation was realized in Ho^{3+}:$LiYF_4$ at 90 K and in Ho^{3+}:$YAlO_3$ at room temperature, both under Xe-flashlamp pumping [Pod76, Kam86]. As with praseodymium, the development of new pump sources in the blue spectral region might allow for further exploitation of the transitions in the visible range offered by the Ho^{3+}-ion.

3 Host Materials

This chapter will give an introduction to the host materials that were investigated in this thesis. The first section will describe the three oxide crystals that were chosen as Pr^{3+} host systems, namely $SrAl_{12}O_{19}$ (SRA), $CaAl_{12}O_{19}$ (CAlO), and $LaMgAl_{11}O_{19}$ (LMA). All of these materials belong to the group of the hexaaluminates.

The second part deals with the two fluoride crystals $LiLuF_4$ (LLF) and LaF_3, where LLF was only employed as a host for Ho^{3+} while LaF_3 served as a Pr^{3+} host as well. The basic crystallographic properties of the systems will be given and their suitability for their respective doping ion will be discussed. Furthermore, the Pr^{3+}-doped crystals will be compared with the most common Pr^{3+} host $LiYF_4$ (YLF).

3.1 Hexaaluminates $SrAl_{12}O_{19}$, $CaAl_{12}O_{19}$, and $LaMgAl_{11}O_{19}$

Recently it was shown that the hexaluminate $SrAl_{12}O_{19}$ is very interesting as a Pr^{3+} host system as it exhibits no ESA on neither the pump nor on any of the possible laser wavelengths [Fec11, Fec12]. This is due to the relatively high energetic position of the multiplets composing the $4f^15d^1$ configuration. The lowest multiplet is located $46 \cdot 10^3\,cm^{-1}$ above the ground state and therefore above the $^1S_0$ manifold of the $4f^2$ configuration. This can be attributed to the high number of 12 ligands coordinating the Sr^{2+}-ion which is an intrinsic attribute of the hexaaluminate structure. Therefore other systems belonging to this class are likely to exhibit similar benificial properties. The two systems $CaAl_{12}O_{19}$ and $LaMgAl_{11}O_{19}$ were identified as the most promising and will be, together with $SrAl_{12}O_{19}$, discussed in detail[1].

Crystallographic Properties

All three crystals share the hexagonal magnetoplumbite structure which belongs to the space group $P6_3/mmc$ (cf. figure 3.1). Their respective lattice constants are 22.0 Å (SRA), 21.89 Å (CAlO), and 21.97 Å (LMA) along the c-axis and 5.57 Å, 5.56 Å, and 5.59 Å along the a-axis [Kim90, Uts88, Efr88]. A unit cell consists of two formula units and 64 ions (see figure 3.1) and exhibits two sites which can be occupied by the Pr^{3+}-ion. Both are $2d$ sites (Wykoff notation) with D_{3h} symmetry. However, in LMA ions occupying this site can experience a displacement if a local Mg deficiency is present. In this case the site becomes a $6h$ [Par97].

[1] At this point it should be noted that several of the experiments concerning Pr,Mg:SRA and Pr:LMA were conducted in colaboration with Daniel-Timo Marzahl within the framework of his diploma thesis. For more information the reader may be referred to [Mar12]

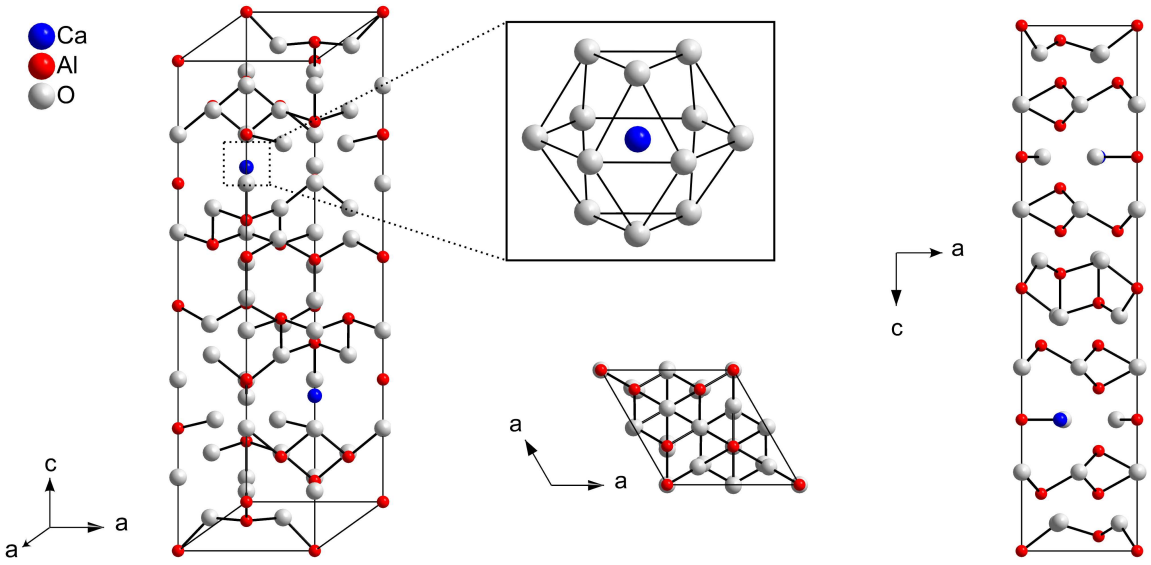

Figure 3.1: Unit cell of $CaAl_{12}O_{19}$ as example for the magnetoplumbite structure. The inset shows the $2d/6h$ Ca^{2+} site with the corresponding cuboctahedral coordination sphere.

The $2d$ as well as the $6h$ species is coordinated by twelve oxygen ligands. Six of these ions form an interspinel hexagonal mirror plane around the site which is oriented perpendicular to the c-axis (see figure 3.1 inset). The distance between each of these six ligands and the coordinated ion is 2.787 Å for SRA, 2.785 Å for CAlO, and 2.798 Å for LMA. The remaining six ions are located outside of this plane in a distance of 2.746 Å, 2,693 Å, and 2.681 Å, respectively [Kim90, Uts88, Efr88]. Dorenbos reported that SRA and LMA exhibit comparable values in terms of barycenter shift and splitting of the $4f^n5d^1$ configuration [Dor02]. Although no data is given for CAlO, the strong similarity of the crystallorgaphic properties suggests comparable values in this regard (cf. section 2.1.3). This indicates that CAlO and LMA are also feasible host materials for trivalent praseodymium.

A disadvantage of SRA and CAlO is their incongruent melting behaviour. The phase diagrams of the respective binary systems are depicted in figure 3.2. It can be seen that if a stoichiometric melt of either of the desired phases SA_6 (SRA) or CA_6 (CAlO) is cooled down, Al_2O_3 will cristallize and the composition of the melt will change. It is therefore not possible to grow either of the two phases from such a melt. However, as both phase diagrams show, it is possible to grow the respective phase from a non-stochiometric melt. This approach was shown for $SrAl_{12}O_{19}$, yielding crystals of sufficient quality to achieve laser operation [Mer96, Fec11]. Since the phase diagram for $CaAl_{12}O_{19}$ is very similar, an analogous melt composition should allow crystals of comparable quality to be obtained. Still, the regions of the phase diagrams which allow single phase growth of either of the two crystals are narrow and therefore the yield of suitable material is limited. Contrary to this, LMA melts congruently which allows it to be grown from a stoichiometric melt [Abr87].

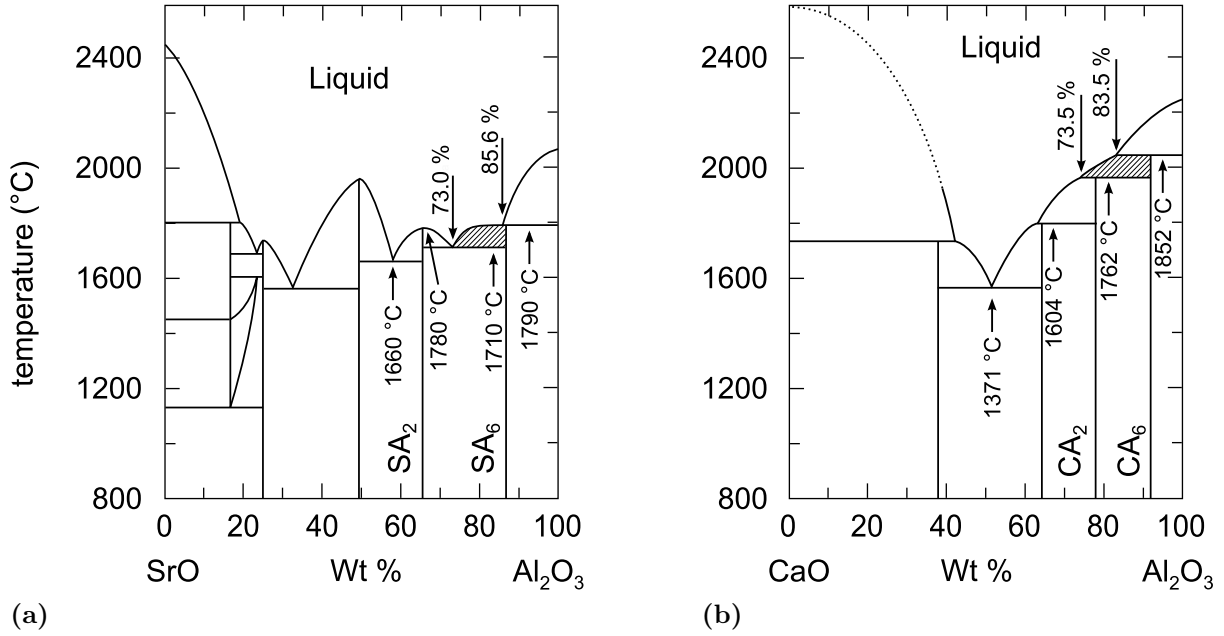

Figure 3.2: Phase diagrams of the binary systems (a) SrO - Al_2O_3 ([Gan79]) and (b) CaO - Al_2O_3 ([Jer01]) displaying the relevant areas. Shaded areas indicate crystallization of the desired phases (SA_6 and CA_6). Peritectic points are at 85.6 % (SRA) and 85.7 % (CAlO).

Although the ionic radius of trivalent praseodymium is smaller than that of divalent strontium (1.18 Å : 1.31 Å, nine-fold coordinated[2] [Sha69]), Merkle *et al.* reported a segregation coefficient of $\kappa_{\mathrm{Pr:SRA}} = 0.91$ for Pr^{3+}:$SrAl_{12}O_{19}$ [Mer96]. This value close to 1 is very beneficial during crystal growth as it allows crystals to be grown with a relatively homogeneous Pr^{3+} concentration throughout the whole boule. This is a strong advantage over the commonly used host YLF where the segregation coefficient is only 0.22 [Ric07], which leads to a strong concentration gradient along the growth direction of the crystals.

In contrast to $SrAl_{12}O_{19}$, Merkle et al. reported that only a small amount of Pr^{3+} is incorporated into $CaAl_{12}O_{19}$ [Mer96]. Since the ionic radii of Sr^{2+} and Ca^{2+} in high order coordination spheres are very similar (1.35 Å : 1.40 Å, twelve-fold coordinated) this seems surprising and will be investigated in more detail.

For LMA no segregration coefficient is reported. However, the radii of La^{3+} and Pr^{3+} are quite comparable (1.15 Å : 1.14 Å, eight-fold coordinated) and a favorable segregation coefficient is thus likely.

The difference in valency between Sr^{2+}, Ca^{2+}, and Pr^{3+} necessitates a charge compensation in Pr^{3+}-doped SRA and CAlO crystals. Both, Merkle [Mer96] and Fechner [Fec11], have reported good results by substituting Al^{3+} with Mg^{2+} in Pr,Mg:SRA. Therefore, in this work this approach will be followed as well. For LMA no charge compensation is necessary since both ions, La^{3+} and Pr^{3+}, share the same valency.

[2]Where ionic radii are not reported for a twelve-fold-coordination sphere, values for the next lower sphere with known values are given.

Multiphonon Processes

In Pr,Mg:$SrAl_{12}O_{19}$ the multiphonon relaxation rate from the $^3P_0$ into the $^1D_2$ manifold is quite low and does not present a dominant depletion channel for population accumulated in the upper laser level [Fec11]. This can be attributed to the low cutoff energy of the phonon spectrum of SRA at 761 cm^{-1} [Fec12] and the energetic distance between the levels $^3P_0$ and $^1D_2$ of $\Delta E \approx 3400\,cm^{-1}$ [Zan97]. Taking these two values into account, the condition stated in section 2.2.1 is fulfilled.

The phonon spectra of $CaAl_{12}O_{19}$ and $LaMgAl_{11}O_{19}$ were obtained by recording the infrared transmission spectra of mixtures of KBr with CAlO and LMA powder samples[3] and are depicted in figure 3.3 [Wei88]. The absorption bands around 3500 cm^{-1} and 1500 cm^{-1} are due to molecular oscillations of the crystallization water of KBr while the peaks around 2900 cm^{-1} are caused by an organic contamination of the aparatus. Due to the band gap of KBr, this method does not yield results below 450 cm^{-1}.

The peak structure below 1000 cm^{-1} represents the phonon spectrum. It shows cutoff

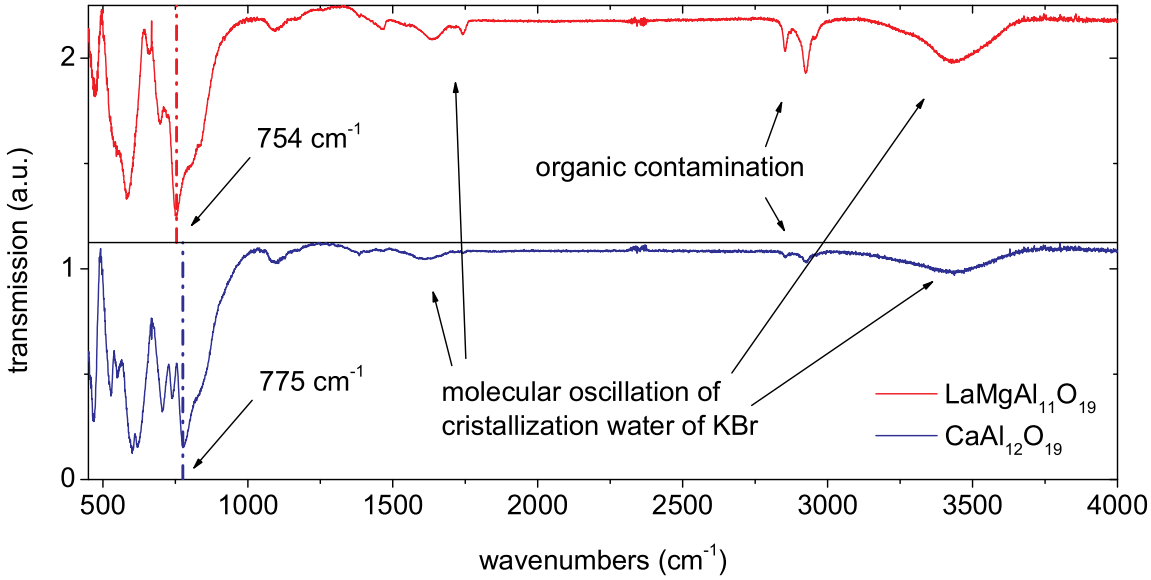

Figure 3.3: Infrared transmission spectra of $CaAl_{12}O_{19}$ and $LaMgAl_{11}O_{19}$ powder deluted in KBr.

energies of 775 cm^{-1} for CAlO and 754 cm^{-1} for LMA and is therefore in both cases in good agreement with that reported for SRA. Since the positions of the $4f^2$ energy levels are only weakly affected by the host system, CAlO and LMA can be expected to show multiphonon relaxation rates comparable to those of SRA.

Thermomechanical Properties

The thermal conductivity κ of a material can be determined by employing the relation

$$\kappa = c_p \, \rho \, \alpha_{th} \tag{3.1}$$

[3]The measurements were carried out by B. Herden at the FH Münster.

with ρ and c_p as the density and specific heat of the system, respectively [Mor98, Mor08]. In uniaxial crystals the thermal diffusivity α_th is dependent on the crystallographic axis, and therefore the thermal conductivity along the c-axis ($\kappa_{\parallel\mathbf{c}}$) and perpendicular to it ($\kappa_{\perp\mathbf{c}}$) will differ.

The thermal diffusivity was determined with an *ai-Phase Mobile 1* by sending temperature waves with varying frequencies ω through samples with thickness d of each crystal and measuring their phase shift $\Delta\Theta$ after passing through the crystal. α_th can then be calculated from

$$\alpha_\mathrm{th} = \frac{\omega}{2}\left(\frac{\Delta\Theta_{\parallel\mathbf{c},\perp\mathbf{c}} + b}{d}\right)^{-2} \tag{3.2}$$

with b being a constant.

Care has to be taken when dopant ions are introduced into the lattice. Such ions act as point defects of the lattice structure which induce phonon scattering. Therefore, the thermal conductivity is expected to change with increasing doping concentration. Phonon scattering can also occur via umklapp processes, but at room temperature the scattering at point defects can be regarded as the dominant factor [Cal60]. In this work the thermal conductivity was investigated in dependence of the doping concentration on 400 µm - 500 µm thick, polished samples from each obtained boule (see section 4.3).

If the thermal conductivities of the undoped and fully doped lattice are known, a prediction of its progression for arbitrary doping concentrations can be made [Kle60]. However, the parameter for a $PrMgAl_{11}O_{19}$ has not been reported so far. Therefore only experimental results will be presented[4].

The results for Pr,Mg:$SrAl_{12}O_{19}$ are plotted in figure 3.4. The density and specific heat used for equation 3.1 are depicted in table 3.1. For a dopant concentration of 0.9 at% Pr^{3+}, thermal conductivities of 10.5 $\mathrm{W\,m^{-1}\,K^{-1}}$ ($\perp\mathbf{c}$) and 5.6 $\mathrm{W\,m^{-1}\,K^{-1}}$ ($\parallel\mathbf{c}$) were determined (cf. table 3.1). These values drop to 8.2 $\mathrm{W\,m^{-1}\,K^{-1}}$ ($\perp\mathbf{c}$) and 4.9 $\mathrm{W\,m^{-1}\,K^{-1}}$ ($\parallel\mathbf{c}$) for a 5 at% doped crystal. Considering the difference in mass between Sr^{2+} and Pr^{3+} this decrease is comparatively small. This can be explained by close examination of the lattice structure. In a simplified approach phonons can be described as linear chains of oscillating lattice ions which follow a distinct crystallographic axis. It then follows from figure 3.1 that only a small number of these chains contain a Sr^{2+}-ion. Since only a small number of these ions are substituted with Pr^{3+}, the perturbation caused by the dopant is comparatively small. This may also explain the strong difference between $\kappa_{\parallel\mathbf{c}}$ and $\kappa_{\perp\mathbf{c}}$, because a phonon travelling along the c-axis is more likely to encounter an Sr^{2+}-ion than a phonon travelling perpendicular to it (cf. figure 3.1). Nevertheless it should be noted that this is a simplified model and does not describe all possible phonon modes.

For LMA the thermal conductivities are considerably lower. In an undoped lattice, the thermal conductivity perpendicular to the c-axis is 4.9 $\mathrm{W\,m^{-1}\,K^{-1}}$ while it is 3.4 $\mathrm{W\,m^{-1}\,K^{-1}}$ parallel to it. The contrast towards SRA is caused by the fact that although all three systems share the same crystallographic strucure, in LMA two of the 24 Al^{3+}-ions in the unit cell are fully replaced by Mg^{2+}-ions. Because of the difference in mass and

[4] Since SRA and CAlO require charge compensation (cf. section 4.3.1 and 4.3.2) these crystals are doped with equal amounts of Pr^{3+} and Mg^{2+} which means that the fully doped lattice for all three systems is $PrMgAl_{11}O_{19}$.

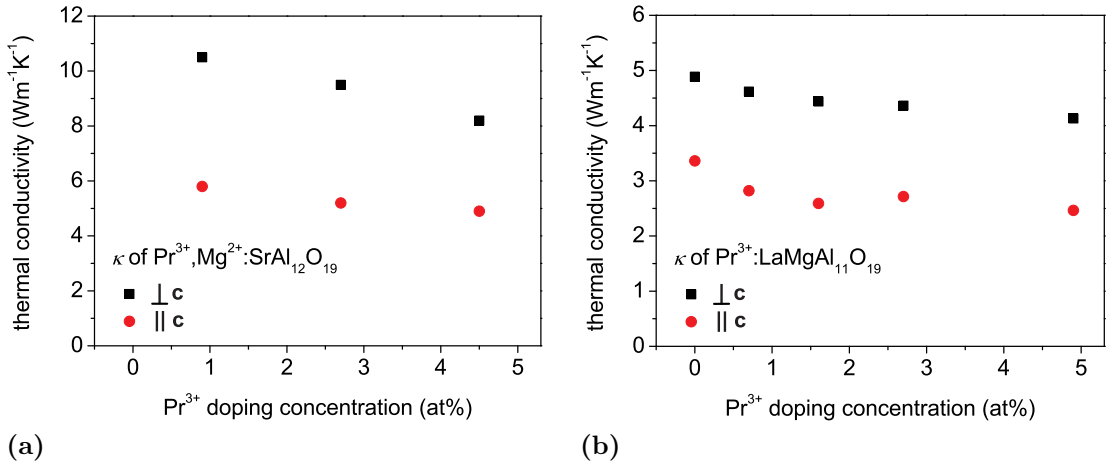

Figure 3.4: Thermal conductivities of Pr,Mg:SRA and Pr:LMA in dependence of the doping concentration.

ionic radius between the two ions ($\Delta m = 2.7\,\mathrm{u} = 10\,\%$; $\Delta r = 0.19\,\text{Å} = 49\,\%$), Mg^{2+}-ions perturb the lattice, causing phonon scattering, and thus lower the thermal conductivity. For an increasing dopant concentration the progression of the thermal conductivity is similar to the case of Pr,Mg:SRA. Both values show a decrease between 15 % and 25 % ($\kappa_{\parallel \mathbf{c}} = 2.5\,\mathrm{W\,m^{-1}\,K^{-1}}$, $\kappa_{\perp \mathbf{c}} = 4.1\,\mathrm{W\,m^{-1}\,K^{-1}}$ for 5 % Pr^{3+}).

Due to the small amount of single crystalline Pr^{3+},Mg^{2+}:$CaAl_{12}O_{19}$ that was obtained, it was not possible to determine the thermal conductivity of this system.

For undoped $LiYF_4$ Aggarval et al. reported thermal conductivities at room temperature of $\kappa_{\parallel \mathbf{c}} = 7.2\,\mathrm{W\,m^{-1}\,K^{-1}}$ and $\kappa_{\perp \mathbf{c}} = 5.3\,\mathrm{W\,m^{-1}\,K^{-1}}$ [Agg05]. Therefore SRA and CAlO are likely to be more resistent to thermal effects.

The hardness of SRA, CAlO, and LMA was classified according to the Mohs scale with values of 9, 8.5, and 8.5, respectively. Fluoride crystals are mostly much softer with YLF exhibiting a value of 4.5 [Sha69]. It is therefore more likely to crack under mechanical stress than the hexaalumintates. Harder materials also mean a more comfortable handling since they are less prone to scratching. All obtained values are listed in table 3.1.

3.2 Fluoride Materials

Although fluorides generally exhibit less favorable thermomechanical properties than oxides and their growth is more challenging, they also have advantages. Compared to oxides they often exhibit higher energetic positions for the $4f^n5d^1$ multiplets which prevents ESA transitions on pump and laser wavelengths. Furthermore, their low phonon energies lead to low non-radiative decay rates for the multiphonon transitions occuring in Pr^{3+} and Ho^{3+}-doped crystals. Therefore two fluoride systems were investigated in this work. LaF_3 was employed as a host for both Pr^{3+} and Ho^{3+} while $LiLuF_4$ (LLF) was only doped with Ho^{3+}. Pr^{3+}:$LiLuF_4$ has already been the subject of previous works [Cor07, Ric07].

3.2.1 $LiLuF_4$

Crystallographic Properties

The system $LiLuF_4$ crystallizes in a tetragonal structure which belongs to spacegroup $I4_1a$. The unit cell is depicted in figure 3.5. Its lattice constants are 10.55 Å along the c-axis and 5.13 Å along the a-axis [Ran02]. Four formula units build one unit cell with 24 ions. Rare earth ions doped into this lattice can substitute each of the four Lu^{3+}-ions which are all located on $4b$ (Wykoff notation) sites with symmetry S_4. Each site is coordinated by eight fluorine ions which form a dodecahedral coordination sphere. The ligands are located in distances between 2.23 Å and 2.28 Å. From data reported by Dorenbos for the shift and splitting of the $4f^n5d^1$ configuration, it can be seen that the edge of the lowest $4f^n5d^1$ band should be above $45 \cdot 10^3\,cm^{-1}$ [Dor00a]. This makes it not only an excellent host material for Pr^{3+} but also for other rare-earth ions.

LLF is, like LaF_3, a congruently melting system and exhibits a melting point of 850 °C [Har83]. Figure 3.6 displays the phase diagram with the relevant LLF phase. Due to various prior experiments conducted at the ILP [Ric08, Gün11a, Han12], the means for fabricating $LiLuF_4$ are well developed and high quality crystals can be produced.

Although the ionic radii of Ho^{3+} and Lu^{3+} are slightly different (1.16 Å : 1.11 Å, eight-fold coordinated [Kam90]), the segregation coefficient is generally assumed to be close to unity [Ver12].

Multiphonon Processes

So far multiphononic transition processes have not been investigated in Ho^{3+}:$LiLuF_4$. However, LLF is isomorphous to YLF and therefore the energetic position of the $4f^{11}$ multiplets of Ho^{3+} varies only marginally [Wal05]. The major factor leading to a difference in the multiphononic decay rates can therefore be assumed to be the difference in phonon energy. For LLF this can be deduced from Raman spectroscopic measurements on $LiYF_4$ and $LiGdF_4$, reported by Zhang *et al.* [Zha94]. They reported phonon cutoff energies of $450\,cm^{-1}$ and $430\,cm^{-1}$, respectively. Since the mass of Lu^{3+} is bigger than Y^{3+} and Gd^{3+} it can be assumed that the cutoff energy of $LiLuF_4$ will be lower than $430\,cm^{-1}$ [Sch04].

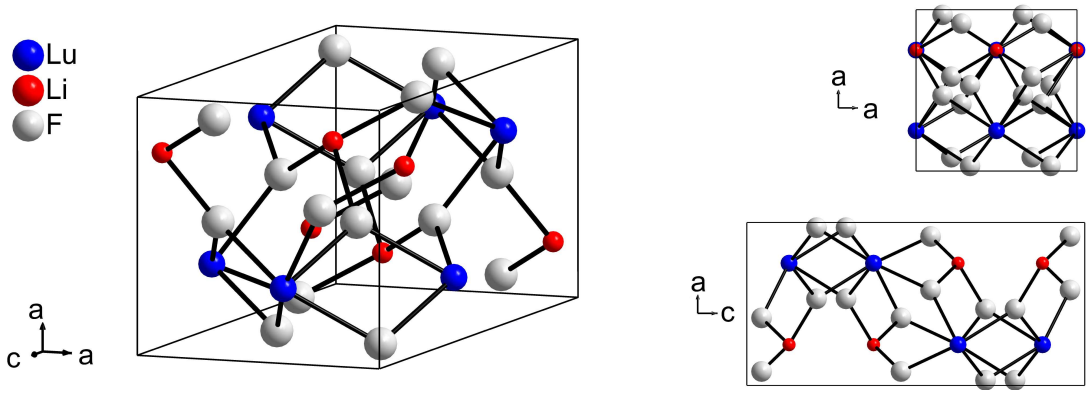

Figure 3.5: Unit cell of $LiLuF_4$.

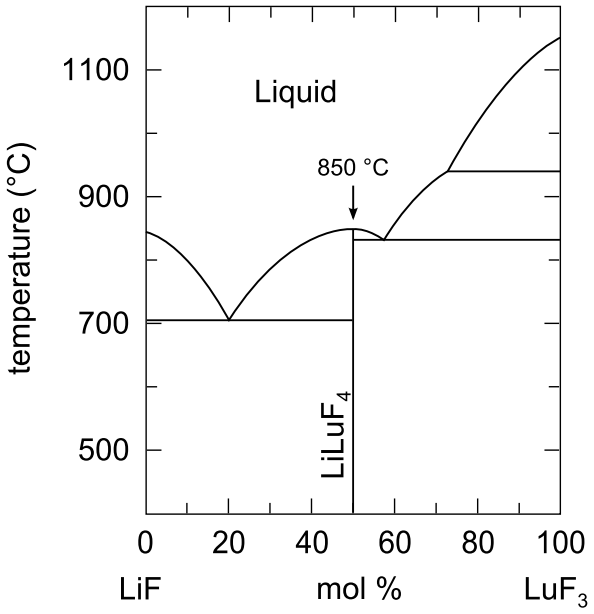

Figure 3.6: Phase diagram of the binary system LiF - LuF_3 with the relevant phase [Har83].

The results presented by Riseberg indicate that for an energy gap of 2800 cm^{-1} and a phonon energy of 430 cm^{-1} the non-radiative decay time should be between a few hundred µs and a few ms [Ris68]. This somewhat contradicts results obtained by Basiev for Ho^{3+}:$LiYF_4$. Here the effective lifetime of the $^5S_2$ manifold is given as 59 µs [Bas96] which together with the radiative lifetime of 468 µs reported by Walsh [Wal05] leads to a non-radiative lifetime in the order of a few ten µs.

It is unclear whether the difference in phonon energy between $LiYF_4$ and $LiLuF_4$ is large enough to cause such deviation. Therefore further spectroscopic measurements are necessary in order to assess the suitibility of Ho^{3+}:LLF as a gain medium for green solid state lasers.

Thermomechanical Properties

The thermal conductivity of undoped $LiLuF_4$ was studied in detail by Aggarwal *et al.* [Agg05]. They reported thermal conductivities at room temperature of $\kappa_{\parallel \mathbf{c}} = 6.3\,\mathrm{W\,m^{-1}\,K^{-1}}$ and $\kappa_{\perp \mathbf{c}} = 5.0\,\mathrm{W\,m^{-1}\,K^{-1}}$ which are slightly lower than the values reported for $LiYF_4$. Like YLF and LaF_3 it is therefore susceptible to cracking by thermally induced stress.

Additionally, like the other fluorides, its hardness is quite low with a value of only 3.5 on the Mohs scale.

3.2.2 LaF_3

Crystallographic Properties

The simple fluoride LaF_3 has a hexagonal structure (cf. figure 3.7) which belongs to the space group $P6_3/cm$. The lattice constants are 7.19 Å and 7.37 Å for the a- and c-axis, respectively [Udo08]. The unit cell contains six formula units and thus 24 ions in total.

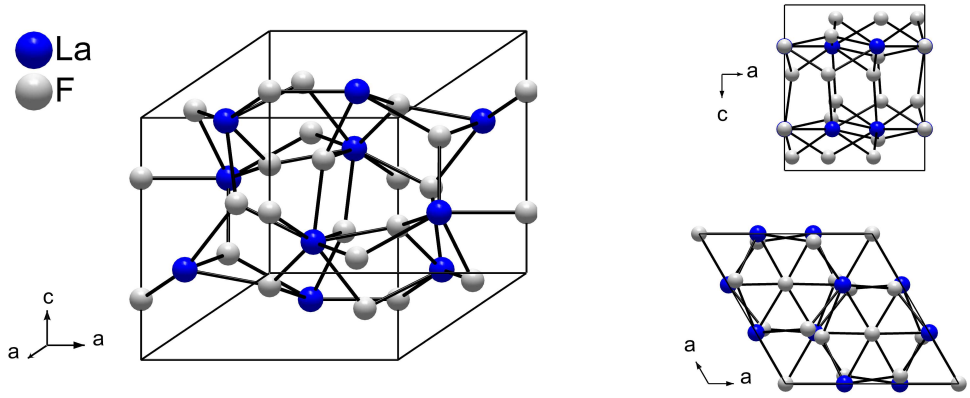

Figure 3.7: Unit cell of LaF_3.

All six La^{3+}-ions occupy $6c$ sites (Wykoff notation) with a C_2 symmetry. Each ion is coordinated by nine fluorine ligands which are located at a distance between 2.416 Å and 2.641 Å in the shape of a five-capped trigonal prism [Dor00a]. The lower symmetry of the coordination sphere causes a splitting of the $4f^n5d^1$ configuration of approximately $11 \cdot 10^3\,cm^{-1}$[Dor00a]. However, the barycenter shifts only about $5600\,cm^{-1}$. This leads to an energetic position of the lowest $5d$ band in direct vicinity of the $^1S_0$ manifold [Kru66] which makes ESA transitions unlikely.

Unlike YLF, LaF_3 melts congruently with a melting temperature of $T_{melt} = 1487\,°C$. Contrary to most other rare-earth trifluorides, no phase transition occurs between the melting point and room temperature [Sta00]. The formation and subsequent inclusion of secondary phases during the growth process can therefore be ruled out.

An advantage of LaF_3 as a Praseodymium host is the very similar ionic radius of La^{3+} and Pr^{3+}. Considering an eight-fold coordination sphere, these radii are 1.28 Å (La^{3+}) and 1.32 Å(Pr^{3+}) [Kam90]. This means that, like in the case of the hexaaluminates, the segregation coefficient of Pr^{3+} in LaF_3 can be expected to be closer to 1 than in $LiYF_4$ and will be investigated further.

Multiphonon Processes

In Pr^{3+}:LaF_3 the multiplets $^3P_0$ and $^1D_2$ have an energetic distance of approximately $3700\,cm^{-1}$ [Car69] while the cutoff frequency of the phonon spectrum is at $340\,cm^{-1}$ [Yen64]. The resulting non-radiative lifetime is therefore in the order of several seconds. Taking into account that the value reported for the radiative lifetime is several orders of magnitude smaller ($\tau_{rad} = 51\,\mu s$ [Heg82]), it can be assumed that almost all ions excited into the ^3P_J multiplet decay radiatively.

A similar situation can be found in Ho^{3+}:LaF_3. Here non-radiative coupling of the manifolds $^5S_2$ and $^5F_5$ must be considered. Although the energetic distance is only $2800\,cm^{-1}$, the reported non-radiative lifetime of the $^5S_2$ at 4 K is approximately 6 ms while the radiative lifetime is 605 µs [Moo70, Ris68]. It follows from equation 2.18 that the radiative quantum efficiency should be in the order of 90 %. However, since processes involving phonons are temperature dependent, the quantum efficiency will decrease towards room temperature.

The low non-radiative decay rates also present problems. In Pr^{3+} the depopulation of the lower laser levels, especially the $^3H_5$ and $^3H_6$ manifolds rely on a non-radiative decay into the $^3H_4$ ground state. The energetic distances $\Delta E_{^3H_6,^3H_5}$ and $\Delta E_{^3H_5,^3H_4}$ are 1900 cm^{-1} and 1700 cm^{-1} respectively and therefore non-radiative lifetimes in the order of a few ten to a few hundred µs are to be expected [Cas65, Car69]. Since the radiative lifetime of the $^3P_0$ manifold is in the same order of magnitude, population trapping in the intermediate levels might occur. This effect could have an influence on the temporal characteristics of a laser and might lead to self terminating behaviour.

Ho^{3+} again exhibits a similar problem. Here the pump ($^5F_3$) and upper laser level ($^5S_2$) are separated by 1800 cm^{-1} and must be coupled via a non-radiative decay to allow for an efficient transfer of population. Riseberg reported a non-radiative decay rate at room temperature of $\approx 5500\,s^{-1}$ which means that the non-radiative lifetime is in the order of 20 µs [Ris68]. Therefore, approximately 72 % of the population excited into the $^5F_3$ manifold will decay via multiphonon relaxation into the $^5F_4$,$^5S_2$ multiplet. Since the lifetime of the $^5F_4$,$^5S_2$ multiplet is an order of magnitude longer, this process can be regarded as sufficiently efficient. However, once laser oscillation sets in, the transfer might not be fast enough to ensure a constant population in the upper laser level. Experiments must determine whether or not this effect presents a problem for laser operation.

Thermomechanical Properties

The thermal conductivity of LaF_3 was reported in two publications. The values given are 2.1 $W\,m^{-1}\,K^{-1}$ and 5.1 $W\,m^{-1}\,K^{-1}$ [Pop12, Kle67] where the first value given is $\kappa_{\parallel \mathbf{c}}$ while the second is not specified. Since the two values deviate quite strongly from each other and furthermore no data is given for $\kappa_{\perp \mathbf{c}}$, the thermal conductivity was measured on several undoped LaF_3 samples with the method presented in section 3.1. The resulting values are 2.1 $W\,m^{-1}\,K^{-1}$ ($\kappa_{\perp \mathbf{c}}$) and 2.6 $W\,m^{-1}\,K^{-1}$ ($\kappa_{\parallel \mathbf{c}}$) and are thus comparable with the more recent publication by Popov *et al.* These low values make LaF_3 very prone to damages caused by thermal stress. Therefore, care must be taken during the growth process and when high pump powers are applied.

			$SrAl_{12}O_{19}$	$CaAl_{12}O_{19}$	$LaMgAl_{11}O_{19}$	LaF_3	$LiLuF_4$
acronym			SRA	CAlO	LMA	LaF	LLF
lattice			hex.	hex.	hex.	hex.	tetr.
space group			194 $P6_3/mmc$	194 $P6_3/mmc$	194 $P6_3/mmc$	185 $P6_3/cm$	88 $I4_1a$
coordination number			12	12	12	9	8
formula units per unit cell			2	2	2	6	4
cation density	[g cm^{-3}] [10^{21} cm^{-3}]		0.49 3.39	0.23 3.41	0.78 3.36	4.21 18.26	4.21 14.49
density	[g cm^{-3}]		4.02	3.84	4.27	5.93	6.19
lattice constants	[Å]	c-axis a-axis	22.00 5.57	21.89 5.56	21.97 5.59	7.35 7.19	10.55 5.13
unit cell volume	[Å^3]		590.43	586.94	594.49	329.26	277.64
thermal conductivity	[W m^{-1} K^{-1}]	$\kappa_{\parallel \mathbf{c}}$ $\kappa_{\perp \mathbf{c}}$	10.5 5.6	- -	3.4 4.9	2.6 2.1	6.3 5.0
Mohs hardness			9	8.5	8.5	3.5	3.5
$E_{\mathrm{phon,max}}$	[cm^{-1}]		761	775	754	340	<430
T_{melt}	[°C]		1790	1852	1910	1487	850
specific heat	[J g^{-1} K^{-1}]		0.8	-	0.7	0.5	0.5
congruent melt			no	no	yes	yes	yes

Table 3.1: Relevant properties of materials investigated in this thesis. The thermal conductivity is given for room temperature. All references can be found in table A.1.

4 Crystal Growth

This chapter will deal with the techniques used to fabricate the rare-earth-doped single crystals investigated in this thesis. Two different techniques and three crystal growth facilities were employed. The first part will introduce the general setups and parameters of the growth methods employed at the Institute of Laser-Physics while the second part will deal with the specifications of the growth facilities. The third part will present the results of the crystal growth experiments.

4.1 Growth Techniques

4.1.1 Czochralski Technique

The main technique for the growth of crystals used in this thesis was the Czochralski method. It was developed by Jan Czochralski in the early 20^{th} century [Czo18]. Due to its widespread use in the semiconductor industry where it is employed to grow large sized silicon crystals it is by now one of the most used methods to grow single crystals. This has led to its ongoing improvement since the 1950s [Sch00].

Setup

The basic setup for the Czochralski method is sketched in figure 4.1. For the growth of oxide crystals, a tube made of fused silica glass is placed on top of a pedestal made from ceramic Al_2O_3 disks. From the inside it is insulated with a layer of ZrO_2 felt mats and filled up with grains of fused ZrO_2. The crucible is placed radially centered inside the bed of grains. The insulation setup minimizes the heat loss through the outer crucible wall. The crucible is then partially closed off with an Ir-ring which acts as a heat shield and serves two purposes. First it reflects part of the heat radiated by the surface of the melt back onto it and thus further reduces the heat loss. Secondly the reflected heat leads to smaller temperature gradients on the surface of the melt which is beneficial for the growth process. Above the crucible, the wall of the tube is insulated with several layers of ZrO_2 felt and on top closed with an Al_2O_3 disk. This dampens the temperature gradients above the crucible and prevents the part of the crystal that exits the crucible from thermal shock and cracking.

The principal setup for the growth of fluoride crystals is very similar, although different materials are used. This is necessary since oxygen based materials would lead to a contamination of the growth atmosphere with O_2. This would facilitate the formation of oxyfluoride compounds in the melt. Incorporated into a crystal, such compounds can cause scattering and would severly affect the optical quality of the boules. Zirconia can therefore not be used for growing fluorides. Instead, the insulation setup consists of an

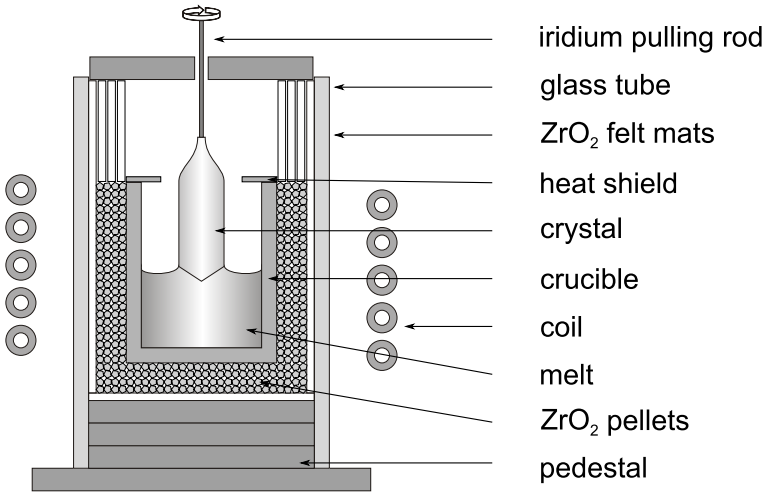

Figure 4.1: Schematic setups for Czochralski growths.

outer crucible made from vitreous carbon which is filled with hollow carbon spheres in which the inner crucible is set. The heat shield is also made of vitreous carbon.

The setup is placed within a watercooled induction coil inside the growth chamber. The coil is driven by a high frequency generator (cf. section 4.2). The generated field inductively heats the crucible. The temperature can be adjusted by changing the applied current and voltage.

The crucible material has to be chosen according to the requirements imposed by the growth parameters. It needs to sustain its mechanical stability at the growth temperature and must be chemically stable against the melt and growth atmosphere. Common crucible materials include platinum, rhodium, iridium, and vitreous carbon. The crucibles used in this work were made of vitreous carbon and iridium, with the first being employed for fluorides while the second served for oxides. Vitreous carbon has the advantage of a high sublimation point ($T_{\text{sublimation}} > 3650\,^{\circ}\text{C}$), is easy to fabricate, and has a low price. A disadvantage is that it is oxidized by melts and atmosphere containing O_2. This makes it unsuited for the growth of oxides. For these crystals iridium was used as the crucible material. It can also sustain the necessary temperatures ($T_{\text{melt}} = 2410\,^{\circ}\text{C}$) and is furthermore uneffected by oxygen rich melts. Oxidizing atmospheres can pose a problem and may lead to a degredation of the crucible. In order to prevent this effect, the amount of O_2 in the growth atmosphere was kept below 2 %. A disadvantage of iridium crucibles is the high price due to the complex fabrication process and high cost of the raw material.

Growth Process

The basic principle of this technique is the growth of crystals from their liquid phase. To achieve this, the basic components of the crystal are mixed in powder form according to its composition. To minimize the amount of impurities, high purity (at least 4N5[1]) powders are being used as starting materials. Since the material has a lower density in powder than in crystalline form, several melt runs are carried out to achieve a sufficient

[1] $\geq 99.995\,\%$

filling factor of the crucible. For this the crucible is filled with a part of the charge and the chamber is then closed and evacuated. In case of fluoride growths, the vacuum inside the chamber is in the range of 10^{-4} mbar. The crucible is heated to a temperature of several hundreds degrees Celsius during the evacuation process to remove H_2O bound in the base material or on the chamber walls. Like molecular oxygen, water vapor could cause the formation of oxyfluorides. For the growths of oxide crystals a pressure in the range of 10^{-1} mbar is sufficient since neither melt nor the setup are negatively affected by the trace amounts of normal atmosphere that remain in the chamber.

After the evacuation process the chamber is filled with the process atmosphere. Fluoride crystals were grown in a 60 %/40 % mixture of Ar/CF_4 [Ran02]. At higher temperature CF_4 becomes increasingly reactive [Sob02] and should further bind O_2 and H_2O which was not removed by the evacuation and heating process. Oxide growths were carried out either in pure N_2 atmospheres or in N_2/O_2 mixtures with an amount of 0.5 % - 2 % O_2.

The crucible is heated to the melting temperature of the material and left to thermalize. When the powder is completly molten the crucible is cooled to ambient temperature. The chamber is then opened and the process repeated untill the crucible contains a sufficient amount of material. In the case of fluoride growths, the hazardous atmosphere makes it necessary to purge the growth chamber before opening it. This is done with pure N_2 at a rate of 15 l min^{-1} for a duration of 1 h.

When the crucible has reached a sufficient filling factor, the pulling rod is installed and centered radially above the crucible. The melt is then heated to its melting temperature. After allowing the melt to thermalize the tip of the pulling rod is lowered into the melt. Because of heat removal through the rod the temperature is locally lowered below the melting point and crystallization takes place. During the growth process the rod is rotated to achieve homogenous temperature gradients within the melt. After again allowing the system to thermalize, the rod is lifted at a rate of 0.5 - 3 mm h^{-1}. More material crystallizes in the interface zone between the crystal and the melt and the boule grows.

Since the initial crystallization is spontaneous and chaotic, various crystallites are present at this stage of the growth process. In order to select one of the crystallites and obtain a single crystalline growth, the diameter of the crystal is narrowed by slowly increasing the temperature of the melt. The narrow bottleneck leads to a selection of ideally only one crystallite which will determine the orientation of the crystal from there on. If available, a seed can be used to initialize the growth process. In this case the crystallizing material will grow according to the structure of the seed crystal and no bottleneck is necessary.

After the selection process the temperature of the melt is decreased again which allows the crystal to accumulate more mass and to increase its diameter. If the crystal is congruently melting, meaning the crystal and the melt share the same composition, it could theoretically grow until no melt is left in the crucible. However, since impuries tend to remain in the residual melt the growth is stopped when 70 % - 80 % of the charge has been accumulated by the crystal. For non congruently melting crystals the composition of the melt changes during the growth process. When it reaches a critical point denoted as the eutectical point, it can no longer support the single phase growth of the crystal and secondary phases will be incorporated. Since this has highly detrimental effects on the optical quality of the boule, the growth can be stopped at this point. This is done by

either increasing the temperature until crystal and melt lose contact or by rapidly pulling the crystal out of melt. Both methods introduce a thermal shock when crystal and melt seperate which might lead the crystal to fracture.

When the growth process is finished, the setup is slowly cooled to ambient temperature in order to minimize a build-up of thermal stress. For oxide crystals the cooling takes place over a period of approximately 12 h. Fluoride crystals, which exhibit a higher sensitivity to thermal stress, are cooled over a period in the order of 24 h - 48 h.

4.1.2 Seedless Cooling Down Method

A disadvantage of the setup used to grow fluoride crystals with the Czochralski setup is the outer crucible. Like the inner crucible it is made of vitreous carbon and is therefore also heated by the RF field. This leads to a non optimal heating of the inner crucible and limits the temperature which can be reached with this setup. To circumvent this problem and to achieve the higher temperatures needed to grow, for example, LaF_3(cf. section 3.2.2), the setup was adjusted in order to implement the seedless cooling down method (SCDM).

Setup

In order to eliminate the outer crucible, the insulating material is changed. The hollow carbon spheres are replaced with rigid carbon foam. Unlike the spheres it does not need a holding vessel and can furthermore be easily machined into any shape. A cylinder is cut and hollowed so it can take up the crucible (cf. figure 4.2). It is then set on a pedestal of carbon foam to adjust the height within the RF-coil. In order to reduce thermal loss by radiation the crucible is covered by a carbon foam lid. The lid has the additional effect of more homogenous temperature gradients in the melt and furthermore reduces the evaporation of LaF_3 (cf. section 4.3.5). A hole in the lid allows the surface of the material to be observed, and therefore the point at which the raw material melts can be determined.

Growth Process

The basic growth parameters are the same as for a Czochralski growth. After evacuating to a pressure of 10^{-4} mbar and heating, the chamber is filled with a 60 %/40 % mixture of Ar/CF_4. The main difference of the seedless cooling down method is that due to the lid, the crystal can no longer be grown by seeding and then pulling it out of the melt. Instead, the material is heated up to a temperature where it is completely molten and then left to thermalize for about an hour (cf. figure 4.3b). Then, over a period of 48 h, the temperature is slowly reduced by a rate of approximately one degree Celsius per hour. Since the melt is heated from everywhere but the top, the center of the surface will be the coolest part of the melt. When the temperature drops below the melting point of the material, crystallization sets in (cf. figure 4.3c). In the ideal case, the slow temperature decrease and the homogenous temperature gradients cause crystallization from a single crystallite. While the temperature decreases further, the crystal now grows through the melt towards the walls of the crucible. When the temperature of the walls falls below the

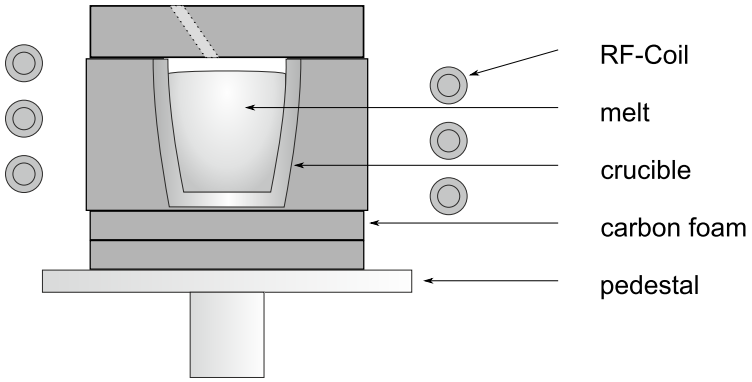

Figure 4.2: Schematic setup for seedless cooling down growth runs.

melting point, all material in the crucible is crystallized (cf. figure 4.3d). The crystal is then cooled down to ambient temperature over a period of at least 24 h.

The major problem of this method is the lack of seeding. This means that there is no control over initialization of the crystallization process which can lead to completely polycrystalline boules. Another problem that arises at temperatures above 1400 °C is a reaction between vitreous carbon and CF_4 [Pas76, Sob02]. Due to this effect, the surface of the crucible which is exposed to the growth atmosphere degrades and can contaminate the melt. This can result in inclusions of macroscopic carbon particles in the crystal which can act as scattering centers.

4.2 Growth Facilities

Three different growth facilities were used for this work. The Heraeus facility and the Crystalox facility are dedicated to the growth of oxide crystals while the F-Growth facility is used for fluorides only.

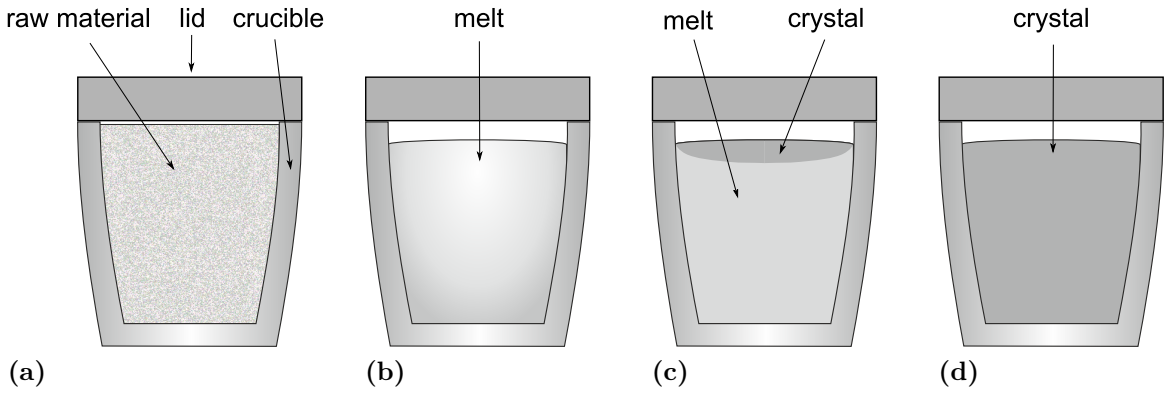

Figure 4.3: Seedless cooling down method.

Heraeus EKZ 150/200

The *EKZ 150/200* was built by *Heraeus*. Its water cooled induction coil has five turns, an inner diameter of 45 mm, and is driven by a *Hüttinger* generator which can put out 36 kW at a maximum voltage and frequency of 10 kV and 400 kHz, respectively. The maximum crucible diameter is limited to 25 mm. The growth chamber allows growths in a closed as well as flowing atmosphere.

All growth parameters for this machine have to be controlled manually. The growth itself can be observed via two viewports on which a camera and a pyrometer can be mounted.

The machine allows small sized crystals to be grown via the Czochralski method in a comparatively short time (<48 h). It enables the quick investigation of varyious effects e.g. melt composition, doping concentration or growth parameters such as pulling or rotational speed.

Crystalox

The *Crystalox* machine was built by *Crystalox crystal growth systems*. Its water cooled induction coil has seven turns, an inner diameter of 110 mm, and is driven by a *Hüttinger* generator which can put out 36 kW at a maximum voltage and frequency of 10 kV and 400 kHz respectively. The maximum crucible diameter is 45 mm. The growth chamber allows growths in a closed as well as with flowing atmosphere.

The Crystalox facility is equipped with a scale which allows the determination of the change in mass of the setup per unit time. Together with the pulling rate and the density of the material the diameter of the crystal can be determined in situ. Software which is programmed with a sketch of the desired crystal shape processes this data and adjusts the current and voltage applied to the coil to achieve a temperature at which the desired mass accumulation takes place.

With this facility high quality crystals can be grown employing the Czochralski method. The boules can be up to 3 cm in diameter while the length is limited only by the amount of melt in the crucible. The automated system allows much longer growth durations than the *Heraeus* machine, with a standard growth time between a few days and a week.

F-Growth

The machine used to grow fluoride crystals was self-built at the ILP. The coil is water cooled, has six turns and an inner diameter of 60 mm. It is driven by a *Hüttinger* generator which can deliver 5 kW at a frequency of 30 - 300 kHz. The crucibles used at this machine are conical with an inner diameter at the top and bottom of 25 mm and 11 mm, respectively.

As it is the case for the *Heraeus* machine, all growth parameters for this machine have to be controlled manually. The growth itself can be observed via a camera mounted on a viewport.

This machine was used to grow crystals with the Czochralski- and the SCD method. The first method allows for boules of up to 15 mm in diameter. With the second method the crystal size is limited only by the dimensions of the crucible. Since the growth rate

of fluorides is mostly kept quite low, the duration of a growth run is usually in the range of several days.

4.3 Growth Results

4.3.1 $SrAl_{12}O_{19}$

Within the framework of earlier investigation conducted at the ILP, several praseodymium doped $SrAl_{12}O_{19}$ crystals were grown with the *Crystallox* facility employing the Czochralski method [Rei10, Fec12]. In each case the basic materials were powders of Pr_6O_{11} (5N), $SrCO_3$ (4N), MgO (5N), and Al_2O_3 (5N). Prior to mixing the $SrCO_3$ was annealed at temperatures above 1200 °C for a duration of at least 48 h. This is necessary in order to ensure a complete reduction to SrO. Otherwise CO_2 seperating off of $SrCO_3$ during the growth could contaminate the melt which would result in carbon inclusions in the boule. Since MgO is known to bind H_2O which would distort the mixing ratio during weighting, it was annealed at 1100 °C for at least 24 h.

Due to the incrongruent melting behaviour, melt compositions close to the point at 85.6 % were chosen (cf. figure 3.2). The doping concentrations of these crystals were 0.9 at%, 2.7 at%, and 4.5 at% (more information on these crystals can be found in [Fec12]).

In addition to the preexisting crystals, a Pr,Mg:$SrAl_{12}O_{19}$ boule was grown from a melt with a composition of 84 wt% Al_2O_3 and 16 wt% SrO. 4 at% of the Sr^{2+}-ions were subsituted by Pr^{3+} and in order to achieve charge compensation an equal amount Al^{3+}-ions was substituted by Mg^{2+}.

The melting temperature of $SrAl_{12}O_{19}$ of $T_{\mathrm{melt}} = 1790\,°C$ allows iridium crucibles to be employed. The growth was carried out in a 98.5 %/1.5 % N_2/O_2 atmosphere and a flow rate of 1 - 2 l min^{-1}. Since no seed material was available from prior growths, a 6 mm diameter Ir-tube was used to initialize crystallization. The growth rate was set to 0.7 mm h^{-1} with a rotational speed of 7 rpm.

The resulting boule is shown in figure 4.4a. It can be seen that while the bottleneck (0 - 2 cm) grew polycrystalline, the rest of the boule starting at approximately 2.3 cm is single crystalline. At a length of about 9 cm the crystal began to incorporate precipitate. At first this only affected the outer part of the boule but with progressing growth time, impurities could also be found in the core region. Fechner showed that these impurities are secondary phases like $SrAl_2O_4$ which are caused by the melt composition shifting towards the eutectical point [Fec11]. The metallic deposition on the outside of the crystal is iridium which was seperated off the crucible due to the O_2 in the growth atmosphere. The crystal also exhibits a cleavage plane starting at around 4 cm. This is a known phenomenon in SRA [Mer96] and allows the growth direction to be easily determined since it occurs perpendicular to the c-axis. From the segregation coefficient of 0.91 [Mer96, Fec12], it can be deduced that the boule had a Pr^{3+} concentration of about 3.6 at%.

Furthermore, a Pr,Mg:SRA crystal was provided by the Leibniz-Insitut für Kristallzüchtung (IKZ) in Berlin, Germany. The melt from which this boule was grown had a composition of 85.6 wt% : 14.4 wt% Al_2O_3 : SrO. To allow a comparison with crystals grown at the ILP, the Pr^{3+} and Mg^{2+} doping concentration of the melt was chosen to

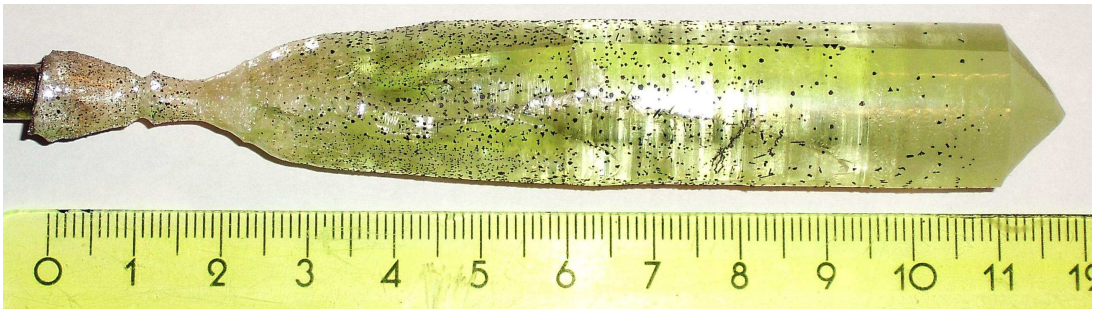

(a)

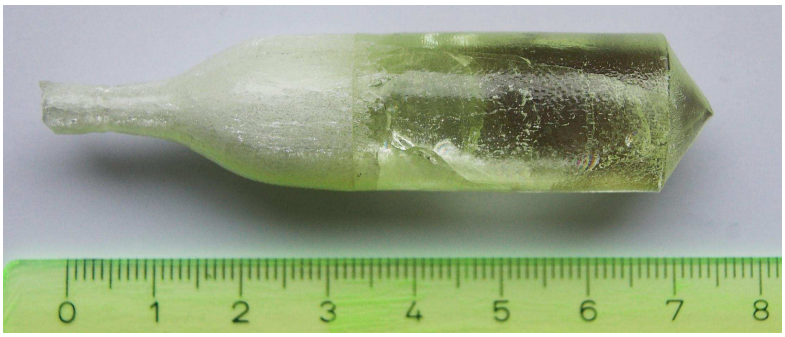

(b)

Figure 4.4: (a) 4 at% doped Pr,Mg:$SrAl_{12}O_{19}$ crystal grown at the ILP. The cleaving plane starting at 4 cm indicates a growth direction perpendicular to the c-axis of the crystal. (b) 3 at% doped Pr,Mg:$SrAl_{12}O_{19}$ crystal grown at the IKZ Berlin. The change from polycrystalline to single crystalline growth can be seen at appr. 3.3 cm.

be 3 at%. It was grown with a rate of 1 mm h^{-1} and a rotational speed of 10 rpm. The atmosphere consisted solely of N_2. The flow rate was 1.5 l min^{-1}.

The crystal is depicted in figure 4.4b. A cut at about 3.3 cm revealed that it grew polycrystalline. It is likely that due to the melt containing too much alumina, Al_2O_3 crystallized and contaminated the boule. This indicates that the reported phase diagram is inaccurate in this region and that the optimal melt composition for the growth of SRA crystals contains less Al_2O_3 [Gan79]. However, at 3.3 cm the melt composition reached a point where single crystalline growth was possible without Al_2O_3 crystallizing. Although in figure 4.4 it seems that no secondary phases are present in the lower part of the boule, a cut at 6 cm revealed that a small amount of impurities had been incorporated in the outer part of the crystal. The boule also exhibited a cleavage plane perpendicular to the growth direction.

4.3.2 $CaAl_{12}O_{19}$

Due to the similarity between the phase diagrams of the systems Al_2O_3 - SrO and Al_2O_3 - CaO, the growth of $CaAl_{12}O_{19}$ crystals was carried out similarly to Pr,Mg:SRA at the *Crystalox* facility. The basic materials were the same as for $SrAl_{12}O_{19}$ with the exception of $SrCO_3$ being replaced by $CaCO_3$. Since several different phase diagrams are reported for the system CaO - Al_2O_3 which all exhibit slight differences between each

other, the charge for the first growth was prepared with only a small excess of CaO [Wis55, Nur65, Cha72, Jer01]. The composition was 85.7 wt% Al_2O_3 and 14.3 wt% CaO. From the boule grown by the IKZ it can be seen that the crystal should adapt the correct phase once a suitable melt composition is reached.

The melting temperature of CAlO is only slightly higher than that of SRA ($T_{\mathrm{melt}} = 1852\,^{\circ}\mathrm{C}$) and thus growth runs were also carried out with iridium crucibles. Because no seed material was available, the crystallization was initialized with the Ir-tube that was also used for SRA. The growth rate was 0.75 mm h^{-1} at 7 rpm. Since Merkle *et al.* reported that only a small amount of Pr^{3+} is incorporated into CAlO, the doping concentration was chosen to be 6 at% in order to achieve a sufficient amount of active ions in the crystal [Mer96]. For charge compensation, Mg^{2+} was added in a ratio of 1:1 with respect to the Pr^{3+}-ions.

The resulting boule can be seen in figure 4.5a. It grew strongly polycrystalline which can most likely be attributed to a too high level of Al_2O_3 in the melt. The boule consistied of a large number of single crystalline pieces with a thickness of 100 µm - 2 mm and areas of up to 0.5 cm^2 (cf. figure 4.5a right). These pieces resulted from cleaving perpendicular to the c-axis. Powder X-ray diffraction (XRD) measurements[2] verified the correct phase of the single crystalline material. Furthermore, the Pr^{3+} concentration of

(a)

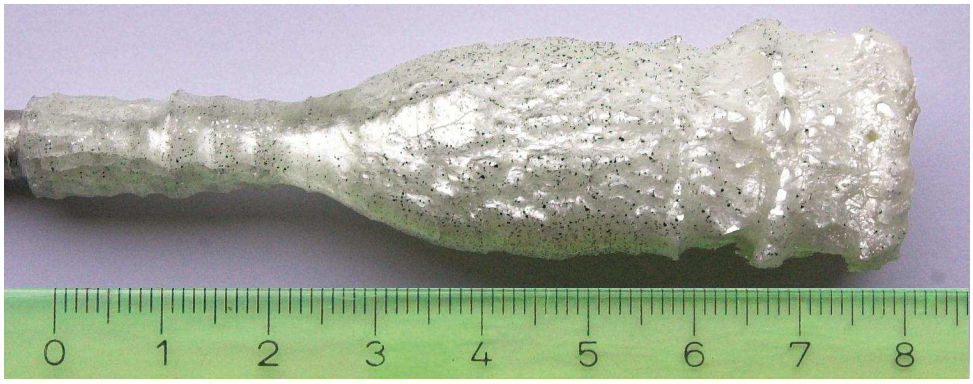

(b)

Figure 4.5: Pr,Mg:$CaAl_{12}O_{19}$ crystals grown at the ILP. Both crystals exhibit a high degree of polycrystalinity. The doping concentration was (a) 6 at% and (b) 1 at%.

[2]The XRD measurements were carried out by B. Herden at the FH Münster.

a sample was investigated by energy dispersive X-ray spectroscopy (EDX). This method showed a value of 6.6 at% Pr^{3+}. Although this contradicts the findings of Merkle *et al.*, it is in good agreement with what would be expected due to the similarity of $CaAl_{12}O_{19}$ and $SrAl_{12}O_{19}$. Unfortunately, the high polycrystallinity of the boule did not allow the segregation coefficient to be determine precisely. The dopant concentration indicates however, that it is close to 1. Several of the obtained single crystalline pieces were of sufficient quality to allow spectroscopic and laser experiments. However, since the high doping concentration is likely to lead to cross relaxation processes, the samples are not suited to obtain unperturbed fluorescence decay dynamics. These parameters are necessary to determine the emission cross sections (cf. section 6.1.4).

A second crystal was therefore grown from a melt exhibiting a Pr^{3+},Mg^{2+} concentration of 1 at%. As the polycrystalline growth behaviour of the first crystal is likely the result of a too small excess of CaO, the melt composition for the second grwoth was changed towards a larger excess (84.1 wt% : 15.9 wt%, Al_2O_3 : CaO).

Additionally, to achieve a more stable crystallization process, the growth rate was reduced to 0.5 mm h^{-1}. The atmosphere was not changed.

The resulting boule is depicted in figure 4.5b. Like the first crystal it is highly polycrystalline. Some larger single crystalline pieces with sizes of several cubic millimeters are present. The reason for this growth behaviour is unclear. It is possible that the amount of CaO must be further increased to achieve a better growth behaviour. This is somewhat contradicted by the Pr,Mg:SRA boule grown at the IKZ which assumed a single crystalline growth bahaviour as soon as it reached a suitable melt composition. Neither of the two Pr,Mg:CAlO crystals shows indications of such a process. Still, further growth experiments with varying melt compositions have to be performed in order to resolve this point. The growth result might be also improved by sintering the powder prior to the growth in order to create the $CaAl_{12}O_{19}$ phase by a solid state reaction.

4.3.3 $LaMgAl_{11}O_{19}$

The *Hereaus* as well as the *Crystalox* machine were used to fabricate Pr^{3+}:$LaMgAl_{11}O_{19}$ crystals. With the *Hereaus* machine several small sized boules with various doping concentrations were grown for spectroscopic investigations. Large sized, high quality boules from which laser samples were cut were obtained with the *Crystalox* machine.

Hereaus

The *Heraeus* facility was used to grow undoped and Pr^{3+}-doped $LaMgAl_{11}O_{19}$ crystals with doping concentrations in the melt between 1 at% and 10 at% (cf. figure 4.6). The MgO and Al_2O_3 used to prepare the charge were the same as for the other two hexaaluminates. Since La_2O_3 is known to bind H_2O it was annealed at 1100 °C for at least 24 h prior to weighing. Since $LaMgAl_{11}O_{19}$ is a congruently melting crystal [Abr87], the melt was composed stoichiometrically (74.4 wt% : 20.3 wt% : 5.3 wt% Al_2O_3 : La_2O_3 : MgO).

The crystals were grown at a rate of 2 - 3 mm h^{-1} at 15 rpm. Growth atmospheres of pure N_2 or N_2/O_2 mixtures containg up to 2 vol% O_2 were used with no distinguishable effect between different compositions. All crystals grew polycrystalline to a certain degree with

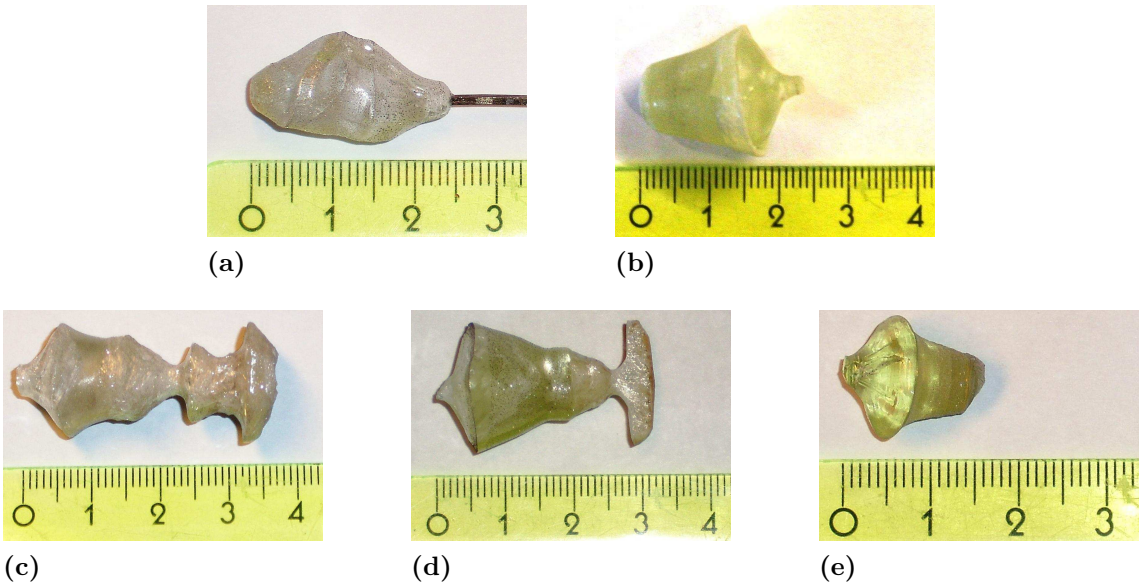

Figure 4.6: Pr:$LaMgAl_{11}O_{19}$ crystals with different doping concentrations grown with the *Hereaus* facility. (a) undoped, (b) 1 at%, (c) 3 at%, (d) 5 at%, (e) 10 at% in the melt.

cleavage planes perpendicular to the c-axis. Nevertheless, single crystalline parts with a quality sufficient for spectroscopic investigations were present and samples were prepared from each boule. The correct phase of the boules was verified by XRD measurements[3].

Crystalox

In order to obtain crystals of laser grade quality, the *Crystalox* machine was used to grow two Pr^{3+}:$LaMgAl_{11}O_{19}$ boules. The first crystal was, in accordance with the experiments at the *Hereaus* machine, grown from a stoichiometric melt. The doping concentration was chosen to be 2.5 at% since the segregation coefficient was assumed to be close to 1 and the best laser results of Pr,Mg:SRA so far were obtained with a crystal that exhibited a similar amount of Pr^{3+}. The growth rate was set to 1 mm h^{-1} with 12 rpm and a 98 %/2 % N_2/O_2 atmosphere.

The resulting boule is depicted in figure 4.7a. It was completely single crystalline, and like SRA and CAlO, grew perpendicular to the c-axis and also exhibits cleavage planes of the same kind. The upper part of the crystal grew ellipically with the long and short axis following the crystallographic a-axis and c-axis respectively. Samples of the upper part of the boule at 2.5 cm and of the lower part at 8.8 cm were investigated by XRD analysis which verified the correct phase of the crystal. Furthermore, microprobe analyses[4] were carried out in order to assess the exact composition of the crystal. This had two reasons. Firstly, it allowed for the determination of the segregation coefficient

[3]XRD measurements on all Pr:LMA samples were carried out by Dr. T. Malcherek of the Mineralogic and Petrographic Institute of the Universität Hamburg.

[4]The microprobing experiments were performed by Dr. H.-J. Bernhard at the Institute of Geology, Mineralogy, and Geophysics of the University of Bochum

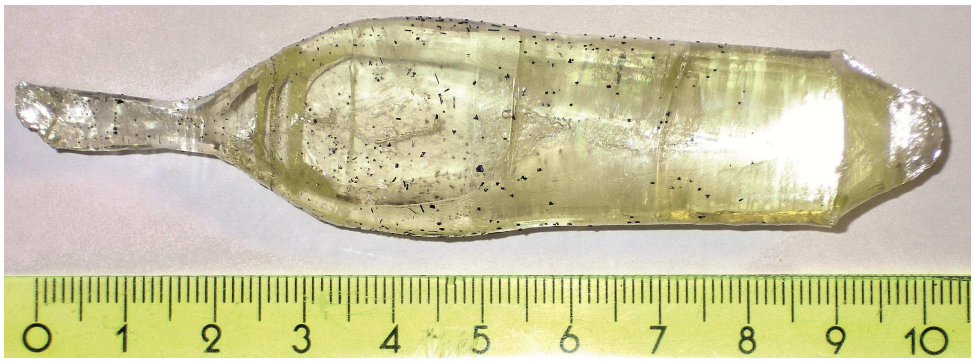

(a)

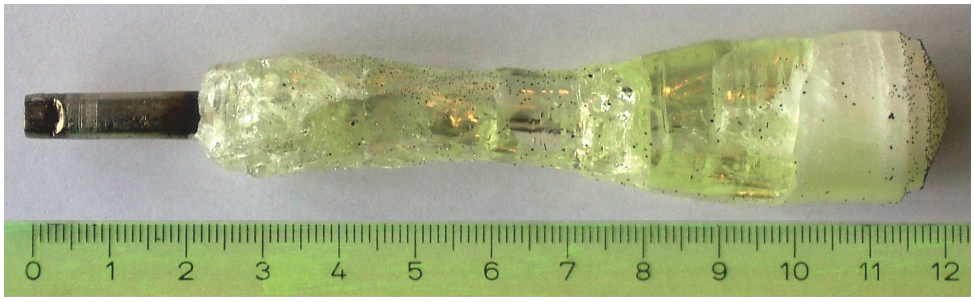

(b)

Figure 4.7: The two Pr:$LaMgAl_{11}O_{19}$ crystals grown with the *Crystalox* facility. The doping concentration was (a) 2.5 % and (b) 6 % in the melt.

of Pr^{3+}, and secondly it showed whether a Mg^{2+} deficit and thus a displacement of the La^{3+}-/Pr^{3+}-ions onto the 6*h* site was present (cf. section 3.1).

The results of the analyses are listed in table 4.1. They show that the actual segregation coefficient of Pr^{3+} in $LaMgAl_{11}O_{19}$ is only $\kappa_{\mathrm{Pr:LMA}} = 0.48$. It is also apparent that a deficit

ion	composition		
	melt	top	bottom
Pr^{3+}	0.025	0.012	0.018
La^{3+}	0.975	1.0	1.03
Mg^{2+}	1	0.75	0.85
Al^{3+}	11	11.16	11.06
O^{-}		19	

Table 4.1: Composition of the 2.5 at% doped Pr^{3+}:$LaMgAl_{11}O_{19}$ crystal determined by microprobe analysis.

of Mg^{2+}-ions was present. The Mg^{2+}-concentration varied between 75 % at the top of the crystal and 85 % at its bottom. The increase can be explained by the fact that the melt composition changed due to the non stoichiometric growth behaviour. This led to a rising amount of Mg^{2+} in the melt which in turn forced more of these ions into the lattice.

Based on the findings of Park *et al.* the deficit of Mg^{2+} is likely to lead toLa^{3+}-/Pr^{3+}-ions occupying 6*h* sites [Par97].

Since it was unclear how the presence of the secondary site affects the spectroscopic properties of the crystal, a second boule was grown to investigate this effect. In order to decrease the deficit, an excess of 20 % Mg^{2+} was added to a stoichiometric mixture of the basic materials. The composition of the melt was therefore 73.6 wt% : 20.1 wt% : 6.4 wt% $Al_2O_3 : La_2O_3 : MgO$. The larger amount of Mg^{2+} present in the melt should facilitate a better inclusion into the lattice which should shift the composition of the crystal closer to the stoichiometric composition. Furthermore, as a result of the smaller than expected Pr^{3+} segregation coefficient, the doping concentration of this crystal was also increased. 6 at% of the La^{3+}-ions were substituted with Pr^{3+} in order to achieve a dopant concentration comparable to that of the Pr,Mg:SRA crystals.

The resulting boule is displayed in figure 4.7b. The irregular shape of the boule was due to a malfunction of the scale which occurred after the growth was started. A high number of cracks were present, particularly in the upper and lower part of the crystal. Nevertheless, parts of the boule, for example around 6.5 cm and 9 cm, grew single crystalline and exhibited a good optical quality. A sample was cut from the area at 6.5 cm and its composition was determined by microprobe analysis to be $(Pr_{0.036}{:}La_{0.946})(Mg_{0.82}Al_{11.11})O_{19}$. This shows, that even with such a high excess of MgO in the melt, the boules exhibits a comparable Mg^{2+} deficit. Samples for experiments were thus prepared from the second boule due to its higher optical quality. The reason for the persistent Mg^{2+} deficit is unclear.

4.3.4 $LiLuF_4$

For the growth of $LiLuF_4$ the F-Growth facility was used. Since the melting temperature of LLF is only 850 °C the Czochralski method and a standard setup was employed. High purity powders of HoF_3 (5N), LiF (5N), and LuF_3 (5N) were used as basic materials. Because LLF is a congruently melting system, the melt composition was chosen to be 10.4 wt% : 89.6 wt% $LiF : LuF_3$ (cf. figure 3.6). Since Ho^{3+} is prone for cross relaxation processes which become more pronounced with rising doping concentration, only a small amount of 0.5 at% of the Lu^{3+}-ions were substituted by Ho^{3+}.

Earlier growth runs carried out with $LiLuF_4$ at the ILP showed that slow growth rates and rotational speeds have a positive effect on the crystal quality [Ric08, Han12]. Based on these results, the growth rate was set to 0.5 mm h^{-1} with a rotational speed of 5 rpm. The growth was carried out in a 60 %/40 % Ar/CF_4 atmosphere at a pressure of 1.2 bar. The overpressure was used to prevent ambient atmopshere from leaking into the growth chamber where it would contaminate the melt and facilitate the formation of oxyfluoride compounds. The crystallization process was initialized with a 1 mm Ir-wire since no seed material was available.

The obtained boule can be seen in figure 4.8. The orientation of the boule was determined by employing two crossed polarizers and a Bertrand lense. This showed that the growth direction was $\approx 45°$ tilted towards the crystallographic *c*-axis. A malfunction of the water circuit cooling the generator and the growth chamber during the growth caused an emergency shut down of the generator. This led to a very short cooling time of the

crystal of only several ten minutes. Furthermore it caused an instantaneous crystallization of the residual melt. Since the boule was still in contact with the melt, both fused together and the bottleneck broke. Nevertheless, the boule is completely single crystalline with no visible cracks or inclusions. In order to check for microscopic scattering centers not visible to the naked eye, an orange laser beam that is not absorbed by Ho^{3+}:$LiLuF_4$ was put through the crystal. This revealed some scattering inside the part of the boule above 1.6 cm. The lower part was free of any scattering and all samples used for further investigations were cut from this area. A sample was investigated by microprobe analysis in order to reveal the Ho^{3+} concentration which yielded a value of 0.6at%[5].

In addition to the boule grown at the ILP, samples with a Ho^{3+} concentration of

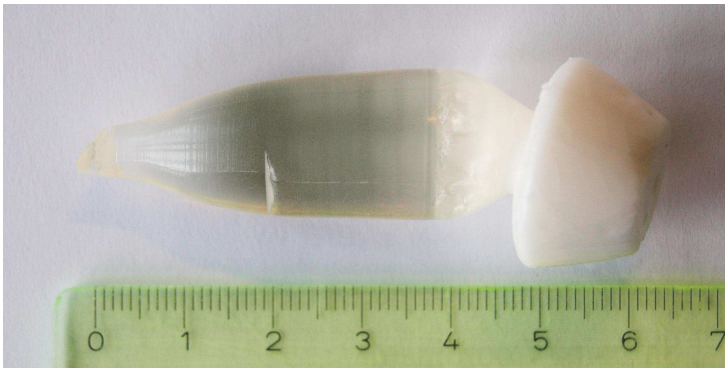

Figure 4.8: As grown 0.5 at% Ho^{3+}:$LiLuF_4$ boule.

0.25 at% were provided by Prof. Dr. Mauro Tonelli of the dipartimento di fisica of the Universita' di Pisa.

4.3.5 LaF_3

First growth experiments showed that the standard setup used at the F-Growth facility does not allow the melting point $T_{melt} = 1487\,°C$ of LaF_3 to be reached. Thus the single crucible setup as introduced in section 4.1.2 was devised with which it was possible to reach the necessary temperature. However, first successful melting experiments revealed a strong tendency of liquid LaF_3 to evaporate. Jones *et al.* reported that this evaporation ceases at a pressure of 1.03 bar [Jon68]. This value seems doubtful since the atmospheric pressure employed in the initial experiments was 1.2 bar. Still, experiments with varying pressures showed a decrease of evaporation with rising pressure. Unfortunately the growth chamber was not designed for pressures above ≈ 2 bar. At this point the evaporation was still too strong to allow a growth with the Czochralski method.

In order to further reduce evaporation, the crucible was covered with a lid. A 5 mm hole was drilled through it to allow the melt surface to be observed. Although at first evaporation still took place through the hole, it soon stopped due to LaF_3 crystallizing at its walls and thus closing it. This effect was independent of the pressure in the growth chamber. Since the lid does not allow the initialization of the crystallization via an Ir-wire

[5]The microprobe analysis were performed by Dr. H.-J. Bernhard at the Institute of Geology, Mineralogy, and Geophysics of the University of Bochum

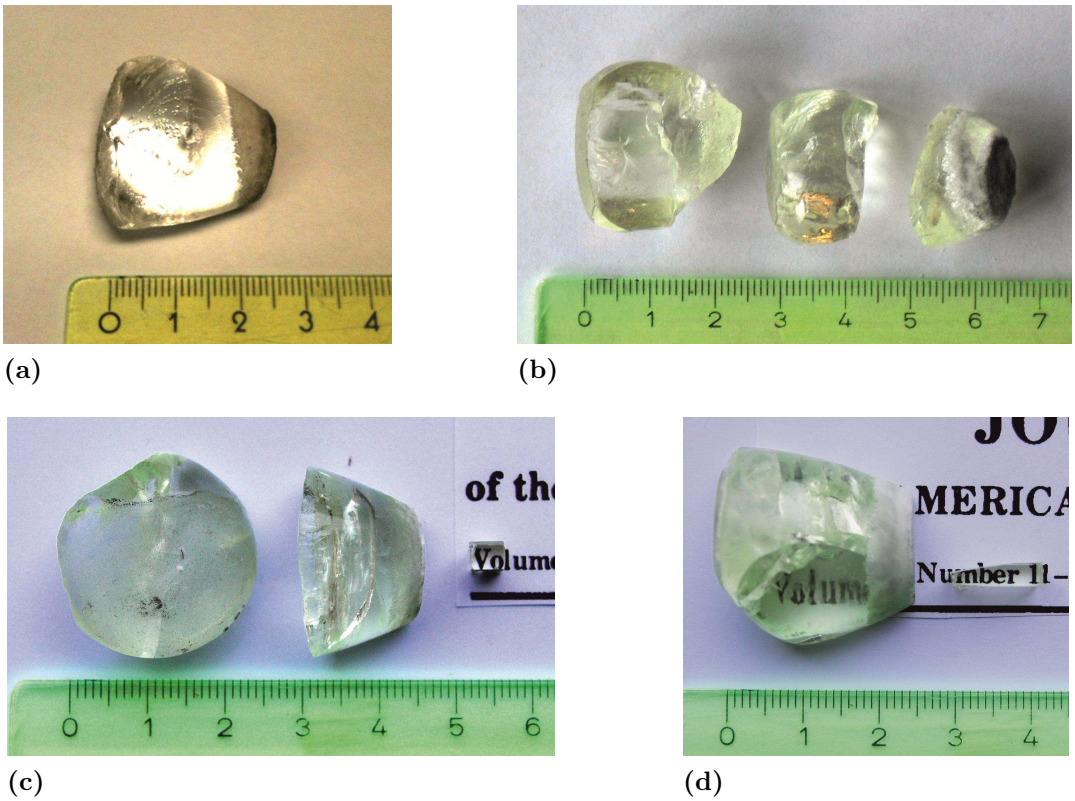

Figure 4.9: Boules of undoped (a) and Pr^{3+}-doped (0.5 at% (b), 0.7 at% (c), and 1 at% (d)) LaF_3 grown with the SCD method.

or seed crystal, the SCD method had to be employed to grow RE doped LaF_3 boules. However, in some cases, LaF_3 which evaporated and then crystallized in the view hole of the lid came into contact with the surface of the melt and seemed to act as a seeding point.

The basic materials for all crystals were PrF_3 (5N), HoF_3 (5N), EuF_3 (5N), and LaF_3 (5N). All growth runs were carried out in 60 %/40 % Ar/CF_4 atmospheres at a pressure of 1.2 bar. The basic materials were heated to several ten degrees above their melting points. The temperature was then reduced at a rate of a few degrees per hour for 48 h (cf. section 4.1.2). After that the crucible was cooled to room temperature over a period of 24 h - 36 h.

With these parameters, six boules were obtained: one undoped, one doped with Ho^{3+} (1 at%), three with Pr^{3+}(0.5 at%, 0.7 at%, and 1 at%), and one doped with Pr^{3+} and Eu^{3+} (0.5 at% : 1 at% $Pr^{3+} : Eu^{3+}$). In each case the dopant substituted the La^{3+}-ion in the lattice. All boules fabricated in this way exhibited large single crystalline volumina as can be seen from samples displayed in figure 4.9. When irradiated with a laser beam it was revealed that the lower parts of the boules exhibit scattering. Thus, spectroscopic and laser samples were always cut from the top part of the boule that usually did not show any scattering.

Samples of the Ho^{3+}:LaF_3 and (0.7 at%)Pr^{3+}:LaF_3 boule were analyzed by microprobe analyses[6] regarding the respective dopant concentration. This revealed compositions of (0.3 at%)Ho^{3+}:LaF_3 and (0.4 at%):Pr^{3+}:LaF_3. Unfortunately, due to the uncontrolled crystallization process, these measurements can not be used to determine the exact segregation coefficient. Nevertheless it is obvious that the segregation coefficient in both cases varies from 1. For Ho^{3+} this is not very surprising since the difference between the ionic radii of La^{3+} and Ho^{3+} is quite large (1.18 Å : 1.02 Å, eight-fold coordinated). For Pr^{3+} however, the situation is different, as it was shown in section 4.3.3. It is unclear why the segregation coefficient is so low, despite the similarity of the La^{3+} and the Pr^{3+}-ion.

The samples were used to determine the absorption cross sections of Pr^{3+}:LaF_3 and Ho^{3+}:LaF_3 (cf. section 6.1.1). The dopant concentration of other samples was henceforth derived spectroscopically.

[6]The microprobe analyses were performed by Dr. H.-J. Bernhard at the Institute of Geology, Mineralogy, and Geophysics of the University of Bochum

5 Waveguide Fabrication and Characterization

As it was recently shown by Calmano *et al.*, waveguiding structures created in Pr,Mg:$SrAl_{12}O_{19}$ by fs-laser inscription can be used to obtain laser operation in the visible spectral range [Cal11, Cal12]. Waveguide lasers have several advantages compared to bulk gain media, for example an excellent overlap of pump and laser mode or the compact setups that can be realized with such systems (cf. section 7.2.2). It was part of this work to further optimize the fabrication parameters, laser characteristics, and emission range of Pr,Mg:SRA waveguide lasers, which will be described in this chapter.

The first section will give a short introduction into the basic principles of waveguiding in crystalline materials as well as into the waveguide fabrication process. The second part will deal with the fabrication setup and parameters while in the third part the characterization of the fabricated waveguides will be presented. For a more detailed description of the topic the reader may refer to [Sie10, Cal13].

5.1 Principles

Davis *et al.* showed that the irradiation of bulk glass material with fs-laser pulses ($\lambda_{\mathrm{em}} = 810\,\mathrm{nm}$) leads to a material modification in the focal volume and to a change of the refractive index in the modified region [Dav96]. This effect can be explained by an energy deposition via photoionization which subsequently leads to a modification of the material. Since the energy of a single photon is not sufficient to bridge the bandgap and thus cause photoionization, nonlinear processes involving several photons are necessary. The high intensity created by the fs-laser pulses enable several nonlinear absorption processes such as tunnel, multiphoton, and avalanche ionization where, for the parameters that are usually employed, the latter two are domninant. Multiphoton ionization (cf. figure 5.1a) takes place while the laser pulse is still passing the medium. In this process several laser photons are taking part in a cooperative process and excite an electron from the valence band into the conduction band. At this point avalanche ionization can set in (cf. figure 5.1b) where in a first step the successive absorption of photons by an electron in the conduction band in combination with phonon scattering leads to further excitations. If a critical level is reached, the electron can decay into the lowest state of the conduction band while transfering its energy E_{crit} to a valence band electron and exciting it into the conduction band, which is denoted as impact ionization.

Due to electron-phonon coupling the excitation energy is transferred to the glass matrix which causes an increase of the temperature and a subsequent decrease. Since in glasses the cooling rate has a direct effect on the refractive index [Brü70], this technique can

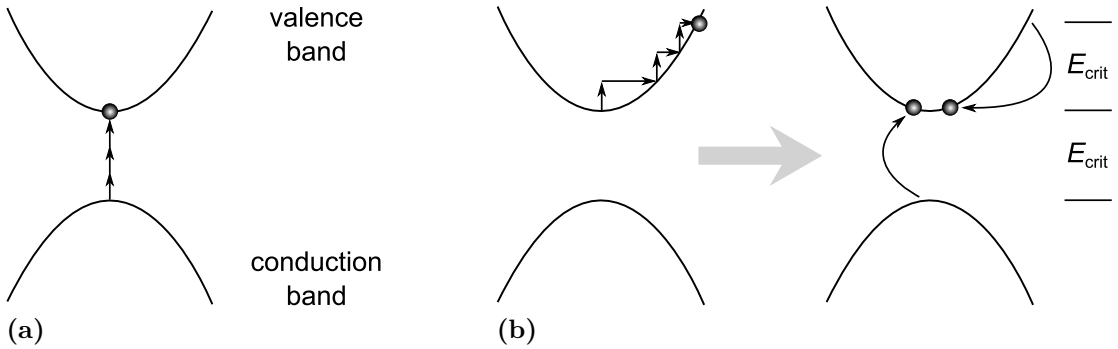

Figure 5.1: Nonlinear processes occuring in the focal region of a fs-laser beam. (a) depicts multiphoton absorption while (b) depicts the two steps of the avalanche ionization.

be used to locally alter the refractive index. Furthermore, the fact that the ionization processes are of a nonlinear nature means that only material in a volume where a critical intensity is reached will be modified [Stu96].

This method can also be applied to crystalline materials, although the effect causing the refractive index change is different. Here the heat generated by the fs-laser pulses leads to a destruction of the crystalline matrix within the focal point. In several crystals the material modified in this way exhibits a lower density than the unmodified lattice and thus exerts stress on the surrounding material. The elasto-optic effect [Wem70] causes an increase of the refractive index in the intact material surrounding the modified area.

By inscribing tracks of modified material into bulk media, three-dimensional structures can be fabricated. In modified glasses as well as crystalline media, material with a refractive index n_1 surrounds material with a refractive index n_2 where $n_1 < n_2$. From the Fresnel equation in combination with Snell's law it follows that if an electro-magnetic wave incides on such a structure under an angle Θ_1, the wave will experience repeated total internal reflection if the angle is smaller than a critical value Θ_{crit} given by

$$\sin(\Theta_1) \geq \frac{n_1}{n_2} = \sin(\Theta_{\text{crit}}). \tag{5.1}$$

This is referred to as waveguiding. Depending on the waveguiding structure several different types of fs-laser written waveguides can be distinguished. In glasses, where the inscription process usually causes a higher refrative index, structures often consist of single tracks and guiding occurs inside these tracks, which is denoted as Type I waveguiding. For crystalline media where the modified material creates a stress field and thus a higher refractive index in the surrounding material, often two tracks are inscribed in close proximity to achieve a more homogeneous stress field. In such double track structures guiding occurs between the two tracks. This is known as Type II waveguiding. In this thesis only Pr,Mg:SRA, a crystalline medium, was investigated and the inscribed structures always consisted of two tracks. Therefore all fabricated waveguides belong to the later group.

A detailed description of the interaction processes between ultrashort laser pulses and crystalline media as well as the guiding of electro-magnetic waves can be found in [Cal13].

5.2 Fabrication

5.2.1 Setup

A schematic of the setup used for the inscription experiments is depicted in figure 5.2. The fs-laser pulses were delivered by a *Clark-MRX CPA-2010* chirped pulse amplifier (cf. [Str85, Sie10]). The CPA system emitted a linearly polarized and nearly diffraction limited output beam ($M^2 = 1.1$) with a central emission wavelength of 775 nm. The system operated at a repetition rate of 1 kHz, a pulse duration of 150 fs, and a maximum pulse energy of 1 mJ. A $\lambda/2$-waveplate in combination with a polarizing beam splitter cube (PBSC) and a neutral density filter allowed the pulse energy to be continuously attenuated down to the µJ level. A power meter could be placed in the beam during power adjustment. After attenuation, the beam was focused with an aspheric lens with a focal length of 4.51 mm and a numerical aperture of 0.55. The lens was mounted on an *Aerotech* ABL 1000 translation stage to adjust the focal point of the beam in the y-direction. The sample was placed on a two axis tilt stage which allowed the surface of the sample to be perpendicularly alligned to the incident beam and thus to achieve a constant depth of the focal point inside the medium. The tilt stage was mounted on two *Aerotech* ABL 1000 linear stages with which the sample could be translated in the x-z-plane while the incident direction of the beam was parallel to the y-direction. The specifications of the linear stages are given in table 5.1. The translation stage was computer controlled and allowed for the inscription of predefined patterns into the sample. In order to achieve a sufficient suppression of vibrations the whole setup was mounted on a granite stage set on an optical table.

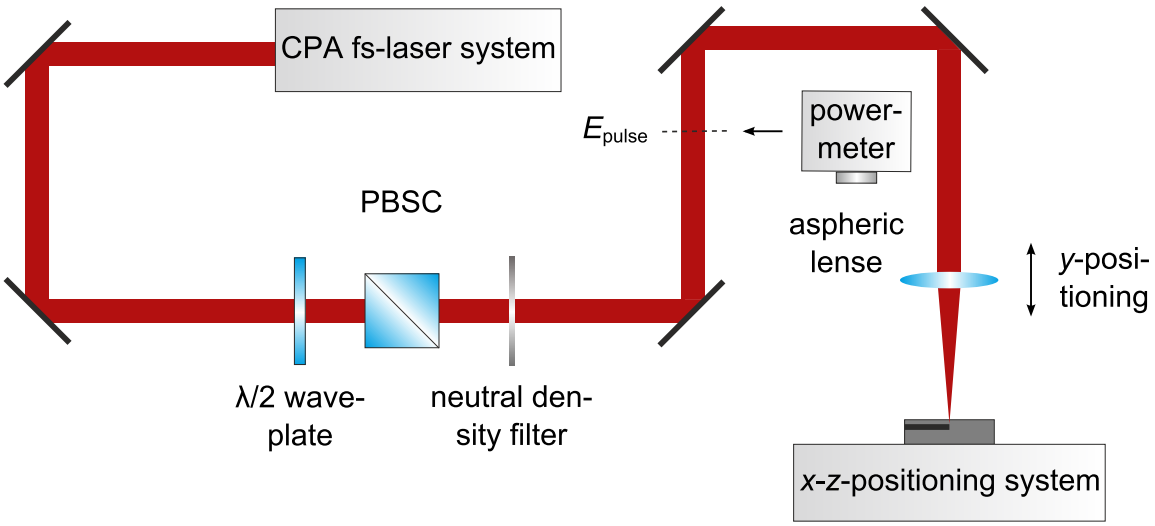

Figure 5.2: Schematic of the setup used for the fs-laser inscription.

axis	x-z	y
straightness/flatness	± 0.25 mm	± 0.5 mm
pitch/yaw	± 2.42 µrad	± 4.85 µrad
resolution	2 nm	2 nm
repeatability	± 50 nm	± 75 nm
maximum travel speed	100 mm s^{-1}	100 mm s^{-1}

Table 5.1: Specification of the linear translation stages.

5.2.2 Parameters

From the setup it is apparent that the modification of the material and the formation of tracks is influenced by a large number of parameters which can be devided into three groups.

The first group deals with the parameters of the pulses delivered by the CPA system and the intensity that can be created in the focal point. The pulse duration τ_{pulse} and energy E_{pulse}, and the wavelength λ_{CPA} at which the system operates belong in this group. In this setup the parameters τ_{pulse} and λ_{CPA} are given by the CPA systems and only E_{pulse} can be adjusted. The intensity in the focal volume is directly dependent on the focal length of the lens, its numerical aperture, and how much of the lens is illuminated by the beam.

The second group of parameters has an influence on the overlap of consecutive pulses. This is determined by the translation speed which, in this system, is defined as $v_{\text{trans}} = \frac{\mathrm{d}z}{\mathrm{d}t}$ (cf. figure 5.3) and the repetition rate of the CPA f_{rep} where the latter is also fixed due to the CPA system.

The third group consists of structural parameters. For the Type II structures fabricated in this work, these are mainly the writing depth Δy and the distance between two tracks in a double track structure (DTS) Δx.

In addition to these parameters, anisotropic systems like Pr,Mg:SRA exhibit different optical properties for different crystallographic axes (cf. section 6.2). The orientation of the DTS within the crystalline matrix will therefore have an influence on the absorption and emission properties of the resulting waveguide structures.

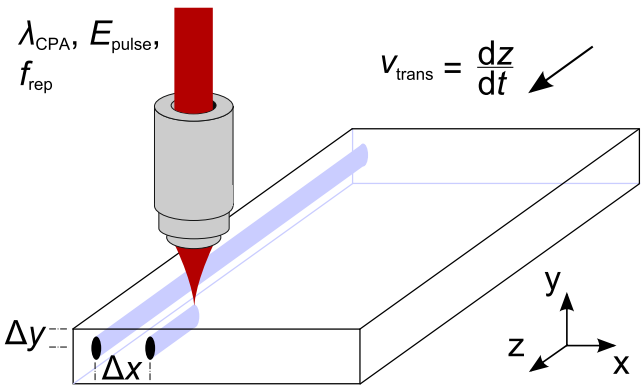

Figure 5.3: Schematic of the sample during the inscription process.

The experiments of Calmano *et al.* were conducted using a lens with focal length $f_{\text{lens}} = 4.51\,\text{mm}$. The pulse energy was varied between 0.18 µJ and 1.3 µJ and the track distance between 22 µm and 28 µm. Writing speeds of $10\,\mu\text{m}\,\text{s}^{-1}$ and $25\,\mu\text{m}\,\text{s}^{-1}$ were employed. The best laser parameters were obtained with a DTS with a track distance of 22 µm inscribed with 1.3 µJ at a speed of $25\,\mu\text{m}\,\text{s}^{-1}$ [Cal11]. The writing depth of the DTS was $300\,\mu\text{m}\,\text{s}^{-1}$. It was furthermore shown that for a Pr,Mg:SRA sample oriented with its c-axis parallel to the x-axis of the system and tracks inscribed along the z-direction, only light polarized to the y-direction is guided. Since this means that the guided polarization coincides with the polarization direction exhibiting the more advantageous ground state absorption and emission cross sections (cf. section 6.2), the sample was oriented $c \| x$.

Higher writing energies and smaller track distances seem to be beneficial for waveguide lasers. Thus, in order to further optimize the characteristics of the waveguides, the inscription parameters employed in this work were chosen accordingly. The writing energy and track distance was varied between 1.3 µJ and 3 µJ, and 16 µm and 22 µm which should also allow for a comparison with the results obtained by Calmano *et al.*

The writing speed and depth was chosen to be $25\,\mu\text{m}\,\text{s}^{-1}$ and 300 µm respectively. In order to achieve comparable focus sizes and intensities in the focal volume, a lens which was identical to the one employed in [Cal11] was used. Furthermore, to achieve a better absorption of the pump light, a Pr,Mg:SRA sample with a length of 19 mm was used. Its height and width were $2\,\text{mm} \times 8\,\text{mm}$. For the writing process the sample was oriented with the c-axis parallel to the x-direction. The crystal had a doping concentration of 3.6 at%.

5.3 Characterization

The inscribed tracks were investigated using bright field and polarization contrast microscopy. This allowed the dimension and quality of the inscribed tracks to be determined and the stress induced birefringence to be shown. The waveguiding structures were furthermore characterized with respect to guiding losses, the mode field diameters $2w_0$ of the guided modes, and the numerical aperture NA of the DTSs. These values help to assess several properties of the waveguides which later have an influence on the laser characteristics. The losses in combination with the transmission of the resonator mirrors directly determine how much gain the active medium must produce in order to achieve laser oscillation. Furthermore, if the mode field diameter and numerical aperture of the waveguides are known, the focussing optic for the laser experiments can be optimized in order to achieve a high input coupling efficiency of the pump radiation.

5.3.1 Microscopy

The bright field image of a DTS with $\Delta x = 22\,\mu\text{m}$ inscribed with a pulse energy of $E_{\text{pulse}} = 1.3\,\mu\text{J}$ is displayed in figure 5.4a. It can be seen that the tracks are completely smooth without any microcracking. On the basis of the image the dimensions of the track were determined to be about 30 µm (y) and 3 µm (x). These values deviate from those reported by Calmano *et al.* [Cal11]. The effect might be due to a variation of the

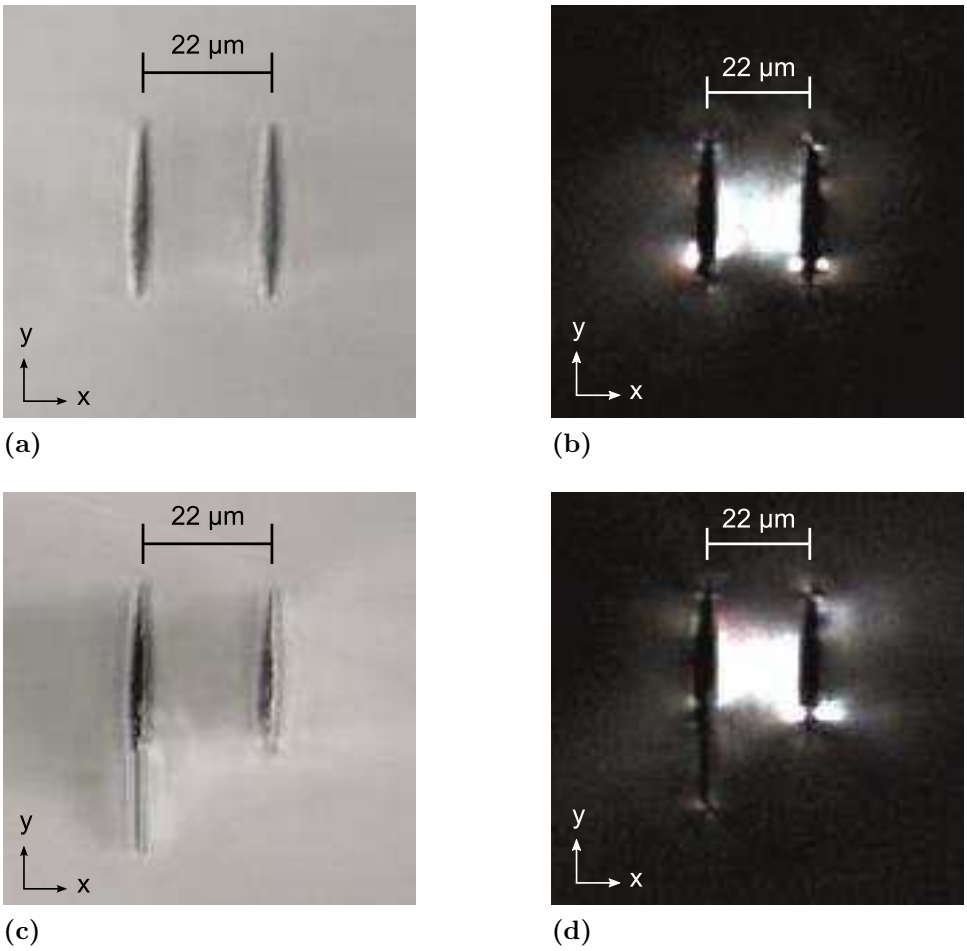

Figure 5.4: Microscope images of DTSs inscribed with $\Delta x = 22\,\mu m$ for different pulse energies. Pictures (a) and (c) are bright field images of DTSs inscribed with 1.3 µJ and 1.5 µJ, respectively while (b) and (d) show the corresponding polarization contrast images.

operating parameters of the CPA which have a direct effect on the intensity in the focal volume and therefore on the modified volume.

The picture shown in figure 5.4b was taken in polarization contrast mode with the *E*-field vector of the incident light parallel to the optical axis. The dark area around the DTS shows that no stress induced birefringence is present in the bulk material. However, the area between and in the direct vicinity of the tracks is bright. This can be attributed to a change in the polarization of the incident light caused by stress induced birefringence.

Not all tracks were free of microcracking, which can be seen by the bright field image of a DTS inscribed with $E_{\text{pulse}} = 1.5\,\mu J$ and $\Delta x = 22\,\mu m$ displayed in figure 5.4c. Here, a microcrack appears parallel to the long axis of the left track. Since the crack was most likely caused by too much stress induced by the modified material it can lead to a dissipation of the stress field and therefore to reduced birefringence. This is not confirmed by the image depicted in figure 5.4d that was taken in polarisation contrast mode. As it was the case for the DTS without cracks, stress induced birefringence can be seen between and directly around the tracks. Therefore, it seems that the formation of microcracks

along the y-direction does not present a critical problem for stressed induced birefringence between the tracks.

5.3.2 Guiding Losses

The guiding losses of the fabricated waveguides were determined with the setup depicted in figure 5.5. The beam of a polarization stabilized HeNe-laser operating at a wavelength of 632.8 nm was sent through a PBSC, a Faraday rotator, and a $\lambda/2$-waveplate. It was then focussed with an aspheric lens into a polarization maintaining single mode fiber (*Newport* F-SM16PM) with a core diameter of $d_{\text{core}} = 16.3\,\mu\text{m}$. At a wavelength of 470 nm the mode field diameter and NA of the fiber were $13.0\,\mu\text{m} \pm 1\,\mu\text{m}$ and 0.051 ± 0.01, respectively [New13]. The end of the fiber was butt coupled to the input coupling facet of the crystal with the inscribed waveguides. The crystal was set on a holder which allowed the pitch and yaw of the sample to be adjusted. The holder itself was mounted on a x-y-translation stage. This system made it possible to optimize the input coupling between fiber and waveguide. The polarization direction of the light inciding on the input coupling facet of the crystal was controlled by adjusting the $\lambda/2$-waveplate. Back reflections occuring at the facet or any of the optical elements which could destabilize the HeNe-laser were filtered out by the combination of Faraday rotator and PBSC. Behind the crystal a 50× microscope objective with a numerical aperture of 0.5 was used to image the guided light onto a power meter in order to measure the transmitted power. The mode field diameters were determined by changing the power meter with a CCD camera. An aperture placed between the microscope objective and CCD chip/power meter allowed scattered light or light guided beside the DTSs which would otherwise distort the measurement to be filter.

The guiding losses were determined by correcting the power measured behind the waveguides for Fresnel reflection and comparing it with the power in front of the crystal.

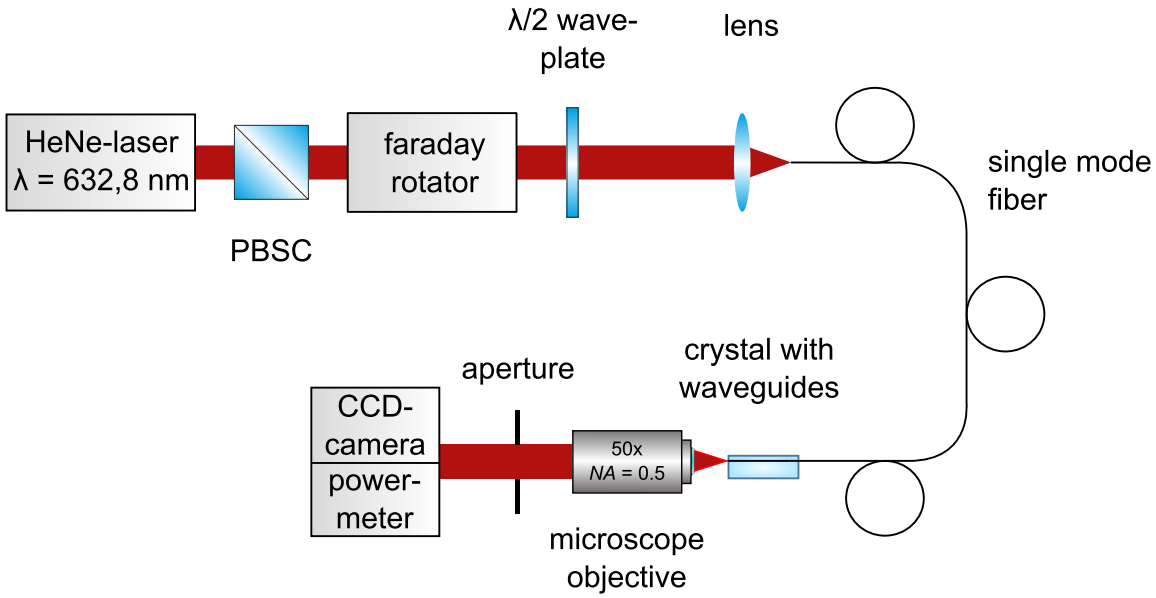

Figure 5.5: Schematic of the setup used for determining waveguiding losses and mode field diameters of the fabricated waveguides.

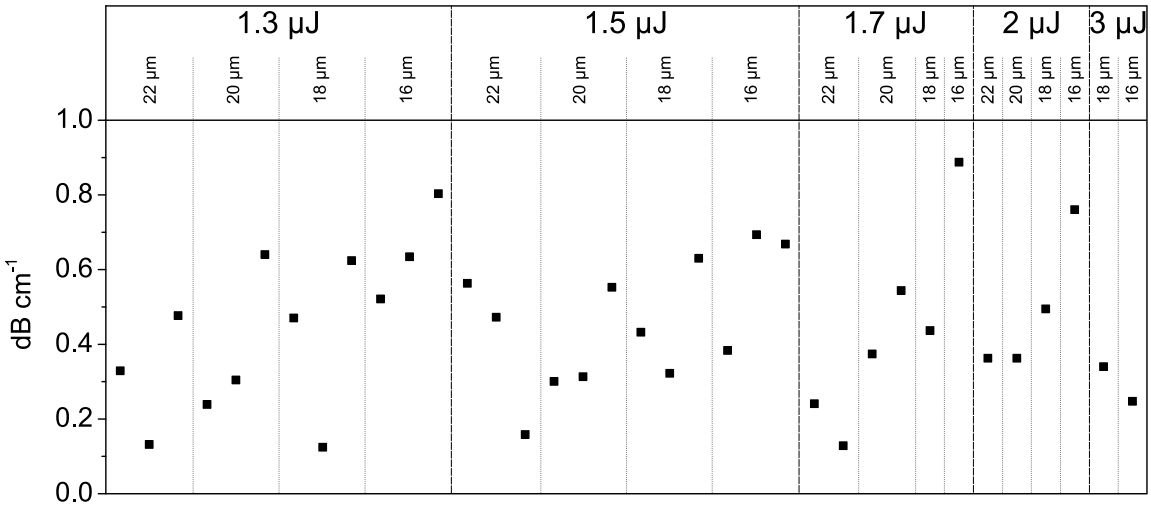

Figure 5.6: Guiding losses of waveguides inscribed in Pr,Mg:SRA in dependence of E_{pulse} and Δx.

However, due to a mismatch of mode field diameter and *NA* between fiber and waveguide, the power which was coupled into each waveguide was actually lower. Since these coupling losses were neglected the obtained values only give an upper limit for the guiding losses.

The results in dependence of pulse energy and track distance are depicted in figure 5.6. The obtained values are between $0.12\,\text{dB}\,\text{cm}^{-1}$ and $0.89\,\text{dB}\,\text{cm}^{-1}$ and thus in good agreement with the results reported by Calmano *et al.* [Cal11]. Furthermore the graph shows that higher inscription energies up to $E_{\text{pulse}} = 3\,\mu\text{J}$ do not affect the propagation losses. For the track distance the situation is different. From figure 5.6 it seems that losses increase towards smaller track distances. However, due to the scattering of the obtained values it is difficult to give a definitive statement on the influence of the track distance on the propagation losses. In addition, no significant difference between DTSs with and without microcracks can be seen.

As it was observed in other Type II waveguides, guiding was strongly dependent on the polarization of the incident light [Sie09, Cal11]. Waveguiding occurred only for light polarized parallel to the y-axis.

The obtained values are among the lowest guiding losses reported for Type II waveguides inscribed into a dielectric crystalline medium. DTSs written into $GdVO_4$, $Y_3Al_5O_{12}$, or $LiYF_4$ exhibit guiding losses in the order of $0.5\,\text{dB}\,\text{cm}^{-1}$, $1\,\text{dB}\,\text{cm}^{-1}$, and $< 3\,\text{dB}\,\text{cm}^{-1}$, respectively [Tan10, Sie09, Bec11]. For $GdVO_4$ measurements were conducted with light of $\lambda = 780\,\text{nm}$ while for $Y_3Al_5O_{12}$ and $LiYF_4$ a wavelength 632.8 nm was employed.

5.3.3 Mode Field Diameter and M^2

By exchanging the power meter with a CCD camera the mode field diameters $2w_0$ of the guided modes as defined by I_0/e^2 were determined. The upper part of figure 5.7 depicts the results in dependence of the pulse energy and track distance. Guided modes were often nearly circular or elliptically shaped with aspect ratios of 1:1 to 1:2 (x:y) and had almost Gaussian intensity profiles. An exemplary mode profile is depicted in figure 5.8a. Depending on the writing parameters mode field diameters of $2w_{0,\text{x}}$ =9.3 µm - 14.8 µm and

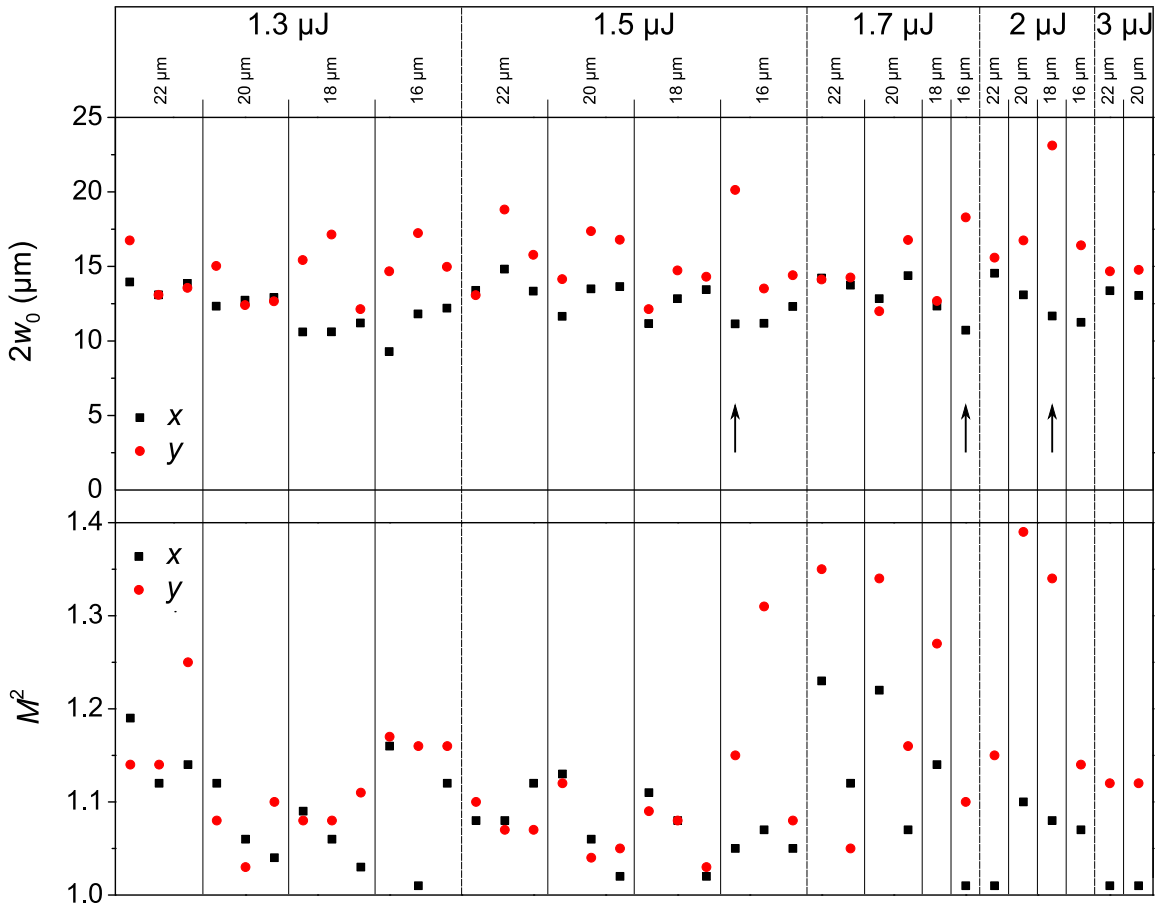

Figure 5.7: Mode field diameters of waveguides inscribed in Pr,Mg:SRA and M^2 values sorted by the inscription parameters E_{pulse} and Δx. Black arrows indicate DTS which exhibited the guidance of a secondary mode.

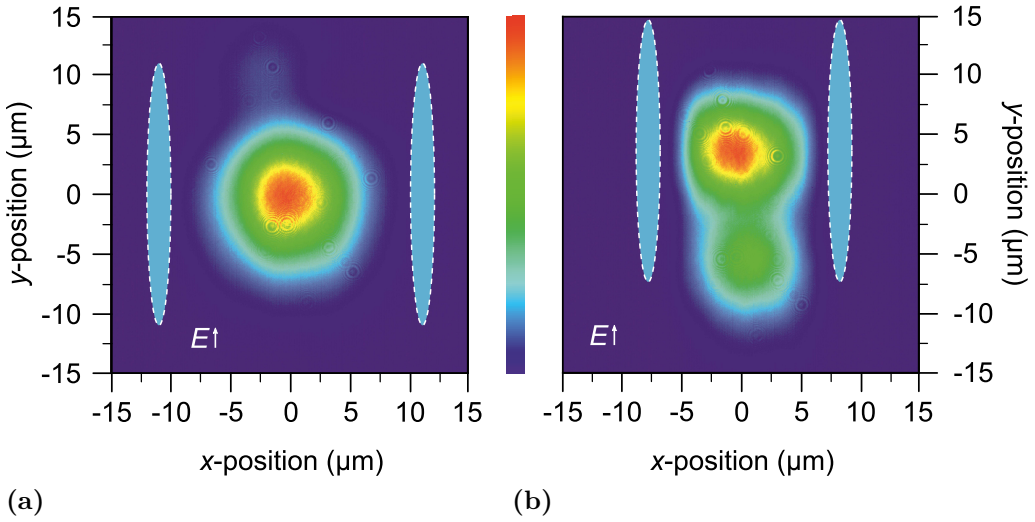

Figure 5.8: Exemplary mode profiles of modes guided in DTSs inscribed with (a) $E_{\mathrm{pulse}} = 1.7\,\mu\mathrm{J}$ and $\Delta x = 22\,\mu\mathrm{m}$ and (b) $E_{\mathrm{pulse}} = 1.5\,\mu\mathrm{J}$ and $\Delta x = 16\,\mu\mathrm{m}$.

$2w_{0,y} = 12.0\,\mu m$ - $23.1\,\mu m$ were measured. As expected, decreasing the track distance lead to a stronger confinement of the mode in x-direction and therefore to a decrease of $2w_{0,x}$. For $2w_{0,y}$ no such effect can be seen. At track distances of $16\,\mu m$ and $18\,\mu m$ a small number of waveguides exhibited guiding of a second mode displaced along the y-axis, which could not be surpressed by optimizing the incoupling (cf. figure 5.8b). Within the investigated parameter range no influence of the pulse energy on the mode field diameters could be observed.

In order to obtain the M^2 of the guided modes, the CCD camera/power meter and the microscope objective were removed from the setup. The beam exiting the waveguide was collimated with a lens and analyzed with a *Spiricon* M200s M^2 measurement device.

The M^2 values which were derived in this way are depicted in the lower part of figure 5.7. The obtained beam qualities were excellent with M^2 values in the x-direction of 1.01 - 1.23 and 1.03 - 1.39 in the y-direction. No clear dependence of the M^2 on either E_{pulse} or Δx can be seen. However, it seems that towards smaller track distances and higher pulse energies the deviation between M_x^2 and M_y^2 increases.

5.3.4 Numerical Aperture and Refractive Index Change

The obtained $2w_0$ and M^2 values allowed the NA of the DTSs to be calculated by employing the relation

$$NA = \sin(\Theta) = \frac{M^2 \cdot \lambda}{\pi \cdot w_0} \tag{5.2}$$

where λ is the wavelength ($\lambda_{\text{HeNe}} = 632.8\,nm$), w_0 the beam waist, and Θ half the opening angle. For small values of Θ it can be assumed that $\sin(\Theta) = \Theta$.

The numerical apertures of the tracks calculated with equation 5.2 are depicted in the upper part of figure 5.9. In the x-direction values between 0.022 and 0.050 were determined, while in the y-direction they were between 0.023 and 0.045.

In a simplified approach the DTSs can be regarded to exhibit a step index profile. This allows for the estimation of the difference in refractive index between the guiding area (n_2) and the surrounding material (n_1) via

$$\Delta n = n_2 - n_1 = \sqrt{NA + n_1^2} - n_1. \tag{5.3}$$

Employing the obtained numerical apertures leads to $\Delta n_x = 2.2{\cdot}10^{-4}$ - $7.1{\cdot}10^{-4}$ and $\Delta n_y = 1.5{\cdot}10^{-4}$ - $5.7{\cdot}10^{-4}$ (see lower part figure 5.9). The obtained numerical apertures and refractive index changes are in good agreement with [Cal13] where the NA for a DTS with $\Delta x = 28\,\mu m$ inscribed with $E_{\text{pulse}} = 1.3\,\mu J$ is reported to be 0.022 and the corresponding Δn is estimated to be $1.4 \cdot 10^{-4}$. The fact that the numerical aperture as well as the mode field diameter are not strongly dependent of the inscription parameters bears an advantage for the laser experiments. It means that it is not necessary to switch between different lenses for waveguides fabricated with different inscription parameters and to still maintain a comparable input coupling efficiency.

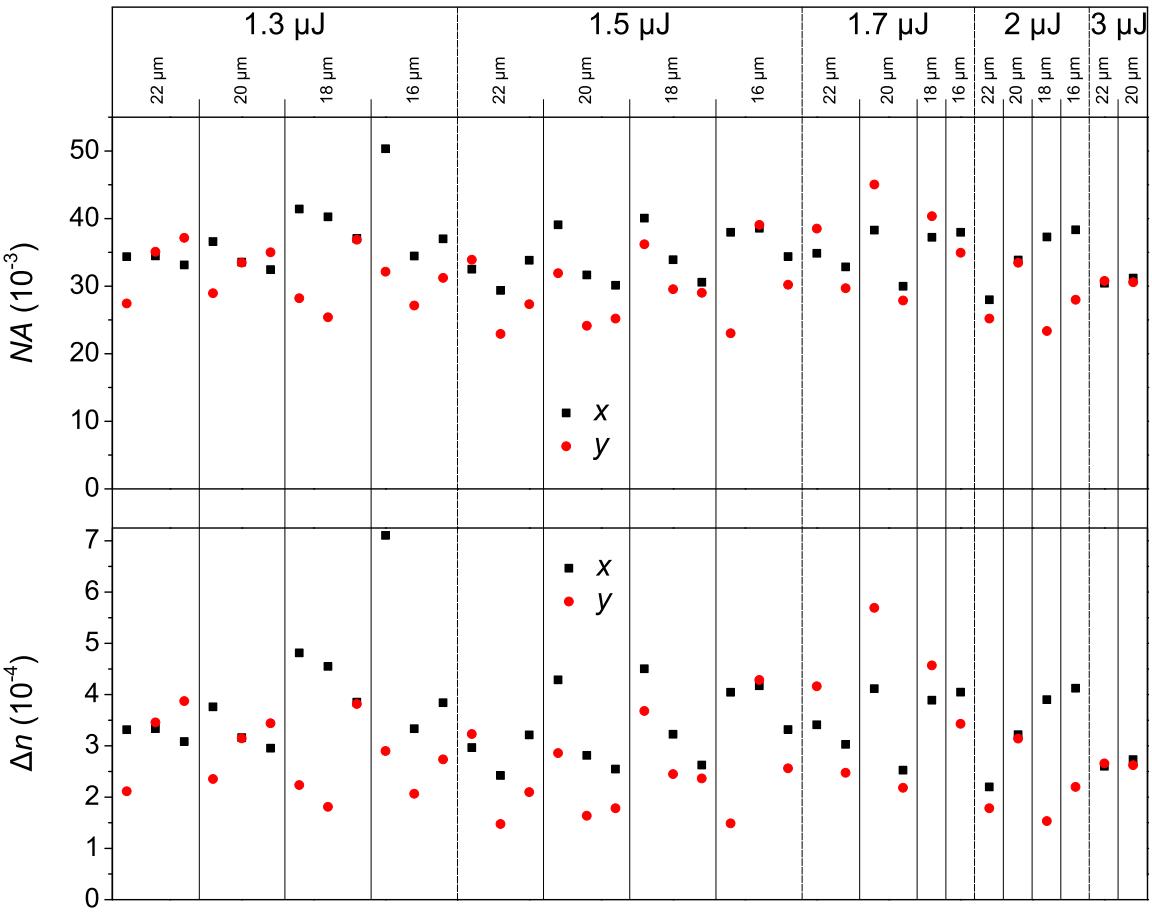

Figure 5.9: Numerical apertures and change of refractive index of waveguides inscribed in Pr,Mg:SRA sorted by the inscription parameters E_{pulse} and Δx.

6 Spectroscopy

All materials which were investigated in this thesis were characterized for their spectroscopic properties. This included determining ground state absorption, fluorescence dynamics and spectra, as well as excited state absorption. Additionally, some materials were also investigated for the energetic positions of the $4f^n$ Stark levels as well as for their excitation and gain characteristics. Depending on material and technique, measurements were carried out at room temperature and/or at cryogenic temperatures. The methods and machines employed for these investigations will be described in the first part of this chapter. In the second part the results of the measurements will be presented and discussed. The chapter closes with a short summary of the obtained results.

6.1 Measurement Techniques

6.1.1 Ground State Absorption

If light with a given wavelength λ and initial intensity $I_0(\lambda)$ is sent through a sample with thickness d, the intensity behind the sample $I(\lambda,\ d)$ can be calculated by employing the Lambert-Beer-Law

$$I(\lambda, d) = I_0(\lambda) \cdot e^{-\alpha(\lambda)\, d} \tag{6.1}$$

with $\alpha(\lambda)$ as the absorption coefficient. Equation 6.1 can be solved for $\alpha(\lambda)$ which leaves

$$\alpha(\lambda) = \frac{1}{d} \cdot \ln\left(\frac{I_0(\lambda)}{I(\lambda, d)}\right). \tag{6.2}$$

In this form the Lambert-Beer-Law allows the ground state absorption (GSA) spectrum of a sample to be calculated from its transmission spectrum. If furthermore the density of active ions in the sample, i.e. the doping concentration N_{dop} is known, the GSA cross sections can be determined via

$$\sigma_{\mathrm{abs}} = \frac{\alpha(\lambda)}{N_{\mathrm{dop}}}. \tag{6.3}$$

A *Varian* Cary 5000 UV-Vis-NIR spectrophotometer was used to record transmission spectra of samples cut from the boules presented in section 4. Each sample was oriented with respect to its optical axis and polished plane parallel. Polarization dependent measurements were made possible by employing a Glan-Thompson-polarizer. The thickness of the samples was chosen individually in order to achieve non-saturated transmission spectra. The resolution of each measurement was adjusted to ensure that all features of the obtained spectra were fully resolved.

6.1.2 Fluorescence Dynamics

The investigation of the fluorescence decay dynamics of a gain medium gives insight into several characteristics of an active medium. It allows, for example, the effective lifetime τ_{eff} of an energy level to be derived by integrating the temporal evolution of the fluorescence intensity and normalizing it with its maximum:

$$\tau_{\text{eff}} = \frac{1}{I_0} \int_0^\infty I(t)\ \mathrm{d}t. \tag{6.4}$$

The effective lifetime is a necessary parameter for determining the time evolution of the upper laser level via rate equations and also in calculations of the laser threshold (cf. section 2.3). Furthermore, if the radiative lifetime τ_{rad} is known and no other processes which affect τ_{eff} are present, the multiphonon decay rate W_{mp} and therefore the quantum efficiency can be calculated via equation 2.18. This allows the suitability of the respective energy level as an upper laser level to be assessed and the material as gain medium in general. The radiative lifetime also allows the emission cross sections to be calculated via the Füchtbauer-Ladenburg method (cf. section 6.1.4). This is a necessary parameter in several equations dealing with various laser characteristics.

If τ_{rad} is not known, measurements with low doped samples at cryogenic temperature can be carried out to derive this value. Low doping concentrations are necessary to minimize energy transfer upconversion (ETU) and cross relaxation processes which are strongly dependent on the distance between active ions and can distort the results. A small number of dopant ions further reduce reabsorption processes which can also affect the measurements. Cryogenetic temperatures lead to a freeze-out of phonon modes and multiphonon processes in equation 2.18 and can therefore be neglected. The resulting decay curve should follow a single exponential decay. If this is the case, τ_{rad} can be derived by fitting a function

$$I(t) = I_0 \exp\left(-\frac{t}{\tau_{\text{rad}}}\right) \tag{6.5}$$

to the decay curve.

However, decay curves recorded at room temperature also hold valuable information. The aforementioned ETU and cross relaxation processes cause the decay curves to become non single exponential, and several models were developed to describe these processes on a microscopic [För48] and also on a macroscopic scale [Ino65, Vor82]. A detailed introduction into these models can be found in [Auz04, Ric08, Fec12].

The setup which was employed to measure the fluorescence dynamics is depicted in figure 6.1. As an excitation source, a continuously tunable optical parametric oscillator (OPO) was used. It was pumped by a frequency tripled, Q-switched Nd:YAG laser and operated at a repetition rate of $f_{\text{rep}} = 10\,\text{Hz}$ with a pulse duration of $\tau_{\text{pulse}} = 10\,\text{ns}$. The tuning range of the OPO was 485 nm - 1300 nm. An additional stage allowed for the frequency doubling of the output of the OPO and therefore the wavelength range of 245 nm - 450 nm to be addressed. The emitted beam was focused with a lens with $f = 150\,\text{mm}$ onto the sample. Two lenses which were set up with their axes orthogonal to the beam of the OPO were used to collimate and image the fluorescence of the sample

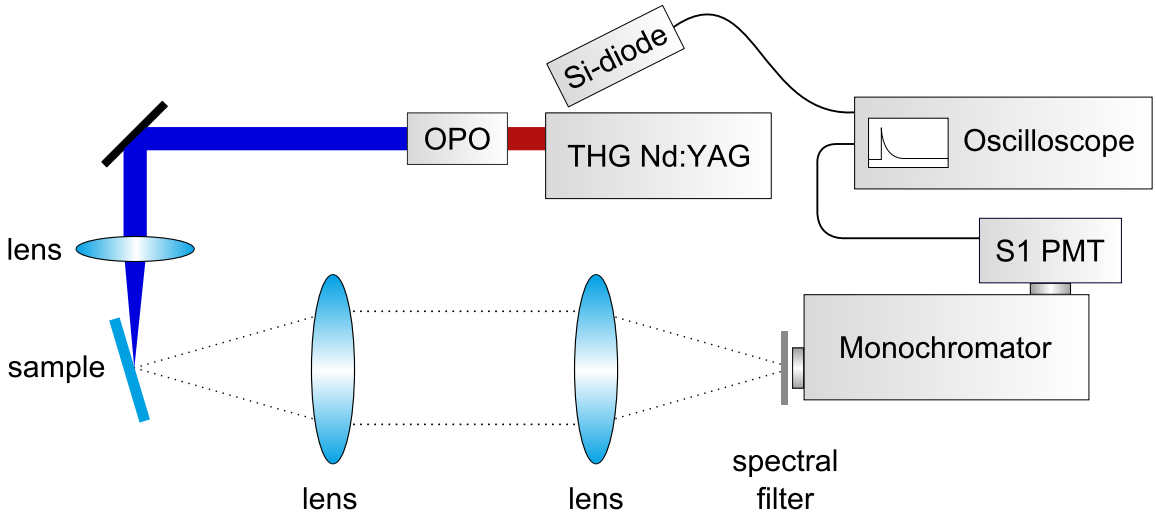

Figure 6.1: Schematic of the setup used to obtain fluorescence dynamics of the active media.

onto the entrance slit of a 0.5 m *SPEX 500* monochromator. In order to prevent residual pump light from entering the monochromator, color filters were placed in front of the slit. A detector at the exit slit of the *SPEX 500* was used to detect the fluorescence. The signal was recorded and averaged over at least 500 pulses by an oscilloscope. The trigger signal for the oscilloscope was delivered by a Si-photodiode which detected residual light of the flash lamp that pumped the Nd:YAG.

The monochromator could be equipped with different gratings and detectors to allow measurements in different spectral regions. For the visible spectral range a grating with 1200 lines/mm, a blaze angle Θ_{blaze} optimized for 500 nm, and a spectral resolution of $\frac{\Delta\lambda}{\Delta x} = 1.6\,\text{nm/mm}$ was used. The fluorescence was detected with a *Products for Research Inc. S1* photomultiplier (PMT).

In order to investigate the fluorescence decay in dependence of the temperature the sample could be mounted in a *Leybold* ROK 10/300 cryostate. This allowed measurements in the temperature range of 10 - 300 K.

6.1.3 Excitation Spectra

Investigations of the excitation characteristics of an active medium at its various emission wavelengths allow the presence of additional optically active centers to be exposed. These can be, for example, an intrinsic property of the host system (e.g. sesquioxides [Pet09, Koo12]) or a clustering of the dopant ion (e.g. Nd:SrF_2 [Pay91]). In either case ions on different sites will be subject to different crystal fields and therefore exhibit distinct spectral properties.

The excitation characteristics were investigated with a *Yobin Yvon* FL 321 Fluorolog-3 (cf. figure 6.2). The light emitted by a 450 W high pressure xenon discharge lamp was focused on the entrace slit of a 2×180 mm double monochromator that was equipped with two gratings (ex1 and ex2, specifications can be found in table 6.1). The monochromator selected a spectrally narrow part of the broad band emission of the Xe-lamp. This allowed the excitation wavelength to be chosen between 250 nm and 1000 nm. The light

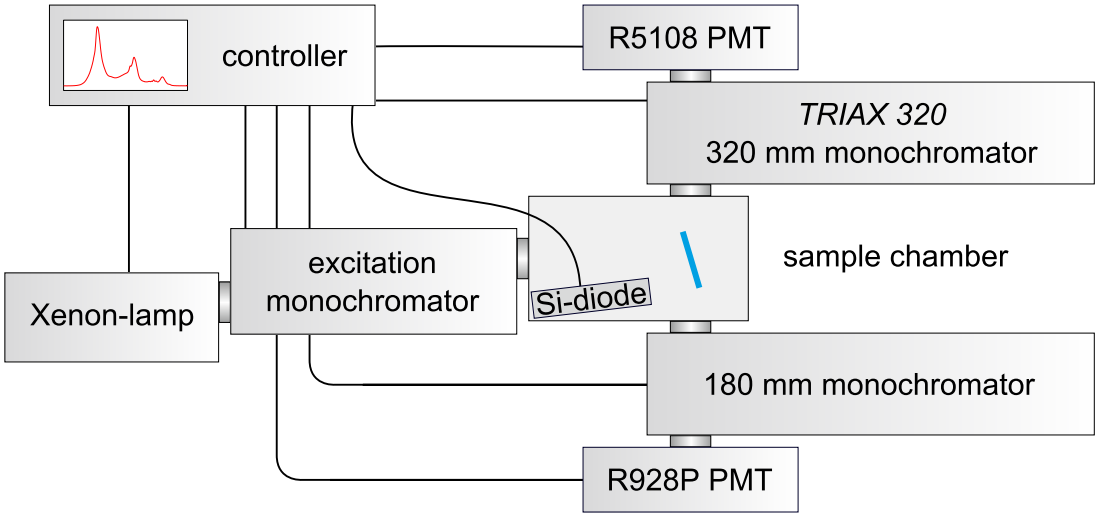

Figure 6.2: Schematic of the *Yobin Yvon* FL 321 Fluorolog-3.

then entered the sample chamber where a Si-diode recorded a reference intensity I_{ref}. The sample was illuminated and the resulting fluorescence could be analyzed by two monochromator/PMT combinations set up orthogonally to the incident direction of the excitation light and facing each other. One combination consisted of a 180 mm monochromator (grating emA1, cf. table 6.1) and a *Hamamatsu R928P* PMT with a detection range of 185 nm - 900 nm. The second combination was a 320 mm *Triax 320* monochromator which allowed the choice of three gratings (emB1-emB3). The fluorescence was detected with a *Hamamatsu R5108* PMT sensitive from 400 nm to 1200 nm.

	lines/mm	$\frac{\Delta\lambda}{\Delta x}\left(\frac{\text{nm}}{\text{mm}}\right)$	λ_{opt} (nm)
ex1/ex2	1200	2.18	250
emA1	1200	4.35	500
emB1	1200	2.64	500
emB2	1200	2.64	250
emB3	300	10.56	250

Table 6.1: Specifications of gratings available in the *Yobin Yvon* FL 321 Fluorolog-3.

All components of this system were controlled by a computer that also processed the recorded reference and signal intensities. I_{sig} was calibrated with the relation

$$I(\lambda) = \frac{I_{\text{sig}}(\lambda)}{I_{\text{ref}}(\lambda)}. \tag{6.6}$$

This was necessary to correct the obtained spectra for effects occuring due to fluctuations of the Xe-lamp and artifacts introduced by the excitation monochromator.

6.1.4 Emission Spectra

Two theoretical approaches were taken in this work to calculate the emission cross sections $\sigma_{\mathrm{em}}(\lambda)$ of an active material. The first method derives the emission cross sections from fluorescence spectra and is referred to as the Füchtbauer-Ladenburg method [Hub75, Mou86]. The second employs absorption spectra and the position of the $4f^{\mathrm{n}}$ energy levels to derive $\sigma_{\mathrm{em}}(\lambda)$ by the principle of equal atomic cross sections [Ein16] and is denoted as the reciprocity method [McC64].

Füchtbauer-Ladenburg Method

For an anisotropic medium the emission cross sections $\sigma_{\mathrm{em}}(\lambda)$ of the active ion can be calculated via

$$\sigma_{\mathrm{em}}^{\alpha_i}(\lambda) = \frac{\lambda^5 \ \beta_{jk}}{8\pi \ n^{\alpha_i}(\lambda)^2 \ c \ \tau_{\mathrm{r}}} \cdot \frac{I^{\alpha_i}(\lambda)}{\int \lambda \ \frac{1}{3} \ \sum_{i=1}^{3} I^{\alpha_i}(\lambda) \ \mathrm{d}\lambda} \tag{6.7}$$

where $I^{\alpha_i}(\lambda)$ gives the fluorescence intensity in dependence of the wavelength λ. α_i is the polarization of the light, n the refractive index of the material and the parameter β_{jk} is the branching ratio between the multiplets j and k [Hub75, Mou86].

The fluorescence spectra which were used to obtain emission cross sections via equation 6.7 were recorded with the setup depicted in figure 6.3. Here the beam of a pump laser was modulated by an optical chopper at a frequency of approximately 1 kHz. It was then focused onto the sample under a flat angle with a lens of $f = 320\,\mathrm{mm}$. The fluorescence emitted by the sample was collimated and then focused onto the entrance slit of a 1 m *SPEX 1000* monochromator. In order to prevent residual pump light from entering the monochromator a spectral filter could be placed in front of the slit. Furthermore, polarization dependent measurements could be carried out by covering the slit with a Glan-Thompson polarizer. The monochromator was equipped with a

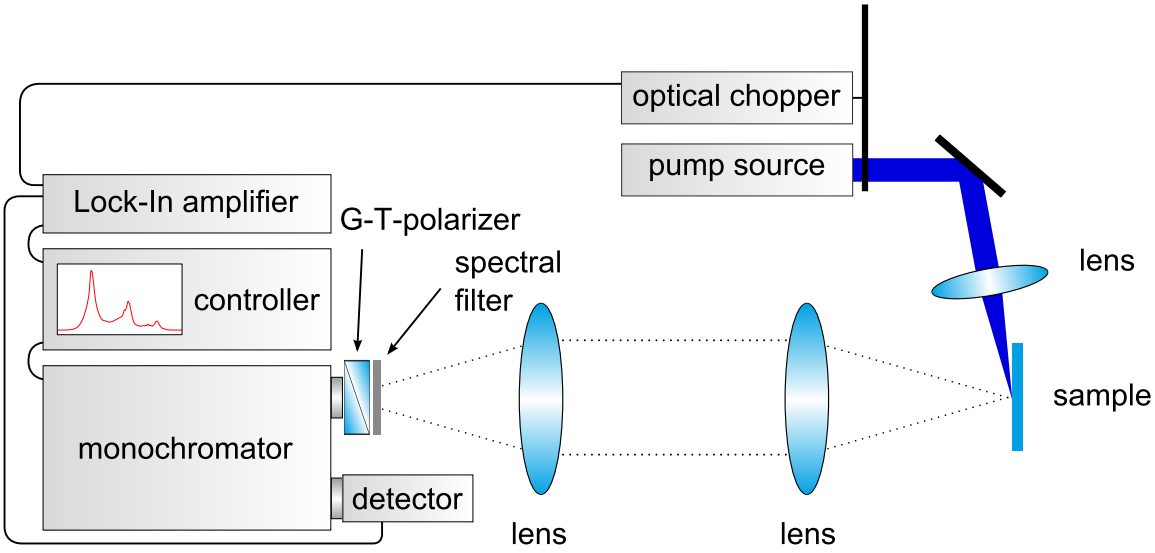

Figure 6.3: Schematic of the setup employed for fluorescence measurements.

1200 lines/mm blazed grating, optimized for a wavelength of 500 nm. The spectral resolution was $\frac{\Delta\lambda}{\Delta x} = 0.8\,\mathrm{nm/mm}$. At the exit slit of the monochromator a Si-diode was employed as detector. In order to maximize the signal-to-noise (s/n) ratio the signal of the diode was sent through a *Stanford Research Inc.* SR 810 DSP lock-in amplifier. The reference signal was provided by the driver of the optical chopper. The resulting signal was recorded by a computer that also controlled the *SPEX 1000*.

In order to correct the obtained spectra for artifacts caused by any part of the optical setup and the sensitivity of the detector, it is necessary to determine the wavelength dependent correction factor $k(\lambda)$. This was done by comparing the measured fluorescence spectrum of a tungsten fillament lamp at $T = 2600\,\mathrm{K}$ with a spectrum that was obtained theoretically. The theoretical spectrum was calculated from the emissivity of tungsten $\epsilon_\mathrm{W}(\lambda)$ and the emission spectrum $I_{\mathrm{bb},2600\,\mathrm{K}}(\lambda)$ of a black body at $T = 2600\,\mathrm{K}$. The correction factor then follows from

$$k(\lambda) = \frac{I_{\mathrm{bb},2600\,\mathrm{K}}(\lambda) \cdot \epsilon_\mathrm{W}(\lambda)}{I_{\mathrm{W},2600\,\mathrm{K}}(\lambda)} \tag{6.8}$$

and the measured fluorescence spectra can be corrected via the simple relation

$$I(\lambda) = k(\lambda) \cdot I_\mathrm{measured}(\lambda). \tag{6.9}$$

The corrected fluorescence spectra were then used to derive the emission cross sections with equation 6.7.

A problem of this method is that measured fluorescence spectra often exhibit reduced fluorescence intensities in wavelength areas where reabsorption occurs. This is problematic specifically when (quasi-)three-level-systems are characterized since in these cases the spectral overlap between the absorption and emission band is often substantial. For four-level-systems this problem is less severe and can be neglected if samples with low doping concentrations are being used, and only small volumina are excited. Nevertheless it should be noted that reabsorption can never be fully eliminated in this type of measurement and emission cross sections obtained with the Füchtbauer-Ladenburg method will therefore always contain a certain degree of error. Further sources of error can be incorrect radiative lifetimes and/or refractive indices.

Reciprocity Method

Another possible approach to obtain $\sigma_\mathrm{em}(\lambda)$ is the reciprocity method, which is also referred to as McCumber method [McC64]. The ansatz for this theorem is that emission and absorption cross sections can both be derived from the atomic cross section $\sigma_\mathrm{at}(\lambda)$ via

$$\sigma_\mathrm{abs} = f_\mathrm{l} \cdot \sigma_\mathrm{at} \qquad \text{and} \tag{6.10}$$

$$\sigma_\mathrm{em} = f_\mathrm{u} \cdot \sigma_\mathrm{at}. \tag{6.11}$$

The parameters f_l and f_u give the Boltzman occupation of the lower and upper Stark multiplet. For an arbitrary Stark level with energy E_i the Boltzmann population follows from

$$f_i = \frac{g_i}{Z} \cdot \exp\left(-\frac{E_i - E_0}{kT}\right) \tag{6.12}$$

with g_i giving the degeneracy of the level, E_0 the energy of the lowest Stark level, and kT the product of the Boltzmann constant and the temperature. Z is the partition function and is given by

$$Z = \sum_i g_i \cdot \exp\left(-\frac{E_i - E_0}{kT}\right). \tag{6.13}$$

Using equations 6.10 - 6.12 the emission cross sections can be derived from the absorption cross sections with

$$\sigma_{\mathrm{em}}(\lambda) = \sigma_{\mathrm{GSA}}(\lambda) \cdot \frac{Z_l}{Z_u} \cdot \exp\left(\frac{E_{\mathrm{ZL}} - \frac{hc}{\lambda}}{k\ T}\right). \tag{6.14}$$

This method has the advantage that reabsorption does not pose a problem. However, the factor $E_{\mathrm{ZL}} - \frac{hc}{\lambda}$ in equation 6.14 causes an amplification of noise of the GSA spectra for $E_{\mathrm{ZL}} \ll \frac{hc}{\lambda}$. In addition, the precise energetic position of the Stark levels of the involved manifold must be known. This method cannot be applied to four-level systems due to the fact that in these cases most radiative transitions do not exhibit a corresponding absorption transition.

Fluorescence Measurements with the *Yobin Yvon* FL 321 Fluorolog-3

In the cases where purely qualitative analyses of a gain material were sufficient, emission measurements were also carried out with the *Yobin Yvon* FL 321 Fluorolog-3. It had the advantage that the Xe-lamp which is used as excitation source allows the excitation wavelength to be choosen between 250 nm and 1000 nm. Like measurements of the excitation characteristics, comparing the emission spectra at different excitation wavelengths can give insight into whether or not a host exhibits multiple dopant sites. Another advantage is the high sensitivity of the PMTs that allowes for much shorter measurement times than the setup presented in figure 6.3. However, due to the employed monochromators the resolution was not sufficient to fully resolve all features of the recorded spectra (cf. table 6.1). Furthermore, it was not possible to correct $I(\lambda)$ for artifacts introduced by the two emission monochromators, which is why the *Fluorolog* could only be employed for qualitative measurements. In addition the *Fluorolog* does not allow polarization dependent measurements.

6.1.5 Determination of Stark Level Positions

The position of the various Stark levels composing ground and excited states of an active ion can be determined by ground state absorption and emission measurements. However, two effects necessitate that such measurements must be conducted at cryogenic temperatures (10 K). Firstly, the population inside a multiplet follows the Boltzmann distribution and thus transitions originate from various Stark levels of the ground and excited state. This results in a large number of absorption and emission peaks which often overlap and can therefore not be used to derive the energy level positions. Depending on the energetic distance between the Stark levels in a manifold, at 10 K most of the population occupies the lowest Stark level. Consequently transitions originate mainly from a single energy

level. Secondly, the electron-phonon coupling is much stronger at room temperature, causing a pronounced inhomogeneous broadening of the absorption and emission bands. The freeze-out of the phonon modes at cryogenic temperatures leads to a narrowing of the bands and the central wavelength can therefore be determined with higher accuracy.

The emission spectra necessary to determine the positions of the Stark levels composing the ground state were recorded with the setup introduced in section 6.1.4 and by placing the sample on the cold finger of a cryostate (cf. section 6.1.2). In order to prevent a heating of the sample, the absorbed pump power was set to a maximum of 20 mW.

Since the *Varian* Cary 5000 UV-Vis-NIR did not support measurements at cryogenic temperatures transmission spectra were recorded with the setup depicted in figure 6.4. The light emitted by a halogen-lamp was modulated with an optical chopper ($f_{\mathrm{rep}} = 1\,\mathrm{kHz}$) and imaged with a lens with $f = 100\,\mathrm{mm}$ onto an iris with variable diameter. It was then imaged with a lens of $f = 105\,\mathrm{mm}$ onto the sample which was placed on a 2 mm aperture inside the cryostate. The diameter of the iris was then adjusted to achieve a spot size smaller than the aperture. This is necessary since an irradiation of the cold finger could cause an increase of its temperature and thus of the sample. Behind the aperture a second $f = 105\,\mathrm{mm}$ lens imaged the transmitted light onto the entrace slit of a *SPEX 1000*. A Si-diode at the exit slit detected the light transmitted through the monochromator and the lock-in setup depicted in section 6.1.4 was employed to optimize the s/n ratio.

6.1.6 Gain Spectra

As described in section 2.3.2, in a (quasi-)three-level-system reabsorption can occur on the prospective laser wavelengths. This has a direct effect on the inversion level β necessary to achieve gain where β is defined by the total number of ions N_{tot} and the number of ions in the upper laser level N_1 via

$$\beta = \frac{N_1}{N_{\mathrm{tot}}}. \tag{6.15}$$

In order to determine the critical inversion level at which gain becomes dominant, the gain cross sections can be derived from the absorption and emission cross sections with

$$\sigma_{\mathrm{gain}}(\lambda) = \beta\ \sigma_{\mathrm{em}}(\lambda) - (1-\beta) \cdot \sigma_{\mathrm{abs}}(\lambda). \tag{6.16}$$

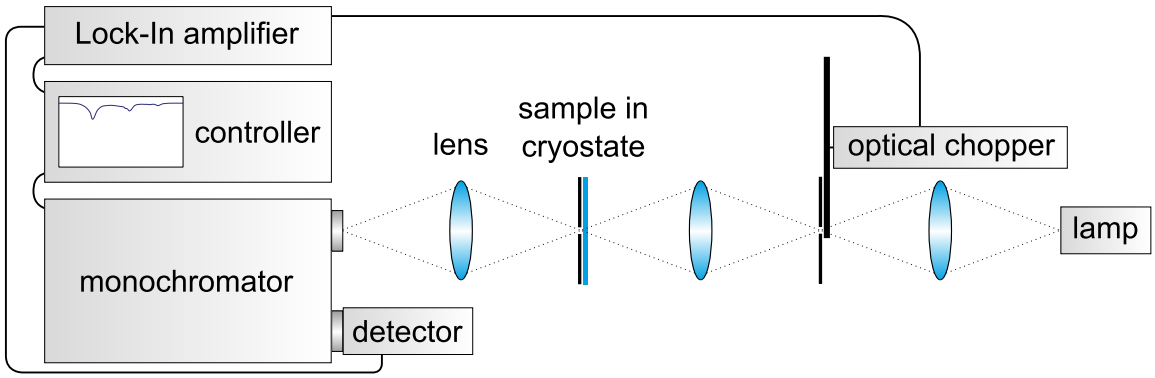

Figure 6.4: Schematic of the setup employed to transmission measurements at cryogenic temperatures.

From equation 6.16 it becomes clear that the spectral shape of the gain spectra will vary in dependence of β. This means that if additional losses are introduced, for example in the form of output coupling through the cavity mirrors, higher inversion levels are necessary to compensate. In such a case the emission wavelength of the laser might strongly depend on the output coupling rate.

6.1.7 Excited State Absorption

The process of population transfer from the upper laser level into an energetically higher level by absorption of laser or pump photons can be highly detrimental for laser operation. In order to investigate whether such ESA transitions are present, the method proposed by Koetke *et al.* was employed [Koe95].

The basic principle of this method is to compare the intensities of light transmitted through an active medium in its ground state $I_{\mathrm{g}}(\lambda)$ and excited state $I_{\mathrm{e}}(\lambda)$. While $I_{\mathrm{g}}(\lambda)$ follows from the Lambert-Beer-Law (cf. equation 6.1), $I_{\mathrm{e}}(\lambda)$ is given by

$$I_{\mathrm{e}}(\lambda) = I_0(\lambda) \cdot \exp\left[-d \cdot (N_{\mathrm{tot}} - N_{\mathrm{e}})\sigma_{\mathrm{abs}}(\lambda) + d \cdot \sum_i N_i \left(\sigma_{\mathrm{em},i}(\lambda) - \sigma_{\mathrm{ESA},i}(\lambda)\right)\right]. \quad (6.17)$$

Here N_{tot} gives the total number of ions and N_{e} the number of excited ions. N_{e} follows from the number of ions in the i available excited multiplets ($N_{\mathrm{e}} = \sum_i N_i$). From equation 6.1 and 6.17 it follows that

$$\ln\left(\frac{I_{\mathrm{e}}(\lambda)}{I_{\mathrm{g}}(\lambda)}\right) = -d\ N_{\mathrm{e}}\left[\sigma_{\mathrm{GSA}}(\lambda) + \sum_i \frac{N_i}{N_{\mathrm{e}}}\left(\sigma_{\mathrm{em,i}}(\lambda) - \sigma_{\mathrm{ESA,i}}(\lambda)\right)\right] \quad (6.18)$$

Assuming that the number of ions in all excited states is small against the total number of ions ($N_{\mathrm{e}} \ll N_{\mathrm{tot}}$) the difference $\Delta I(\lambda)$ between $I_g(\lambda)$ and $I_{\mathrm{e}}(\lambda)$ is small against either signal:

$$\Delta I = I_g(\lambda) - I_{\mathrm{e}}(\lambda) \ll I_g(\lambda), I_{\mathrm{e}}(\lambda). \quad (6.19)$$

This allows the logarithm in equation 6.18 to be approximated as

$$\ln\left(\frac{I_{\mathrm{e}}(\lambda)}{I_{\mathrm{g}}(\lambda)}\right) = \ln\left(1 + \frac{I_{\mathrm{e}}(\lambda) - I_{\mathrm{g}}(\lambda)}{I_{\mathrm{g}}(\lambda)}\right) = \ln\left(1 + \frac{\Delta I(\lambda)}{I_{\mathrm{g}}(\lambda)}\right) \approx \frac{\Delta I(\lambda)}{I_g(\lambda)}. \quad (6.20)$$

The term $\frac{\Delta I(\lambda)}{I_g(\lambda)}$ can now be determined by using a pump and probe technique. The setup employed in this work is depicted in figure 6.5. The probe beam was delivered by spectrally broad light sources, either a halogen- (Ha) or a xenon-lamp (Xe). Due to the different designs of the light sources, the probe light was either imaged (Ha) or focused (Xe) onto the sample with a lens of $f = 105\,\mathrm{mm}$. An optical chopper placed between source and sample modulated the probe beam with a frequency of $f_{\mathrm{rep,I}} = 0.6\text{ - }1\,\mathrm{kHz}$. The light which was transmitted through the sample was imaged with a second $f = 105\,\mathrm{mm}$ lens onto the entrace slit of a 1 m *SPEX 1000* monochromator. At the exit slit a Si-diode served as detector (cf. section 6.1.4). The pump beam was delivered by a laser with an emission wavelength fitting to an absorption band of the gain medium. The beam was

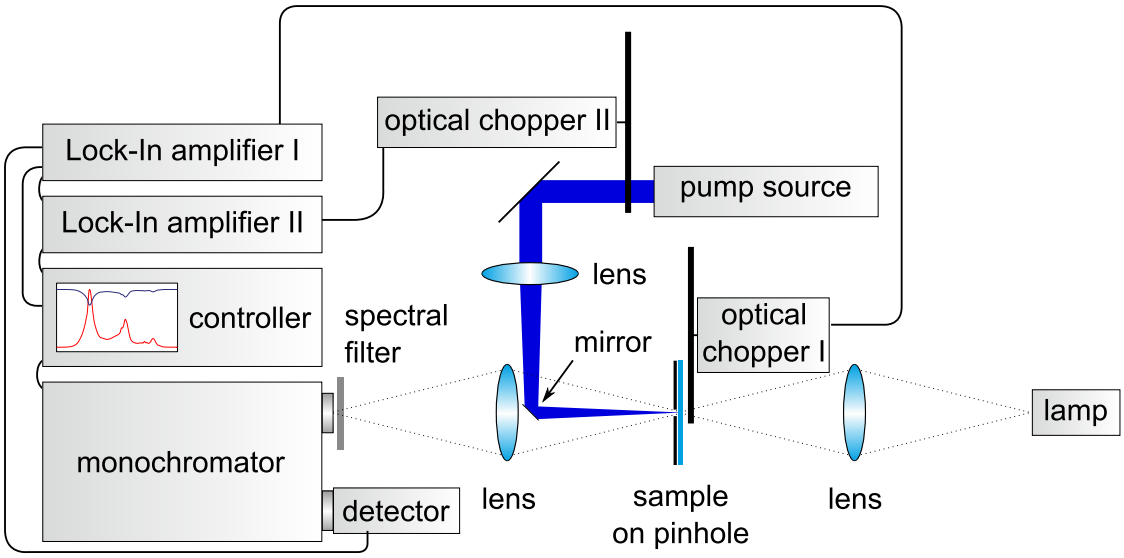

Figure 6.5: Schematic of the setup employed to record excited state absorption spectra.

focused with a lens with $f = 320\,\text{mm}$ via a small deflection mirror placed on the optical axis of the probe light onto the sample. This is necessary to achieve a sufficient overlap of pump and probe light. The pump beam was furthermore modulated by a second optical chopper with $f_{\text{rep,II}} = 6\text{ - }10\,\text{Hz}$. A 500 µm aperture was placed on the surface of the sample in order to prevent light which did not originate from the area of overlap between pump and probe beam to distort the measurement. The signal I measured by the Si-diode was sent into a *Stanford Research Inc.* SR 810 DSP lock-in amplifier for which the first optical chopper provided the reference signal. Depending on whether or not the second optical chopper blocked the pump beam, the signal measured by the diode was either $I_g(\lambda)$ or $I_e(\lambda)$ respectively. A second lock-in amplifier which was provided with the signal of lock-in I and the reference signal of optical chopper II could then derive the difference $\Delta I(\lambda)$ between $I_g(\lambda)$ and $I_e(\lambda)$. The output of lock-in I and II was recorded by a computer.

Since the modulation between $I_g(\lambda)$ and $I_e(\lambda)$ is very small, $I_g(\lambda)$ can be approximated by $I(\lambda)$ and it follows from equation 6.20 that

$$\frac{\Delta I(\lambda)}{I_g(\lambda)} \approx \frac{\Delta I(\lambda)}{I(\lambda)}. \tag{6.21}$$

Therefore, equation 6.18 transforms into

$$\frac{\Delta I(\lambda)}{I(\lambda)} = A\ d\ N_e \left[\sigma_{GSA}(\lambda) + \sum_i \frac{N_i}{N_e}\left(\sigma_{em,i}(\lambda) - \sigma_{ESA,i}(\lambda)\right)\right]. \tag{6.22}$$

The parameter A is introduced in order to account for the amplification factor of the lock-in amplifiers. In order to derive the ESA cross sections it is necessary to identify a spectral region where only GSA is present. Equation 6.22 then becomes

$$\frac{\Delta I(\lambda)}{I(\lambda)} = A\ d\ N_e\ \sigma_{GSA}(\lambda) \tag{6.23}$$

which allows the factor $A\ d\ N_e$ to be determined from a GSA spectrum and the measured spectra to be calibrated.

6.2 Results: Praseodymium Doped Materials

In this section the results of the spectroscopic investigations of the Pr^{3+}-doped materials will be presented. All systems were characterized in terms of ground state absorption, emission, and excited state absorption characteristics. Contrary to Pr,Mg:SRA and Pr:LaF_3, the fluorescence decay dynamics of Pr,Mg:CAlO and Pr:LMA have not been investigated so far. Therefore measurements were carried out to determine the radiative lifetime of both materials. Furthermore, the excitation characteristics of Pr:LMA were recorded in order to investigate whether or not additional optically active centers were present as indicated by the Mg^{2+}-defficiency (cf. section 4.3.3).

6.2.1 Ground State Absorption

The polarization dependent ground state absorption spectra of all systems were recorded with a resolution of 0.15 nm in order to ensure fully resolved spectra. Measurements were carried out in the blue to cyan spectral range of 415 nm - 510 nm where the absorption bands of the prospective pump transitions $^3H_4 \rightarrow {}^3P_J$, $^1I_6$ are located. Since reabsorption occuring on the $^3H_4 \rightarrow {}^1D_2$ transition might affect the lasers operating in the orange spectral region, the absorption between 565 nm and 630 nm was also investigated. All spectra are depicted in figure 6.6. The peak positions and cross sections with the corresponding transition, polarization, and, where useful, linewidth[1] are listed in table 6.2.

In the case of the three hexaaluminates the absorption spectra show a relatively strong dependence on the polarization of the incident light. While for σ-polarized light strong absorption bands are present, the corresponding peaks for π-polarized light are much less pronounced. This can be explained by the high degree of symmetry the coordination sphere exhibits in the a-plane (cf. figure 3.1) which leads to a weak addition of interconfigurational $4f^15d^1$-states. The transition matrix elements and probabilities are therefore small which is reflected in small absorption cross sections for π-polarized light. Stronger absorption for σ-polarized light is favorable since crystals can be prepared in c-cut, which on the one hand exploits the higher absorption cross sections, and on the other allows the polarization of the pump light to be neglected. Pr:YLF crystals must be prepared in a-cut in order to be able to address the stronger absorption bands for π-polarized light [Ric08].

Ground state absorption spectra of Pr,Mg:SRA were measured on a 3.1 mm thick sample of the crystal provided by the IKZ. The peak positions of the absorption maxima are at wavelengths of 444.5 nm, 466.9 nm, and 486.3 nm with corresponding absorption cross sections of $1.3 \cdot 10^{-20}\,cm^2$, $3.0 \cdot 10^{-20}\,cm^2$, and $2.1 \cdot 10^{-20}\,cm^2$, respectively. The maximum value is therefore more than seven times smaller than that of Pr:YLF [Ric08]. However, a very interesting feature is the broad absorption band around 444.5 nm which can be adressed with InGaN laser diodes (LDs). Neglecting the structure of the band the full width at half maximum ($\Delta\lambda$) is approximately 8 nm. The $\Delta\lambda$ of the corresponding peak in Pr:YLF is only 2 nm. This is advantageous since InGaN LDs can exhibit a strong shift of the central emission wavelength from one diode to the next (cf. section 7.1). Because of the larger $\Delta\lambda$ Pr,Mg:SRA is less sensitive towards such shifts and less care has to be taken

[1] The linewidths $\Delta\lambda$ given in this work are defined as full width at half maximum (FWHM).

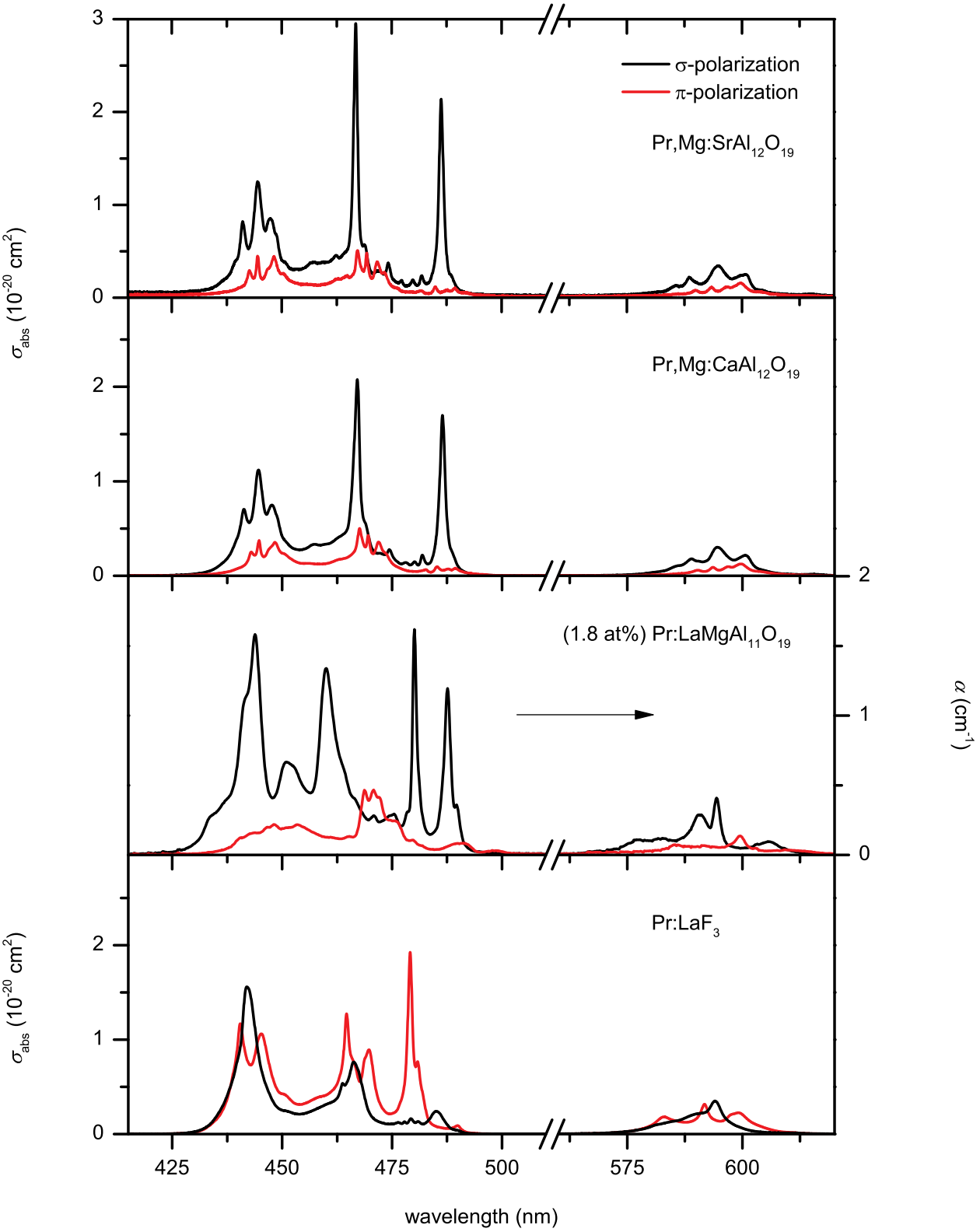

Figure 6.6: Polarization dependent ground state absorption spectra derived for the investigated Pr^{3+}-doped systems. Due to the potential presence of several optically active centers absorption cross sections of Pr:LMA can not be given and absorption coefficients for an 1.8 at% doped sample are listed instead.

system	λ_{gsa} (nm)	σ_{abs} (10^{-20} cm^2)	$\Delta\lambda$ (nm)	polarization	transition
Pr,Mg:$SrAl_{12}O_{19}$	444.5	1.3	(8.0)	σ	$^3H_4 \rightarrow {}^3P_2$
	466.9	3.0	1.1	σ	$^3H_4 \rightarrow {}^3P_1$
	486.3	2.1	1.2	σ	$^3H_4 \rightarrow {}^3P_0$
	594.7	0.3	-	σ	$^3H_4 \rightarrow {}^1D_2$
	444.5	0.5	-	π	$^3H_4 \rightarrow {}^3P_2$
	467.3	0.5	-	π	$^3H_4 \rightarrow {}^3P_1$
Pr,Mg:$CaAl_{12}O_{19}$	444.6	1.2	(8.6)	σ	$^3H_4 \rightarrow {}^3P_2$
	467.0	2.2	1.8	σ	$^3H_4 \rightarrow {}^3P_1$
	486.5	1.8	1.6	σ	$^3H_4 \rightarrow {}^3P_0$
	594.6	0.3	-	σ	$^3H_4 \rightarrow {}^1D_2$
	447.7	0.4	-	π	$^3H_4 \rightarrow {}^3P_2$
	467.6	0.5	-	π	$^3H_4 \rightarrow {}^3P_1$
Pr:LaF_3	442.0	1.6	5.0	σ	$^3H_4 \rightarrow {}^3P_2$
	466.3	0.8	6.4	σ	$^3H_4 \rightarrow {}^3P_1$
	485.0	0.2	-	σ	$^3H_4 \rightarrow {}^3P_0$
	594.0	0.3	-	σ	$^3H_4 \rightarrow {}^1D_2$
	440.5	1.2	(9.4)	π	$^3H_4 \rightarrow {}^3P_2$
	445.3	1.1		π	$^3H_4 \rightarrow {}^3P_2$
	464.7	1.3	4.0	π	$^3H_4 \rightarrow {}^3P_1$
	479.1	1.9	1.6	π	$^3H_4 \rightarrow {}^3P_0$
	591.8	0.3	-	π	$^3H_4 \rightarrow {}^1D_2$

system	λ_{gsa} (nm)	α (cm^{-1})	$\Delta\lambda$ (nm)	polarization	transition
Pr:$LaMgAl_{11}O_{19}$	443.8	1.6	5.4	σ	$^3H_4 \rightarrow {}^3P_2$
	460.0	1.3	5.3	σ	$^3H_4 \rightarrow {}^3P_1$
	480.1	1.6	1.2	σ	$^3H_4 \rightarrow {}^3P_0$
	487.6	1.2	1.9	σ	$^3H_4 \rightarrow {}^3P_0$
	594.4	0.4	-	σ	$^3H_4 \rightarrow {}^1D_2$
	470.8	0.5	-	π	$^3H_4 \rightarrow {}^3P_1$
	599.5	0.1	-	π	$^3H_4 \rightarrow {}^1D_2$

Table 6.2: Peak ground state absorption cross sections of Pr^{3+}-doped media with corresponding polarization and transition. Linewidths given in parantheses indicate a structure of the corresponding absorption peak and values are given for the whole band. Due to the potential presence of several optically active centers absorption cross sections of Pr:LMA can not be given and absorption coefficients for an 1.8 at% doped sample are listed instead.

during the selection process of the LDs. The peaks at 466.9 nm and 486.3 nm exhibit a $\Delta\lambda$ of 1.1 nm and 1.2 nm respectively. The narrow linewidth of these absorption bands is less problematic since they are usually adressed with specifically designed systems based on frequency doubled solid state or semiconductor lasers (cf. [Xu11, Ric07]) that exhibit linewidths of $\Delta\lambda \leq 0.5$ nm. However, because of the complexity and high cost of these systems, for the moment such pump schemes can only be regarded as proof of principle concepts.

Measurements of Pr,Mg:CAlO were carried out on a 5.2 mm long, *a*-cut 6.6 at% doped sample (cf. section 4.3.2). The recorded spectra show a striking similarity with those of Pr,Mg:SRA. The difference in the peak positions (444.6 nm, 467.0 nm, and 486.5 nm) and linewidths (8.6 nm, 1.8 nm, and 1.6 nm) is only marginal and the corresponding absorption cross sections are also comparable ($1.2 \cdot 10^{-20}$ cm^2, $2.2 \cdot 10^{-20}$ cm^2, and $1.8 \cdot 10^{-20}$ cm^2, respectively). Pr,Mg:CAlO therefore shares the beneficial linewidth of the absorption band corresponding to the $^3H_4 \rightarrow {}^3P_2$ transition.

The absorption characteristics of Pr:LMA were investigated on a 2.8 mm long, *a*-cut 1.8 at% doped sample of the lower part of the first boule grown with the *Crystalox* facility (cf. section 4.3.3). Due to the possible presence of several optically active centers indicated by the Mg^{2+}-deficiency, absorption cross sections for Pr:LMA can not be given. Like the other two hexaaluminates, Pr:LMA exhibits a more pronounced absorption for σ-polarized light. However, despite the close crystallographic similarity between the three systems, the absorption spectra strongly deviate from each other. The position of the peaks corresponding to the $^3H_4 \rightarrow {}^3P_J$, $^1I_6$ transitions can be found at wavelengths of 443.8 nm, 460.0 nm, and 480.1 nm. The linewidths are 5.4 nm, 5.3 nm, and 1.2 nm. Although the linewidth of the $^3H_4 \rightarrow {}^3P_2$-transition is smaller than that of the other two hexaaluminates, it is still larger than the corresponding $\Delta\lambda$ in Pr:YLF and can be regarded as an efficient pump channel. The deviation towards the other hexaaluminates might be attributed to the change of the crystal field caused by the replacement of an Al^{3+}-ion by a Mg^{2+}-ion.

Pr:LaF_3 absorption spectra were investigated with a 1.2 mm long, *a*-cut 0.4 at% doped sample (cf. section 4.3.5). The peak positions of the spectra are at wavelengths of 442.0 nm, 464.6 nm, and 479.0 nm with the first being more pronounced for σ-polarized light and the second and third for π-polarized light. The maximum absorption cross sections of the three bands are as high as $1.6 \cdot 10^{-20}$ cm^2, $1.3 \cdot 10^{-20}$ cm^2, and $1.9 \cdot 10^{-20}$ cm^2 respectively. The $^3H_4 \rightarrow {}^3P_2$ transition which is interesting for InGaN LD pumping also exhibits a pronounced band for π-polarized light which is comprised of two peaks with maxima at wavelengths of 440.5 nm and 445.3 nm. They exhibit absorption cross sections of $1.2 \cdot 10^{-20}$ cm^2 and $1.1 \cdot 10^{-20}$ cm^2 and a combined linewidth of 9.4 nm. Like the hexaaluminates it is on one hand less sensitive to shifts of the central emission wavelengths of the LDs, and on the other it absorbs pump light less efficient than Pr:YLF. The linewidth of the peaks corresponding to the transitions $^3H_4 \rightarrow {}^3P_1$ and $^3H_4 \rightarrow {}^3P_0$ are 4.0 nm and 1.6 nm respectively.

6.2.2 Decay Dynamics

The decay dynamics of Pr^{3+},Mg^{2+}:$CaAl_{12}O_{19}$ and Pr^{3+}:$LaMgAl_{11}O_{19}$ were investigated with the setup described in section 6.1.2. Measurements were carried out with samples

exhibiting varying dopant concentrations to reveal the possible interionic processes. Furthermore, low doped samples were investigated at temperatures between 300 K and 10 K in order to obtain lifetimes unperturbed by concentration quenching and/or non-radiative processes. Excitation wavelengths corresponding to the $^3H_4 \rightarrow {}^3P_0$ transition were used for all measurements. Since fluorescence originating from the $^1D_2 \rightarrow {}^3H_4$ transition might distort a signal recorded in the orange to red spectral region, the $^3P_0 \rightarrow {}^3F_4$ transition was chosen for detection. Because of the intensity of the corresponding emission peak and the high sensitivity of the employed photomultiplier in this spectral region, this wavelength bears the further advantage of an excellent signal-to-noise ratio.

The decay dynamics of the ^3P_J manifold in Pr,Mg:$CaAl_{12}O_{19}$ were obtained with samples exhibiting a dopant concentration of 1 at% and 6.6 at%. The excitation and signal wavelength were chosen to be 486 nm and 725 nm respecively. Figure 6.7a depicts the room temperature decay curves for the two samples in a semi-logarithmic graph. It can be seen that the 1 at% doped sample exhibits a linear decay curve. Therefore the effective lifetime was determined by employing equation 6.4 which yielded a value of $\tau_{\text{eff}} = 38\,\mu\text{s}$. The 6.6 at% doped sample exhibits nonlinearity within the first 60 µs after which the decay becomes linear. The effective lifetime derived by integrating over the whole curve is $\tau_{\text{eff}} = 25\,\mu\text{s}$. However, a line fit to the linear part of the decay curve yields $\tau_{\text{eff}} = 32\,\mu\text{s}$. The non-linearity does not follow the model proposed by Inokuti and Hirayama [Ino65]. It is more likely that due to the high doping level quenching takes place [Auz04]. In addition to the decreased lifetime, the curve exhibits a very fast decay within approximately the first 200 ns after the excitation pulse (cf. inset figure 6.7a). This effect was also reported by Fechner for 4.5 at% doped Pr,Mg:SRA [Fec12] and can be attributed to a fast donor-acceptor energy transfer between dopant-ions which are homogeneously distributed around the excited Pr^{3+}-ion [Vor82]. Figure 6.7b compares the decay curves recorded with the sample at various temperatures between 100 K and 300 K. At lower temperatures no decay curves could be recorded. This was due to the fact that the excitation wavelength of 486 nm is at the very edge of the emission spectrum of the employed OPO and the pulse energy is therefore quite low ($E_{\text{pulse}} < 0.5\,\mu\text{J}$). In combination with the fact that the linewidth of the absorption band decreases towards lower temperatures, this caused a decrease of the absorbed excitation energy. The obtained curves exhibit a strictly linear behaviour. This is also shown by the small deviation of less than 4 % between the lifetimes obtained by integrating and by fitting. Furthermore, it can be seen that the decrease of the effective lifetime is negligible. Assuming that no further processes are involved, the depopulation of the ^3P_J,$^1I_6$ manifold caused by non-radiative multiphonon transitions is less than 5 % and therefore marginal (cf. equation 2.18). The radiative lifetime of the $^3P_0$ level in Pr,Mg:$CaAl_{12}O_{19}$ was determined to be $\tau_{\text{rad}} = 40\,\mu\text{s}$.

For the measurement of the decay dynamics in Pr:$LaMgAl_{11}O_{19}$ samples prepared from the crystals grown with the *Hereaus* machine were used. The samples exhibited dopant concentrations of 0.7 at%, 1.6 at%, 2.7 at%, and 4.9 at%. During prelimenary measurements it became apparent that depending on the emission wavelength different lifetimes could be obtained. Therefore, the decay dynamics of Pr:LMA were characterized at two different emission wavelengths, $\lambda_1 = 729\,\text{nm}$ and $\lambda_2 = 742\,\text{nm}$. For the shorter wavelength the excitation wavelength yielding the highest fluorescence intensity was 486 nm while it was 489 nm for the longer wavelength. The decay curves recorded at room temperature

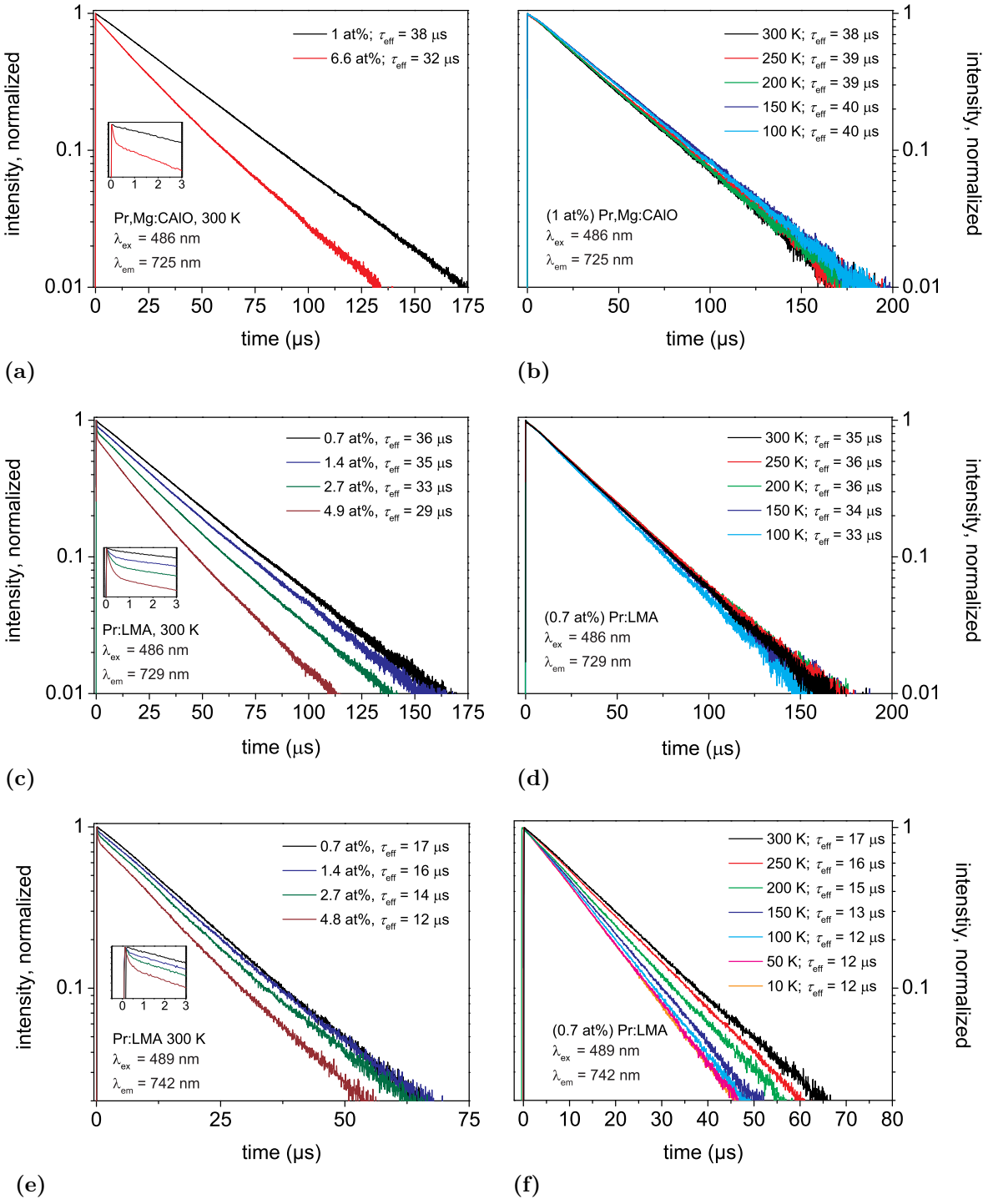

Figure 6.7: Decay dynamics of the $^3P_0$ manifold in Pr,Mg:CAlO and Pr:LMA. (a) and (c) show decay curves at room temperature for varying dopant concentration while in (b) and (d) low doped samples were investigated at temperatures between 50 K and 300 K.

are depicted in figure 6.7c and 6.7e respectively. With the exception of the decay curve recorded for λ_2 with the 0.7 at% doped sample, all curves exhibit a non exponential beginning and become exponential after 65 µs (λ_1) and 30 µs (λ_2) respectively. Therefore the effective lifetime was derived using equation 6.4. For both emission wavelengths τ_{eff} decreases with rising doping concentration. The effective lifetime drops from 36 µs to 29 µs for λ_1 and from 17 µs to 12 µs for λ_2. Furthermore, above a dopant concentration of 1.4 at% a fast decay evolves within the first 300 - 400 ns which can be attributed to the same effect as in the case for Pr,Mg:CAlO (cf. inset in figure 6.7c and 6.7e.). Again, the Inokuti-Hirayama model does not fit to the decay dynamics. It is likely that the non-linear behaviour as well as the decreasing lifetimes can therefore be attributed to concentration quenching. Figure 6.7d and 6.7f depict the temperature dependent decay curves obtained for λ_1 and λ_2 which were recorded with the 0.7 at% doped sample. All curves are linear and show a decrease of the lifetime towards lower temperatures. This initially counterintuitive result could be explained by several effects. The lower Stark levels of the $^3P_0$-multiplet might exhibit higher transition probabilities than levels of higher energy. Towards lower temperatures the population accumulates in the lower Stark levels and the lifetime therefore decreases. Another possibility is a stronger cross relaxation due to a better spectral overlap of the transitions $^3P_{0,S0} \rightarrow {}^1D_2$ and $^3P_{0,S0} \rightarrow {}^1G_4$ with the corresponding absorption processes $^3H_4 \rightarrow {}^3H_6$ and $^3P_{0,S0} \rightarrow {}^1G_4$, respectively. Here the index S0 denotes that the transition originates from the lowest Stark level. From figure 6.7d and 6.7f it can be seen that the shortening of the τ_{eff} is more pronounced for λ_2 than for λ_1. Due to this effect, it is not possible to determine the radiative lifetime of Pr:LMA. It is furthermore not possible to derive the multiphonon decay rate of the $^3P_0 \rightarrow {}^1D_2$-transition. In general, the fact that two distinct lifetimes are present for wavelengths which can be attributed to the same transition is most likely due to the presence of two different active centers. For $LaMgAl_{11}O_{19}$ this is further indicated by the reported displacement of La^{3+}-ions in the vicinity of a Mg^{2+} deficiency thus creating a second site with a different symmetry [Par97]. However, the close to exponential decay curves indicate that no significant cross-talk between the two centers occurs. Still, the number of Pr^{3+}-ions on the secondary site and their influence on the spectral characteristics can not be derived from these measurements.

6.2.3 Site Selective Excitation and Emission Spectra

In order to obtain further information on the characteristics of the two active centers, excitation and emission measurements were carried out with the *Fluorolog*. For the excitation measurements, the fluorescence intensity at λ_1 and λ_2 were recorded with the 0.7 at% doped sample for excitation wavelengths between 400 nm and 500 nm. The resolution was set to 0.6 nm with a step width of 0.2 nm. The emission characteristics were obtained by exciting the sample at 486 nm and 489 nm, the two wavelengths employed for the fluorescence decay dynamics. The resolution and stepping was the same as for the excitation measurements. Since the *Fluorolog* does not allow polarization dependent measurements, the sample was not moved during the different measurements. This ensured that a change in the spectrum was not the result of a different ratio of σ- and π-polarization caused by a changed orientation of the sample.

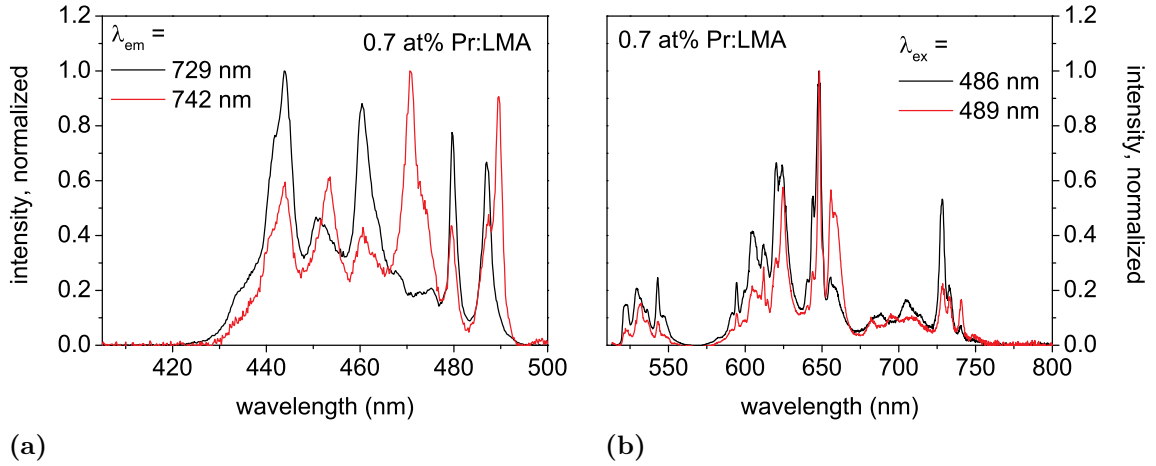

Figure 6.8: Excitation and emission spectra of 0.7 at% doped Pr:LMA. Excitation spectra were recorded for $\lambda_{em} = 729\,nm$ and 742 nm (a), emission spectra for $\lambda_{ex} = 486\,nm$ and 489 nm (b).

The recorded excitation spectra were normalized with the maximum intensity and are depicted in figure 6.8a. It can be seen that the two emission wavelengths exhibit varying excitation spectra. At 470.6 nm and 489.6 nm pronounced excitation peaks are present in the spectrum recorded for λ_2 but not in the spectrum for λ_1. This further indicates the presence of a second active center. Besides the differences there are also similarities. Both spectra show excitation peaks at 443 nm, 460 nm, 480 nm, and 487 nm, albeit with varying intensities of the peaks between the two spectra. This can be explained by a spectral overlap of the emission bands of the two centers which, due to the comparably broad linewidths of the bands, is not surprising. In general, the excitation spectrum recorded for λ_1 exhibits a good overlap with the GSA spectrum recorded for Pr:LMA depicted in figure 6.6. Still, the GSA spectra show peaks in the 470 nm region and at 489 nm which can be attributed to absorption of the center corresponding to λ_2. Since the ratio of Pr^{3+}-ions on the two centers is not known, this means that GSA cross sections can not be given.

The emission characteristics obtained with $\lambda_{ex} = 486\,nm$ and 489 nm are depicted in figure 6.8b. Both spectra exhibit similar peak positions. Examining the ratio of the peak fluorescence intensities reveals strong differences between the two spectra. Relatively speaking, the emission spectrum recorded with $\lambda_{ex} = 486\,nm$ exhibits stronger emission bands in the orange spectral region as well as in the deep red at 728 nm. In turn, the emission spectrum obtained with $\lambda_{ex} = 489\,nm$ shows more intense emission in the red spectral range around 658 nm and in the deep red at 741 nm. However, due to the overlap of the excitation bands of the two centers, it is not possible to selectively excite only a single site. Therefore, to a certain degree each spectrum contains fluorescence originating from both centers. It is furthermore unclear how the exact ratio between $2d$ and $6h$ sites is, and also if the probability of incorporating a Pr^{3+}-ion is the same for both sites. Quantitative statements can therefore not be made.

6.2.4 Emission Spectra

The polarization dependent fluorescence spectra of all Pr^{3+}-doped systems were recorded in the spectral range between 465 nm and 750 nm with the setup described in section 6.1.4. The resolution of the measurements for Pr,Mg:SRA, Pr,Mg:CAlO, and Pr:LaF_3 was chosen to be 0.15 nm. For Pr:LMA it was chosen to be 0.4 nm which was due to the generally broader linewidth of the peaks. For Pr,Mg:SRA measurements were conducted with a sample of the 0.9 at% doped boule (cf. section 4.3.1). The samples for Pr,Mg:CAlO, Pr:LMA, and Pr:LaF_3 were the same as for the absorption measurements. The Füchtbauer-Ladenburg method (cf. section 6.1.4) was employed to derive the emission cross sections of all systems. The radiative lifetimes of Pr,Mg:SRA ($\tau_{\mathrm{rad}} = 40$µs) and Pr:LaF_3 ($\tau_{\mathrm{rad}} = 51$µs) were taken from [Fec12] and [Heg82] respectively. For Pr,Mg:$CaAl_{12}O_{19}$ the value determined in section 6.2.2 ($\tau_{\mathrm{rad}} = 40$ µs) was used. For Pr:LMA the situation is complicated by the fact that the spectra consist of fluorescence originating from two active centers, and the contribution of each center is uncertain. However, the obtained spectra lack the distinct peak at 740.8 nm that is only present in one of the two emission spectra depicted in figure 6.8. It was therefore assumed that the main contribution to these spectra originate from the center with an effective lifetime of $\tau_{\mathrm{eff}} = 36$ µs. The average refractive indices of SRA and LMA at 589 nm were taken to be n = 1.76 and 1.79 [Ack11, Ack12]. No value has been reported for CAlO but because of the close similarity to SRA it was assumed to be 1.76, too. For LaF_3 a refractive index of 1.60 has been reported [Bas01]. Since in the wavelength range of interest the refractive index of comparable crystals usually only changes in the order of 10^{-2}, the dependency on λ was neglected. The resulting spectra are depicted in figure 6.9. The position of the maxima together with the corresponding cross section, polarization, and transition are listed in table 6.3. Where possible the linewidth of the emission band is given.

As it was the case for the absorption cross sections, the emission spectra derived for the three hexaaluminates show more pronounced peaks for σ-polarization which can again be attributed to the symmetry of the coordination sphere. A *c*-cut crystal therefore not only allows the exploitation of the stronger absorption cross sections for σ-polarized light but also the more favorable emission characteristics for this polarization axis.

The spectra obtained for Pr,Mg:SRA show maximum emission cross sections at wavelengths of 486.3 nm, 622.8 nm, 643.5 nm, and 724.4 nm with values of $9.7 \cdot 10^{-20}\,\mathrm{cm}^2$, $3.8 \cdot 10^{-20}\,\mathrm{cm}^2$, $9.7 \cdot 10^{-20}\,\mathrm{cm}^2$, and $10.0 \cdot 10^{-20}\,\mathrm{cm}^2$ respectively. Small emission peaks are also present in the green spectral range for both polarization axes. Maxima occur at wavelengths of 525.3 nm (σ) and 541.3 nm (π) and exhibit values of $6.2 \cdot 10^{-21}\,\mathrm{cm}^2$ and $6.7 \cdot 10^{-21}\,\mathrm{cm}^2$. An interesting feature of the spectrum recorded for σ-polarized light is a peak at 670.6 nm with an emission cross section of $6.0 \cdot 10^{-21}\,\mathrm{cm}^2$. A laser operating on this peak is interesting for magnetooptical traps for ^{7}Li [Pra98, Eis13]. While the emission cross sections in the blue, red, and deep red spectral range are quite comparable with those of Pr:YLF, they are smaller by a factor of 4 in the green spectral region. The pump power necessary to achieve laser oscillation will therefore increase accordingly (cf. section 2.3.1).

The shape of the emission spectra derived for Pr,Mg:CAlO is very similar to that of the Pr,Mg:SRA spectra. Highest emission cross sections are again present in σ-polarization.

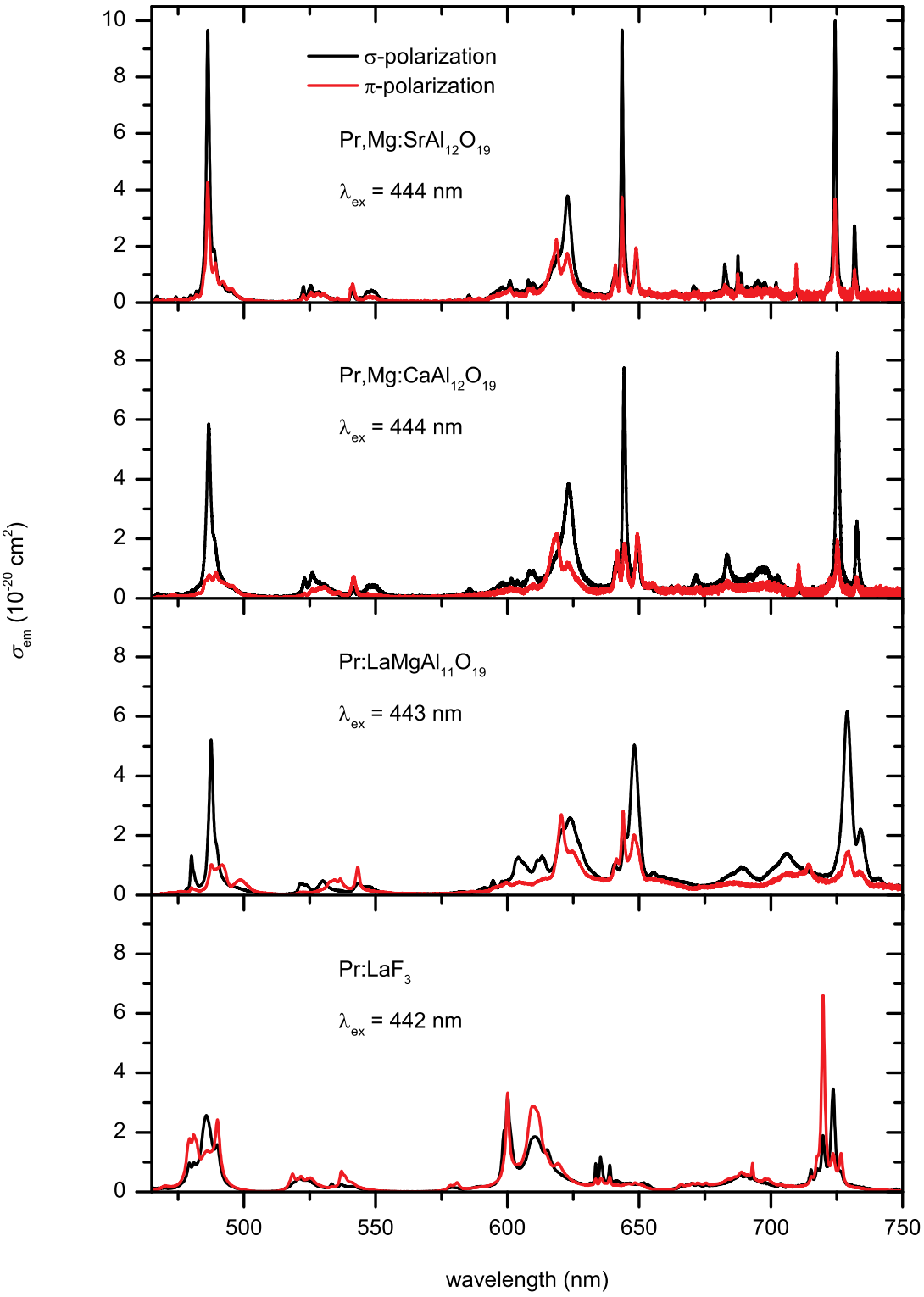

Figure 6.9: Polarization dependent emission spectra derived for the investigated Pr^{3+}-doped systems.

The peak positions are furthermore red shifted with maxima at wavelengths of 486.7 nm, 623.3 nm, 644.3 nm, and 725.2 nm. The corresponding emission cross sections are $5.85 \cdot 10^{-20}\,cm^2$, $3.7 \cdot 10^{-20}\,cm^2$, $7.7 \cdot 10^{-20}\,cm^2$, and $8.3 \cdot 10^{-20}\,cm^2$ respectively, and are therefore slightly lower than in the case of Pr,Mg:SRA. The maximum emission cross section in the green spectral range can be found at 526.1 nm and (σ) and 541.6 nm (π) with values of $9.0 \cdot 10^{-21}\,cm^2$ and $7.4 \cdot 10^{-21}\,cm^2$ higher. A peak can also be found at 671.6 nm with a cross section of $7.4 \cdot 10^{-21}\,cm^2$.

In contrast to the ground state absorption spectra of Pr:LMA the shape of the emission spectra bears a close resemblance to the spectra of the other two hexaaluminates. The σ-polarization again exhibits the strongest emission peaks in the blue (487.5 nm), red (648.1 nm) and deep red (729.1 nm) spectral regions with values of $5.2 \cdot 10^{-20}\,cm^2$, $5.0 \cdot 10^{-20}\,cm^2$, and $6.2 \cdot 10^{-20}\,cm^2$. In the orange spectral range pronounced peaks are present for both polarization axes (σ: 624.0 nm, $2.6 \cdot 10^{-20}\,cm^2$; π: 620.5 nm, $2.7 \cdot 10^{-20}\,cm^2$). In the green spectral region the maximum emission cross section is present in π-polarization at 543.2 nm and exhibits a value of $9.4 \cdot 10^{-21}\,cm^2$. A difference towards Pr,Mg:SRA and Pr,Mg:CAlO which becomes apparent in the spectra is the broader linewidth of most emission peaks of Pr:LMA. This might be caused by a superposition of emission lines originating from the two active centers or by the replacement of an Al^{3+}-ion by an Mg^{2+}-ion in the unit cell and a subsequent inhomogeneous broadening of the lines.

The spectra recorded for Pr:LaF_3 show emission peaks for both polarization axes. For the σ-polarization maxima can be found at 485.7 nm, 600.1 nm, and 723.7 nm which exhibit cross sections of $2.57 \cdot 10^{-20}\,cm^2$, $3.29 \cdot 10^{-20}\,cm^2$, and $3.46 \cdot 10^{-20}\,cm^2$, respectively. Small peaks are also present in the green (521.4 nm) and red (635.4 nm) spectral range with maxima of $4.4 \cdot 10^{-21}\,cm^2$ and $1.17 \cdot 10^{-20}\,cm^2$, respectively. The maxima in π-polarization are at 490.5 nm, 600.1 nm, 610 nm, and 719.8 nm with values of $2.43 \cdot 10^{-20}\,cm^2$, $3.33 \cdot 10^{-20}\,cm^2$, $2.89 \cdot 10^{-20}\,cm^2$, and $6.62 \cdot 10^{-20}\,cm^2$, respectively. In the green spectral region a peak with a cross section of $7.1 \cdot 10^{-21}\,cm^2$ can be found at 537.1 nm. An interesting feature of the spectrum are the emission peaks in the orange spectral range. The band centered at 610 nm has a linewidth of more than 7 nm. A laser operating on the $^3P_0 \rightarrow {}^3H_6$ transition might therefore be tunable in a comparatively broad wavelength range. The other peak, centered at 600.1 nm, exhibits a rather short central wavelength compared to other Pr^{3+}-doped systems (cf. [Ric08]). Xu *et al.* have reported similar characteristics in Pr^{3+}:KYF_4 [Xu13] and propose that the two emission bands might stem from Pr^{3+}-ions on different sites resulting from the disordered structure of KYF_4 [Syt91, LeF92]. LaF_3, however, only exibits a single site which can be occupied by the active ion. The low doping concentration of the sample also makes a clustering of Pr^{3+}-ions unlikely. Another possibility is that the lower energy emission band results from a cooperative photon-phonon process [DeL94]. Hansen has shown, for example, that for Pr^{3+}:$LiYF_4$ the emission in the orange spectral region can partially be ascribed to such processes [Cas75, Han12]. To resolve this issue emission measurements were carried out with the sample cooled to 10 K. The recorded spectra are depicted in Figure 6.10. The emission bands are plotted according to their energetic distance towards the zero phonon line of the transition $^3P_0 \rightarrow {}^3H_6$. Peaks which correspond to an electronic transition between two Stark levels are indicated with arrows (cf. [Cas65]).

system	λ_{em} (nm)	$\sigma_{em}(\lambda)$ (10^{-20} cm^2)	polarization	transition
$Pr,Mg:SrAl_{12}O_{19}$	486.3	9.7	σ	$^3P_0 \rightarrow {}^3H_4$
	525.3	0.6	σ	$^3P_1 \rightarrow {}^3H_5$
	622.8	3.8	σ	$^3P_0 \rightarrow {}^3H_6$
	643.5	9.7	σ	$^3P_0 \rightarrow {}^3F_2$
	670.6	0.6	σ	$^3P_0 \rightarrow {}^3F_3$
	724.4	10.0	σ	$^3P_0 \rightarrow {}^3F_4$
	486.2	4.3	π	$^3P_0 \rightarrow {}^3H_4$
	541.3	0.7	π	$^3P_0 \rightarrow {}^3H_5$
$Pr,Mg:CaAl_{12}O_{19}$	486.7	5.8	σ	$^3P_0 \rightarrow {}^3H_4$
	526.1	0.9	σ	$^3P_1 \rightarrow {}^3H_5$
	623.3	3.9	σ	$^3P_0 \rightarrow {}^3H_6$
	644.3	7.7	σ	$^3P_0 \rightarrow {}^3F_2$
	671.6	0.7	σ	$^3P_0 \rightarrow {}^3F_3$
	725.2	8.3	σ	$^3P_0 \rightarrow {}^3F_4$
	541.6	0.7	π	$^3P_0 \rightarrow {}^3H_5$
$Pr:LaMgAl_{11}O_{19}$	487.5	5.2	σ	$^3P_0 \rightarrow {}^3H_4$
	529.8	0.5	σ	$^3P_1 \rightarrow {}^3H_5$
	624.0	2.6	σ	$^3P_0 \rightarrow {}^3H_6$
	648.1	5.0	σ	$^3P_0 \rightarrow {}^3F_2$
	729.1	6.2	σ	$^3P_0 \rightarrow {}^3F_4$
	543.2	0.9	π	$^3P_0 \rightarrow {}^3H_5$
	620.5	2.7	π	$^3P_0 \rightarrow {}^3H_6$
$Pr:LaF_3$	485.7	2.6	σ	$^3P_0 \rightarrow {}^3H_4$
	521.4	0.4	σ	$^3P_1 \rightarrow {}^3H_5$
	600.1	3.3	σ	$^3P_0 \rightarrow {}^3H_6$
	635.4	1.2	σ	$^3P_0 \rightarrow {}^3F_2$
	723.7	3.5	σ	$^3P_0 \rightarrow {}^3F_4$
	490.5	2.4	π	$^3P_0 \rightarrow {}^3H_4$
	537.1	0.7	π	$^3P_0 \rightarrow {}^3H_5$
	600.1	3.3	π	$^3P_0 \rightarrow {}^3H_6$
	610.0	2.9	π	$^3P_0 \rightarrow {}^3H_6$
	693.1	1.0	π	$^3P_0 \rightarrow {}^3F_3$
	719.8	6.6	π	$^3P_0 \rightarrow {}^3F_4$

Table 6.3: Peak emission cross sections of Pr^{3+}-doped media with corresponding polarization and transition.

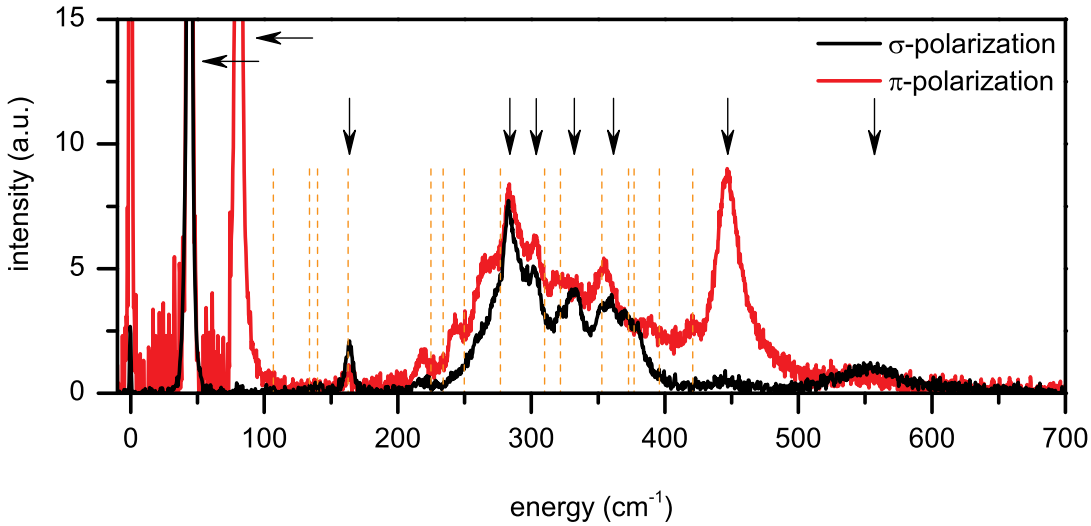

Figure 6.10: Polarization dependent emission spectra of the transition $^3P_0 \rightarrow {}^3H_6$ at 10 K in Pr:LaF_3. The spectra are plotted against the energy in cm^{-1} and normalized with the energy of the zero-phonon transition between the lowest Stark levels of the manifold $^3P_0$ and $^3H_6$. Arrows indicate electronic transitions based on the energy level positions reported in [Cas65]. Vertical orange lines correspond to phonon energies reported by [Yen64] assuming a coupling to the second lowest electronic transition at 44 cm^{-1}.

Assuming a phonon assisted transition terminating in the third lowest Stark level of the $^3H_6$ multiplet, a theoretical spectrum based on the phonon energies reported by Yen *et al.* was derived [Yen64]. It is indicated in figure 6.10 by orange lines.

It can be seen that the recorded spectra exhibit a reasonable overlap with the spectrum derived from coupling between the third lowest $^3H_6$ Stark level and the phonon spectrum. At room temperature, the pronounced orange emission band at 610 nm can therefore be attributed to a strong coupling of the phonon spectrum to the $^3P_0 \rightarrow {}^3H_6$ transition. No indication can be found of the presence of a second optically active center.

6.2.5 Excited State Absorption Spectra

Polarization dependent ESA measurements for the upper laser manifold ^3P_J,$^1I_6$ were carried out with all four materials with the setup introduced in section 6.1.7. As pump sources, InGaN LDs with central emission wavelengths corresponding to the respective absorption band of the $^3H_4 \rightarrow {}^3P_2$ transition were employed. The probe light was generated by a 450 W high pressure xenon discharge lamp. Since the difference in signal intensity between pumped and unpumped state is minute, the resolution was set to 0.8 nm in order to obtain an acceptable s/n ratio. This resolution has the disadvantage that narrow linewidth emission peaks are not fully resolved resulting in lower peak cross sections. Spectra were recorded in the wavelength range between 320 nm and 750 nm. This allowed the onset of ESA transitions terminating in the $4f^15d^1$ manifolds to be revealed. The spectral region around the excitation wavelength was omitted because pump light which was scattered and reflected on the input coupling facet of the samples oversaturated the detector. Measurements in the spectral region where only GSA is present were therefore

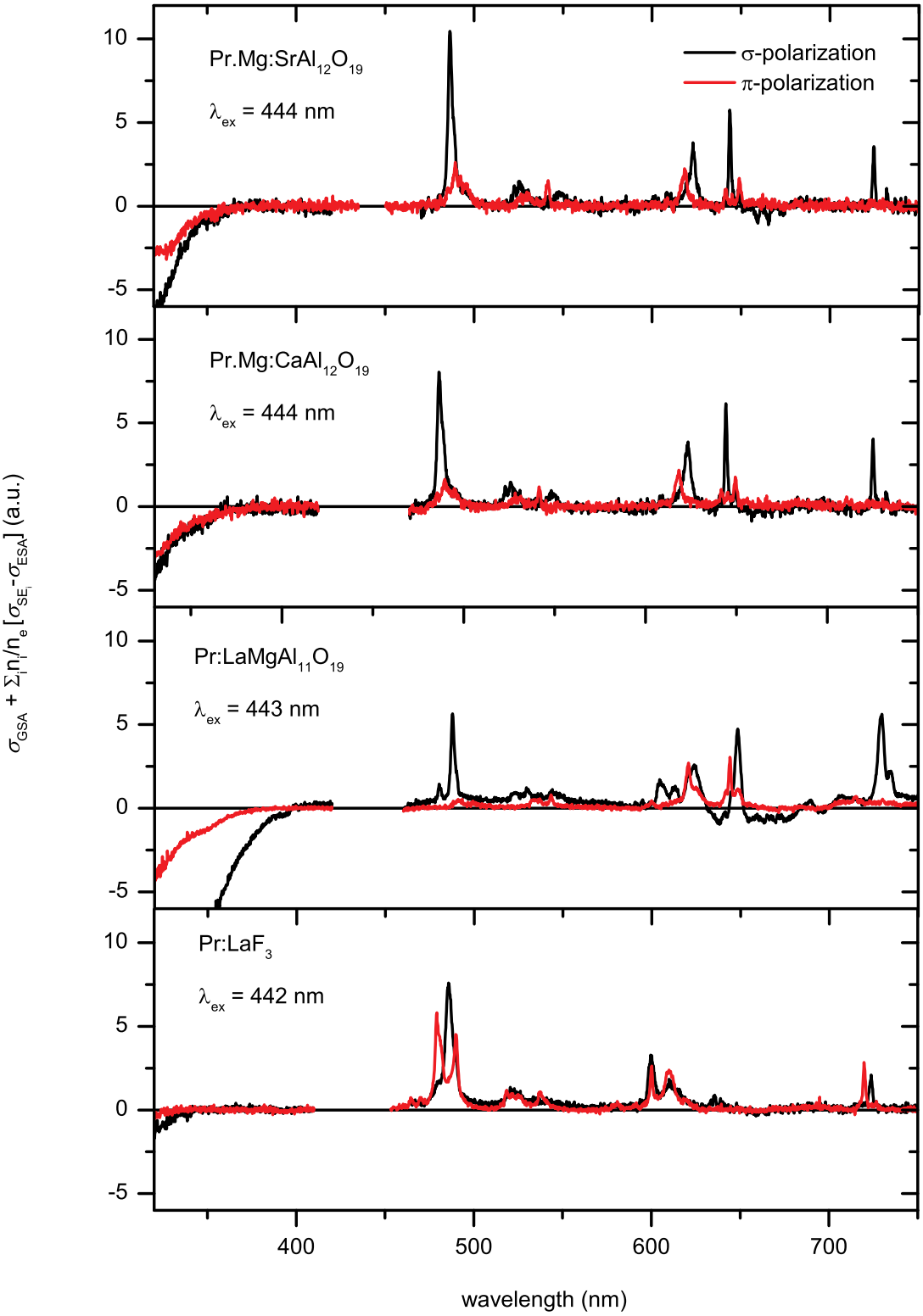

Figure 6.11: Polarization dependent excited state absorption spectra of Pr^{3+}-doped host systems.

not possible and the recorded ESA spectra could not be calibrated with the priorly obtained GSA spectra. A qualitative statement on the presence of ESA on the pump or prospective laser transitions can be made nonetheless. All obtained spectra are depicted in figure 6.11.

Spectra for Pr,Mg:$SrAl_{12}O_{19}$ were obtained with a 3.1 mm thick *a*-cut sample prepared from the crystal provided by the IKZ Berlin. ESA transitions terminating in the $4f^15d^1$ manifolds can be seen in the spectral region below approximately 360 nm. Above this wavelength no broad ESA bands corresponding to an interconfigurational transition can be made out. Although the area around the pump wavelength was omitted from the spectrum it seems likely that no ESA is present in this region. This can be deduced from the fact that the linewidth of the interconfigurational ESA transitions is usually broader than the omitted region (cf. [Che94] and [Thi08]). Therefore, if such broad ESA transitions would be present in this wavelength region, they would still be recognizable. It follows that for Pr,Mg:$SrAl_{12}O_{19}$ neither the pump transitions nor any of the prospective laser transitions are affected by ESA. Laser operation should thus be possible on all transitions offered by the Pr^{3+} energy level scheme.

The results obtained with Pr,Mg:$CaAl_{12}O_{19}$ are quite comparable. The spectra, which were recorded with the sample used for the GSA measurements, show very similar characteristics compared to Pr,Mg:SRA. The onset of the ESA is also in the region around 360 nm with no further ESA bands in the longer wavelength range up to 750 nm. The conclusion is therefore the same as for Pr,Mg:SRA: laser operation should be possible on all prospective laser transitions.

For Pr:LMA it can be seen that in contrast to the other two hexaalumnates, the spectra, which were obtained with an *a*-cut 1.8 at% doped sample grown with the *Crystalox* facility, show an onset of ESA bands as early as 400 nm. The onset at a longer wavelength however is consistent with what would be expected from the data reported for the crystal field splitting and centroid line shift (cf. [Dor02]). Despite the red shifted ESA bands neither the pump nor the prospective laser transitions are affected. The slight positive and negative offset in the areas 470 nm - 600 nm and 620 nm - 685 nm can be attributed to either a drift of the frequency of the slow chopper and/or to an imperfect phase setting on either of the two lock-in amplifiers. At this point it should be noted that compared to the standard Pr^{3+} host $LiYF_4$, the onset of the ESA bands is blue shifted for all three hexaaluminates [Han12].

The spectra of Pr^{3+}:LaF_3 were recorded with a sample prepared from the 0.7 at% doped boule. Compared to Pr^{3+}:$LiYF_4$ the ESA bands exibit an even further blue shift of the onset than the hexaalumnates. Excited state absorption can be seen to set in below a wavelength of approximately 340 nm. This is also indicated by the comparatively small centroid line shift and weak crystal field splitting reported for Ce^{3+}:LaF_3 by Dorenbos *et al.* [Dor00a]. In terms of interconfigurational ESA transitions LaF_3 therefore seems to be an excellent host material for Pr^{3+} with no ESA in the visible spectral region.

6.3 Results: Holmium Doped Materials

The Ho^{3+}-doped systems were analyzed for their ground state absorption characteristics which subsequently allowed their respective emission cross sections to be derived via the reciprocity method. If necessary, transmission measurements at 10 K were carried out to reveal the positions of Stark levels composing the involved manifolds which have so far not been reported. The obtained absorption and emission cross sections were used to calculate the gain spectra. Additionally, measurements were carried out concerning the presence of ESA on prospective pump and laser wavelengths. Furthermore, the decay dynamics of the manifolds $^5S_2$ and $^5F_3$ were investigated in order to derive the multiphonon decay rates.

6.3.1 Ground State Absorption

The polarization dependent ground state absorption spectra of Ho^{3+}:LaF_3 and Ho^{3+}:$LiLuF_4$ were measured in two wavelength regions. The spectral range between 430 nm and 495 nm is interesting for pumping with InGaN LDs or 2ωOPSLs, while the absorption characteristics in the green spectral region between 515 nm and 555 nm are necessary to determine the emission cross sections and the reabsorption occuring on the respective laser wavelengths.

Measurements were carried out with *a*-cut samples with thicknesses of 3.1 mm (Ho^{3+}:$LiLuF_4$) and 3.0 mm (Ho^{3+}:LaF_3). The dopant concentrations were 0.6 at% and 0.4 at% respectively. The resolution was chosen in accordance to the minimum linewidths of the spectra and was set to 0.3 nm for both systems. The recorded spectra are depicted in figure 6.12 with a summary of the most prominent peaks in table 6.4.

Maxima in the ground state absorption spectra of Ho^{3+}:$LiLuF_4$ can be found at wavelengths of 452.9 nm (π), 486.0 nm (π), and 535.2 nm (π) with absorption cross sections of $3.8 \cdot 10^{-20}\,cm^2$, $2.0 \cdot 10^{-20}\,cm^2$, and $8.3 \cdot 10^{-20}\,cm^2$ respectively. The shape of the obtained spectra and the values of the absorption cross sections in the green spectral region are in good agreement with the corresponding spectra reported by Walsh *et al.* for the isomorphic system Ho^{3+}:$LiYF_4$ [Wal98]. Unfortunately the absorption band which could be adressed with InGaN LDs consists of several narrow linewidth peaks ($\Delta\lambda \approx 0.6$ nm) which leads to a mediocre overlap between pump and absorption spectrum.

The maxima of the absorption bands of Ho^{3+}:LaF_3 can be found at wavelengths of 447.3 nm (σ), 482.7 nm (π), and 533.8 nm (π). The corresponding peak absorption cross sections are $1.4 \cdot 10^{-20}\,cm^2$, $0.3 \cdot 10^{-20}\,cm^2$, and $0.8 \cdot 10^{-20}\,cm^2$ and are therefore smaller than in Ho^{3+}:$LiLuF_4$. An interesting feature is that the absorption band in the green spectral region exhibits a cross section of $3.3 \cdot 10^{-21}\,cm^2$ at a wavelength of 532.0 nm. An inband pumping scheme employing frequency doubled Nd^{3+} lasers or, in the future, green emitting laser diodes as pump sources might therefore be feasable.

6.3.2 Determination of the Stark Level Positions

The transmission properties of a 2 mm thick, 0.3 at%-doped Ho^{3+}:LaF_3 sample at 10 K were investigated with the setup introduced in section 6.1.5. The spectral region between

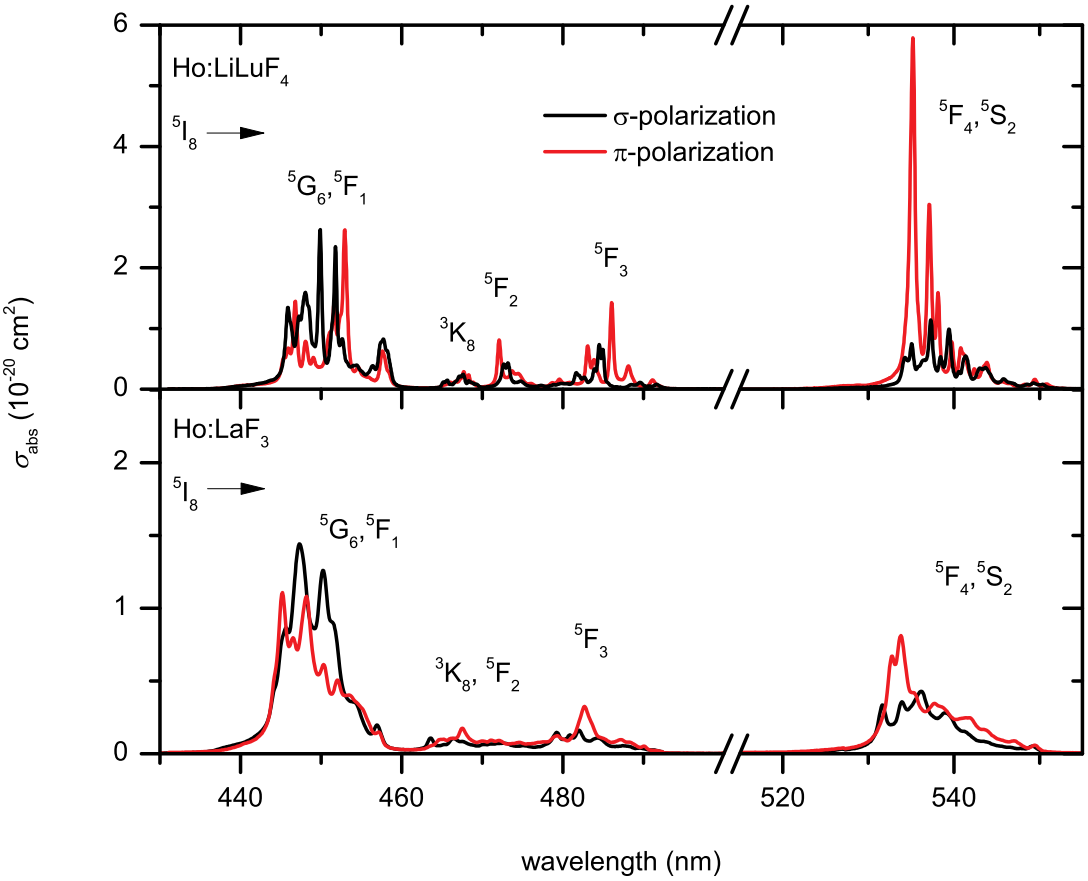

Figure 6.12: Polarization dependent ground state absorption spectra derived for the investigated Ho^{3+}-doped systems.

system	λ_{gsa} (nm)	σ_{abs} (10^{-20} cm^2)	$\Delta\lambda$ (nm)	polarization	transition
Ho^{3+}:$LiLuF_4$	449.9	3.6	0.6	σ	$^5I_8 \rightarrow {}^5F_1, {}^5G_6$
	484.5	1.1	1.0	σ	$^5I_8 \rightarrow {}^5F_3$
	537.3	1.6	0.9	σ	$^5I_8 \rightarrow {}^5F_4, {}^5S_2$
	452.9	3.8	0.9	π	$^5I_8 \rightarrow {}^5F_1, {}^5G_6$
	486.0	2.0	0.6	π	$^5I_8 \rightarrow {}^5F_3$
	535.2	8.3	0.7	π	$^5I_8 \rightarrow {}^5F_4, {}^5S_2$
Ho^{3+}:LaF_3	447.3	1.4	(7.2)	σ	$^5I_8 \rightarrow {}^5F_1, {}^5G_6$
	536.2	0.4	-	σ	$^5I_8 \rightarrow {}^5F_4, {}^5S_2$
	445.2	1.1	(6.4)	π	$^5I_8 \rightarrow {}^5F_1, {}^5G_6$
	482.7	0.3	2.2	π	$^5I_8 \rightarrow {}^5F_3$
	533.8	0.8	(3.3)	π	$^5I_8 \rightarrow {}^5F_4, {}^5S_2$

Table 6.4: Peak ground state absorption cross sections of the Ho^{3+}-doped systems with corresponding polarization and transition. Linewidths given in parantheses indicate a structure of the corresponding absorption peak and values are given for the whole band.

536 nm and 538 nm was investigated in order to determine the energetic positions of the five Stark levels composing the $^5S_2$ manifold. In order to fully resolve each peak the resolution was set to 40 pm.

Figure 6.13 depicts the obtained transmission spectrum. The spectrum shows five peaks which can be attributed to the $^5I_8 \rightarrow ^5S_2$ transition. Since at 10 K the absorption bands assume a Gaussian line shape, corresponding functions were fitted to each peak which yielded an excellent overlap. The obtained peak positions are listed in table 6.5. Secondary absorption lines comparable to those observed by Koopmann in low temperature absorption measurements of Ho^{3+}:Lu_2O_3 can not be seen [Koo12].

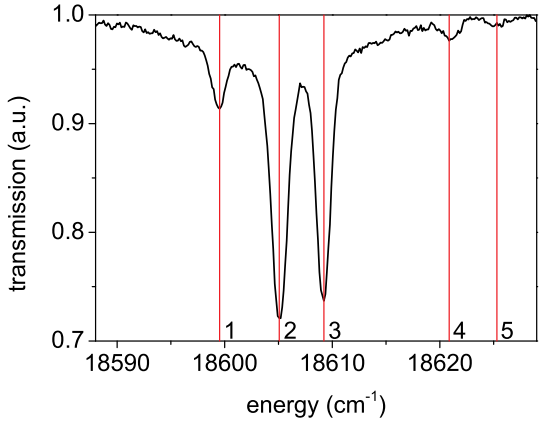

Figure 6.13: Transmission spectrum of Ho^{3+}:LaF_3 at 10 K. The red lines 1 - 5 mark the energetic positions of the five Stark levels composing the $^5S_2$ manifold.

	No.	energy (cm^{-1})	wavelength (nm)
	1	18600	537.65
	2	18605	537.49
$^5S_2$	3	18609	537.37
	4	18621	537.03
	5	18625	536.91

Table 6.5: Energetic positions of the five Stark levels composing the $^5S_2$ manifold in Ho^{3+}:LaF_3.

6.3.3 Emission Spectra

The obtained ground state absorption cross sections were used to derive the emission cross sections of the $^5F_4$,$^5S_2 \rightarrow ^5I_8$ transition via the reciprocity method. For Ho^{3+}:$LiLuF_4$ the necessary energetic positions of the involved manifolds were determined by Walsh *et al.* [Wal98] while in the case of Ho^{3+}:LaF_3 Caspers *et al.* reported the data for the multiplets $^5I_8$ and $^5F_4$ [Cas70]. The position of the five Stark levels composing the $^5S_2$ manifold were taken from section 6.3.2. For comparison, fluorescence measurements were carried out with the setup introduced in section 6.1.4 by employing the same samples which

were used to measure the GSA spectra. In order to reduce reabsorption effects, only small volumina were excited by the pump beam. The spectra were calibrated with those obtained by the reciprocity method. Since the short wavelength range of the fluorescence is prone for reabsorption, the peak at the long wavelength edge was used as point of reference.

The emission spectra of Ho^{3+}:$LiLuF_4$ derived via the reciprocity method are depicted in figure 6.14a. It can be seen that the emission band corresponding to the $^5S_2 \rightarrow {}^5I_8$ transition consists of several narrow linewidth peaks. The maximum emission cross section of $19.1 \cdot 10^{-21}\,cm^2$ can be found in the spectrum for π-polarized light at a wavelength of 535.3 nm. Since the peaks in the long wavelength part of the spectrum are less affected by reabsorption, the maxima at 549.5 nm and 550.9 nm with emission cross sections of $5.4 \cdot 10^{-21}\,cm^2$ and $3.6 \cdot 10^{-21}\,cm^2$ respectively are also points of interest. The rising noise level towards the longer wavelength part of the spectrum is a known artifact in spectra derived with the reciprocity method. It is caused by the last term in equation 6.14 which causes an amplification of the noise floor of the employed GSA spectra which increases

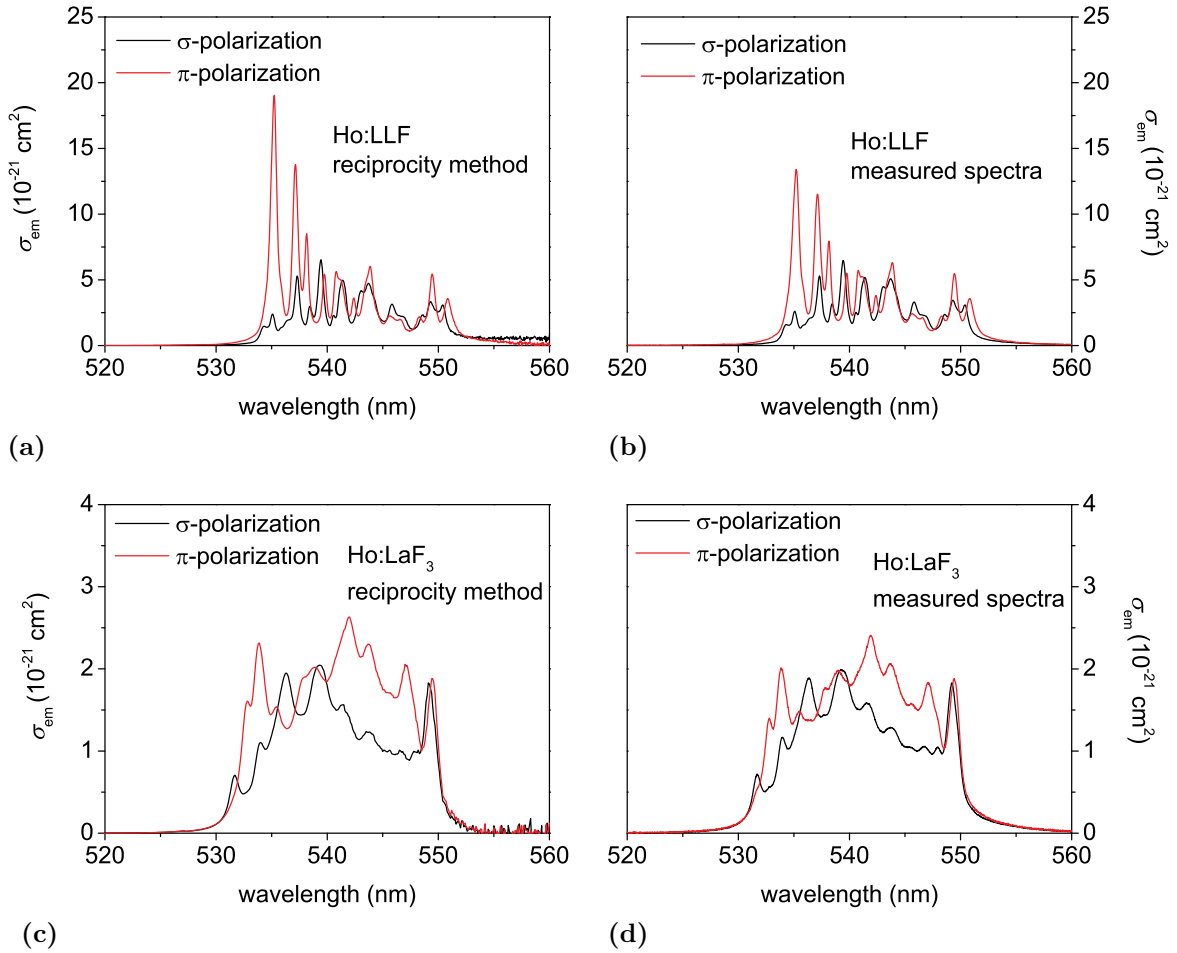

Figure 6.14: Polarization dependent emission spectra of the $^5F_4$,$^5S_2 \rightarrow {}^5I_8$ transition in Ho^{3+}:$LiLuF_4$ (a,b) and Ho^{3+}:LaF_3 (c,d). Graphs (a) and (c) were derived via the reciprocity method. Graphs (b) and (d) are measured fluorescence spectra which were calibrated at the long wavelength peaks with the emission cross sections obtained by the reciprocity method.

system	λ_{em} (nm)	$\sigma_{em}(\lambda)$ (10^{-21} cm^2)	$\Delta\lambda$ (nm)	polarization	transition
Ho^{3+}:$LiLuF_4$	532.3	19.1	0.6	π	$^5F_4$,$^5S_2$→$^5I_8$
	549.5	5.4	1.0	π	
	550.8	3.6	0.9	π	
Ho^{3+}:LaF_3	533.9	2.3	(8.6)	π	$^5F_4$,$^5S_2$→$^5I_8$
	542.0	2.6	1.6	π	
	549.4	1.9	-	π	

Table 6.6: Peak emission cross sections of Ho^{3+}-doped media with corresponding polarization and transition.

towards longer wavelengths. Figure 6.14b shows the measured and calibrated fluorescence spectra. Except for the peak at 535.3 nm the overlap with the spectra derived via the reciprocity method is very good (cf. appendix B). The smaller peak cross section of the short wavelength maximum can be attributed to reabsorption which occurs despite the low dopant concentration and the small volumina that was excited by the pump beam. Furthermore, the shape of the spectrum as well as the values of the peak emission cross sections are in good agreement with those reported by Walsh *et al.* for the isomorphic system Ho^{3+}:$LiYF_4$ [Wal98].

The emission spectra of Ho^{3+}:LaF_3 resulting from the reciprocity method are depicted in figure 6.14c. In contrast to Ho^{3+}:$LiLuF_4$ the emission peaks exhibit broader linewidths but also smaller emission cross sections. The maximum value of $2.6 \cdot 10^{-21}$ cm^2 can be found at a wavelength of 542.0 nm (π). At the long wavelength edge of the emission band a peak with an emission cross section of $1.9 \cdot 10^{-21}$ cm^2 can be found at 549.4 nm. The overlap between the spectra derived via the reciprocity method and those obtained by measurement (cf. figure 6.14d) is again very good (cf. appendix B).

6.3.4 Gain Spectra

Since a laser operating on the $^5S_2$→$^5I_8$ transition belongs to the three-level type it will be affected by reabsorption. Therefore the obtained GSA and emission spectra were employed to derive the gain spectra of Ho^{3+}:$LiLuF_4$ and Ho^{3+}:LaF_3 via equation 6.16. For these calculations the measured emission spectra were used due to their lower noise level in the long wavelength region. This is justified by the excellent overlap between measured and derived emission spectra especially in the long wavelength region where the reabsorption will be bleached first. Gain spectra were derived for various values of β in order to estimate at which point the reabsorption should be bleached and gain becomes the dominant effect.

The gain spectra resulting for σ- and π-polarization for Ho^{3+}:$LiLuF_4$ are depicted in figure 6.15a and figure 6.15b respectively. From the spectra it becomes apparent that for both polarization states an inversion level of roughly 20 % is necessary to bleach the reabsorption. Above this level in both spectra two gain peaks emerge at wavelengths of

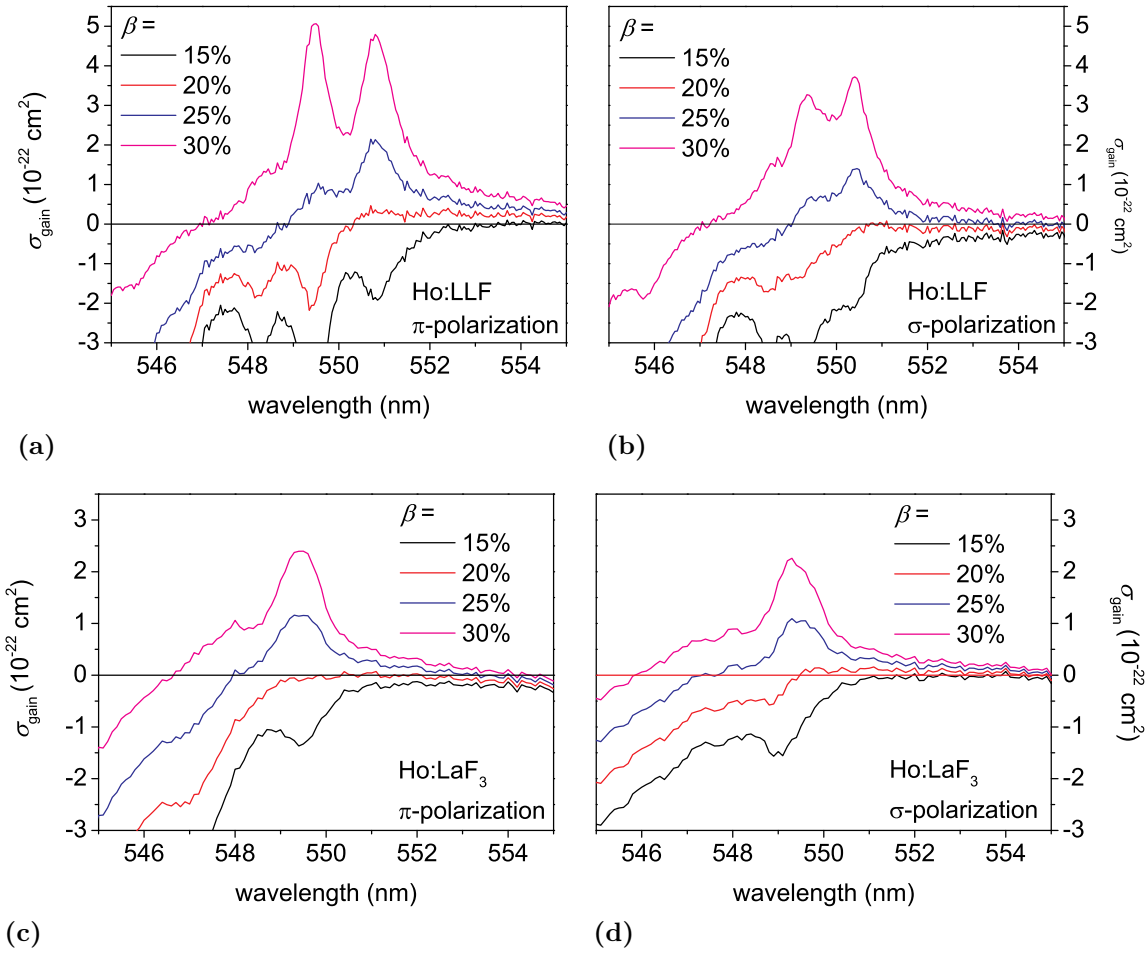

Figure 6.15: Polarization dependent gain spectra derived for Ho^{3+}:$LiLuF_4$ (a,b) and Ho^{3+}:LaF_3 (c,d). The graphs depict gain curves for various values of β.

approximately 549.5 nm and 550.5 nm. At inversion level between 20 % and 30 % the long wavelength peak exhibits higher cross sections. For π-polarized light and inversion levels above 30 % the peak at 549.5 nm becomes domninant.

For Ho^{3+}:LaF_3 the situation is quite comparable. The spectra depicted in figure 6.15c and figure 6.15d show that independent of the polarization the threshold inversion level necessary to achieve gain is also approximately 20 %. The emerging peak has a central wavelength of 549.3 nm.

The high inversion densities necessary to bleach the reabsorption in Ho^{3+}-doped fluoride materials can be attributed to a strong overlap of absorption and emission bands. This is due to the relatively weak Stark splitting, especially of the $^5I_8$ ground state which causes a non-negligible Boltzman population even for higher laying Stark levels. The high number of levels composing the ground state ($2l + 1 = 17$) therefore present numerous starting points for possible absorption transitions. However, host systems where the involved levels exhibit a stronger splitting, e.g. Ho^{3+}:$Y_3Al_5O_{12}$ [Gru91] or Ho^{3+}:Sc_2O_3 [Moh01] have higher phonon energies and therefore less favorable non-radiative decay rates of the $^5S_2$ manifold (cf. section 2.2.1).

Given the spectroscopic data obtained so far, it follows from equation 2.33 that due to the strong reabsorption, the pump power necessary to achieve laser operation will be quite high especially compared to the four-level-lasers realized with Pr^{3+} doped gain media.

6.3.5 Decay Dynamics

In order to gain more insight into the multiphonon decay of the $^5F_3$ and $^5F_4$,$^5S_2$ multiplets, the decay dynamics of these manifolds were investigated for Ho^{3+}:$LiLuF_4$ and Ho^{3+}:LaF_3 employing the setup described in section 6.1.2. Investigations of the $^5F_4$,$^5S_2$ multiplet were conducted by exciting the Ho^{3+}-ion in the respective host lattice directly into this manifold. For the $^5F_3$ multiplet this was not possible since the OPO could not deliver light with the necessary wavelength. Therefore pumping was achieved on the $^5I_8 \rightarrow {}^5F_1$, $^5G_6$ transition. Assuming that the shortening of the lifetime towards room temperature can be solely attributed to multiphonon decay, equation 2.18 can be employed to derive the multiphonon decay rate. Unfortunately, the employed setup involving the cryostat does not allow measurement techniques which yield reabsorption free lifetimes [Küh07]. Therefore, the obtained effective lifetimes will carry a certain error. This effect is temperature dependent since rising temperatures induce population of higher Stark levels of the $^5I_8$ ground state, which increases the spectral overlap between absorption and emission lines. It follows that the error increases with rising temperature. Since reabsorption leads to an increase of the measured lifetimes, the reabsorption free lifetimes are in fact shorter than the obtained values. This means that estimations based on reabsorption effected measurements give a lower boundary of the multiphonon decay rate. Still, the dopant concentration of the samples used for these measurements was low (Ho^{3+}:$LiLuF_4 = 0.25\,\text{at\%}$; Ho^{3+}:$LaF_3 = 0.4\,\text{at\%}$) and the error caused by reabsorption is therefore assumed to be marginal. For Ho^{3+}:LaF_3 similar measurements were performed by Riseberg *et al.* [Ris68]. However, due to the relatively high dopant concentration of 1 at% Ho^{3+} it seems likely that the reported lifetimes are shortened due to concentration quenching.

The decay curves obtained for the $^5F_4$,$^5S_2$ multiplet in Ho^{3+}:$LiLuF_4$ at various temperatures are depicted in figure 6.16a. Excitation of the $^5F_4$,$^5S_2$ multiplet was achieved with the OPO tuned to a wavelength of $\lambda_{ex} = 537\,\text{nm}$ while the signal was detected at $\lambda_{em} = 549\,\text{nm}$. All curves obtained for the $^5F_4$,$^5S_2$ multiplet exhibit single exponential decays. The difference between effective lifetimes derived by integrating and line fit is less than 5 %. Values of τ_{eff} range from 99 µs at 300 K up to 234 µs at 50 K. It follows from equation 2.18 that the quantum efficiency is approximately 40 %. Employing the radiative lifetime of $\tau_{rad} = 460\,\mu\text{s}$ reported by Walsh *et al.* it even drops to 20 % [Wal05].

The decay curves obtained for the $^3F_3$ multiplet are shown in figure 6.16b. Measurements were carried out with $\lambda_{ex} = 447\,\text{nm}$ and $\lambda_{em} = 485\,\text{nm}$. The high noise level can be attributed to two main factors. Firstly, the employed excitation wavelength is at the edge of the spectrum which can be delivered by the employed OPO/SHG combination and the pulse energy is therefore less than 0.5 µJ. The second reason becomes obvious from the obtained decay curves and by considering the radiative lifetime of the $^3F_3$ multiplet of 287 µs as it was reported by Walsh *et al.* [Wal05]. Even at low temperatures the effective lifetime is less than 1 µs and the ratio of ions decaying radiatively and non radiatively is

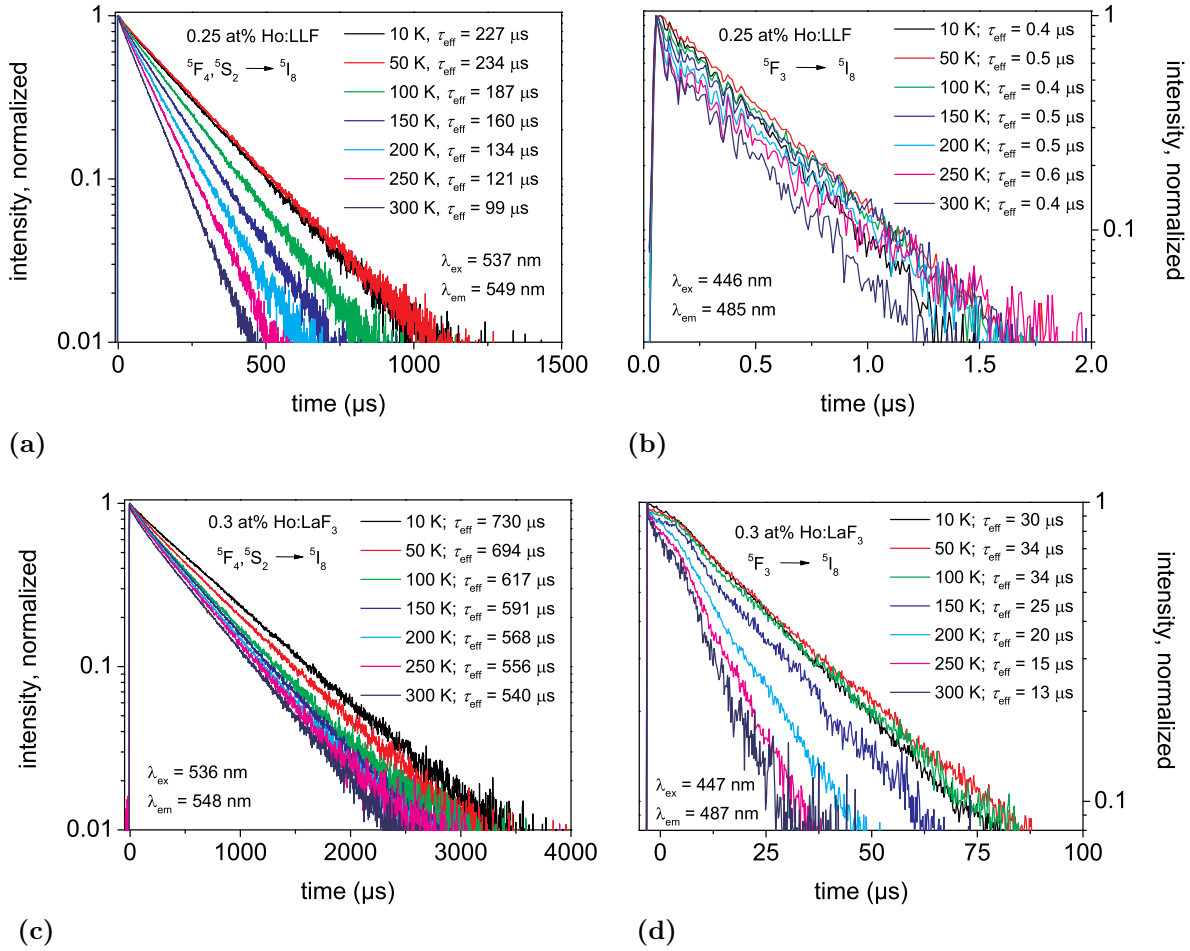

Figure 6.16: Temperature dependent decay dynamics of the $^5F_3$ and $^5F_4$,$^5S_2$ multiplets in Ho^{3+}:$LiLuF_4$ and Ho^{3+}:LaF_3.

therefore less than 1:200. This means that more than 99 % of the ions excited on any of the 420 nm - 495 nm absorption bands will decay non radiatively into the upper laser level. However, due to the low quantum efficiency of the $^5F_4$,$^5S_2$ manifold it is unclear whether or not inversion densities sufficient to achieve gain can be generated. The strong multi-phonon decay of the upper laser level furthermore means that population is transferred into the $^5I_7$ multiplett by a non radiative transfer $^5F_4$,$^5S_2 \rightarrow ^5F_5 \rightarrow ^5I_4 \rightarrow ^5I_5 \rightarrow ^5I_6 \rightarrow ^5I_7$. Since this level exhibits a radiative lifetime of 13.5 ms it is likely that a non-negligible amount of the population will be accumulated in this multiplet. This creates an additional excited manifold from which ESA processes can originate.

Figure 6.16c shows the decay dynamics of the $^5F_4$,$^5S_2$ multiplet in Ho^{3+}:LaF_3. The curves were recorded with the OPO tuned to a wavelength of $\lambda_{ex} = 536$ nm while the signal was recorded at $\lambda_{em} = 548$ nm. All curves exhibit a non-linear component during the first 300 µs after the OPO pulse. At longer times the decay becomes strictly linear. The effect of the non-linear beginning increases towards higher temperatures. While the difference between τ_{eff} obtained by fitting and integrating is less than 4 % at 10 K it increases to 14 % at 300 K. The recorded decay curves can not be explained by the Inokuti-Hirayama model. However, Gomes *et al.* found that for Ho^{3+}:$LiYF_4$ it is possible for one donor Ho^{3+}-ion

with an electron excited into the $^5F_4$,$^5S_2$ manifold to undergo a $^5F_4$,$^5S_2 \rightarrow {}^5I_6$ transition and transfer the excess energy to two acceptor ions which then execute a $^5I_8 \rightarrow {}^5I_7$ transition (cf. figure 6.17a and [Gom96]). Although the reported threshold doping concentration for Ho^{3+}:$LiYF_4$ was 1 at%, it is well possible that this value is lower for Ho^{3+}:LaF_3. This cross-relaxation process would be consistent with the observed increase of the effect towards higher temperatures, since the increasing population of higher energetic Stark levels leads to an increase of the energetic overlap between the involved transitions. The curves also show that the shortening of τ_{eff} of the $^5F_4$,$^5S_2$ multiplet in Ho^{3+}:LaF_3 is much less severe than it is in Ho^{3+}:$LiLuF_4$. The effective lifetime decreases from 730 µs at 10 K to 540 µs at 300 K. The resulting quantum efficiency is approximately 75 % . Taking into account the high inversion densities necessary to achieve gain, Ho^{3+}:LaF_3 therefore seems to be a more viable candidate for laser operation on the $^5S_2 \rightarrow {}^5I_8$ transition.

Figure 6.16d shows the decay dynamics of the $^5F_3$ manifold in Ho^{3+}:LaF_3. The strong noise of the curves can again be attributed to the low signal at the emission wavelength and the low pulse energy of the OPO/SHG combination at the employed excitation wavelength. From the deformation of the excitation curve in the first 13 µs it can be concluded that the transition of population from the terminal pump manifold $^5G_6$ into the emitting $^5F_3$ manifold can not be regarded as instantaneous. This is most likely due to the energetic distance between the manifolds $^5F_1$ and $^3K_8$ of 675 cm^{-1} in combination with the low phonon energy of LaF_3 (cf. figure 6.17b). Unfortunately, the employed OPO/SHG does not allow the $^3K_8$ or $^5F_2$ manifold to be directly pumped which would circumvent this problem. Effective lifetimes were therefore obtained by line fits to the part of the decay curves which were not affected. It can be seen that τ_{eff} drops from 30 µs at 10 K to 13 µs at 300 K. This yields a quantum efficiency of approximately 57 %. It is likely though that the radiative lifetime of the $^3F_3$ manifold is longer than the value obtained at 10 K. A comparison with the corresponding radiative lifetime of Ho^{3+}:$LiLuF_4$ shows a difference of one order of magnitude. Therefore, it seems likely that the actual quantum yield is larger than what can be expected from these measurements.

6.3.6 Excited State Absorption Spectra

Due to the large number of $4f^{11}$ multiplets in Ho^{3+}, ESA measurements of the $^5F_4$,$^5S_2$ manifold in Ho^{3+}:$LiLuF_4$ and Ho^{3+}:LaF_3 were carried out in the wavelength region of 400 nm - 800 nm. In a first set of measurements polarization dependent spectra were obtained by pumping with an InGaN LD (Ho^{3+}:$LiLuF_4$: $\lambda_{\text{ex}} = 449$ nm; Ho^{3+}:LaF_3: $\lambda_{\text{ex}} = 447$ nm). A second set of spectra was then recorded by employing a Nd^{3+}:YVO_4 laser operating at 1064 nm which was frequency doubled to 532 nm as pump source. This approach was taken since scattering and reflection of the pump light cause an oversaturation of the detector in the spectral region of the respective excitation wavelength. In order to gain complete spectra in which ESA in the green as well as in the blue spectral region can be identified, the spectra obtained with different pump sources were calibrated to each other and then combined to yield a spectrum without gaps. Since the decay dynamics in Ho^{3+}:$LiLuF_4$ showed that it is likely that population will accumulate in the $^5I_7$ manifold, ESA measurements for this system were also carried out by pumping with a Tm^{3+}:Lu_2O_3 laser operating at a wavelength of 2065 nm [Koo12]. Comparing these

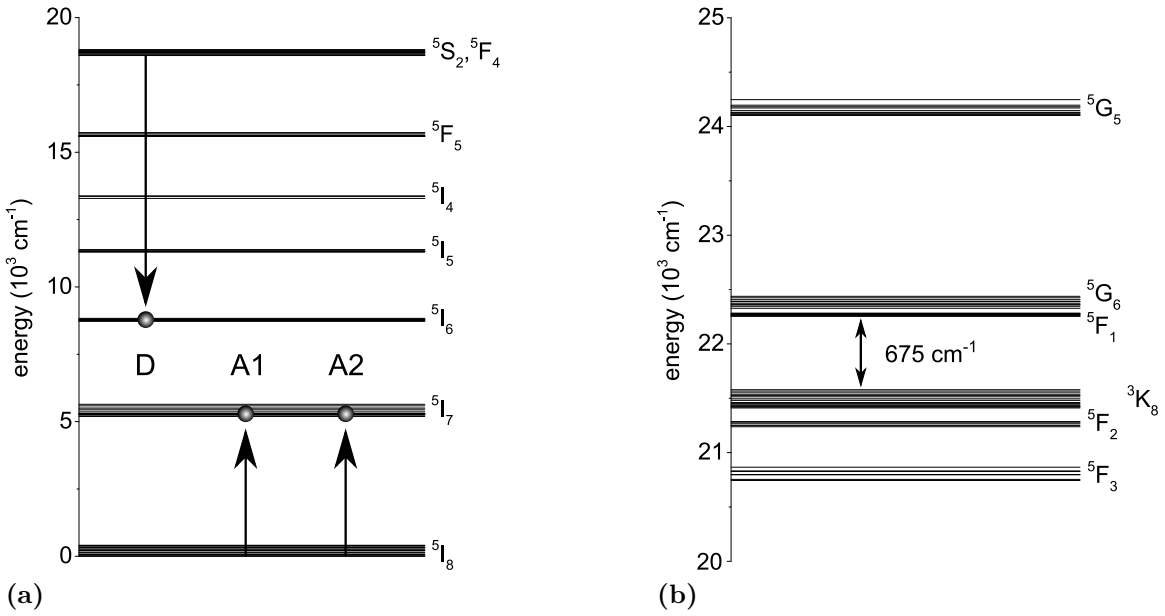

Figure 6.17: Energy level schemes of Ho^{3+}.(a) depicts the possible cross relaxation process between one Ho^{3+}-ion in the $^5F_4$,$^5S_2$ multiplet and two in the ground state [Gom96]. (b) shows the terminal pump multiplet.

ESA spectra with those obtained for the $^5F_4$,$^5S_2$ multiplet then allowed the starting manifold for the observed ESA transitions to be distinguished. Measurements were carried out with a resolution of 0.8 nm and by employing a 450 W Xe-lamp as probe source. Calibration was achieved with GSA spectra recorded with the same resolution. The ground state absorption was then subtracted from the measured curves yielding spectra which show only stimulated emission and excited state absorption.

The spectra obtained for Ho^{3+}:$LiLuF_4$ are depicted in figure 6.18. It can be seen that the upper spectra which were obtained with excitation wavelengths of $\lambda_{ex} = 449$ nm and 532 nm and the lower spectra obtained with $\lambda_{ex} = 2065$ nm exhibit a striking similarity. The six ESA bands present when pumped in the blue spectral region can also be seen under pumping with 2 µm. Since at $\lambda_{ex} = 2065$ nm it is not possible to accumulate a noteworthy amount of population in the $^5F_4$,$^5S_2$ manifold, the ESA bands in both graphs must be due to transitions originating from the $^5I_7$ multiplet. Figure 6.19 depicts the energy level scheme of Ho^{3+} with the six arrows corresponding to the peak wavelengths of the ESA bands. For all six bands transitions with the corresponding energy starting from the $^5I_7$ multiplet can be found. Due to the small energetic distance between the several manifolds of the ^5G_J multiplet, it can then be assumed that population transferred by any of the six ESA transitions depicted in figure 6.18 will decay non-radiatively into the upper laser level. These ESA transitions are therefore not a loss channel but have an effect similar to reabsorption. Still, the possibility of ESA transition originating from the $^5F_4$,$^5S_2$ multiplet can not be ruled out completely since they might be concealed in the obtained spectra by the more pronounced transitions starting from the $^5I_7$. However, the upper graph clearly shows a peak at 550 nm. Since this peak is not present in the lower spectrum it can be attributed to stimulated emission originating from the $^5S_2 \rightarrow {}^5I_8$

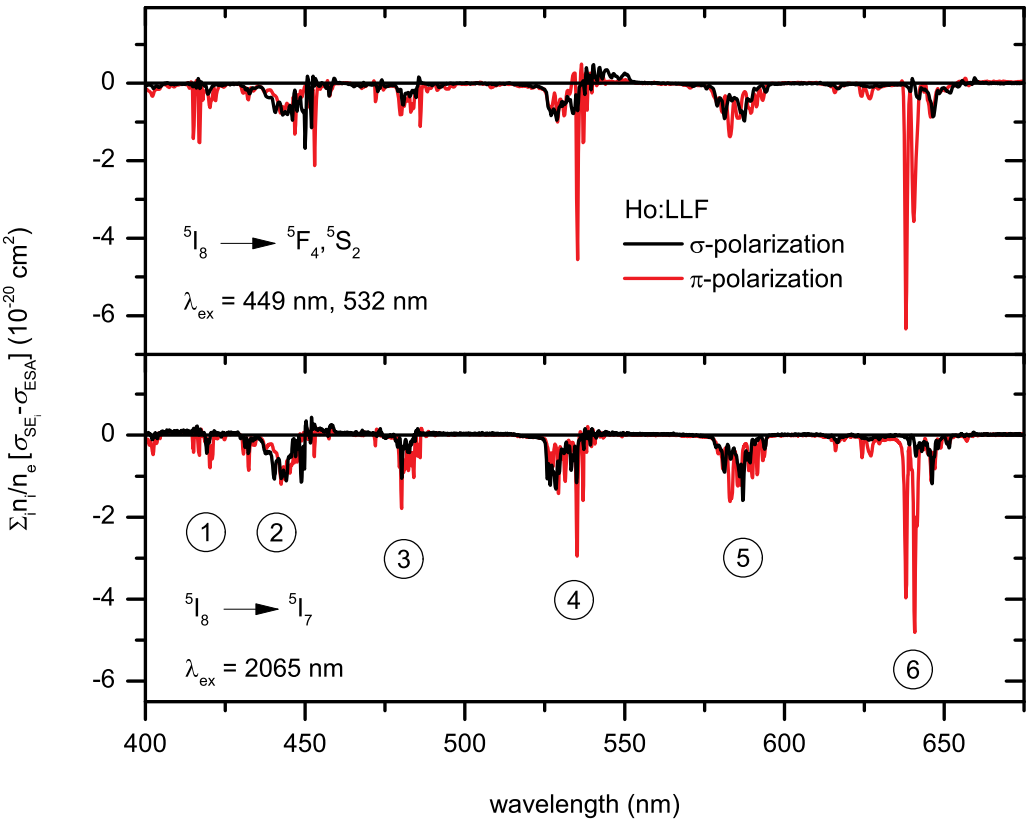

Figure 6.18: Polarization dependent excited state absorption spectra of Ho^{3+}:$LiLuF_4$. Measurements were carried out with $\lambda_{ex} = 449\,nm$ and $532\,nm$ (upper graph) and $\lambda_{ex} = 2065\,nm$ (lower graph). The numbered ESA peaks can be attributed to the transitions depicted in figure 6.19.

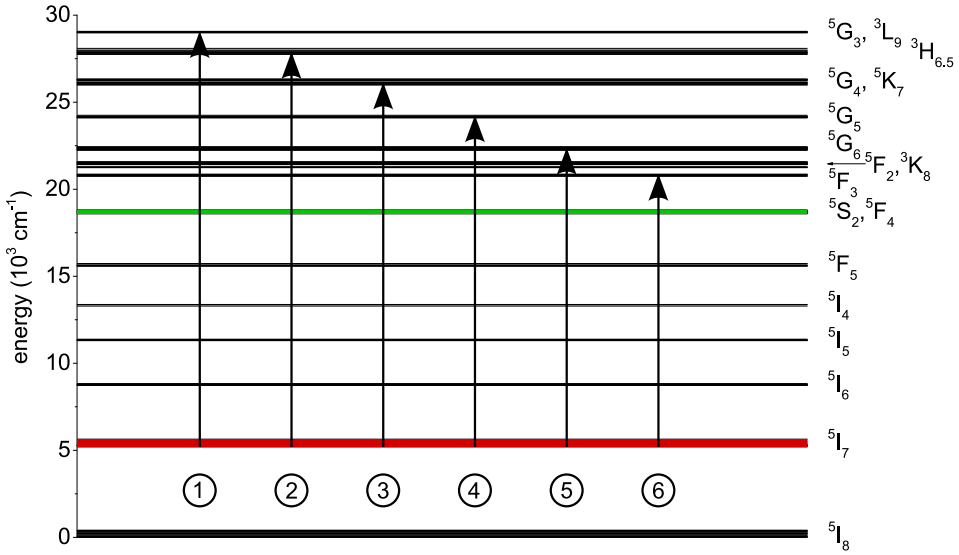

Figure 6.19: Schematic energy level scheme of Ho^{3+} with ESA transitions starting from the $^5I_7$ manifold. The upper laser manifold $^5F_4$,$^5S_2$ is colored green, the ESA starting manifold $^5I_7$ red.

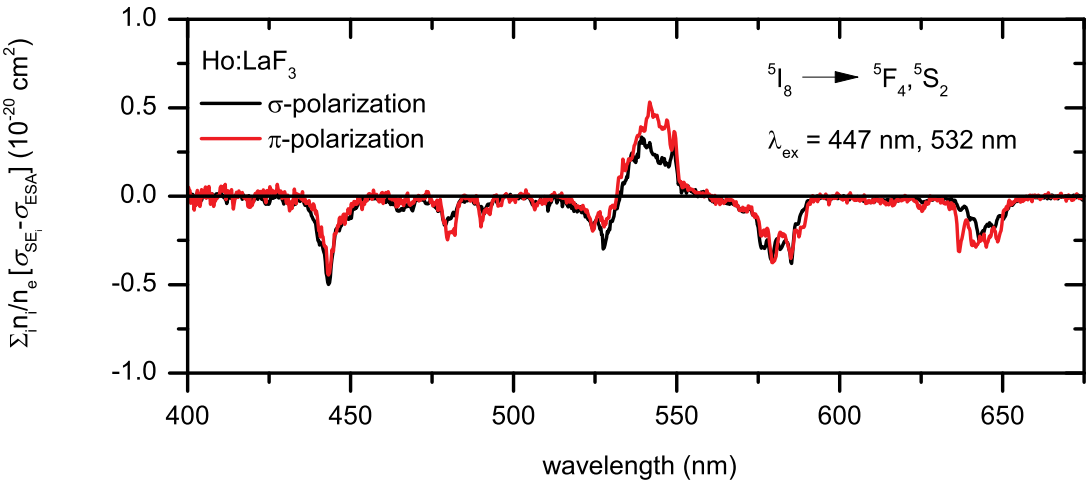

Figure 6.20: Polarization dependent excited state absorption spectra of Ho^{3+}:LaF_3. Measurements were carried out with $\lambda_{ex} = 447\,nm$ and $532\,nm$.

transition. This shows that stimulated emission dominates in the wavelength region in which, according to the gain spectra, laser operation will first occur when the necessary inversion is reached (cf. section 6.3.5).

Figure 6.20 depicts the polarization dependent spectra recorded for Ho^{3+}:LaF_3. It can be seen that ESA bands are present at similar wavelengths as in Ho^{3+}:$LiLuF_4$. It seems that although the $^5S_2$ manifold exhibits a lower non-radiative decay rate, a non-negligible amount of the population accumulates in the $^5I_7$ multiplet. However, this effect is much less pronounced than in Ho^{3+}:$LiLuF_4$. This can be seen, for example, from the ratio of the peak cross sections of ESA and stimulated emission. The spectra also show a pronounced stimulated emission peak around 550 nm which can be attributed to the $^5S_2 \rightarrow {}^5I_8$ transition. Therefore, as in the case of Ho:LLF, based on the gain spectra, the wavelength range in which laser operation can be expected to first set in is dominated by stimulated emission.

6.4 Summary: Spectroscopy

6.4.1 Praseodymium Doped Materials

The materials Pr^{3+},Mg^{2+}:$SrAl_{12}O_{19}$, Pr^{3+},Mg^{2+}:$CaAl_{12}O_{19}$, Pr^{3+}:$LaMgAl_{11}O_{19}$, and Pr^{3+}:LaF_3 were investigated in terms of their ground state absorbtion, stimulated emission and excited state absorption characteristics. It was shown that all four materials exhibit absorption bands which can be adressed with InGaN laser diodes or frequency doubled OPS lasers. The absorption cross sections of Pr,Mg:SRA, Pr,Mg:CAlO, and Pr:LaF_3 are in the order of $10^{-21}\,cm^2$. Due to the possibility of a second optically active center in Pr:LMA, no absorption cross section can be given. The emission spectra show the well known peaks in the cyan, green, orange, red, and deep spectral regions, also with cross section in the order of $10^{-21}\,cm^2$. Especially interesting are the unusually strong emission characteristics of Pr^{3+}:LaF_3 in the orange spectral region, and the linewidth

of one of the peaks of more than 7 nm which might allow tunable laser operation and the generation of short pulses. Excited state absorption spectra revealed the presence of interconfigurational transitions starting from the ^3P_J manifold and terminating in $4f^15d^1$ multiplets for all systems. However, in any of the four active media these transitions can be found at wavelengths larger than 400 nm. ESA on either pump or on any of the prospective laser wavelengths is therefore expected.

In addition, the fluorescence decay dynamics of Pr:LMA were investigated in order to derive the radiative lifetime. These measurements showed two distinct lifetimes for emission wavelengths that correspond to the $^3P_0 \rightarrow {}^3F_4$ transition. The presence of a second optically active center, which is also indicated by the crystallographic properties, was investigated with site-selective excitation and emission measurements. The obtained spectra exhibit varying characteristics depending on the excitation and observed emission wavelength. These results, in combination with the Mg^{2+} deficiency revealed by the microprobe analysis, strongly indicate that two optically active centers are present.

Furthermore, low temperature emission measurements were conducted with Pr^{3+}:LaF_3 in order to investigate the unusual emission characteristics in the orange spectral region. The obtained spectra revealed that parts of the emissions bands can be attributed to pronounced phonon assisted transitions.

6.4.2 Holmium Doped Materials

Ho^{3+}:$LiLuF_4$ and Ho^{3+}:LaF_3 were both characterized for their ground state absorption characteristics which showed absorption bands that can be adressed with InGaN LDs and 2ωOPSLs. The peak cross sections of the absorption bands were in the order of 10^{-20} cm^2. For Ho^{3+}:LaF_3 transmission measurements at cryogenic temperature were conducted in order to obtain the energetic positions of the Stark levels composing the $^5S_2$ manifold. The recorded spectra were employed to derive the emission cross sections of the $^5S_2 \rightarrow {}^5I_8$ transition via the reciprocity method. As a comparison, fluorescence measurements of both materials were conducted. For both systems, a good overlap between the spectra obtained via the reciprocity method and measurement can be seen. Peak emission cross sections were in the order of 10^{-21} cm^2. GSA and emission spectra were used to derive the gain spectra for both systems. These revealed that for both active media an inversion level of at least 20 % is necessary to achieve gain. Above this level gain can be expected at approximately 550 nm. The fluorescence decay dynamics of the multiplets $^5F_3$ and $^5F_4$,$^5S_2$ were investigated to give an insight into depopulation by means of non radiative processes. This revealed a quantum yield of less than 40 % for Ho:LLF and approximately 75 % for Ho:LaF_3. The measurements furthermore showed that for both materials nearly all of the population transferred into the terminal pump multiplet $^3F_3$ decays non-radiatively into the upper laser level. Excited state absorption measurements revealed the presence of ESA transitions starting in the $^5I_7$ manifold and terminating in multiplets that are non-radiatively coupled to the $^5F_4$,$^5S_2$ manifold, therefore transfering population back into the upper laser level. Population of the multiplet $^5I_7$ takes place by a chain of multiphonon decays starting from the $^5S_2$ multiplet. The ESA spectra furthermore show dominant stimulated emission in the spectral region around 550 nm.

7 Laser Experiments

In this chapter the laser experiments conducted in the framework of this thesis are presented. The first section introduces the employed pump sources with their respective characteristics, advantages, and disadvantages. The second and third part start with a short introduction into state of the art visible lasers based on Pr^{3+}- and Ho^{3+}-doped materials, respectively. After this the laser experiments conducted with the various materials will be presented in detail.

7.1 Pump Sources

Two different types of pump sources have been employed in this thesis. The first were blue emitting laser diodes based on indium gallium nitride (InGaN). The second were optically pumped semiconductor lasers emitting in the near infrared which were then frequency doubled into the cyan spectral region.

7.1.1 InGaN Based Laser Diodes

The material indium gallium nitride belongs to the group of the III-V semiconductors. The first LD based on InGaN was introduced by Nakamura *et al.* in 1996 [Nak96]. It operated in pulsed mode in the violet spectral range at a central emission wavelength of $\lambda_L = 417\,\text{nm}$ and delivered 430 mW at a current of 2.3 A. Since then the development of this type of LD has made some progress and today efficient LDs emitting in a wide spectral range from the ultraviolet to the green can be fabricated [Nic13a]. At the moment, highest output powers ($P_{\text{out,max}} = 1.6\,\text{W}$) and efficiencies ($\eta_{\text{wallplug}} = 24\%$ - 36%, [Nic13b]) are reached in the wavelength range of 440 nm - 450 nm which makes these LDs very interesting for pumping Pr^{3+}- and Ho^{3+}-doped materials. The big advantages of these devices are their small overall size, high efficiency, and low cost.

Unfortunately these LDs also exhibit some drawbacks. Due to the geometry and dimensions of the emitter they operate in a transversal and longitudinal multimode regime. Depending on the maximum output power of the model this leads to beam quality factors of $M_x^2 = 1.5$ and $M_y^2 = 2.9$ ($P_{\text{out,max}} = 0.5\,\text{W}$) or $M_x^2 = 1.5$ and $M_y^2 = 5.8$ ($P_{\text{out,max}} = 1\,\text{W}$) where x denotes the fast and y the slow axis [Han10]. The emission spectrum of InGaN LDs furthermore exhibits a linewidth of approximately 1.7 nm and the central emission wavelength can vary by up to 10 nm between diodes. An exemplary spectrum was recorded with a *Bruker* Equinox 55 fourier transform spectrometer and is depicted in figure 7.1a. The current applied to a LD also has a strong influence on the emission spectrum which can be seen in figure 7.1b. In addition a dependency on the casing temperature can be observed, however the effect is much less pronounced ($0.1\,\text{nm}\,\text{K}^{-1}$). This means that when

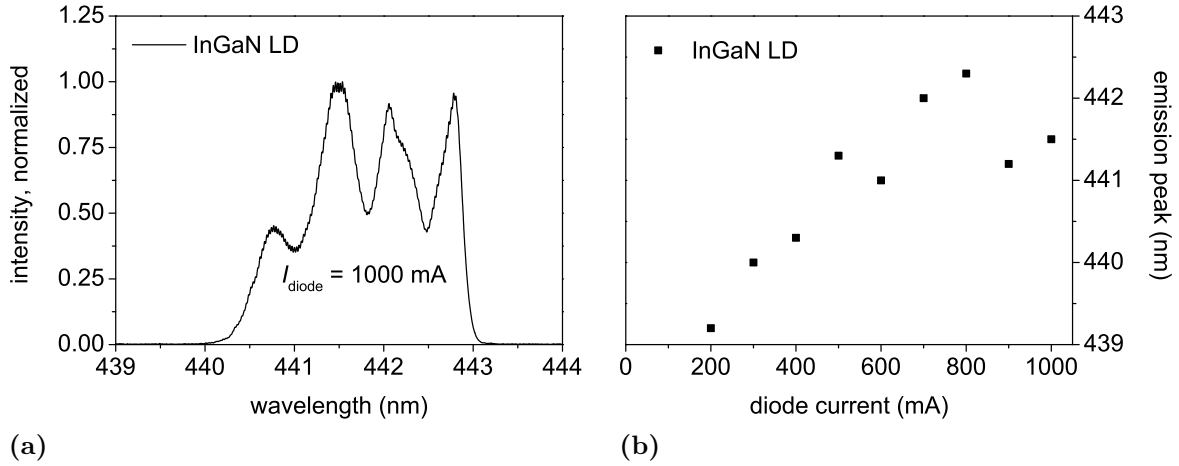

Figure 7.1: Spectral characteristics of an InGaN laser diode at $T = 19\,°C$. (a) emission spectrum at $I_{diode} = 1\,A$ and (b) spectral shift in dependence of the output power.

using these devices as pump sources for Pr^{3+}- and Ho^{3+}-doped materials care has to be taken in choosing a diode with a suitable emission spectrum and furthermore in terms of the operating parameters. Otherwise the spectrum of the pump light might only yield a poor overlap with the absorption bands of the gain medium.

By employing InGaN LDs as pump sources it was already possible to demonstrate compact and efficient diode pumped solid state lasers based on Pr^{3+}-doped materials with emission in the visible spectral range [Ric04, Fib09, Fec11, Gün11c].

A number of different LDs have been employed in this work. All were specified for a maximum output power of $P_{out} = 1\,W$ at $I_{diode} = 1\,A$ and emitted a linearly polarized beam. In order to obtain an optimal spectral overlap between their respective emission spectrum and the absorption band of the active material, some diodes were operated with a current of up to $I_{diode} = 1.2\,A$. Due to the strong dependence of the spectrum on the current this led to a shift of emission spectrum of the respective laser diode and furthermore increased the output power to up to 1.2 W.

Since the LDs emitted a divergent beam with a rectangular profile collimation, beam shaping optics were necessary. Here a two step approach was employed. In the first step the fast axis of the beam was collimated with an aspheric lens with $f = 4.5\,mm$ ($NA = 0.6$). The second step consisted of a pair of cylindrial lenses (*Schäfter + Kirchhoff* 5AN-3-V-35) which collimated the slow axis and led to a more homogeneous beam profile. While this usually resulted in a sufficient collimation, the aspect ratio of the beam strongly varyied between different LDs. In optimal cases a quadratic beam profile with an aspect ratio of approximately 1:1 could be achieved. However, the beams of most LDs exhibited a rectangular profile with aspect ratios as high as 1:3.

7.1.2 Frequency Doubled Optically Pumped Semiconductor Lasers

Frequency doubled optically pumped semiconductor lasers (2ωOPSLs) are vertical external cavity surface emitting lasers (VECSELs) [Kuz97]. The gain medium is a multi

quantum well structure for example based on InGaAs. This allows the realization of VECSELs operating in a broad spectral range from the near to the mid infrared [Tro04]. Resonator internal frequency doubling of these VECSELs allows the cyan spectral region to be adressed [McI03]. This makes these devices interesting for pumping Pr^{3+}- and Ho^{3+}-doped media in the 480 nm region.

2ωOPSLs have a number of advantages compared to InGaN LDs. The pump diodes used for these devices are well developed since they are standard commercially available pump sources for Nd^{3+}-doped gain media. They are available with high output powers, good efficiency, and at low cost. Furthermore, the chip employed in the VECSEL has a thickness in the order of several ten micrometers which allows an efficient heat removal. Power scaling of 2ωOPSLs is thus not limited by the available pump power or thermal effects in the VECSEL chip [Chi04].

However, theses devices also exhibit several disadvantages. The nonlinear crystals employed for the intracavity frequency doubling require critical phase matching in order to achieve an efficient second harmonic generation [Boy92]. Changing the emission wavelength of a once built 2ωOPSL is thus complex and requires replacing the nonlinear crystal. Another point is the low wallplug efficiency of these devices which is in the order of $\eta_{\mathrm{wallplug}} = 1\,\%$ [COH13a]. Also, the high power pump diodes require adequate cooling which makes the footprint of these devices much larger than, for example, that of InGaN LDs. The overall complexity of the system makes 2ωOPSLs costly, especially in the multi-Watt output power range. Experiments conducted with these pump sources in this work thus have to be considered as proof of principle experiments.

2ωOPSLs have been employed as pump sources for Pr^{3+}-doped materials with excellent results [Osi04, Ric07, Met12].

In this work, two different 2ωOPSLs which were both manufactured by *COHERENT Inc.* were employed. One was a model Genesis CX specified with $\lambda_{\mathrm{em}} = 486.2\,\mathrm{nm}$[1], a maximum output power of $P_{\mathrm{out}} = 4\,\mathrm{W}$ and a nearly diffraction limited beam quality of $M^2 < 1.1$. The second was a model Genesis Taipan specified with $\lambda_{\mathrm{em}} = 479.1\,\mathrm{nm}$, a maximum output power of $P_{\mathrm{out}} = 5\,\mathrm{W}$ and $M^2_{x,y} = 2.9,\ 2.7$. The Genesis Taipan as well as the Genesis CX emit linearly polarized beams. Exemplary emission spectra of both devices were recorded with a *Bruker* Equinox 55 fourier transform spectrometer and are depicted in figure 7.2a. It can be seen that the linewidth in both cases is less than 0.1 nm and is therefore far smaller than the linewidth of the absorption bands of the investigated Pr^{3+}- and Ho^{3+}-doped materials (cf. table 6.2 and 6.4). Furthermore, they were characterized in terms of their spectral shift in dependence of the output power which is shown in figure 7.2b. This revealed that the central emission wavelength of the Genesis Taipan shifts towards shorter wavelengths when the output power is increased. The rate of the shift is roughly $0.04\,\mathrm{nm\,W^{-1}}$. The overall shift is therefore approximately 0.2 nm. Taking the linewidths of the active media into account, it follows that in terms of a changing spectral overlap between pump light and absorption band this shift does not pose a problem. It can also be seen from figure 7.2b that no such shift is present for the Genesis CX. Both

[1] It should be noted, that the Genesis CX was initially delivered with an emission wavelength of 487.6 nm which fitted to one of the absorption lines of Pr:LMA. After the laser experiments with this material, the device was returned to the manufacturer and tuned to $\lambda_{\mathrm{em}} = 486.2\,\mathrm{nm}$ to fit Pr,Mg:SRA. The maximum output power and beam quality did not change during this process.

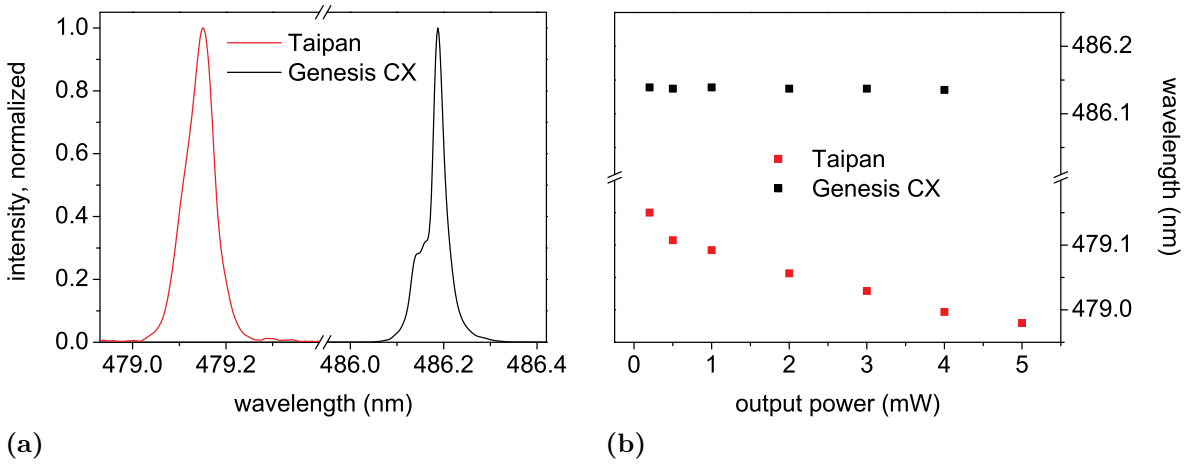

Figure 7.2: Spectral characteristics of the 2ωOPSLs employed in this work. (a) emission spectrum and (b) spectral shift.

devices emit a collimated, circular beam which means that no further beam shaping is necessary.

7.2 Lasers Based on Pr-Doped Materials

7.2.1 State of the Art

The first laser operation of a Pr^{3+}-doped gain medium dates back as far as 1962. Yariv *et al.* employed Xe-flash lamps to obtain laser radiation from Pr^{3+}:$CaWO_4$ at cryogenic temperatures [Yar62]. However, due to the narrow linewidths of the Pr^{3+} absorption bands the optical-to-optical efficiency of these early systems was quite poor. The same is true for the later developed pump schemes involving Ar-ion lasers emitting on several narrow lines in the blue spectral region [Bri64]. These devices allowed efficient laser operation in terms of output versus absorbed power with gain media like Pr^{3+}:$LiYF_4$, Pr^{3+}:$LiGdF_4$, Pr^{3+}:KYF_4, and Pr^{3+}:$YAlO_3$ [San94, Dan94a]. But again the mediocre spectral overlap between the emission peaks of such Ar-ion lasers and the absorption lines of the Pr^{3+}-ion results in low optical-to-optical efficiencies.

The development of blue emitting InGaN laser diodes and 2ωOPSLs in the 1990s gave rise to pump sources which could be specifically fabricated to yield an optimal absorption of the pump light. Richter *et al.* and Osiac *et al.* demonstrated laser operation of Pr^{3+}:$LiYF_4$ pumped by InGaN LDs and 2ωOPSLs, respectively [Ric04, Osi04]. Recently these results have been further improved yielding laser operation in the visible spectral range with output powers on the multi Watt scale and optical-to-optical efficiencies of 50 % and more [Gün11c, Met12]. In addition to Pr^{3+}:$LiYF_4$ several other Pr^{3+}-doped host systems have been employed to obtain visible laser radiation with such pump sources. These were mostly fluoride systems like Pr^{3+}:$LiLuF_4$, Pr^{3+}:$LiGdF_4$, Pr^{3+}:BaY_2F_8, and Pr^{3+}:KY_3F_{10} [Ric04, Cor07, Pab11, Cam07]. But also Pr^{3+}-doped oxide crystals can be used which is shown by results obtained with Pr^{3+}:$YAlO_3$ and Pr^{3+}:$LuAlO_3$ [Fib09, Fec09]. These systems have the advantage of higher thermal conductivities and a better mecha-

nical and chemical stability compared to fluorides. However, while Pr^{3+}:$YAlO_3$ exhibits ESA on the pump wavelength [Dan94b], Pr^{3+}:$LuAlO_3$ suffers from the formation of color centers caused by pump radiation in the 450 nm region [Fec12]. Both effects are detrimental to laser operation. The system Pr,Mg:SRA, which is one of the materials discussed in this thesis, exhibits neither of the two problems (cf. section 6.2).

Another advantage of Pr^{3+}-doped gain media is that they allow coherent radiation in the UV spectral region to be obtained via a single step of intracavity frequency doubling. Here, Pr^{3+}:$LiYF_4$ and Pr^{3+}:$YAlO_3$ have been employed to obtain up to 500 mW and 60 mW of output power, respectively [Gün11b, Fu11]. In both experiments InGaN LDs were used as pump sources.

7.2.2 Pr,Mg:$SrAl_{12}O_{19}$

The first laser operation of Pr,Mg:SRA was realized by Merkle *et al.* in a pulsed regime by employing a coumarin dye laser as pump source [Mer96]. They demonstrated laser emission at wavelengths of 641 nm and 486 nm at temperatures of 120 K and 15 K respectively. Recently Fechner *et al.* demonstrated efficient laser operation at room temperature by employing InGaN LDs as pump source [Fec11]. Furthermore Pr,Mg:SRA has become the first dielectric crystalline material to allow visible laser operation in a waveguide geometry [Cal11].

InGaN LD Pumped Bulk Lasers

An inherent problem of the InGaN LDs which were available for this work is their low output power. A simple way to double the total incident pump power is to incoherently combine the beams of two diodes using polarizing beamsplitter cubes (PBSC). A further increase of the incident pump power can be achieved by employing a two sided longitudinal pump scheme [Gün11c]. The basic scheme of such a setup is depicted in figure 7.3. For Pr^{3+}:$LiYF_4$ this leads to the problem that due to the much higher absorption cross sections for π-polarized light (cf. [Ric08]), the part of the beam which is polarized parallel to the crystals a-axis experiences a significantly smaller absorption. For Pr,Mg:SRA the situation is different. As it can be seen in figure 6.6 the absorption is much stronger for σ-polarized light. The crystals employed for the laser experiments were thus prepared in a c-cut. The k-vectors of pump and laser light were therfore parallel to the c-axis of the crystal while the E-field vectors were always perpendicular to it. Therefore, the pump light, indepent of its polarization, is always optimally absorbed.

As resonator design a hemispherical V-type cavity as depicted in figure 7.4 was chosen. It consisted of two plane mirrors M1 and M2 and one curved output coupling mirror M3 with $r_{OC} = 100$ mm. As M1 and M2 dielectrically coated mirrors which were anti-reflective (AR) for the pump wavelength λ_P and high reflective (HR) for the laser wavelength λ_L were chosen. Several different mirrors with various output coupling rates T_{OC} were available as M3. The crystal could be set in a water cooled copper heat sink. The temperature of the water could be adjusted by a chiller from 5 °C - 30 °C.

The pump light was delivered by four InGaN LDs which all exhibited a central emission wavelength of 444.5 nm. In order to prevent a spectral shift of the pump light, all diodes

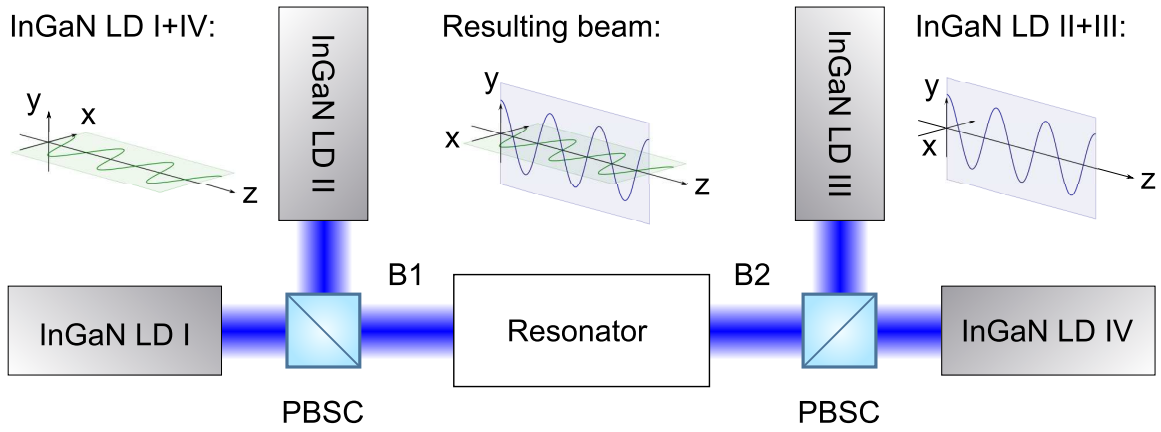

Figure 7.3: Scheme for polarization coupling of InGaN laser diodes.

were operated at a constant current. The power delivered by each diode was adjusted with a $\lambda/2$-waveplate between the LD and the PBSC. Depending on the initial polarization of the LD, an attenuation of the $\lambda/2$-waveplate caused more light to be reflected (LD I and IV) or transmitted (LD II and III) at the PBSC and thus allowed the pump power inciding on the active medium to be adjusted. The two pump beams B1 and B2 resulting from the coupling of the beams emitted by LD I and II, and III and IV were focussed into the crystal with achromatic lenses (L1 and L2) through the mirrors M1 and M2 respectively. Preliminary tests were conducted with lenses with focal lengths of $f = 30\,\text{mm}$, $50\,\text{mm}$, $75\,\text{mm}$, and $100\,\text{mm}$. These experiments showed that for pumping with InGaN LDs a focal length of $50\,\text{mm}$ was optimal.

Besides the possibility of pumping from two sides this setup has another advantage. By placing a powermeter between M2 and L2 the transmitted pump power of B1 can be accurately determined during laser operation. This is preferable to a measurement without laser operation since it would neglect the fact that above the laser threshold the inversion is fixed and therefore bleaching of the GSA does not occur (cf. 2.3). From the measurements conducted for B1 the corresponding values for B2 can be extrapolated and the total amount of absorbed pump power can be determined accurately.

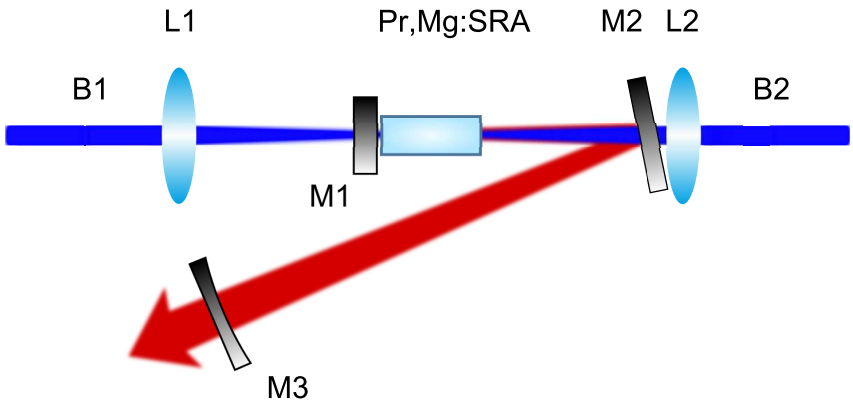

Figure 7.4: Schematic of the V-type resonator design used for the laser experiments.

Laser crystals were prepared from each of the Pr,Mg:$SrAl_{12}O_{19}$ boules grown at the ILP (cf. section 4.3.1). Three different crystals were available for the laser experiments. The samples had dopant concentration of 2.7 at%, 3.6 at%, and 4.5 at% and lengths of 5.9 mm, 5.9 mm, and 7.6 mm, respectively. It should be noted that while the first two crystals were prepared in *a*-cut, the higher doped crystal was *c*-cut. However, the first set of experiments had the goal of finding the optimal dopant concentration. For this purpose pumping with only a single InGaN LD was sufficient. The dopant concentration is an important factor because of the proneness of the Pr^{3+}-ion for cross relaxation processes which can have a detrimental effect on the laser characteristics (cf. section 2.4.1 and [Heg82, Der03]). For these experiments the resonator was set up for operation at a wavelength of $\lambda_L = 724.4$ nm corresponding to the $^3P_0 \rightarrow {}^3F_4$ transition. The output coupling rate of M3 was $T_{OC} = 2.8$ % and the crystal was not cooled.

The recorded input-output curves are depicted in figure 7.5. It can be seen that the slope efficiency increases towards lower dopant concentration. While it is 27 % for 4.5 at%, it is 32 % for 3.6 at% and reaches a maximum of 47 % for 2.7 at%. The threshold pump powers are 173 mW, 136 mW, and 120 mW, respectively. These results indicate that best laser performance can be expected from the low doped sample. This is in good agreement with experiments conducted by Fechner in a similar setup for $\lambda_L = 643.5$ nm [Fec12]. Therefore, this crystal was used for all subsequent laser experiments. It was set in a copper heat sink which was water cooled to a temperature of $T = 6$ °C. In order to investigate the scalability of the system and the laser characteristics at higher pump powers, in the next step four InGaN LDs and various output coupling rates were employed. Power curves were recorded by operating all four diodes with their respective maximum current ($I_{LD\,I} = 1.25$ A, $I_{LD\,II} = 1.2$ A, $I_{LD\,III} = 1.05$ A, $I_{LD\,IV} = 1.1$ A). By attenuating the $\lambda/2$-waveplate positioned between LD IV and the PBSC the power transmitted through the cube and thus the power inciding on the crystal was decreased. LD IV was switched off when all its pump radiation was being reflected at the PBSC. In the next step the process was repeated with LD III, then LD II, and finally with LD I.

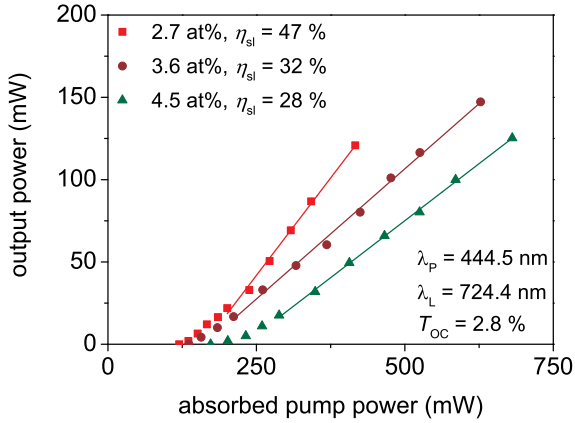

Figure 7.5: Input-output curves of InGaN LD pumped Pr,Mg:$SrAl_{12}O_{19}$ crystals with different dopant concentrations. The lasers operated at a wavelength of $\lambda_L = 724.4$ nm with a output coupling rate of $T_{OC} = 2.8$ %.

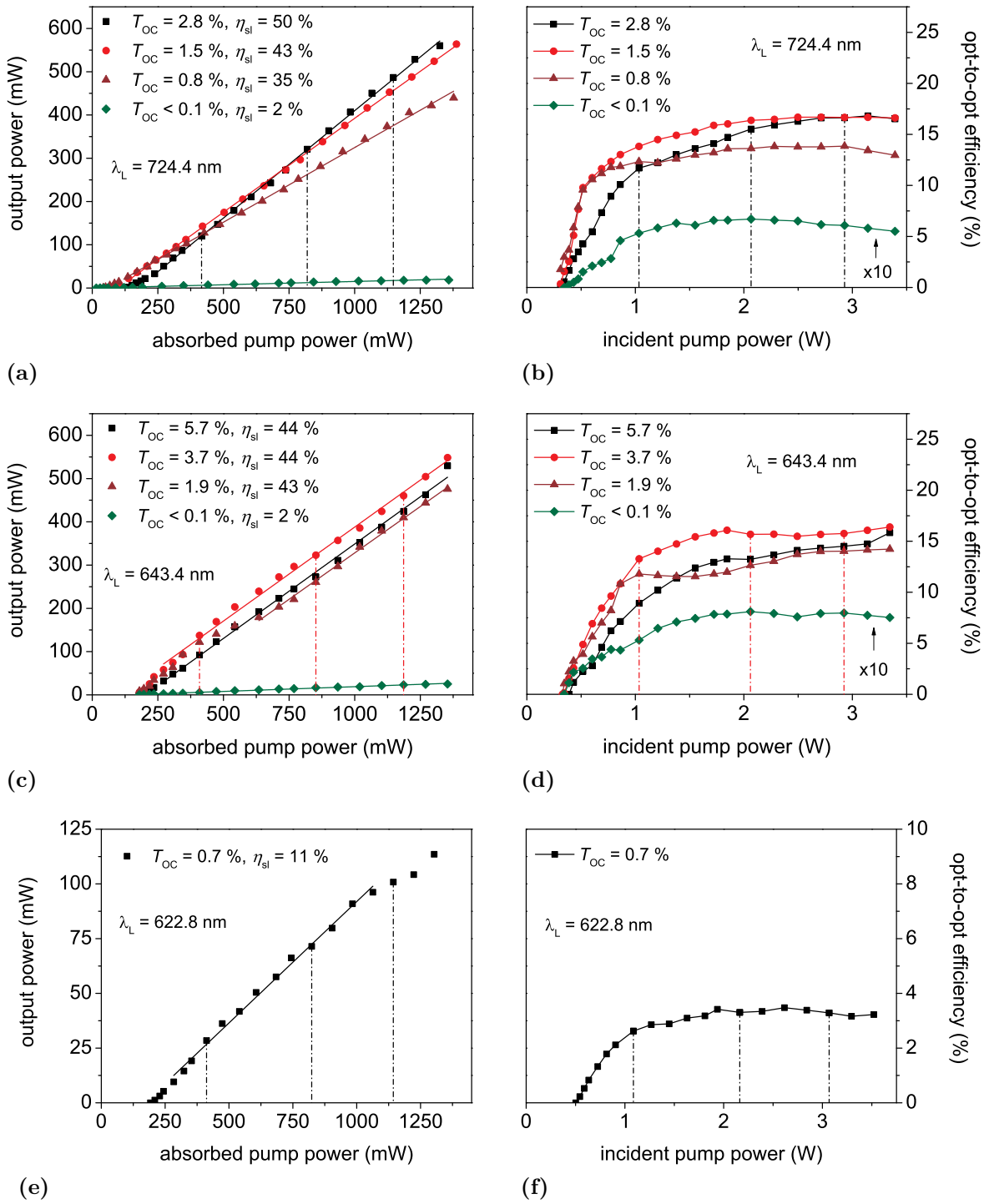

Figure 7.6: Input-output characteristics and optical to optical efficiencies for Pr,Mg:SRA lasers pumped by four InGaN laser diodes. (a,b) $\lambda_L = 724.4\,\text{nm}$, (c,d) $\lambda_L = 643.4\,\text{nm}$, and (e,f) $\lambda_L = 622.8\,\text{nm}$. Vertical lines indicate points at which subsequent LDs were added. The color coding of these lines corresponds to that of the output coupling rates. Note that in (b) and (d) the curves for $T_{OC} < 0.1\,\%$ are increased by a factor of 10.

The input-output curves obtained for $\lambda_L = 724.4\,\text{nm}$ are depicted in figure 7.6a. The maximum output power of $P_{out} = 564\,\text{mW}$ was achieved with an output coupling rate of $T_{OC} = 2.8\,\%$ and a slope efficiency of $\eta_{sl} = 50\,\%$. The threshold was $P_{thr} = 120\,\text{mW}$. The vertical black lines in figure 7.6a indicate at which point additional LDs were switched on during the experiment with $T_{OC} = 2.8\,\%$. It can be seen that the curve exhibits no break which would indicate a misalignment of the four beams. The evolution of the corresponding optical-to-optical (opt-to-opt) efficiency[2] which is depicted in figure 7.6b shows a similar behaviour with no distinguishable changes at the points where further LDs were added. The maximum optical-to-optical (opt-to-opt) efficiency was $\eta_{opt} = 17\,\%$ which was realized with $T_{OC} = 2.8\,\%$ and $1.5\,\%$. The graphs furthermore show that for these two output coupling rates no sign of a thermal rollover is present. The curve for $T_{OC} = 0.8\,\%$ exhibits a marginal drop of η_{opt} at pump powers close to 4 W. Whether this is the onset of a thermal rollover can not be said. From the progression of both graphs it seems likely that the laser characteristics could be further improved by employing even higher output coupling rates. Unfortunately such mirrors were not available at the time of this experiment. All laser parameters are listed in table 7.1

The resonator was then reset for operation at a wavelength of 643.4 nm which corresponds to the $^3P_0 \rightarrow {}^3F_2$ transition. The resulting input-output curves are depicted in figure 7.6c. The maximum output at this wavelength was 548 mW at $T_{OC} = 3.7\,\%$, $\eta_{sl} = 44\,\%$, and $P_{thr} = 180\,\text{mW}$. Comparable results were also obtained with output coupling rates of $1.9\,\%$ and $5.7\,\%$. However, although no breaks in the curves are present, some exhibit a behaviour that is not perfectly linear. This can also be seen from the evolution of the opt-to-opt efficiencies which are depicted in figure 7.6d. Points where additional LDs were switched on mark changes in the progression of the curve which leads to the conclusion that the alignment of the four beams was not perfect. Nevertheless, opt-to-opt efficiencies of up to $16\,\%$ were achieved for $T_{OC} = 3.7\,\%$. No thermal rollover can be seen for any of the four different output coupling rates.

Experiments were also carried out with the resonator set up for laser operation on the $^3P_0 \rightarrow {}^3H_6$ transition at a wavelength of $\lambda_L = 622.8\,\text{nm}$. In this case the high emission cross sections at 643.4 nm proved problematic. Since most available mirrors were optimized for the emission characteristics of Pr:YLF (cf. [Ric08]), mirrors with suitable transmission rates at 622.8 nm had unfavorable transmission rates for 643.4 nm. This often lead to undesired laser operation in the red spectral region on the $^3P_0 \rightarrow {}^3F_2$ transition. Only one set of mirrors allowed operation in the orange spectral range on the $^3P_0 \rightarrow {}^3H_6$ transition. However, the input coupling and folding mirror had the downside of non-negligible transmission rates for 622.8 nm. The combined output coupling rate of M1, M2, and M3 was determined to be $0.7\,\%$. Output coupling occurred through all three mirrors with two different outputs behind M2, where one was on axis with each arm of the resonator. Output powers were measured behind M3 and on the output behind M2 which was not collinear with B2. Since all three mirrors had the same coating, these measurements allowed the extrapolation of the output that was colinear to either B1 and B2 and which could therefore not be measured directly. The maximum combined output power was 114 mW (cf. figure 7.6e). The slope efficiency and threshold pump power were $11\,\%$ and

[2] In this work, the optical-to-optical efficiency is defined as the ratio between the output power of the laser and the pump power inciding on the front facet of the crystal.

192 mW, respectively. An opt-to-opt efficiency of 3.2 % was achieved (cf. figure 7.6f). It seems very likely that these results could be substantially improved with more suitable cavity mirrors and by employing a higher output coupling rate.

With the resonator set up for operation on the $^3P_1 \rightarrow {}^3H_5$ transition it was also possible to demonstrate laser operation in the green spectral region. All mirrors in this experiment were highly reflective ($T_{OC} < 0.1\,\%$) for the wavelength region where laser operation was expected. However, the available pump power was only sufficient to marginally exceed the laser threshold. It was therefore not possible to record input-output curves or to further characterize the laser.

In addition to the laser characteristics, the beam qualities of the lasers operating at 724.9 nm, 643.4 nm, and 622.8 nm were determined by collimating the beam behind M3 and analyzing it with a *Spiricon* M200s. The measurements were carried out at the respective maximum output power. The recorded caustics are depicted in figure 7.7. It can be seen that the beams of all three laser had M^2 values between 1.3 and 1.5. The beam profiles were circular or slightly elliptic with gaussian intensity profiles.

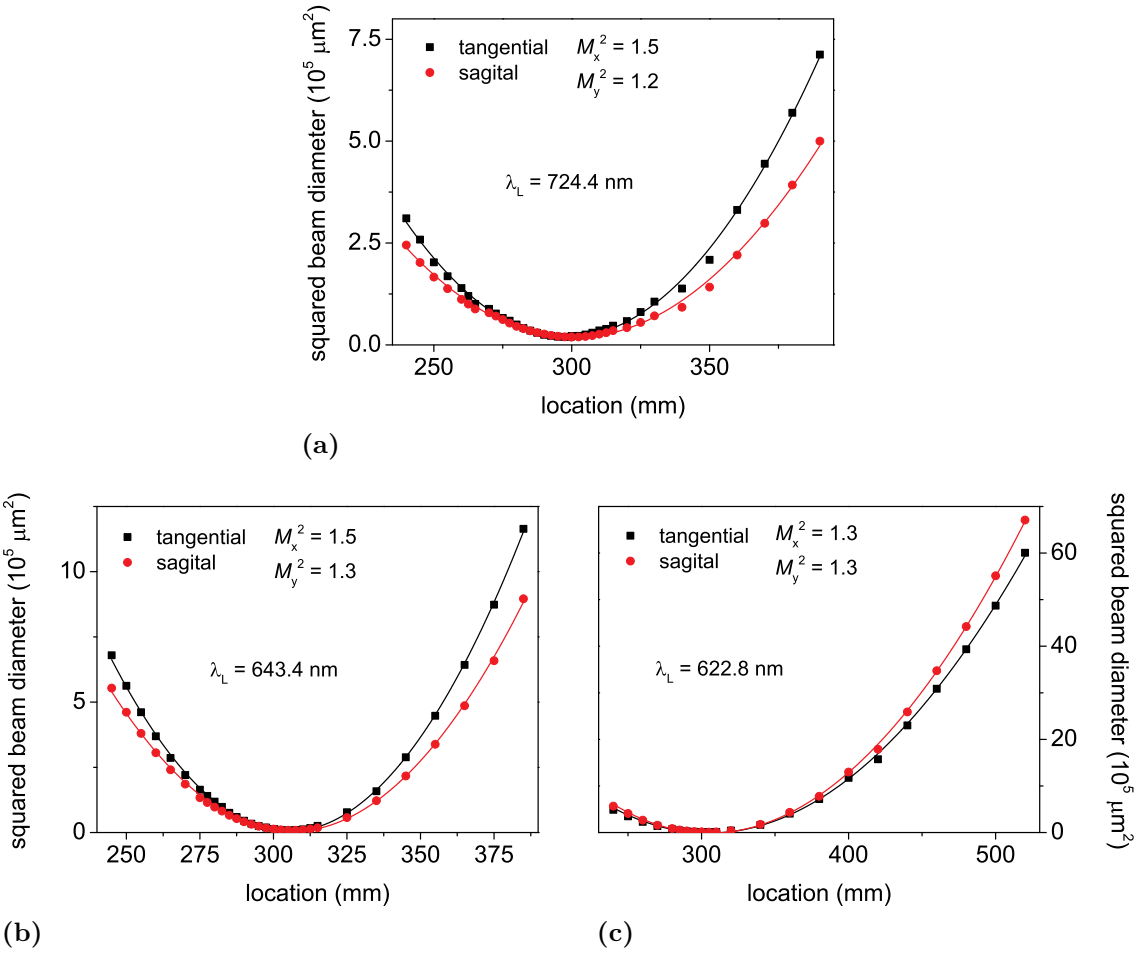

Figure 7.7: Caustics of diode pumped Pr,Mg:SRA lasers at (a) $\lambda_L = 724.4$ nm, (b) $\lambda_L = 643.4$ nm, and (c) $\lambda_L = 622.8$ nm.

λ_L (nm)	P_{out} (mW)	P_{thr} (mW)	η_{sl} (%)	η_{opt} (%)	η_{St} (%)	T_{OC} (%)	M_x^2	M_y^2
724.4	564	120	50	17	61.4	2.8	1.5	1.2
643.6	548	180	44	16	69.1	3.7	1.5	1.3
622.8	114	192	11	3.2	71.3	0.7	1.3	1.3

Table 7.1: Laser characteristics of InGaN LD pumped Pr,Mg:$SrAl_{12}O_{19}$ lasers. Note that P_{out} for $\lambda_L = 643.6\,nm$ was obtained with $T_{OC} = 5.7\,\%$, all other values with $T_{OC} = 3.6\,\%$.

In order to estimate the maximum resonator internal losses at the various laser wavelengths equation 2.29 was employed. The resulting values are $\gamma_i = 0.3\,\%$, $0.6\,\%$, and $1.9\,\%$ for $\lambda_L = 724.4\,nm$, $643.4\,nm$, and $622.8\,nm$, respectively. The value in the orange spectral region can only be regarded as an estimate since only a single output coupling rate was available. Higher output coupling rates are likely to improve the slope efficiency significantly and thus lead to lower values of γ_i.

These results represent an improvement to prior results obtained with diode pumped Pr,Mg:SRA [Fec11]. They show the excellent scalability of the system and that even towards higher pump powers no thermal problems occur. However, several problems arise from using InGaN LDs as pump source. Due to the beam quality of the LDs and the length of the laser samples, the overlap between pump and laser mode will be far from optimal. A certain part of the pump power will therefore not be available for the laser process. Employing shorter laser crystals might to some degree circumvent this problem. In turn this would lead to a lower over all absorption of the pump radiation and thus the optical-to-optical efficiency would decrease.

2ωOPSL Pumped Bulk Lasers

Laser experiments with the 2.7 at% doped sample were also carried out by employing the Genesis CX 2ωOPSL as pump source. This device has the advantage of a better beam quality compared to the LDs and the pump radiation is, due to the emission wavelength of 486.2 nm, also absorbed more efficiently by Pr,Mg:$SrAl_{12}O_{19}$ (cf. figure 6.6, table 6.2). This pump wavelength also leads to higher Stokes factors and therefore to an increase of the maximum possible slope efficiencies. Furthermore the maximum output power is 4 W. The incident pump power is therefore the same as with four LDs. However, since the pump power is contained in a single beam, the complexity of the pump scheme is reduced and the setup is less prone for misalignment. The basic resonator geometry was the same as for the experiments with InGaN LDs (cf. figure 7.4). The beam emitted by the 2ωOPSL corresponds to B1. Preliminary experiments showed that due to the good beam quality of the pump laser reflections occuring on the input coupling facet of the crystal had the potential to be collimated by the lens L1 and to enter and destabilize the 2ωOPSL. In order to prevent power fluctuations and possible damage of the Genesis CX, the beam was put through an optical isolator placed between the output window of the

laser head and the focusing lens. As in the previous experiments, the crystal was cooled to a temperature of 6 °C.

Since all parameters of the beam emitted by the 2ωOPSL were known (cf. [COH13b]), it was possible to simulate the overlap between pump and laser mode in dependence of the focussing lens. This lead to the conclusion that a lens with $f = 100\,\mathrm{mm}$ results in an optimal overlap which was confirmed by preliminary experiments.

Laser experiments were then carried out with the resonator set up for operation at wavelengths of $\lambda_L = 724.4\,\mathrm{nm}$, $\lambda_L = 643.4\,\mathrm{nm}$, $\lambda_L = 622.8\,\mathrm{nm}$, and $\lambda_L = 525.3\,\mathrm{nm}$. For each wavelength mirrors which were anti-reflective coated for the pump wavelength and high reflective coated for the laser wavelength were available as M1 and M2. As output coupler M3 various mirrors with different output coupling rates could be employed with the exception of $\lambda_L = 622.8\,\mathrm{nm}$ were only a mirror with $T_{OC} = 7.5\,\%$ was available. Figure 7.8a depicts the optimal input-output curves for each wavelength. Slope efficiencies of 59 % ($T_{OC} = 7.6\,\%$), 59 % ($T_{OC} = 3.6\,\%$), 44 % ($T_{OC} = 7.5\,\%$), and 13 % ($T_{OC} = 1.3\,\%$) have been obtained for the laser operating at wavelengths of $\lambda_L = 724.4\,\mathrm{nm}$, 643.4 nm, 622.8 nm, and 525.3 nm, respectively. The corresponding output powers were 1174 mW, 1182 mW, 830 mW, and 188 mW while the threshold pump powers were 340 mW, 331 mW, 394 mW, and 1168 mW, respectively. It should be noted that experiments in the green spectral region were carried out with the 3.6 at% doped sample. This was due to the high threshold of the laser and the stronger absorption of the pump light in this sample. The improvement of the laser characteristics compared to the results obtained by LD pumping can be attributed to the much better beam quality of the 2ωOPSL which leads to an improved overlap between laser and pump mode throughout the whole length of the crystal. It follows that a higher percentage of the absorbed pump power is available for the laser process. This in part might explain why it was possible to obtain stable laser operation in the green spectral region at an absorbed pump power which was also available with the previously introduced LD pumped setup. The respective optical-to-optical efficiencies

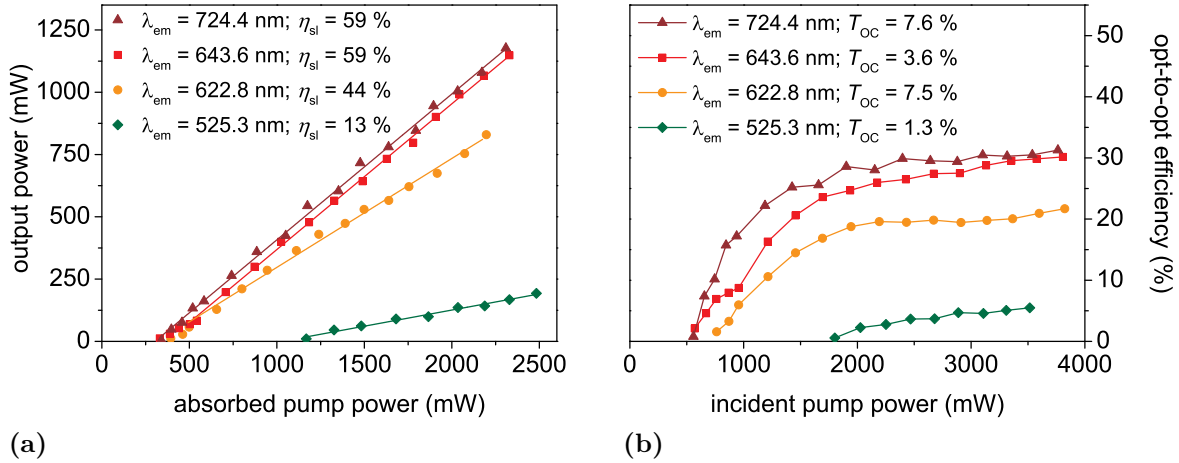

Figure 7.8: Characteristics of Pr,Mg:$SrAl_{12}O_{19}$ lasers pumped by a 2ωOPSL. (a) shows the obtained input-output curves while (b) depicts the corresponding optical-to-optical efficiencies. Lasers in the deep red, red, and orange spectral region were realized with the 2.7 at% doped sample while for the green emitting laser the 3.6 at% doped crystal was used.

are shown in figure 7.8b. Maximum values of 31 % ($\lambda_L = 724.4\,nm$), 30 % ($\lambda_L = 643.6\,nm$), 22 % ($\lambda_L = 622.8\,nm$), and 6 % ($\lambda_L = 525.3\,nm$) have been obtained. None of the curves shows any sign of a thermal rollover. A *Spiricon* M200s was used to analyze the beam quality of lasers operating with optimum parameters. The recorded caustics yielded M^2 values between 1.1 and 1.4. All obtained laser parameters are listed in table 7.2.

However, while the lasers operating in the deep red and red region exhibit slope efficiencies which are quite close to the optimum values as defined by the Stokes factor, this can not be said for the laser operating in the green. While the higher threshold can be attributed to the much smaller peak emission cross section for the $^3P_1 \rightarrow {}^3H_5$ transition in the green spectral region [Fec12] this should have no effect on the slope efficiency. ESA transitions which could explain this effect have been ruled out by the spectroscopic investigations (cf. section 6.2.5). These experiments showed furthermore no indication for other detrimental effects for example the formation of color centers. A point that remains is the optical quality of the laser samples. Fechner reported inclusions of secondary phases in $SrAl_{12}O_{19}$ crystals which are a result of the non-stoichiometric melt composition [Fec12]. Although the laser samples had no observable inclusions it is possible that microscopic precipitate was present which then caused Rayleigh scattering. Depending on the size of the inclusions it is possible that the longer laser wavelengths are less affected by this than shorter ones. Rearranging equation 2.28 for η_{sl} shows that this could decrease the slope efficiency. Further investigations of the scattering in Pr,Mg:$SrAl_{12}O_{19}$ crystals will be necessary to clarify whether or not this is the main factor or if additional effects occur.

In order to compare the crystals grown at the ILP against those of other sources, a *c*-cut sample with a length of 5.9 mm and doping concentration of 2.7 at% was prepared from the boule provided by the IKZ Berlin (cf. section 4.3.1). It was set in a copper heat sink and cooled to 6 °C. The resonator which was already used for the aforementioned experiments was set up for operation at $\lambda_L = 643.6\,nm$ on the $^3P_0 \rightarrow {}^3F_2$ transition with an ouput coupling rate of $T_{OC} = 5.9\,\%$ to allow a comparison with previous results.

The obtained input-ouput curve is depicted in figure 7.9a. Although it was possible to increase P_{out} to 1355 mW the corresponding slope efficiency was only 47 % and therefore considerably lower than in the experiments with the crystals grown at the ILP. During the experiments it became apparent that this behaviour can most likely be attributed to

λ_L (nm)	P_{out} (mW)	P_{thr} (mW)	η_{sl} (%)	η_{opt} (%)	η_{St} (%)	T_{OC} (%)	M_x^2	M_y^2
724.4	1174	340	59	30	67.1	1.3	1.2	1.1
643.6	1182	331	59	31	75.6	7.5	1.2	1.2
622.8	830	394	44	22	78.1	3.6	1.3	1.4
525.3	188	1168	13	6	92.4	7.6	1.2	1.3

Table 7.2: Characteristics of 2ωOPSL pumped Pr,Mg:$SrAl_{12}O_{19}$ lasers. Lasers in the deep red, red, and orange spectral region were realized with the 2.7 at% doped sample while for the green emitting laser the 3.6 at% doped crystal was used. Note that P_{out} for $\lambda_L = 643.6\,nm$ was obtained with $T_{OC} = 5.7\,\%$, all other values with $T_{OC} = 3.6\,\%$.

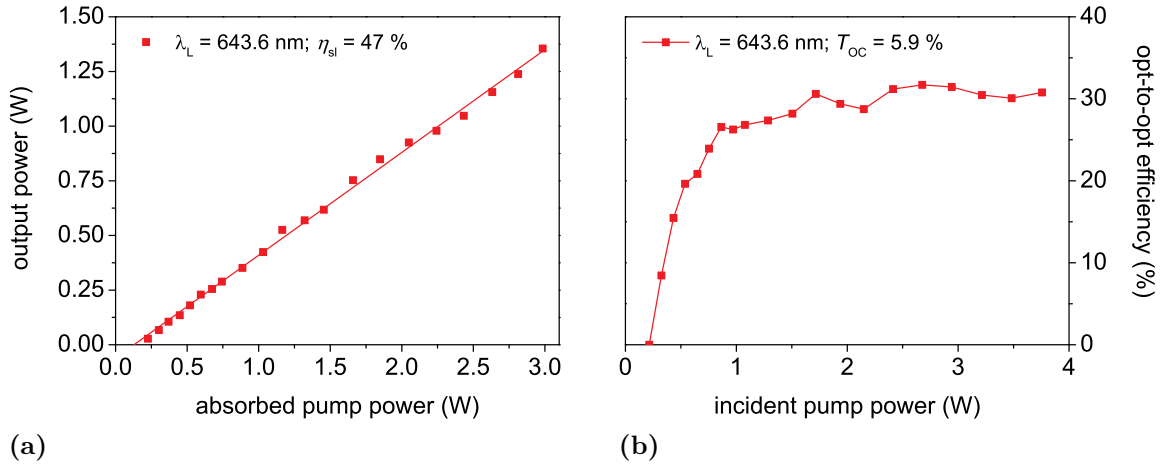

Figure 7.9: Laser characteristics obtained with a sample of the Pr,Mg:SRA crystal provided by the IKZ Berlin. (a) shows the obtained input-output curves while (b) depictes the corresponding optical-to-optical efficiencies.

the optical quality of the sample. Laser operation could only be achieved in certain areas of the sample and would often switch off when it was translated. This indicates that the crystal is inhomogenous. This was further indicated by a strongly asymmetric laser mode and by the fact that the pump beam exhibited a diffraction pattern after passing the sample. Therefore, microsope images of the sample were taken in bright field and phase contrast mode and are depicted in figure 7.10a and 7.10b. In both images a diagonal pattern can be seen throughout the sample. The presence of the pattern in the phase contrast image shows that it can be linked to the formation of areas with varying refractive indices. Taking the orientation of the sample (*c*-axis perpendicular to the image plane) and the observed preferred growth behaviour (perpendicular to the *c*-axis) into account, it seems likely that the difference in refractive index was caused by an inhomogenous growth process at the liquid-crystal interface region. However, it can not be said whether this is present throughout the whole crystal or if it is a localized effect. Further experiments with samples from different parts of the boule have to be performed to clarify this point. Still, the fact that these results were obtained even with such an inhomogeneous sample

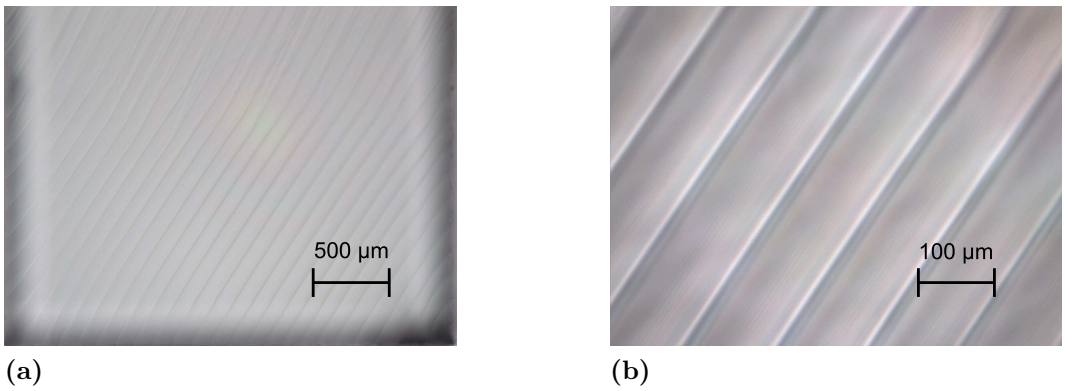

Figure 7.10: Microscopy images of the laser sample prepared from the Pr,Mg:$SrAl_{12}O_{19}$ boule grown at the IKZ Berlin. Pictures were taken in (a) bright field (b) phase contrast mode.

indicates that the laser parameters might be further improved with a homogeneous sample from this boule.

Thin Disk Lasers

Preliminary laser experiments in a thin disk geometry were conducted in cooperation with the Institut für Strahlwerkzeuge (IFSW) in Stuttgart, Germany. The basic concept of the thin disk laser (TDL) was introduced in 1994 by Giesen *et al.* [Gie94]. In this setup the gain medium is a thin disk typically with a thickness of some several hundred micrometer. Due to the thickness of the disk, a multi-pass pump scheme is necessary to achieve a sufficient absorption of the pump radiation. This is achieved by a combination of a parabolic mirror (PM) and several deflection prisms (DF) as depicted in figure 7.11. The beam, which is often delivered by an optical fiber is collimated by an input coupling unit and incides on the parabolic mirror which is highly reflective for the pump radiation. The PM reflects and focuses the beam onto the gain medium. The facet F2 which is facing the PM is dielectrically coated and anti relective for the pump and laser wavelength. The back side F1 of the disk is highly reflective for both wavelengths. The pump beam passes the gain medium and is reflected at F1. It diverges, passes the medium a second time, and is again reflected by the PM which then collimates the beam. In the next step a pair of prisms deflects the beam back onto the parabolic mirror thus enabling the next pass of the pump radiation through the gain medium. Nowadays, commercially available thin disk modules usually allow 16 - 32 passes of the pump beam through the disk. The laser cavity in this setup consists of the back facet F1 of the disk and an end mirror placed behind a hole in the center of the parabolic mirror. Resonator geometries in which F1 acts as a folding mirror are also possible. This type of cavity is often employed to achieve a higher gain via multiple passes of the laser mode through the active medium.

The basic concept of the thin disk laser has several advantages over conventional bulk setups. The thin gain medium allows an efficient cooling with temperature gradients parallel to the resonator axis. Thus thermal lensing which in bulk gain media is caused by radial temperature gradients is much less severe. Power scaling in such a setup can be achieved by increasing the diameter of the pump spot and keeping the power density in the gain medium constant.

For these experiments *c*-cut Pr,Mg:SRA disks with a thickness of 300 µm and diameter 6 mm were prepared from the 3.6 at% doped boule (cf. section 4.3.1). The higher dopant concentration was chosen to achieve a higher absorption of the pump radiation. Both facets of the disks were dielectrically coated. The disks were then contact bonded to copper heat sinks with F1 facing towards the heat sink. Microsope images of several disks showed a grating structure similar to that depicted in figure 7.10. This indicates that the Pr,Mg:SRA crystals grown at the ILP also suffer, at least partially, from the same inhomogeneous growth behaviour as the crystal grown at the IKZ. The pump beam was delivered by 24 InGaN LDs with a central emission wavelength of 444 nm which were coupled into a fiber with a core diameter of $d_{\mathrm{core}} = 200\,\mu\mathrm{m}$ and a numerical aprterture of $NA = 0.2$. The maximum output power behind the fiber was 17 W. The beam was collimated using an $f = 60\,\mathrm{mm}$ achromatic lens. The pump module was equipped with a parabolic mirror with a focal length of $f = 32.5\,\mathrm{mm}$ which was HR coated for the pump

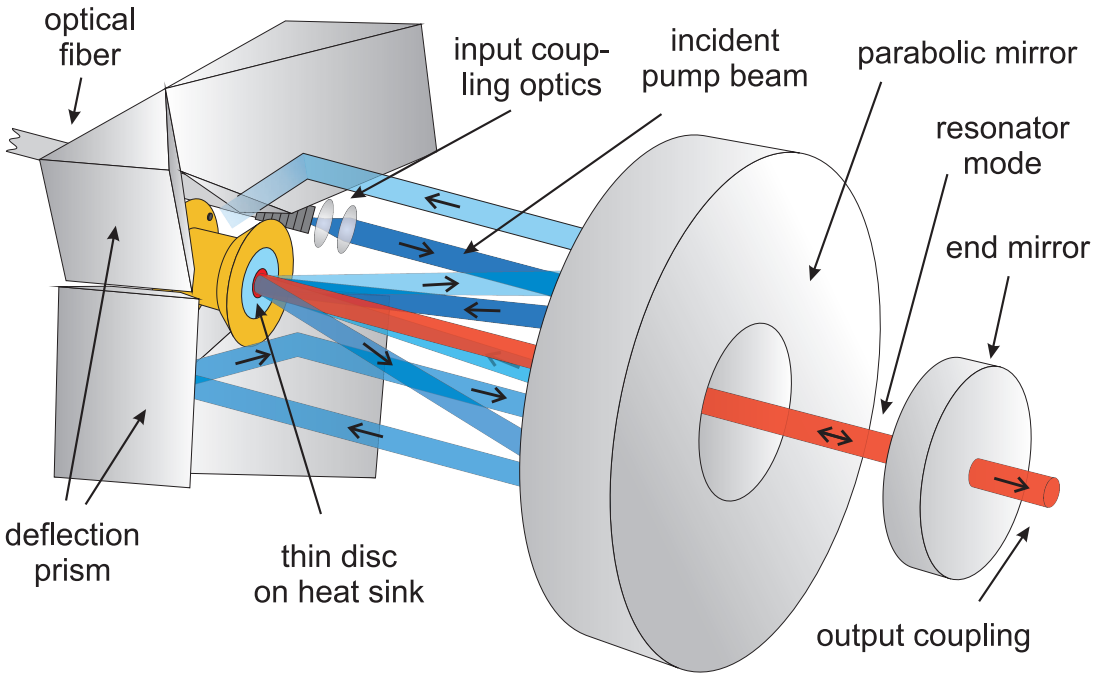

Figure 7.11: Schematic of the thin disk laser setup [Krä08].

wavelength. Different telescopes could be used for adjusting the beam diameter prior to the first reflection of the pump beam on the parabolic mirror. These allowed spot sizes of $d_{\mathrm{spot}} = 0.7\,\mathrm{mm}$, $1.1\,\mathrm{mm}$, $1.2\,\mathrm{mm}$, and $1.3\,\mathrm{mm}$ on the disk. The module allowed 24 passes of the pump light through the disk which could be doubled to 48 by inserting a prism which radially displaced the pump beam. Preliminary measurements in fluorescence mode showed that for 48 passes approximately 60 % of the incident pump radiation is absorbed by the disk. The resonator was hemispherical and consisted of the facet F1 of the disk and a concave end mirror M1 with a radius of curvature of $r_{\mathrm{OC}} = 100\,\mathrm{mm}$. Mirrors with different output coupling rates were available as M1.

With this setup it was possible to demonstrate the first laser operation of a Pr^{3+}-doped gain medium in the TDL geometry. Laser emission was realized on the transition $^3P_0 \rightarrow {}^3H_4$ at a wavelength of 643.6 nm. Priliminary experiments showed that larger pump spot diameters were benificial for laser operation with best results for $d_{\mathrm{spot}} = 1.3\,\mathrm{mm}$. With this parameter experiments with different output coupling rates were conducted. The resulting input-output curves are depicted in figure 7.12a and the corresponding laser parameters can be found in table 7.3. It can be seen that the highest output power of 785 mW was obtained with an output coupling rate of $T_{\mathrm{OC}} = 0.1\,\%$. The corresponding slope efficiency was 10 %. It has to be noted that due to the pump geometry it was not possible to determine the exact amount of the absorbed pump power during laser operation. The slope efficiency is therefore given with respect to the incident pump power. The optical-to-optical efficiencies are depicted in figure 7.12b and show a maximum value of $\eta_{\mathrm{opt}} = 8\,\%$. Furthermore it becomes apparent that for all employed output coupling rates a pronounced rollover is present which can likely be linked to thermal issues caused by the low conversion of absorbed power into laser power. Therefore experiments were carried out in a quasi cw mode with a repetition rate of 25 Hz and various duty cycles. The resonator

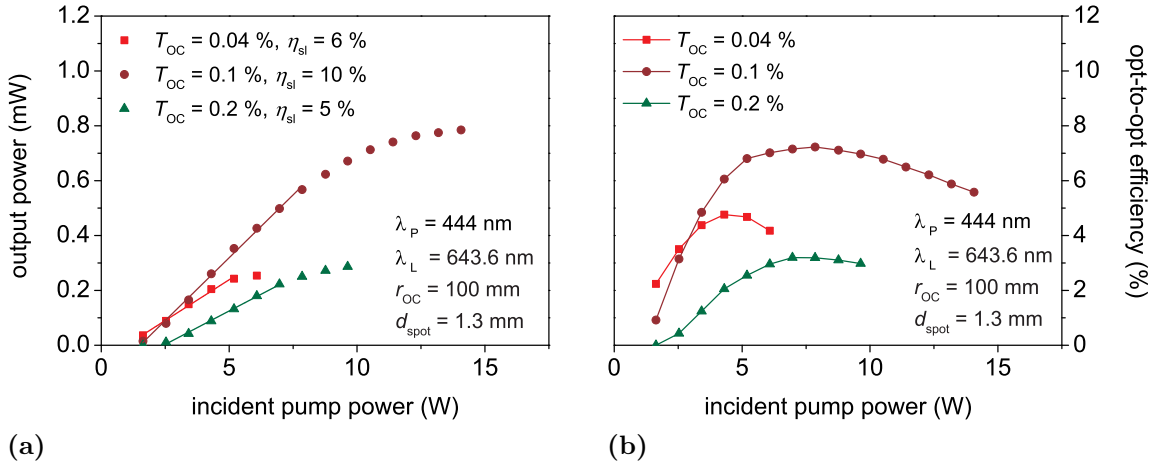

Figure 7.12: Characteristics of Pr,Mg:$SrAl_{12}O_{19}$ thin disk lasers for different output coupling rates. (a) shows the obtained input-output curves while (b) depictes the corresponding optical-to-optical efficiencies.

setup was not changed and the output coupling rate was again $T_{OC} = 0.1\,\%$. The spot size was slightly decreased to $d_{spot} = 1.2\,\text{mm}$. The obtained input-output characteristics are depicted in figure 7.13a. All power values given in the graph were extrapolated for a duty cycle of 100 %. As it can be seen in figure 7.13a, the performance of the laser increases for smaller duty cycles. The highest output power of 1.67 W and slope efficiency of 16 % was obtained with a duty cycle of 10 %. The corresponding input-output curve shows no indication of a rollover. The same is true for the curve of the optical-to-optical efficiency which is depicted in figure 7.13b. Only the curve for a duty cycle of 100 % shows a decrease towards maximum pump power which is consistent with the previous results. However, the reason for the low efficiency remains unclear. From the experiments conducted with bulk gain media much higher values seem possible (cf. figure 7.6 and 7.8). Nevertheless it must be kept in mind that these were only preliminary results. Further experiments are necessary to optimize the parameters of the setup and the disks which

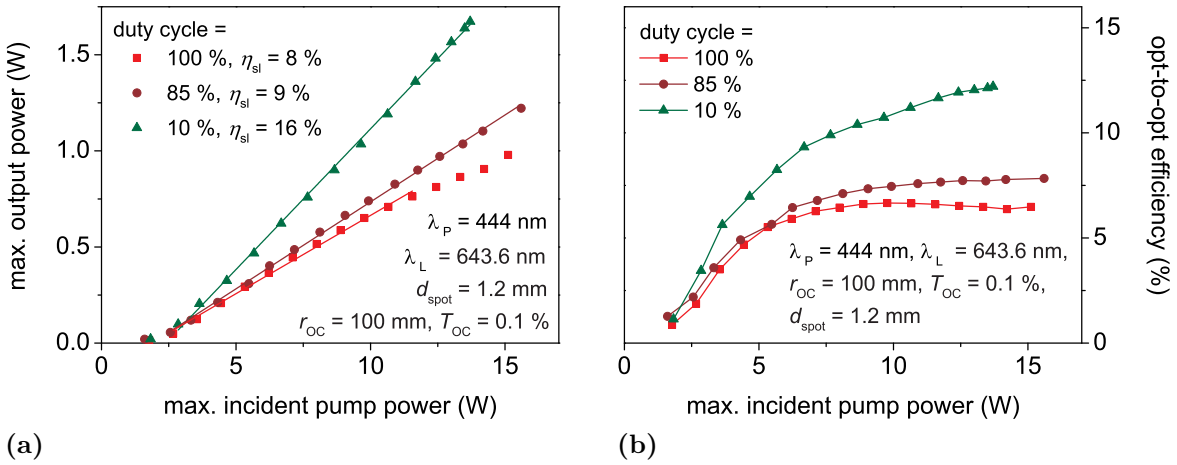

Figure 7.13: Characteristics of Pr,Mg:$SrAl_{12}O_{19}$ thin disk lasers for different duty cycles. (a) shows the obtained input-output curves while (b) depictes the corresponding optical-to-optical efficiencies. All power values given in the graph were extrapolated for a duty cycle of 100 %.

λ_L(nm)	P_{out} (W)	η_{sl} (%)	d_{spot} (mm)	T_{OC} (%)	mode
643.6	0.79	10	1.3	0.1	cw
	1.67	16	1.2		qcw

Table 7.3: Laser characteristics of Pr,Mg:SRA thin disk lasers.

then may allow to obtain higher output powers and efficiencies. Points which should be investigated are the effect of the striations in the disks as well as increased upconversion processes due to the high excitation density in the disk.

fs-Laser Written Waveguide Lasers

Laser experiments were carried out by employing the fabricated waveguides (cf. section 5). For these experiments the setup depicted in figure 7.14 was used. The resonator consisted of the mirrors M1 and M2 where the latter was directly coated onto the end facet of the crystal. M1 was holdered on a piezo element which allowed for the translation of the mirror along the resonator axis. This was necessary because M1, the input coupling facet of the crystal, and the air gap d_{gap} in between form a system with varying transmission [Hel10]. The piezo element thus allowed the transmission to be optimized by controlling d_{gap}. Since the main task was to demonstrate laser operation in the green spectral region, M2 was chosen to be highly reflective for 525 nm ($T_{OC} < 0.1\,\%$). To compensate for the much higher emission cross sections in the red and deep red region the corresponding transmission rates were as high as possible ($T_{OC,\,deep\,red} = 98\,\%$; $T_{OC,\,red} = 92\,\%$; $T_{OC,\,orange} = 88\,\%$; the complete spectrum can be found in appendix C). Therefore green laser emission will be coupled out through M1. However, since d_{gap} was adjusted during the measurements, it follows that the transmission rate through the system M1, d_{gap}, and input coupling facet also changes. Thus the output coupling rate for lasers operating on the $^3P_1 \rightarrow {}^3H_5$ transition in the green spectral region is not constant. Slope efficiencies for these lasers

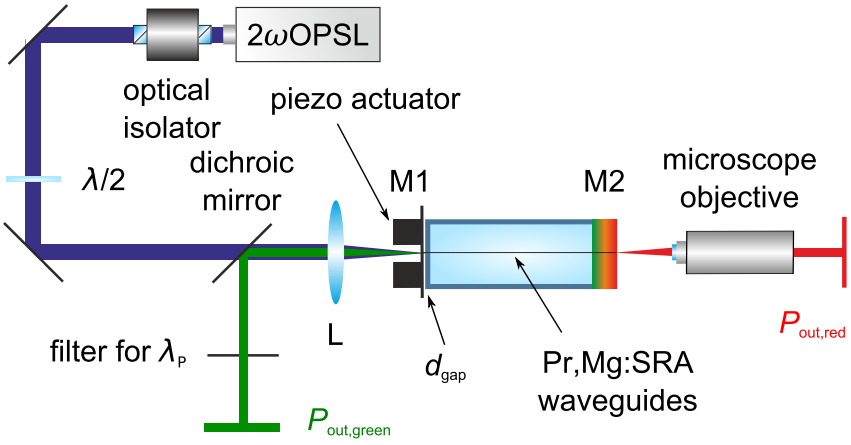

Figure 7.14: Schematic of the setup used for the waveguide laser experiments.

can therefore not be given. For emission in the deep red, red, and orange spectral region this does not pose a problem since suitable output coupling mirrors ensure that output coupling occurs only through M2. As in the previous 2ωOPSL pumped experiments, the pump beam which was delivered by the Genesis CX was put through an optical isolator in order to prevent damage or destabilization of the pump source due to collimated back reflection. A $\lambda/2$-waveplate behind the optical isolator allowed the polarization direction of the pump light to be adjusted in order to achieve an optimal match with the polarization direction guided within the waveguides. The beam was focussed onto the input coupling facet of the crystal by a lens L with $f = 40\,\mathrm{mm}$. This focal length was chosen based on the properties of the pump beam as well as on the obtained mode field diameters and divergences of the waveguides (cf. section 5.3) in order to achieve a good modematch between pump and waveguide mode. In front of L a dichroic splitter mirror which was HR for $\lambda_\mathrm{L} = 525.3\,\mathrm{nm}$ and AR for $\lambda_\mathrm{P} = 486.2\,\mathrm{nm}$ seperated laser and pump beam. Output occuring through M2 was imaged by a microscope objective ($50\times$, $NA = 0.5$). The crystal was holdered on an aluminum bridge without any active cooling.

By employing different mirrors as M1, this setup allowed stable laser operation at wavelengths of $\lambda_\mathrm{L} = 724.9\,\mathrm{nm}$, 644.0 nm, and 525.3 nm to be realized. In general it was possible to realize laser operation in the deep red and red spectral region with all waveguides independent of their writing parameters. Only two double track structures (DTSs) allowed laser operation in the green spectral region. The inscription parameters of the DTSs which yielded the best results are, together with various other parameters, listed in table 7.4. The input-output curves which were recorded for these waveguide lasers are depicted in figure 7.15a. Maximum output powers of 504 mW, 1065 mW, and 36 mW were obtained at laser wavelengths of 724.9 nm, 644.0 nm, and 525.3 nm. The corresponding slope efficiencies in the deep red and red spectral region are 25 % and 37 %, respectively. It should be noted that for these laser η_sl was determined with respect to the incident pump power. However, it can be assumed that due to the optimized input coupling and

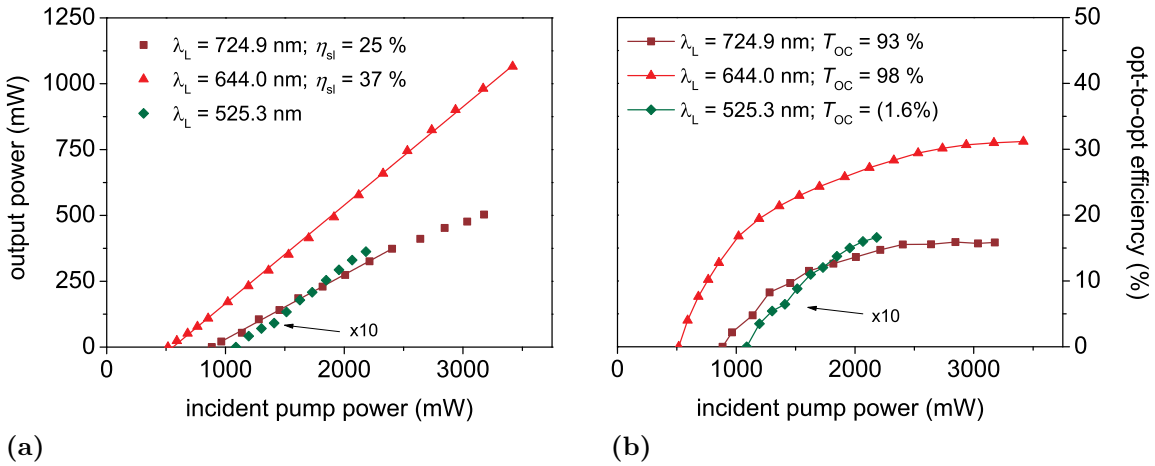

Figure 7.15: Characteristics of Pr,Mg:$SrAl_{12}O_{19}$ waveguide lasers. (a) shows the obtained input-output curves while (b) depicts the corresponding opt-to-opt efficiencies. Curves for $\lambda_\mathrm{L} = 525.3\,\mathrm{nm}$ were multiplied by a factor of 10 to allow a better comparability. Inscription parameters for DTSs yielding best results can be found in table 7.4.

λ_L (nm)	P_{out} (mW)	P_{thr} (mW)	η_{sl} (%)	η_{opt} (%)	T_{M1} (%)	T_{M2} (%)	M_x^2	M_y^2	Δx (µm)	E_{pulse} (µJ)
724.9	504	885	25	16	≤ 0.1	98	<1.1	<1.1	20	1.3
644.0	1065	516	37	31	≤ 0.1	92.5	<1.1	<1.1	22	1.5
525.3	36	1088	-	2	(1.6)	≤ 0.1	1.3	1.2	22	1.3

Table 7.4: Laser characteristics and mirror parameters of 2ωOPSL pumped Pr,Mg:$SrAl_{12}O_{19}$ waveguide lasers together with inscription parameters of the DTS yielding best results. The output coupling rate for $\lambda_L = 525.3\,nm$ varied from the nominal transmissivity of the mirror M1.

length of the crystal all incident pump power was absorbed and available for the laser process. The corresponding opt-to-opt efficiencies are shown in figure 7.15b. The highest obtained values were $\eta_{opt} = 16\,\%$ (deep red), 31 % (red), and 2 % (green). Despite the lack of active cooling, none of the curves exhibits a thermal rollover. For each transition the beam of the waveguide lasers yielding the highest output power was collimated with a lens and analyzed with the *Spiricon* M200s in order to determine the beam quality. All beams exhibited a circular beam and a gaussian intensity profile and a nearly diffraction limited beam quality (cf. table 7.4).

In addition to laser operation on a single wavelength, several waveguides exhibited simultaneous laser oscillation on two wavelengths where after several seconds the $^3P_0 \rightarrow {}^3F_2$ transition (red) often proved to be dominant. Furthermore it was possible to obtain laser emission at a wavelength of $\lambda_L = 622.8\,nm$. However, laser operation was not stable and switched to the red or deep red wavelength after a few seconds. It seems likely that this can be attributed to increasing reabsorption losses on the transition $^3H_4 \rightarrow {}^1D_2$ caused by a heating of the active region and subsequently a stronger Boltzmann population of higher laying Stark levels of the $^3H_4$ manifold.

Compared to the results reported by Calmano *et al.* these experiments present an improvement of the output power for the laser operating in the red spectral region by more than an order of magnitude [Cal12]. The optical-to-optical efficiency was increased by a factor of three. This can be attributed to several reasons. The 2ωOPSL which was employed in this work had a better beam quality than the InGaN LD employed by Calmano *et al.* This allowed the input coupling efficiency to be improved. Also the Genesis CX delivers a higher output power compared to the InGaN LD. In combination with the longer crystal and the higher absorption cross sections for $\lambda_P = 486.2\,nm$ this leads to a higher absorbed pump power. These experiments also present the first demonstration of green laser emission from Pr^{3+}-doped crystalline waveguides. The only other crystalline waveguide lasers with direct emission in the green spectral region demonstrated so far were realized by Moglia *et al.* in Er^{3+}:$LiLuF_4$ [Mog12]. Green emission from dielectric crystalline waveguides was also achieved by second harmonic generation in a Nd:YVO_4/KTP hybrid system [Don11b] or by employing the self frequency doubling effect in Nd:$YAl_3(BO_3)_4$ [Don11a].

7.2.3 Pr,Mg:$CaAl_{12}O_{19}$

For the laser experiments with Pr,Mg:$CaAl_{12}O_{19}$ a sample with a doping concentration of 6.6 at% was prepared. Due to the high number of cleaving planes of the boule (cf. 4.3.2) sufficiently long samples could only be prepared in *a*-cut. The resulting crystal had a length of 5.2 mm and contained several visible inclusions and defects. Due to the poor quality of the boule it was furthermore not possible to bring the sample into a shape that would fit into any of the available heat sinks. Therefore the crystal was not actively cooled during the laser experiments. As pump source the Genesis CX was chosen since the corresponding Stokes shifts for the various laser wavelengths are smaller than for InGaN LDs and therefore the subsequent heating of the crystal is likely to be less severe. The resonator design was the *V*-type cavity that was used in the previous experiments (cf. figure 7.4).

Laser operation was realized at wavelengths of $\lambda_L = 725.2$ nm and 644.3 nm for various output coupling rates. The obtained input-output curves are depicted in figure 7.16a and 7.16c, respectively. All laser parameters are also listed in table 7.5. Since the crystal was not cooled, the available pump power was often not fully exploited in order to prevent damaging the sample. Nevertheless it was possible to obtain maximum output powers of 354 mW and 321 mW in the deep red and red spectral region respectively. The corresponding slope efficiencies were as high as 25 % and 27 % with threshold pump powers of 151 mW and 289 mW. All lasers exhibited unstable operation especially towards higher pump powers which necessitated a constant readjustment of the cavity. This can likely be attributed to thermal effects in the crystal which is also indicated by the evolution of the optical-to-optical efficiencies. The corresponding curves are depicted in figure 7.16b (deep red) and 7.16d (red). Almost all curves show decreasing values of η_{opt} towards higher pump powers. Maximum optical-to-optical efficiencies for $\lambda_L = 725.3$ nm and 644.3 nm were as high as 16 % ($T_{OC} = 5.7$ %) and 17 % ($T_{OC} = 2.8$ %) respectively. The internal losses were determined via equation 2.29 to be $\gamma_i = 1.0$ % and 1.9 %. Due to the unstable laser operation it was not possible to analyze the beam quality of the lasers since the thermal drifting occurred on a timescale much shorter than the time required by the *Spiricon* M200s for a single measurement.

Despite the far from optimal optical quality of the laser crystal these results are in good agreement with those reported by Fechner for a similarly doped Pr,Mg:SRA crystal and under InGaN LD pumping [Fec12]. This means that it is likely that with a more suitable, i.e. lower dopant concentration and crystals of higher optical quality, Pr,Mg:CAlO should allow to obtain results comparable to those presented for Pr,Mg:SRA (cf. section 7.2.2, [Fec11, Cal11]).

7.2.4 Pr:$LaMgAl_{11}O_{19}$

For the laser experiments with Pr:$LaMgAl_{11}O_{19}$ several samples were prepared from the boule depicted in figure 4.7a. Since the composition was closer to the stoichiometry at the bottom than at the top (cf. table 4.1), two samples were prepared from this part. One sample had a length of 6.2 mm and was *a*-cut while the second one was 4.8 mm long and *c*-cut. According to the microprobe analysis both samples had a Pr^{3+} concentration of

1.8 at%. As resonator design a simple linear hemispherical cavity as depicted in figure 7.17 was set up. The beam of the Genesis CX ($\lambda_{em} = 487.6$ nm, cf. section 7.1.2) was focussed with a lens L with $f = 50$ mm through the input coupling mirror M1 into the laser crystal. M1 was dielectrically coated and AR for the pump wavelength and HR for the respective laser wavelength. The end mirror M2 was concave with $r_{OC} = 100$ mm. Various mirrors with different output coupling rates for each laser wavelength were available. This setup had the disadvange that the absorbed pump power could not be measured during laser operation. Therefore, measurements of the pump power before and behind the crystal were carried out without mirror M2 in place. In order to account for the constant inversion density above the laser threshold, the ratio of incident to absorbed pump power at this point was used to extrapolate the values for the remaining part of the respective curve. Since the Genesis CX is wavelength stable (cf. figure 7.2b) the spectral overlap between pump and absorption spectrum can be assumed to be constant.

First experiments showed that under cw pumping laser operation ceased after 10 min to 15 min. This effect reversed itself after 30 min without irradation with pump light. This is a strong indication for the presence of long living color centers. However, no

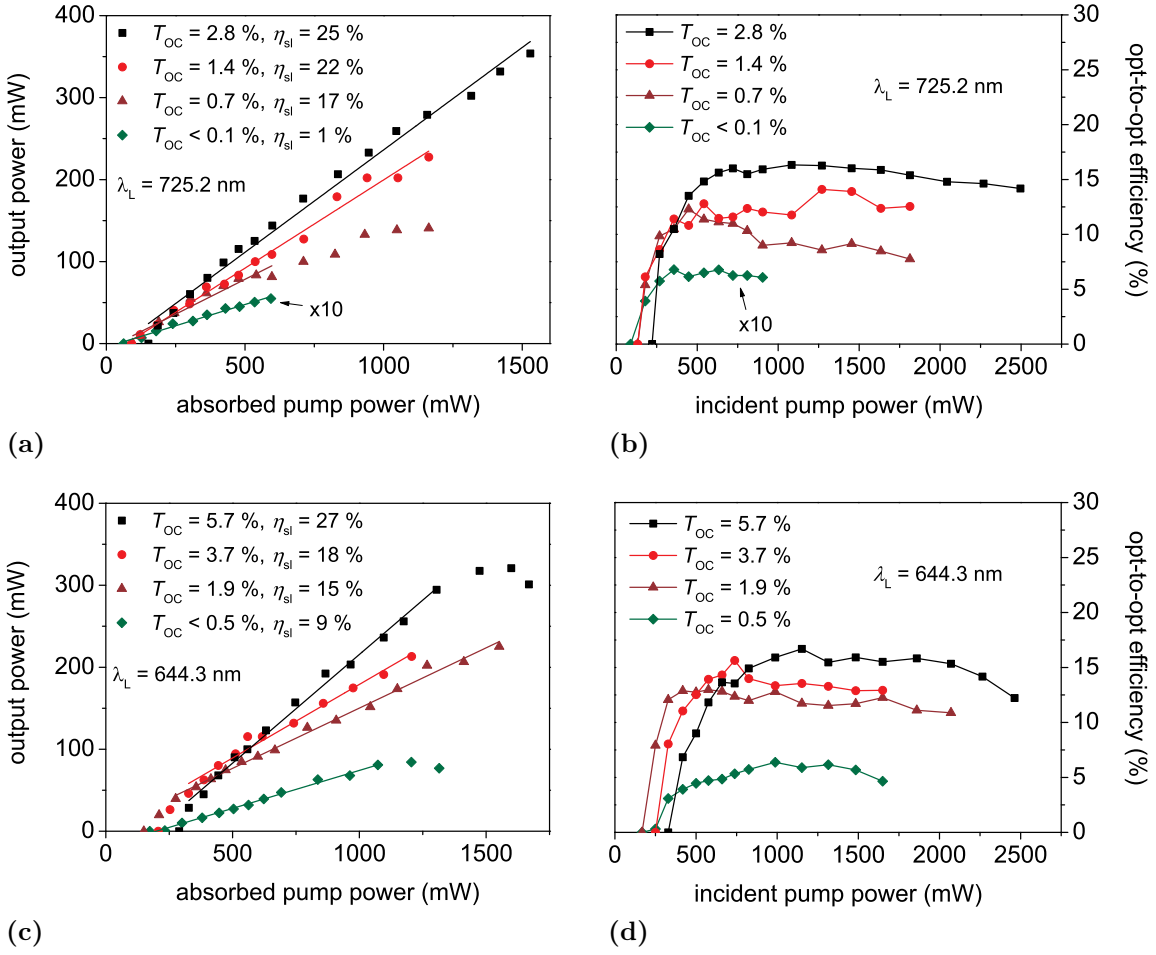

Figure 7.16: Input-output characteristics and optical-to-optical efficiencies of 2ωOPSL pumped Pr,Mg:CAlO lasers. (a,b) $\lambda_L = 725.2$ nm and (c,d) $\lambda_L = 644.3$ nm. Note that in (a) and (b) the curves for $T_{OC} < 0.1$ % are increased by a factor of 10.

λ_L (nm)	P_{out} (mW)	P_{thr} (mW)	η_{sl} (%)	η_{opt} (%)	η_{St} (%)	T_{OC} (%)
725.2	354	151	25	16	67.0	5.7
644.3	321	289	27	17	75.5	2.8

Table 7.5: Laser characteristics of 2ωOPSL pumped Pr,Mg:$CaAl_{12}O_{19}$ lasers.

change of the crystal color as it has been reported for example for Pr:LuAP [Fec09] could be observed. By inserting an optical chopper ($f_{rep} = 250$ Hz, duty cycle 1:2) it was possible to realize stable quasi cw operation at wavelengths of $\lambda_L = 729.1$ nm, 648.1 nm, and 620.4 nm for various output coupling rates. The recorded input-output curves are shown in figure 7.18a, 7.18c, and 7.18e. Maximum averaged output powers of 64 mW (deep red), 10.1 mW (red), and 2.9 mW (orange) have been obtained with slope efficiencies of 12 %, 4 %, and 2 %, respectively. Compared to the results obtained with the other Pr^{3+}-doped gain media, these values are quite poor. It can be seen from the graphs that towards higher pump powers the input-output curves recorded for $\lambda_L = 648.1$ and 620.1 nm do not follow a linear behaviour. The reason for this behaviour might be found in the abnormal absorption behaviour which becomes apparent by plotting the ratio of absorbed pump power against incident pump power in fluorescence mode. Without any additional effects the ratio should decrease towards higher pump powers and then saturate because of absorption bleaching. However, as it can be seen from figure 7.19 in Pr:LMA the absorption stays roughly constant at about 27.6 % and above a certain incident pump power, in this case 1 W, the absorption increases linearly to a maximum value of 37.5 %. It seems that above a certain pump intensity an additional absorption channel is created which increases linearly with the incident pump power. In combination with the fact that the laser switches off under cw pumping, this is another strong indication for the presence of color centers. Despite the poor slope efficiencies and low output powers, the beam quality of the lasers was good with values between M^2 =1.1 and 1.6. All laser parameters are listed in table 7.6.

In addition to the 2ωOPSL, InGaN LDs were also employed as pump source. Experiments were carried out with the *c*-cut sample in the *V*-type cavity (cf. figure 7.4).

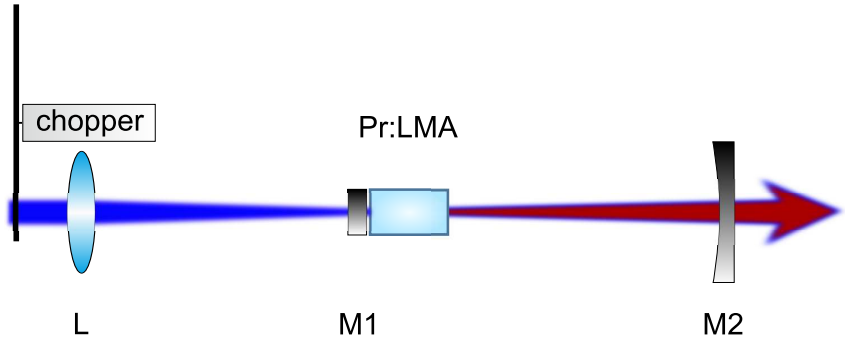

Figure 7.17: Schematic of the linear resonator design used for the laser experiments with Pr:LMA.

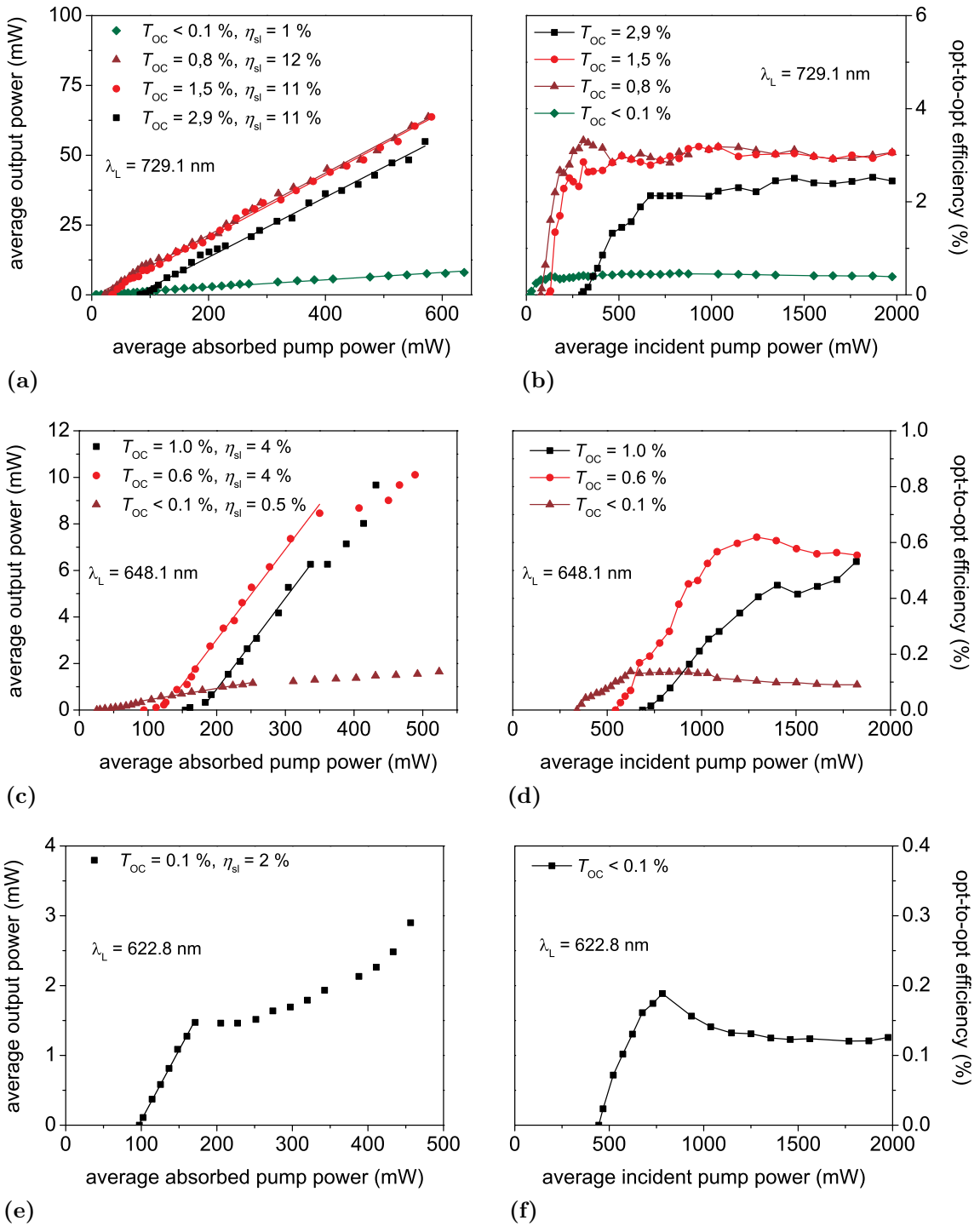

Figure 7.18: Input-output characteristics and optical-to-optical efficiencies of 2ωOPSL pumped Pr:LMA lasers. (a,b) $\lambda_L = 729.1\,\text{nm}$, (c,d) $\lambda_L = 648.1\,\text{nm}$, and (e,f) $\lambda_L = 620.4\,\text{nm}$.

λ_L (nm)	P_{out} (mW)	P_{thr} (mW)	η_{sl} (%)	η_{opt} (%)	T_{OC} (%)	M_x^2	M_y^2
729.1	64	22	12	3.3	0.8	1.6	1.5
648.1	10.1	94	4	0.6	0.6	<1.1	<1.1
620.4	2.9	97	2	0.2	0.1	1.1	1.1

Table 7.6: Laser characteristics and mirror parameters of 2ωOPSL pumped Pr:$LaMgAl_{11}O_{19}$ lasers.

Two InGaN LDs with central emission wavelengths of $\lambda_{em} = 443.8\,nm$ were coupled (B1) and focussed with a lens (L) with $f = 50\,mm$ into the crystal. Several experiments were conducted with the resonator set for different laser wavelengths and by employing various output coupling rates. However, despite the fact that the absorbed pump power exceeded the thresholds which were determined during the experiments under 2ωOPSL pumping, no laser operation could be obtained on any transition. This might be attributed to the shorter wavelength of the pump radiation delivered by the LDs and the correspondingly higher energy per pump photon. It might be possible that the abnormal absorption which can be seen in figure 7.19 increases towards shorter wavelengths and at $\lambda = 444\,nm$ has reached a value which prevents laser operation altogether. This fact in combination with the poor laser performance under 2ωOPSL pumping leads to the conclusion that unless the additional absorption channel can be suppressed, $LaMgAl_{11}O_{19}$ is not a suitable host system for Pr^{3+} and does not allow the realization of efficient solid state lasers in the visible spectral region.

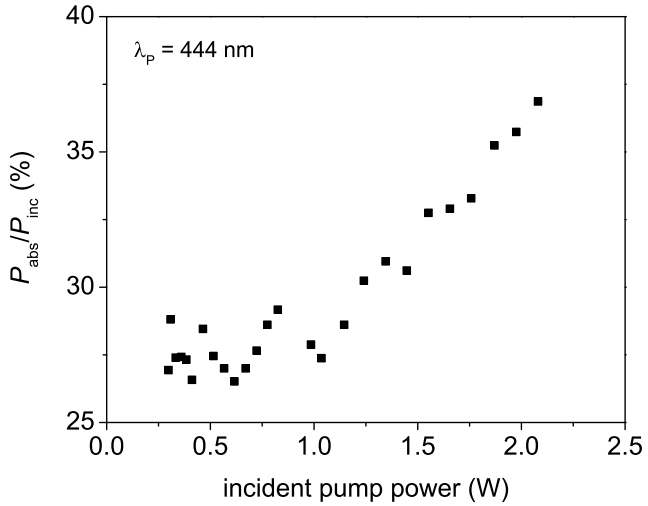

Figure 7.19: Ratio of absorbed pump power and incident power with respect to the incident power for Pr:LMA in fluorescence mode under InGaN LD pumping.

7.2.5 Pr:LaF_3

Laser operation of Pr:LaF_3 was first shown by Solomon and Mueller as early as 1963 [Sol63]. They demonstrated laser emission at a wavelength of $\lambda_L = 598.5\,\text{nm}$ on the transition $^3P_0 \rightarrow {}^3H_6$. The pump source for this experiment was a Xe-flash lamp and the crystal was cooled to 77 K. Recently, Grigoryan *et al.* have demonstrated laser operation at room temperature on several other transitions by pumping with a dye laser [Gri05].

For the laser experiments which were conducted with Pr:LaF_3 four *a*-cut crystals were prepared, one from each of the boules which contained only Pr^{3+} and an additional sample from the boule that was Pr^{3+},Eu^{3+}-doped. The crystals had lengths of 5.1 mm, 4.4 mm, 5.2 mm, and 5.6 mm and dopant concentrations of 0.3 at%, 0.4 at%, 0.8 at%, and 0.3 at%/0.6 at%, respectively[3].

Free Running Operation

Laser experiments in free running operation mode were carried out with a *V*-type cavity (cf. figure 7.4). Mirrors M1 and M2 were plane while M3 had a radius of curvature of $r_{OC} = 100\,\text{mm}$. As pump source the Genesis Taipan emitting at a wavelength of $\lambda_P = 479.1$ was employed. The first experiments dealt with the optimal focal length of L and also the optimal Pr^{3+}-doping concentration. The resonator was prepared for laser operation at 719.8 nm corresponding to the $^3P_0 \rightarrow {}^3F_4$ transition. The output coupling rate of M3 was chosen to be $T_{OC} = 0.9\,\%$. The input-output curves with the different lenses were recorded with the 0.3 at% doped crystal which was set in a copper heat sink and water cooled to 10 °C. Optimal results were obtained with a focal length of L of $f = 75\,\text{mm}$ (cf. figure 7.20a). With this lens input-output curves were also recorded for the 0.4 at% and 0.8 at% doped sample. For both experiments the maximum incident pump power was 1 W. The obtained curves are depicted in figure 7.20b. As it was the case for Pr,Mg:SRA the lowest doped sample exhibits the best results and was thus used for all subsequent laser experiments.

The resonator was then reset for laser operation on the various other transitions the Pr^{3+}-ion offers. Laser emission was achieved at wavelengths of $\lambda_L = 719.8\,\text{nm}$, 635.4 nm, 609.7 nm, and 537.1 nm and the recorded input-output curves are depicted in figure 7.21a. Maximum output powers of 498 mW, 63 mW, 139 mW, and 138 mW and slope efficiencies of 25 %, 15 %, 14 %, and 20 % were obtained, respectively (cf. table 7.7). The threshold pump powers were 38 mW, 142 mW, 120 mW, and 135 mW. It has to be noted that the maximum output power of the deep red laser was obtained with an output coupling rate of $T_{OC} = 0.6\,\%$ while the highest slope efficiency and the corresponding threshold were obtained with $T_{OC} = 0.9\,\%$. The slightly lower efficiency of the laser operating in the deep red spectral region compared to the earlier results can be attributed to the worse performance at higher absorbed pump powers. This effect can also be seen for the lasers operating in the red, orange, and green spectral region. Figure 7.21a shows that all lasers became unstable towards higher absorbed pump powers. This is also apparent from the rollover of the optical-to-optical efficiencies which are depicted in figure 7.21b. After

[3]The dopant concentrations were determined from absorption measurement. Since no absorption cross sections are known for Eu^{3+}:LaF_3 it was assumed that the ratio between Eu^{3+} and Pr^{3+} is in accordance to the melt composition.

reaching maxima of 14 % (deep red), 6 % (red), 5 % (orange), and 5 % (green) all values decline by up to one third. All laser parameters are listed in table 7.7.

It should be noted that with mirrors which were highly reflective in the wavelength region of 600 nm - 650 nm, laser operation was observed on up to six wavelengths simultaneously. These wavelengths could be mainly attributed to the transition $^3P_0 \rightarrow {}^3H_6$ but also to $^3P_0 \rightarrow {}^3F_2$ in the orange and red spectral region, respectively.

The comparatively low slope efficiencies and the decreasing optical-to-optical efficiencies can most likely be linked to a trapping of population in the multiplets $^3H_5$ and $^3H_6$ due to a comparatively low multi-phonon decay rate of these manifolds. In addition to this, thermal issues may arise from the low thermal conductivities of LaF_3 (cf. section 3.2.2). In order to achieve a more efficient depletion of the trapping manifolds, Eu^{3+} was added as a codopant. The idea is to achieve a cross-relaxation process and transfering excitation energy from the $^3H_6$ and $^3H_5$ manifolds of a Pr^{3+}-ion to the $^7F_5$ and $^7F_3$ manifolds of

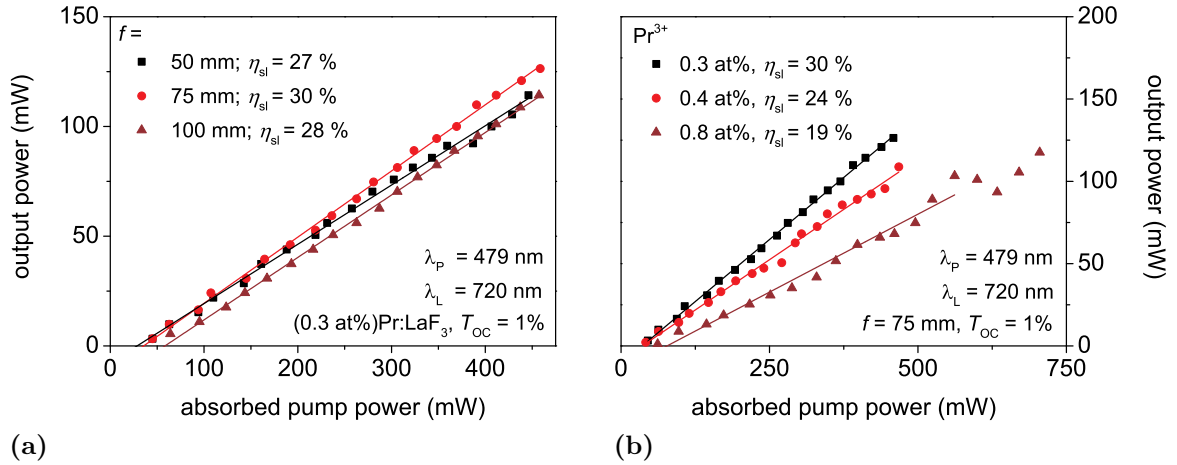

Figure 7.20: Comparison of laser performance of Pr:LaF_3 at $\lambda_L = 719.8$ nm under 2ωOPSL pumping. (a) for different focal lengths of L and (b) and different dopant concentration.

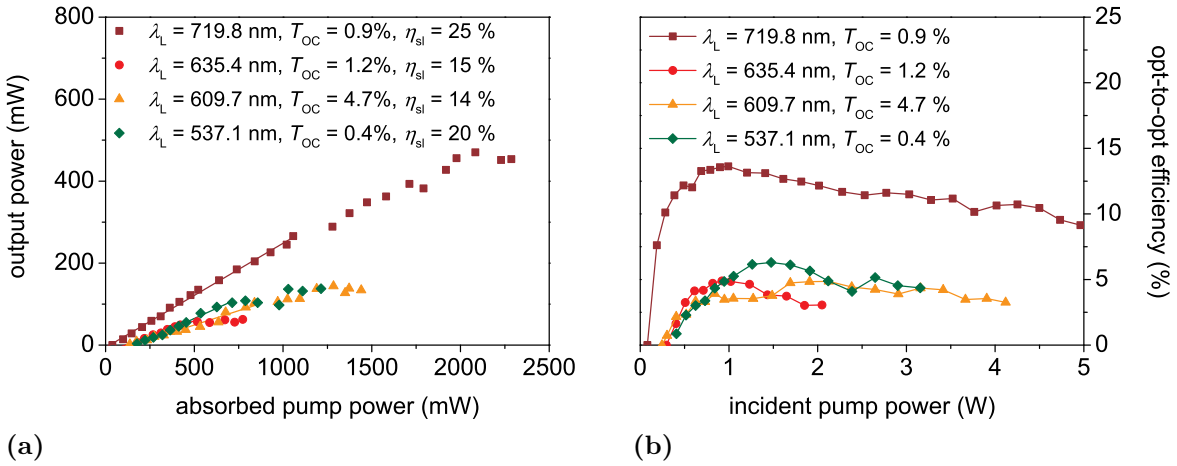

Figure 7.21: Characteristics of Pr:LaF_3 lasers pumped by a 2ωOPSL. (a) shows the obtained input-output curves while (b) depictes the corresponding optical-to-optical efficiencies.

λ_L (nm)	P_{out} (mW)	P_{thr} (mW)	η_{sl} (%)	η_{opt} (%)	η_{St} (%)	T_{OC} (%)	M_x^2	M_y^2
719.8	498	38	25	14	66.5	0.9	1.2	1.1
635.4	63	142	15	5	75.4	1.2	1.2	1.2
609.7	139	120	14	5	78.6	4.7	1.3	1.4
527.1	138	135	20	6	90.8	0.4	1.2	1.3

Table 7.7: Laser characteristics of 2ωOPSL pumped Pr:LaF_3 lasers. Note that P_{out} for $\lambda_L = 719.8\,nm$ was obtained with $T_{OC} = 0.6\,\%$, all other values with $T_{OC} = 0.9\,\%$.

an Eu^{3+}-ion, respectively (cf. figure 7.22). The closer spacing of the energy levels in the Eu^{3+}-ion should then allow a fast non-radiative decay into the ground state. However, since the energetic distance between the multiplets $^3P_0$ and the $^1D_2$ in praseodymium is comparable with the energetic distance between the multiplets $^7F_5$ and $^7F_0$ in Eu^{3+}, the codoping also bears the potential to depopulate the upper laser level by a similar process.

Laser experiments with the 5.6 mm long *a*-cut crystal were carried out in the *V*-type cavity set up for operation on the $^3P_0 \rightarrow {}^3F_4$ transition at $\lambda_L = 719.8\,nm$. In order to allow a comparison with the previously obtained results the output coupling rate was chosen to be $T_{OC} = 0.9\,\%$. The recorded input-ouput curve is depicted in figure 7.23a. The maximum output power that has been achieved was 177 mW with a slope efficiency of 22 % and an maximum optical-to-optical efficiency of 12 %. The threshold pump power was 55 mW (cf. figure 7.23b). These results are quite comparable with those obtained

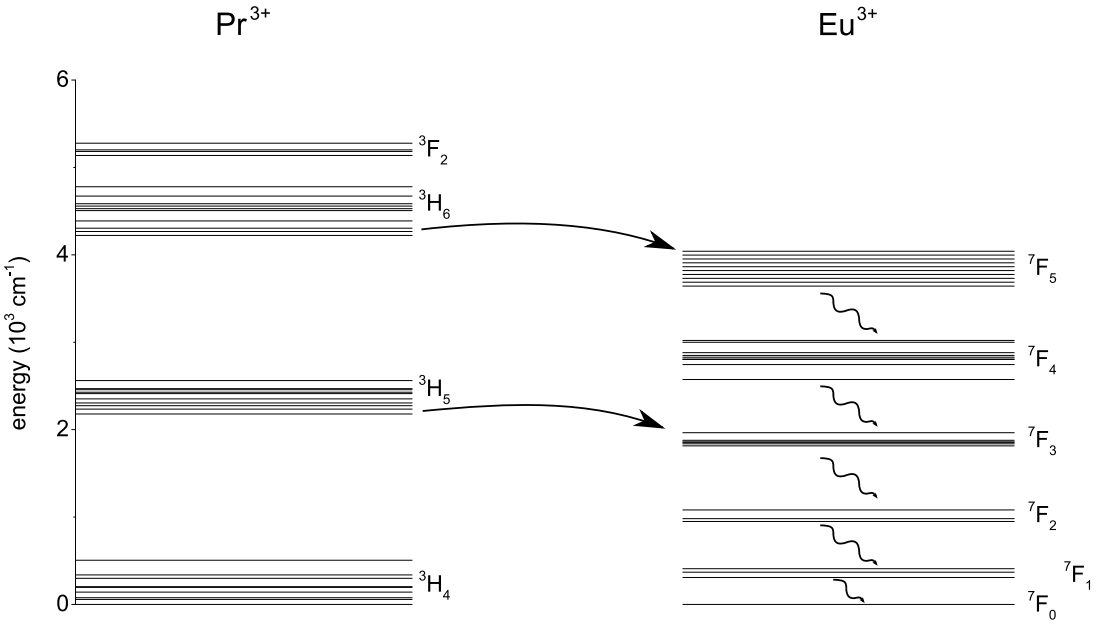

Figure 7.22: Schematic of the energy transfer process between a Pr^{3+} donor and an Eu^{3+} acceptor. Positions of the energy levels of Eu^{3+}:LaF_3 were taken from [Kum77]. Since only the energy range but no exact positions of the Stark levels of the $^7F_5$ are given, they were approximated as equidistantly spaced.

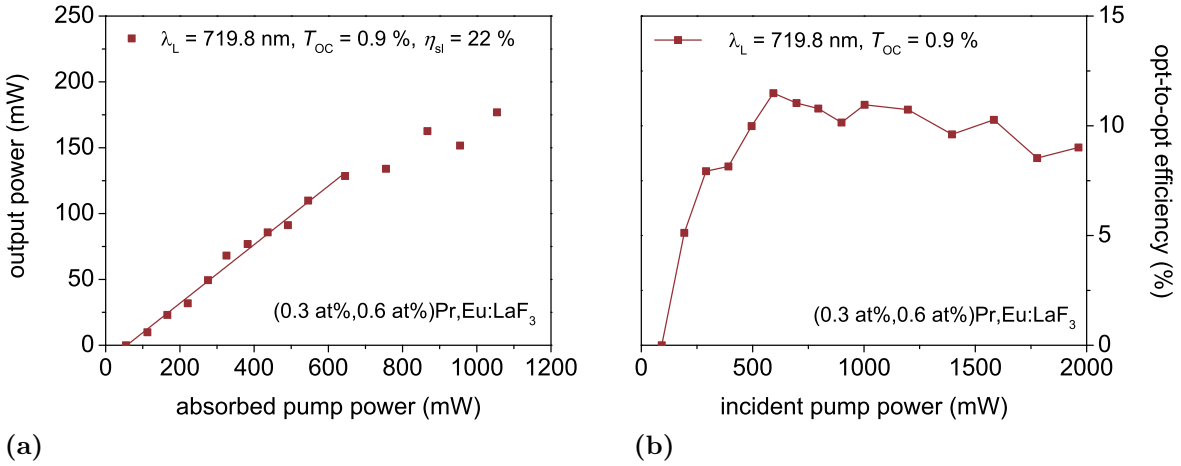

Figure 7.23: Laser performance of a 0.3 at%/0.6 at% doped Pr,Eu:LaF_3 under 2ωOPSL pumping. The laser operated at a wavelength of $\lambda_L = 719.8$ nm. (a) shows the obtained input-output curves while (b) depicts the optical-to-optical efficiencies.

with pure Pr:LaF_3. The slightly lower values of P_{out} and η_{sl} may be attributed to a worse crystal quality and/or polishing. The lack of improvement might be explained by the fact that the proposed cross relaxation processes are highly dependent on the interionic distance between donor and acceptor ion. Hence, if the Eu^{3+} dopant concentration is too low, the efficiency of the process will be poor. Increasing the Eu^{3+} concentration might therefore facilitate a higher efficiency of the involved cross relaxation processes and thus an improvement of the laser characteristics. However, this may also lead to a quenching of the ^3P_J manifold.

Tuning experiments

The broad emission band of Pr:LaF_3 in the orange spectral region corresponding to the $^3P_0 \rightarrow {}^3H_6$ transition makes this material interesting for the realization of tunable laser operation. In order to investigate the tuning range of the laser, a linear resonator as depicted in figure 7.17 was set up. As wavelength selection element a 2.5 mm thick birefringent filter made of quartz was inserted into the cavity under Brewster's angle. As pump source for these experiments an InGaN LD with a central emission wavelength of 442.0 nm was chosen. Compared to the Genesis Taipan the LD has the advantage that the LD-driver (*Thorlabs* ITC4005) allowed arbitrary durations ($\tau_{pump,\,min} = 100$ µs) and repetition rates of the pump interval ($f_{rep,\,min} = 0.2$ Hz) to be chosen and therefore to partially circumvent the thermal and population trapping issues which were observed in the cw pumped experiments. Due to the different beam parameters of the InGaN LD, as focussing element a lens with a focal length of $f = 50$ mm was chosen. Since the absorption cross sections at 442.0 nm are slightly lower than in the cyan spectral region, the Pr:LaF_3 sample with a dopant concentration of 0.4 at% and length of 4.9 mm was employed for these experiments. The emission wavelength of the laser was determined with an *Ocean Optics* HR2000+.

With this setup tunable laser operation was achieved in the wavelength region between 609.2 nm and 622.7 nm with an overall tuning range of 13.5 nm. Best results were achieved

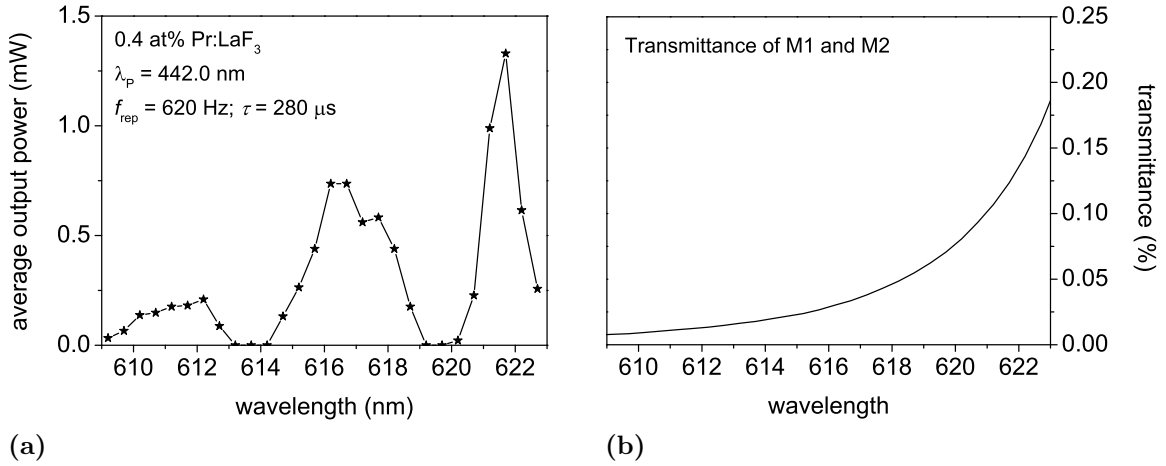

Figure 7.24: (a) Tuning curve obtained with InGaN LD pumped 0.4 at% doped Pr:LaF_3. (b) Transmittance of mirrors M1 and M2 in the tuning range.

for $\tau_{\mathrm{pump}} = 280\,\mu\mathrm{s}$ and $f_{\mathrm{rep}} = 620\,\mathrm{Hz}$. An exemplary tuning curve is depicted in figure 7.24a. It can be seen that except for two gaps in the region of 613.2 nm - 614.2 nm and 619.2 nm - 619.7 nm tuning was continuous. However, the tuning range was strongly dependent on the location of the laser mode on the birefringent filter. If other areas of the filter were used laser operation was also achieved in the region of the gaps but with an smaller overall tuning range. This indicates an inhomogeneity of this element. A filter of higher quality might therefore allow a continuous tunability and maybe a wider overall tuning range. The higher output powers towards longer wavelengths can be explained by the transmittance of the cavity mirrors (cf. figure 7.24b). The tuning bandwidth reported for Pr:$LiYF_4$ is quite comparable (604.6 - 622.0 nm, cf. [Han12]). However, it exhibits a higher number of gaps and therefore continuous tuning is possible in a much smaller wavelength range.

7.3 Lasers Based on Ho-Doped Materials

7.3.1 State of the Art in the Visible Spectral Region

Although it is long known that the Ho^{3+}-ion exhibits transitions corresponding to emission in the visible spectral region [Vor66, Mor75], very few publications deal with visible laser emission obtained with Ho^{3+}-doped gain media. The first realization of such a laser was reported as early as 1965 by Voron'ko *et al.* [Vor65]. In their experiments a Ho^{3+}:CaF_2 crystal cooled to 77 K was pumped by a Xe-lamp and pulsed laser operation was achieved at $\lambda_L = 551.2$ nm which corresponds to the $^5S_2 \rightarrow {}^5I_8$ transition. Johnson and Guggenheim reported pulsed laser oscillation on the same transition in Ho^{3+}:BaY_2F_8, also at cryogenic temperatures and under xenon flash lamp pumping [Joh71]. Podkolzina *et al.* demonstrated first laser operation on the $^5S_2 \rightarrow {}^5I_7$ transition with Ho^{3+}:$LiYF_4$. The crystal was cooled to 90 K and pumped by a Xe-flash lamp [Pod76]. The emission wavelength was $\lambda_L = 750$ nm. Shortly after Chiklis *et al.* reported the first laser oscillation at room temperature, again on the transition $^5S_2 \rightarrow {}^5I_7$ in Ho^{3+}:$LiYF_4$ under xenon flash lamp pumping [Chi77]. Room temperature laser operation was also reported for flash lamp pumped Ho:$YAlO_3$ by Kaminskii *et al.* [Kam86]. However, room temperature laser emission of a Ho^{3+}-doped crystalline medium in the green spectral region has so far not been reported.

7.3.2 Ho^{3+}:$LiLuF_4$

Laser experiments with Ho^{3+}:$LiLuF_4$ were carried out in a linear resonator of the type depicted in figure 7.17 with an end mirror M2 with a radius of curvature of $r_{OC} = 50$ mm. The shorter design was chosen in order to achieve a smaller mode size in the active medium. The smaller volume of the laser mode should make it easier to generate the high inversion densities necessary to bleach the reabsorption and to achieve gain. A 3.0 mm long sample with a dopant concentration of 0.6 at% was prepared in *a*-cut orientation from the boule grown at the ILP (cf. section 4.3.4). In addition an *a*-cut, 2.3 mm long sample with a dopant concentration of 0.25 at% was prepared from the crystal provided by Università di Pisa (cf. section 4.3.4).

First experiments were carried out with the resonator setup for operation in the green spectral region. As pump source the Genesis CX was chosen due to its better beam quality and corresponding focusability compared to InGaN LDs. Both mirrors were coated highly reflective for the prospective laser wavelength $\lambda_L = 549.5$ nm (cf. section 6.3) and M1 also anti-reflective for the pump wavelength. Lenses with focal lengths of $f = 25$ mm, 30 mm and 50 mm were employed. Independent of laser sample and focussing lens no laser operation was achieved even at the maximum of the available pump power. It is likely that this can be attributed to a combination of the high inversion density necessary to achieve gain and to the low quantum efficiency of the upper laser level. In order to exclude crystal quality issues the resonator was reset for operation on the $^5S_2 \rightarrow {}^5I_7$ transition at 750 nm (cf. [Chi77]) but again no laser oscillation could be established. However, for this transition the long lifetime of the lower laser manifold $^5I_7$ ($\tau_{rad} = 13.3$ ms, cf. [Wal05]) most likely causes population trapping and thus prevents laser operation under cw pumping. Therefore, the pump source was changed to an InGaN LD with a central

emission wavelength of $\lambda_P = 449\,\text{nm}$ which was driven by a *Thorlabs* ITC4005. This device allowed pumping in the quasi-cw regime (cf. section 7.2.5). The pump beam was focussed with a $f = 25\,\text{mm}$ lens.

With this setup and the 0.6 at% doped and 3.0 mm thick sample it was possible to achieve laser operation at 750.6 nm. The pump parameters were $f_{\text{rep}} = 50\,\text{Hz}$ and $\tau_{\text{pump}} = 100\,\mu\text{s}$. For longer pump intervals and/or higher repetition rates the laser shut off. These parameters are in good agreement with the reported lifetime of the lower laser level. An emission spectrum of the laser is depicted in figure 7.25a while figure 7.25b shows the temporal evolution of the laser. It can be seen that it operates in a spiking regime and no cw oscillation is achieved. However, since the duration of the pump intervals is much smaller than the radiative lifetime of the upper laser manifold ($\tau_{\text{rad}} = 460\,\mu\text{s}$) this is

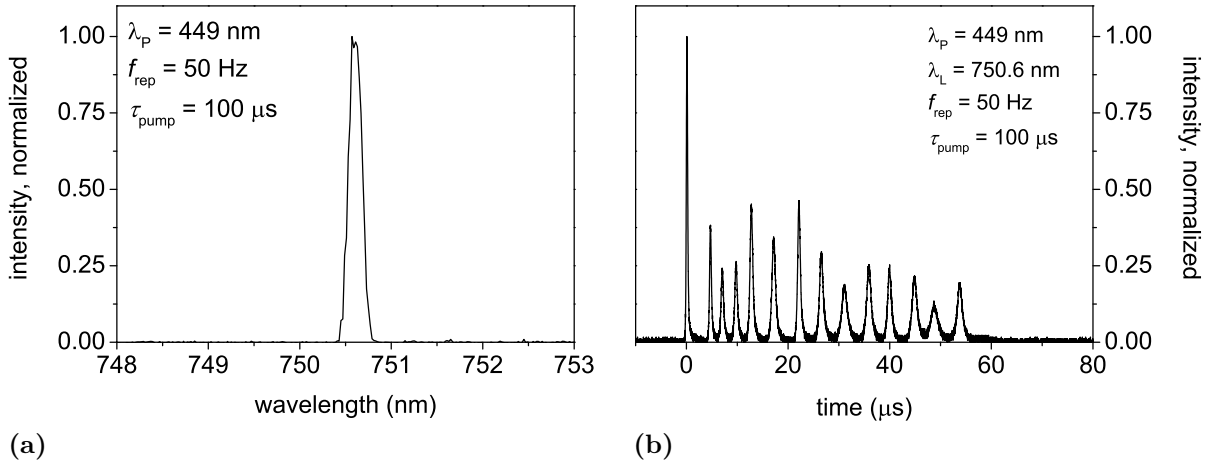

Figure 7.25: Laser characteristics of the Ho^{3+}:$LiLuF_4$ laser operating on the $^5S_2 \rightarrow {}^5I_7$ transition. (a) depicts the spectral characteristics which were recorded with a *Yokogawa* AQ6370C Optical Spectrum Analyzer while (b) shows the temporal evolution of the laser.

not surprising. The averaged output power was in the order of a hundred µW. Although no input-ouput characteristics were recorded, this results shows that laser operation is in priciple possible with this crystal. The fact that no laser operation was observed in the green spectral region is therefore likely to be linked to the decay dynamics of the $^5S_2$ manifold in Ho^{3+}:$LiLuF_4$ (cf. 6.3.5). This leads to the conclusion that Ho^{3+}:$LiLuF_4$ is not a suitable gain medium for the realization of solid state lasers with emission in the visible spectral region.

7.3.3 Ho^{3+}:LaF_3

For experiments with Ho^{3+}:LaF_3 a 3 mm thick *a*-cut sample was prepared from the boule doped with 1.0 at% Ho^{3+} in the melt (cf. section 4.3.5). The dopant concentration was determined by absorption spectroscopy to be 0.4 at%. The resonator design was the same as for the experiments conducted with Ho^{3+}:$LiLuF_4$. As pump source the Genesis Taipan was chosen since it yielded a better spectral overlap with the absorption spectrum of Ho^{3+}:LaF_3 than the Genesis CX. Nevertheless the absorption cross sections at this wavelength are very small ($\sigma_{\text{abs, 479 nm}} = 1.3 \cdot 10^{-21}\,\text{cm}^2$, cf. figure 6.12) and therefore

much less than 10 % of the pump light is expected to be absorbed by the sample. The pump beam was focussed by a lens with a focal length of $f = 30\,\text{mm}$. The sample was placed in a copper heat sink which was water cooled to 6 °C.

With this setup self-pulsed laser operation on the $^5S_2 \rightarrow {}^5I_8$ transition was realized at a wavelength of 549.4 nm. Mirrors with output coupling rates of up to $T_{OC} = 0.9\,\%$ were employed. However, these mirrors also exhibited very high reflectivities for the pump wavelengths ($T_{OC,\,479\,nm} \leq 15\,\%$). Since it was not possible to make an accurate prediction of the overlap between the laser mode and the back reflected pump light in the crystal, the input-output curves depicted in figure 7.26a are given with respect to the incident pump power. A maximum average output power of 7.7 mW was achieved with an output coupling rate of $T_{OC} = 0.9\,\%$. The corresponding slope efficiency and threshold pump power were 0.4 % and 2074 mW, respectively. However, it should be noted that these values were derived with respect to the incident pump power. Due to the very weak absorption caused by the small spectral overlap of the pump light and the absorption spectrum, the corresponding values with respect to absorbed pump power will be much higher.

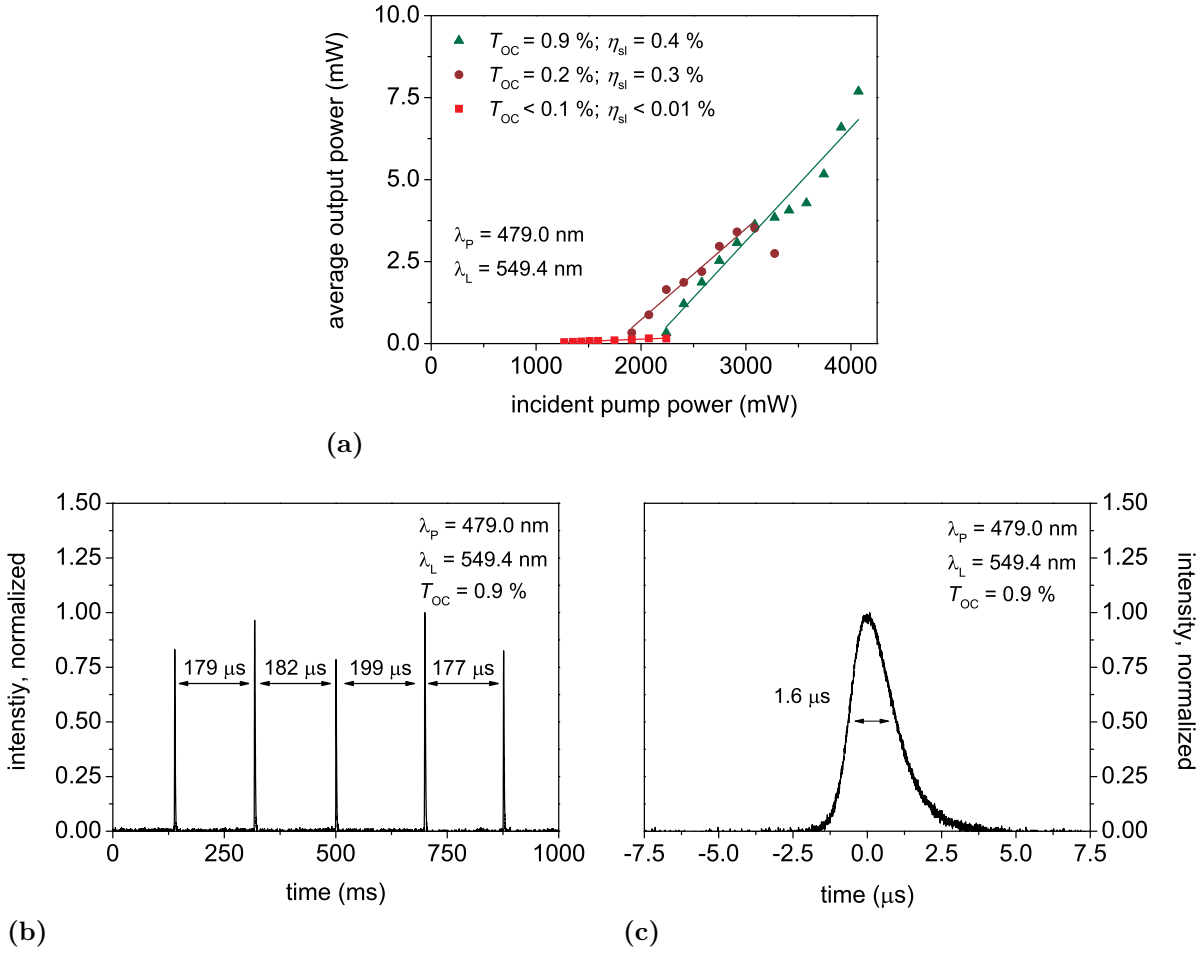

Figure 7.26: Laser characteristics of the Ho^{3+}:LaF_3 laser operating on the $^5S_2 \rightarrow {}^5I_8$ transition at $\lambda_L = 549\,\text{nm}$ under cw pumping. (a) shows input-output curves for different output coupling rates, (b) a sequence of several pulses, and (c) a single pulse.

The temporal characteristics of the laser operating with $T_{OC} = 0.9\,\%$ were recorded with a fast Si-photodiode. From the pulse train depicted in figure 7.26b it can be seen that the laser operated with a repetition rate of approximately $f_{rep} = 5.4\,\mathrm{kHz}$. Figure 7.26c shows that a single puls has a full width at half maximum of about 1.6 µs. The corresponding pulse energy and peak power are thus 1.4 µJ and 0.9 W respectively. The reason for the self pulsing behaviour is unclear. A theoretical approach via modelling the system by employing the rate equations might help to understand the underlying processes. However, the fact that due to the non-radiative decay of the $^5S_2$ manifold an unknown but non-negligible amount of population accumulates in the levels $^5F_5$, $^5I_4$, $^5I_5$, $^5I_6$, and $^5I_7$ (cf. figure 6.19) prevents such simulations. Further complications arise from the fact that due to excited state absorption processes in the region of the pump wavelength also higher levels are populated to an unknown degree (cf. figure 6.20). Nevertheless the self pulsing seems to be an intrinsic property of the ion rather than a problem of the host lattice. It is therefore highly questionable if the Ho^{3+}-ion in general is a suitable ion for the realization of efficient solid state lasers emitting in the visible spectral region. This is further underlined by the strict requirements in terms of non-radiative decay rates of the manifolds $^5S_2$ and $^5F_4$ for potential host systems (cf. section 6.3.5).

7.4 Summary: Laser Experiments

7.4.1 Praseodymium Doped Materials

Laser experiments were conducted by employing Pr,Mg:$SrAl_{12}O_{19}$, Pr,Mg:$CaAl_{12}O_{19}$, Pr:$LaMgAl_{11}O_{19}$, and Pr:LaF_3 samples as gain media and laser operation was achieved with all four materials.

Best results were obtained with Pr,Mg:$SrAl_{12}O_{19}$ which allowed efficient laser operation with Watt-level output powers in the deep red and red spectral region. In the orange region several hundred milliwatts were demonstrated. This material also allowed the first realization of green cw laser emission from an Pr^{3+}-doped oxide. Furthermore it was possible to realize laser operation in the thin disk geometry.

In addition to the experiments with bulk crystals, waveguiding structures inscribed into Pr,Mg:SRA samples were employed to achieve laser operation. In the deep red and red spectral range Watt-level output powers were achieved with nearly diffraction limited beam quality. Furthermore laser emission in the green spectral region from Pr^{3+}-doped crystalline waveguides was demonstrated for the first time.

First laser oscillation was also realized with Pr,Mg:$CaAl_{12}O_{19}$ with operation on the transitions $^3P_0 \rightarrow {}^3F_4$ and $^3P_0 \rightarrow {}^3F_2$ in the deep red and red spectral region with several hundred mW of output power. It is likely that by improving the sample quality and dopant concentration results comparable to those achieved with Pr,Mg:$SrAl_{12}O_{19}$ can be obtained.

This can not be said about Pr:$LaMgAl_{11}O_{19}$. Although quasi-cw laser operation was demonstrated in the deep red, red, and orange spectral region, the obtained output powers and efficiencies are low. This can probably be attributed to the formation of color centers by the pump radiation.

With Pr:LaF_3 cw laser operation was demonstrated for the first time in the deep red, red, orange, and green spectral region with output powers up to several hundred mW. However, the efficiencies are only morderate which is most likely linked to population trapping in the manifolds $^3H_5$ and $^3H_6$. Experiments with a Pr^{3+},Eu^{3+}:LaF_3 sample where a donor-acceptor energy transfer from Pr^{3+}- to Eu^{3+}-ions should circumvent this problem showed no improvement. However, higher Eu^{3+} concentrations might have an effect. Besides experiments in a free running regime, a wavelength selection element allowed tunable laser operation on the $^3P_0 \rightarrow {}^3H_6$ transition in the orange spectral region between 609.2 nm and 622.7 nm with two small gaps.

7.4.2 Holmium Doped Materials

Laser operation of Ho^{3+}:$LiLuF_4$ was achieved on the $^5S_2 \rightarrow {}^5I_7$ transition at a wavelength of 750 nm. The laser could only be operated in a pulsed regime which was probably due to a population trapping in the lower laser level. No laser emission could be obtained in the green spectral region which is likely a result of the strong non-radiative decay and corresponding low quantum efficiency of the upper laser level.

With Ho^{3+}:LaF_3 laser emission could be obtained at 549.4 nm corresponding to the transition $^5S_2 \rightarrow {}^5I_8$ which represents the first laser oscillation on this transition at room temperature. However, the laser operated in a self pulsed regime. The reason for this behaviour is likely to be found in the population of intermediate levels caused by a non-radiative decay of the upper laser level which enables ESA transitions into higher levels.

8 Conclusion

8.1 Summary

Within the framework of this thesis several Pr^{3+}- as well as Ho^{3+}-doped crystals were grown, characterized for their thermomechanical and spectroscopic properties, and subsequently used to realize solid state laser emitting in the visible spectral region. In addition, fs-laser inscription was used to fabricate low loss waveguiding structures which also allowed to achieve laser operation in the visible spectral range.

8.1.1 Pr-doped Materials

Praseodymium-doped single crystals of the three hexaaluminates $SrAl_{12}O_{19}$ (SRA), $CaAl_{12}O_{19}$ (CAlO), and $LaMgAl_{11}O_{19}$ (LMA) as well as the fluoride LaF_3 were grown with various doping concentrations by employing the Czochralski and the seedless cooling down method respectively. In order to improve the optical quality of the non-congruently melting crystals SRA and CAlO, different melt compositions and growth parameters were employed. Samples of SRA, LMA, and LaF_3 were used to determine the thermal conductivity in dependance of the crystallographic axis. These measurements revealed higher values perpendicular to the c-axis for the oxide crystals and parallel to the c-axis in case of the fluoride.

Ground state absorption spectra of the Pr^{3+}-doped materials revealed pronounced maxima in the order of $10^{-20}\,cm^2$ in the wavelength region between 430 nm and 490 nm. Several of these peaks are suitable for efficient pumping with InGaN laser diodes (440 nm - 450 nm) or 2ωOPSLs (480 nm - 490 nm). For the oxide crystals it was found that absorption cross sections were generally higher for σ-polarized light which can most likely be linked to the symmetry of the coordination sphere of the active ion. Pr:LaF_3 showed comparable cross sections for σ- and π-polarized light. Pr:LMA was furthermore investigated by means of site-selective excitation and temperature dependent decay dynamics measurements which strongly indicated the presence of two different optically active centers.

Emission measurements showed distinct maxima in the blue, green, orange, red, and deep red spectral region for all systems which correspond to various transitions originating from the ^3P_J manifold. The peak cross sections were in the order of $10^{-20}\,cm^2$. In the case of Pr:LaF_3 an unusually broad emission band with a full width at half maximum of 7 nm was found in the orange spectral region around 610 nm. Low temperature emission measurements revealed this to be caused by a phonon assisted process.

Measurements of the excited state absorption (ESA) for all systems showed broad ESA bands corresponding to interconfigurational $4f^2 \rightarrow 4f^1 5d^1$ transitions starting from the ^3P_J manifold. However, these bands were located at wavelengths below 400 nm. In

all investigated active materials the visible spectral region and therefore the prospective pump and laser transitions were free of ESA bands.

Continuous wave laser operation was realized with all hexaaluminates under 2ωOPSL pumping. With a 2.7 at% doped Pr:SRA maximum output powers in excess of 1 W were reached in the red and deep red spectral region with corresponding slope efficiencies of almost 60 %. Furthermore cw green laser emission at room temperature was realized for the first time in an oxide crystal. In addition to experiments with bulk gain media, Pr,Mg:SRA was used for the realization of laser operation in the thin disk geometry.

Pr:SRA was also used to fabricate fs-laser written channel waveguides. Propagation losses at $\lambda = 632.8$ nm were as low as 0.12 dB cm^{-1} which are the lowest losses measured for this type of waveguide structure so far. Measurements were conducted regarding the mode field diameters and M^2 values. The obtained values were used to derive the corresponding numerical apertures and refractive index changes. Laser experiments were carried out yielding emission in the deep red, red, orange, and, for the fist time in a Pr^{3+} doped crystalline waveguide, green spectral region. A maximum output power of more than 1 W and a slope efficiency of 37 % was obtained at a laser wavelength of 644.0 nm.

Laser oscillation was also realized for the first time by employing a 6.6 at% Pr:CAlO crystal as gain medium. Here several hundred milliwatts of cw output power and slope efficiencies of up to 27 % were obtained in the red and deep red spectral range. The lower values compared to Pr:SRA are likely to be the result of the high dopant concentration.

With Pr:LMA only quasi-cw laser operation could be obtained which can most likely be attributed to a color center formation caused by the pump radiation.

Laser operation of Pr:LaF_3 was demonstrated for the first time in a continuous wave regime. Laser emission was obtained in the green, orange, red and deep red spectral region with highest output powers in the order of 0.5 W and slope efficiency of 25 % (deep red). The comparatively low efficiencies in this material can most likely be attributed to a population trapping effect in the lower laser manifolds which is caused by a low non-radiative decay rate. Experiments with Eu^{3+} as a codopant which should increase the depopulation of the trapping manifolds via a $Pr^{3+} \rightarrow Eu^{3+}$ energy transfer showed no significant improvement. In addition to the free running experiments, tunable laser operation was demonstrated in the orange spectral region with a tuning range of several nanometers.

8.1.2 Ho-doped Materials

Holmium doped $LiLuF_4$ (LLF) and LaF_3 single crystals were grown by the Czochralski and seedless cooling down method, respectively.

The ground state absorption characteristics of both systems were determined. Maxima which could be addressed via InGaN laser diodes were found for both systems around 450 nm for σ-polarized light. Further peaks which could be addressed with 2ωOPSLs were also present in the cyan spectral range, in this case for π-polarized light. The reciprocity method was employed to derive the emission spectra of both active media. Since the Stark level positions of the $^5S_2$ manifold in Ho:LaF_3 were not reported so far, transmission measurements were conducted at cryogenic temperatures. The obtained emission spectra of both systems exhibit maxima between 530 nm and 555 nm. In combination

with the absorption spectra the gain cross sections were determined for different inversion levels. This revealed, that for Ho:LLF as well as for Ho:LaF_3 at least 20 % of the active ions have to be excited into the upper laser level to bleach the occuring reabsorption. Measurements of the decay dynamics of the upper laser level $^5S_2$ were carried out at temperatures between 10 K - 300 K. This allowed to derive the quantum efficiency of this level to be less than 40 % in Ho:LLF and about 75 % in Ho:LaF_3. ESA measurements conducted with Ho:LLF excited in the blue 440 nm spectral range revealed strong ESA bands. Comparative measurements with a pump source emitting at 2 µm showed that the corresponding ESA transitions do not originate from the upper laser level but from the first exited manifold above the ground state. Furthermore, for Ho:LLF as well as for Ho:LaF_3 no ESA bands are present at the long wavelength edge of the emission band in the green region.

It was not possible to obtain laser emission in the green spectral region with Ho:LLF. This can most likely be attributed to a combination of the low quantum efficiency and the high inversion density necessary to achieve gain. However, by employing Ho:LaF_3 as gain medium, it was possible to demonstrate room temperature laser operation of a Ho^{3+} doped gain medium in the green spectral region for the first time. The laser operated in a self pulsed regime at a repetion rate of 5.4 kHz, a pulse duration of 1.6 µs, and with a peak pulse power of 0.9 W.

8.2 Outlook

For the two hexaaluminates Pr:SRA and Pr:CAlO which allowed efficient laser operation the quality of the crystals still proved to be an issue. An optimization of the melt composition and parameters for the growth of these systems is thus likely to further improve the laser parameters. Another possibility to obtain samples of higher quality might be to grow mixed crystals containing the congruent system $BaAl_{12}O_{19}$. Growth experiments which are currently being conducted at the ILP deal with both approaches.

The waveguide lasers already realized with Pr:SRA could benefit from replacing the input coupling mirror with a dielectric coating on the front facet. This would allow a completely monolithic and thus highly stable setup. However, fabricating coatings that can withstand the high intensity which occurs on the input coupling facet, is challenging. Therefore specialized manufacturers must be employed.

A closer investigation concerning the optimal Pr^{3+} doping concentration in Pr:CAlO is likely to allow a drastic improvement of the laser charactistics of this material in terms of output power and efficiency. Due to the close similarity with Pr:SRA it is likely that comparable dopant concentrations are feasable and should be further investigated. If the laser parameters of Pr:CAlO can be improved, experiments concerning the realization of channel waveguide lasers in this gain medium might also be worthwhile.

To improve the laser characteristics of Pr:LaF_3 further experiments with higher doping concentrations of Eu^{3+} could be carried out. This may allow to improve the efficiency of the energy transfer process and thus mitigate the population trapping. In addition, spectroscopic measurements in the mid-infrared spectral region could allow to derive the radiative and non-radiative lifetimes of the trapping manifolds. A way to increase the

tuning range of the laser operating in the orange spectral region could be to employ birefringent filters of higher quality or a Lyot filter. The broad linewidth of this transition could also be employed for the generation of ultra short pulses in the visible spectral region via mode-locking.

Since the self pulsed operation of Ho:LaF_3 is most likely linked to the intrinsic properties of the active ion, it seems unlikely that continous wave output can be achieved with this material. Nonetheless, the long lifetime of the upper laser level might make it interesting to employ this gain medium for Q-switched laser operation in the green spectral region.

A References for Table 3.1

		$SrAl_{12}O_{19}$	$CaAl_{12}O_{19}$	$LaMgAl_{11}O_{19}$	LaF_3	$LiLuF_4$
acronym		SRA	CAlO	LMA	LaF	LLF
lattice		[Kim90]	[Uts88]	[Efr88]	[Udo08]	[Web75]
space group		[Kim90]	[Uts88]	[Efr88]	[Udo08]	[Web75]
coordination number		[Kim90]	[Uts88]	[Efr88]	[Udo08]	[Web75]
formula units per unit cell		[Kim90]	[Uts88]	[Efr88]	[Udo08]	[Web75]
cation density	[g cm^{-3}]	[Kim90]	[Uts88]	[Efr88]	[Udo08]	[Ran02]
	[10^{21} cm^{-3}]	[Kim90]	[Uts88]	[Efr88]	[Udo08]	[Ran02]
density [g cm^{-3}]		[Kim90]	[Uts88]	[Efr88]	[Udo08]	[Ran02]
lattice constants [Å]	c-axis	[Kim90]	[Uts88]	[Efr88]	[Udo08]	[Ran02]
	a-axis	[Kim90]	[Uts88]	[Efr88]	[Udo08]	[Ran02]
unit cell volume	[$Å^3$]	[Kim90]	[Uts88]	[Efr88]	[Udo08]	[Ran02]
thermal conductivity [W m^{-1} K^{-1}]	$\kappa_{\parallel \mathbf{c}}$	this work	-	this work	this work	[Agg05]
	$\kappa_{\perp \mathbf{c}}$	this work	-	this work	this work	[Agg05]
Mohs hardness		this work	this work	this work	this work	[Kam93]
$E_{\mathrm{phon,max}}$ [cm^{-1}]		[Fec10]	this work	this work	[Yen64]	[Zha94]
T_{melt} [°C]		[Gan79]	[Jer01]	[Wyo90]	[Buc96]	[Har83]
specific heat [J g^{-1} K^{-1}]		[Fec12]	-	this work	this work	[Agg05]
congruent melt		[Gan79]	[Jer01]	[Wyo90]	n/a	[Har83]

Table A.1: References for Table 3.1.

B Additional Spectroscopic Data

Comparison of the Emission Spectra of Ho^{3+}-doped active Obtained by the McCumber and the Füchtbauer-Ladenburg Method

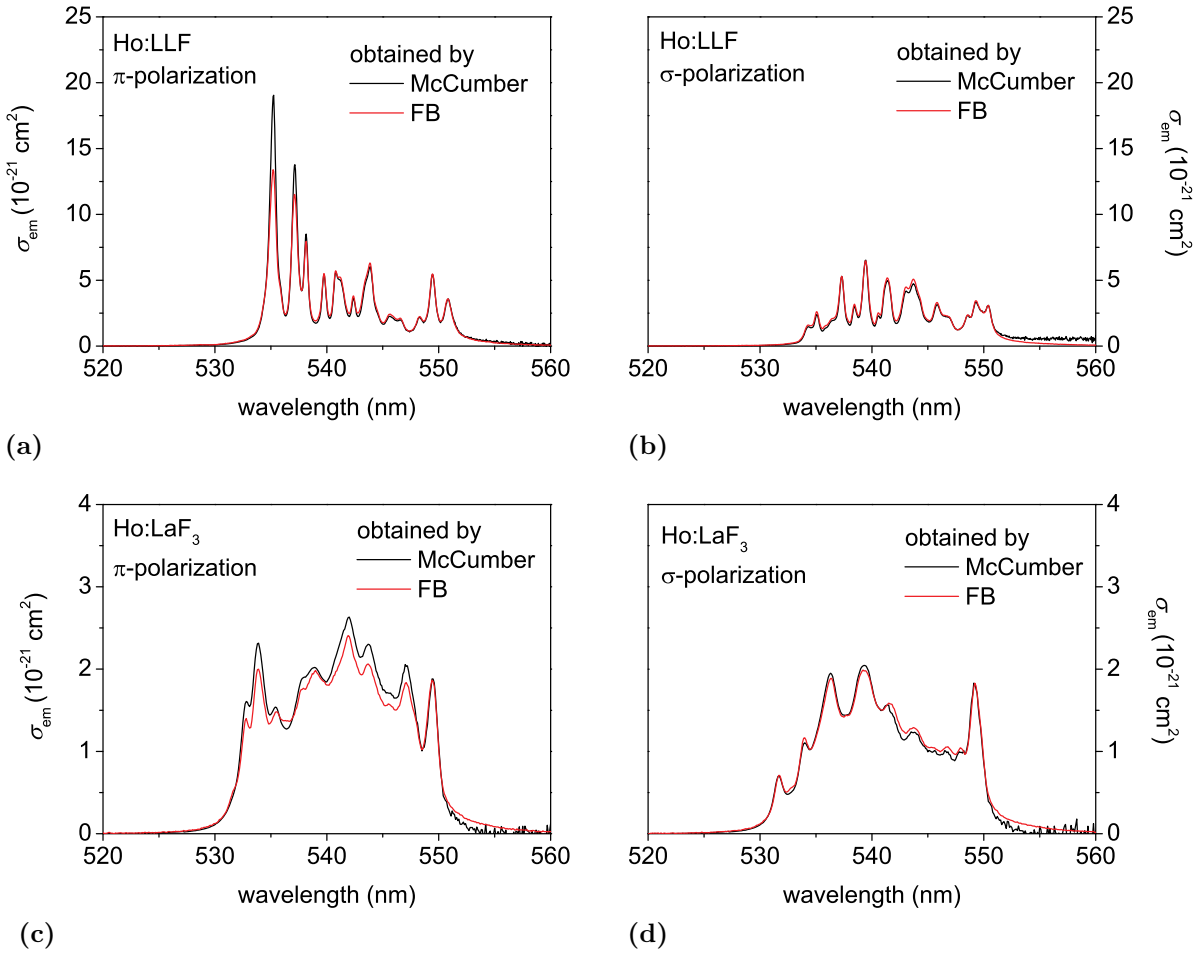

Figure B.1: Input.

C Additional Laser Parameters

Reflectivity of the Coating of the Pr,Mg:$SrAl_{12}O_{19}$ Waveguides

The coating of the crystal inscribed with waveguides was done by Dieter Barlösius. The reflectivity for the spectral region 400 -750 nm is depicted in figure C.1.

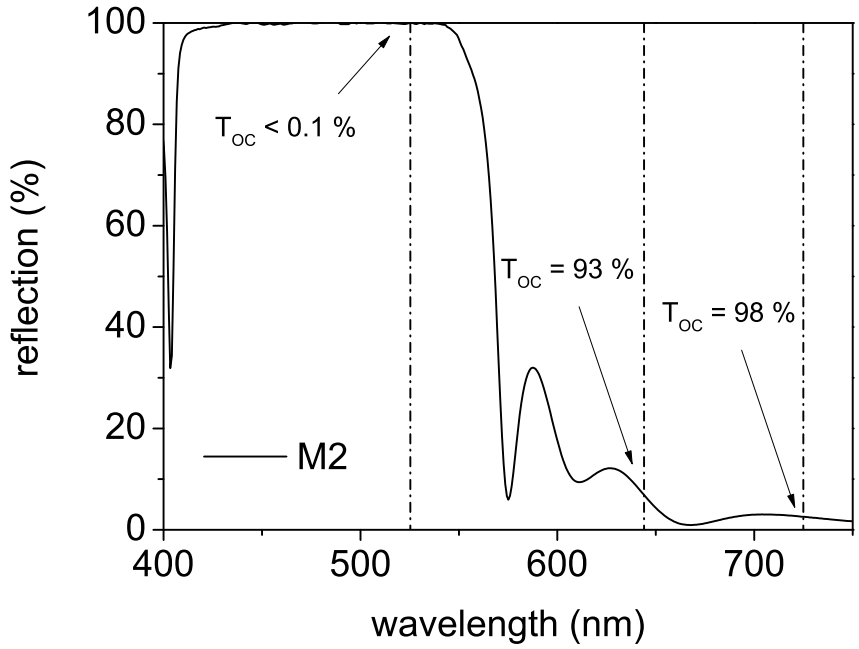

Figure C.1: Reflectivity of the Coating of the Pr,Mg:$SrAl_{12}O_{19}$ Waveguides.

Bibliography

[Abr87] S. C. Abrahams, P. Marsh, and C. D. Brandle. *Laser and phosphor host $La_{1-x}MgAl_{11+x}O_{19}$ ($x = 0.050$): Crystal structure at 295 K*. The Journal of Chemical Physics **86** (7), 4221 (1987).

[Ack11] L. Ackermann. *Personal correspondence* (2011).

[Ack12] L. Ackermann. *Personal correspondence* (2012).

[Agg05] R. L. Aggarwal, D. J. Ripin, J. R. Ochoa, and T. Y. Fan. *Measurement of thermo-optic properties of $Y_3Al_5O_{12}$, $Lu_3Al_5O_{12}$, $YAIO_3$, $LiYF_4$, $LiLuF_4$, BaY_2F_8, $KGd(WO_4)_2$, and $KY(WO_4)_2$ laser crystals in the 80–300 K temperature range*. Journal of Applied Physics **98** (10), 103514 (2005).

[Asp61] L. B. Asprey and T. K. Keenan. *Tetravalent lanthanides I - Sodium praseodymium(IV) fluorides*. Journal of Inorganic and Nuclear Chemistry **16** (3?4), 260 (1961).

[Aul86] B. F. Aull and H. P. Jenssen. *Impact of ion-host interactions on the 5d-to-4f spectra of lanthanide rare-earth-metal ions. I. A phenomenological crystal-field model*. Phys. Rev. B **34**, 6640 (1986).

[Auz04] F. Auzel. *Upconversion and Anti-Stokes Processes with f and d Ions in Solids*. Chemical Reviews **104** (1), 139 (2004).

[Bas96] T. Basiev, Y. Orlovskii, K. Pukhov, V. Sigachev, M. Doroshenko, and I. Vorob'ev. *Multiphonon relaxation rates measurements and theoretical calculations in the frame of non-linear and non-Coulomb model of a rare-earth ion-ligand interaction*. Journal of Luminescence **68** (5), 241 (1996).

[Bas01] M. Bass. *Handbook of Optics: Devices, measurements, and properties* (McGraw-Hill, New York, USA, 2001).

[Bec11] D. Beckmann, D. Esser, and J. Gottmann. *Characterization of channel waveguides in Pr:$YLiF_4$ crystals fabricated by direct femtosecond laser writing*. Applied Physics B **104**, 619 (2011).

[Bel10] A.-R. Bellancourt, U. Mackens, H. Moench, and U. Weichmann. *Blue diode pumped solid-state lasers for digital projection*. Laser Physics **20** (3), 643 (2010).

[Boy92] R. W. Boyd. *Nonlinear optics* (Academic Press Inc., San Diego, USA, 1992).

[Brü70] R. Brückner. *Properties and structure of vitreous silica. I.* Journal of Non-Crystalline Solids **5** (2), 123 (1970).

[Bra03] B. H. Brandsen and C. J. Joachain. *Physics of Atoms and Molecules* (Pearson Educatioal Limited, Harlow, England, 2003), 2. edition.

[Bri64] W. B. Bridges. *Laser oscillation in singly ionized argon in the visible spectrum.* Applied Physics Letters **4** (7), 128 (1964).

[Buc96] C. Buchal, T. Siegrist, D. C. Jacobson, and J. M. Poate. *1.5 µm photoluminescence of Er^{3+} in YF_3, LuF_3, and LaF_3 thin fims.* Applied Physics Letters **68** (4), 438 (1996).

[Cal60] J. Callaway and H. C. Baeyer. *Effect of Point Imperfections on Lattice Thermal Conductivity.* Physical Review **120**, 1149 (1960).

[Cal11] T. Calmano, J. Siebenmorgen, F. Reichert, M. Fechner, A.-G. Paschke, N.-O. Hansen, K. Petermann, and G. Huber. *Crystalline $Pr:SrAl_{12}O_{19}$ waveguide laser in the visible spectral region.* Optics Letters **36** (23), 4620 (2011).

[Cal12] T. Calmano, S. Müller, F. Reichert, M. Fechner, N.-O. Hansen, and G. Huber. *Dual Wavelength and Switchable Laser Operation of Visible $Pr:SrAl_{12}O_{19}$ Waveguide Lasers.* In: *5th EPS-QEOD EUROPHOTON Conference paper FrB.2, Stockholm, Sweden* (2012).

[Cal13] T. Calmano. *Femtosekundenlaser-geschriebene kristalline Wellenleiterlaser im sichtbaren und nahen infraroten Spektralbereich.* Ph.D. thesis, University of Hamburg (2013).

[Cam07] P. Camy, J. L. Doualan, R. Moncorgé, J. Bengoechea, and U. Weichmann. *Diode-pumped $Pr^{3+}:KY_3F_{10}$ red laser.* Optics Letters **32** (11), 1462 (2007).

[Car69] W. T. Carnall, P. R. Fields, and R. Sarup. *$^1S_0$ Level of Pr^{3+} in Crystal Matrices and Energy-Level Parameters for the $4f^2$ Configuration of Pr^{3+} in LaF_3.* The Journal of Chemical Physics **51** (6), 2587 (1969).

[Cas65] H. H. Caspers, H. E. Rast, and R. A. Buchanan. *Energy Levels of $Pr^{3+}:LaF_3$.* The Journal of Chemical Physics **43** (6), 2124 (1965).

[Cas70] H. H. Caspers, H. E. Rast, and J. L. Fry. *Absorption, Fluorescence, and Energy Levels of Ho^{3+} in LaF_3.* The Journal of Chemical Physics **53** (8), 3208 (1970).

[Cas75] H. Caspers and H. Rast. *Electronic and vibronic spectra of Pr^{3+} in $LiYF_4$.* Journal of Luminescence **10** (6), 347 (1975).

[Cha72] A. Chatterjee and G. Zhmoidin. *The phase equilibrium diagram of the system CaO-Al_2O_3-CaF_2.* Journal of Materials Science **7** (1), 93 (1972).

[Che94] Y. M. Cheung and S. K. Gayen. *Excited-state absorption in $Pr^{3+}:Y_3Al_5O_{12}$.* Physical Review B **49** (21), 14827 (1994).

[Chi77] E. Chicklis, C. Naiman, L. Esterowitz, and R. Allen. *Deep red laser emission in Ho:YLF*. Quantum Electronics, IEEE Journal of **13** (11), 893 (1977).

[Chi04] J. L. A. Chilla, S. D. Butterworth, A. Zeitschel, J. P. Charles, A. L. Caprara, M. K. Reed, and L. Spinelli. *High-power optically pumped semiconductor lasers*. Proc. SPIE **5332**, 143 (2004).

[COH13a] COHERENT. *Data Sheet Genesis CX STM-Series* (2013).

[COH13b] COHERENT. *Genesis CX STM-Series specification sheet for serial number 1180660* (2013).

[Cor07] F. Cornacchia, A. Richter, E. Heumann, G. Huber, D. Parisi, and M. Tonelli. *Visible laser emission of solid state pumped $LiLuF_4:Pr^{3+}$*. Opt. Express **15** (3), 992 (2007).

[Cor08] F. Cornacchia, A. D. Lieto, M. Tonelli, A. Richter, E. Heumann, and G. Huber. *Efficient visible laser emission of GaN laser diode pumped Pr-doped fluoridescheelite crystals*. Opt. Express **16** (20), 15932 (2008).

[CT99] C. Cohen-Tannoudji, B. Diu, and F. Laloe. *Quantum Mechanics* (Walter de Gruyter, Berlin, New York, 1999).

[Czo18] J. Czochralski. *Ein neues Verfahren zur Messung der Kristallisationsgeschwindigkeit der Metalle*. Zeitschrift fuer Physikalische Chemie **92**, 219 (1918).

[Dan94a] T. Danger, A. Bleckmann, and G. Huber. *Stimulated emission and laser action of Pr^{3+}-doped $YAlO_3$*. Applied Physics B **58** (5), 413 (1994).

[Dan94b] T. Danger, J. Koetke, R. Brede, E. Heumann, G. Huber, and B. H. T. Chai. *Spectroscopy and green upconversion laser emission of Er^{3+}-doped crystals at room temperature*. Journal of Applied Physics **76** (3), 1413 (1994).

[Dav96] K. M. Davis, K. Miura, N. Sugimoto, and K. Hirao. *Writing waveguides in glass with a femtosecond laser*. Opt. Lett. **21** (21), 1729 (1996).

[DeL94] L. D. DeLoach, S. A. Payne, W. L. Kway, J. B. Tassano, S. N. Dixit, and W. F. Krupke. *Vibrational structure in the emission spectra of Yb^{3+}-doped apatite crystals*. Journal of Luminescence **62** (2), 85 (1994).

[Der03] P. J. Deren, A. Bednarkiewicz, R. Mahiou, and W. Strek. *On spectroscopic properties of the $KYb(WO_4)_2:Pr^{3+}$ crystal*. Molecular Physics **101** (7), 951 (2003).

[Der07] A. Dergachev, D. Armstrong, A. Smith, T. Drake, and M. Dubois. *3.4 µm ZGP RISTRA nanosecond optical parametric oscillator pumped by a 2.05 µm Ho:YLF MOPA system*. Opt. Express **15** (22), 14404 (2007).

[Die63] G. H. Dieke and H. M. Crosswhite. *The Spectra of the Doubly and Triply Ionized Rare Earths.* Appl. Opt. **2** (7), 675 (1963).

[Don11a] N. Dong, J. M. de Mendivil, E. Cantelar, G. Lifante, J. V. de Aldana, G. A. Torchia, F. Chen, and D. Jaque. *Self-frequency-doubling of ultrafast laser inscribed neodymium doped yttrium aluminum borate waveguides.* Applied Physics Letters **98** (18), 181103 (2011).

[Don11b] N. Dong, Y. Tan, A. Benayas, J. V. de Aldana, D. Jaque, C. Romero, F. Chen, and Q. Lu. *Femtosecond laser writing of multifunctional optical waveguides in a Nd:YVO_4 + KTP hybrid system.* Opt. Lett. **36** (6), 975 (2011).

[Dor00a] P. Dorenbos. *5d-level energies of Ce^{3+} and the crystalline environment. I. Fluoride compounds.* Phys. Rev. B **62**, 15640 (2000).

[Dor00b] P. Dorenbos. *5d-level energies of Ce^{3+} and the crystalline environment. II. Chloride, bromide, and iodide compounds.* Phys. Rev. B **62**, 15650 (2000).

[Dor01] P. Dorenbos. *5d-level energies of Ce^{3+} and the crystalline environment. III. Oxides containing ionic complexes.* Phys. Rev. B **64**, 125117 (2001).

[Dor02] P. Dorenbos. *5d-level energies of Ce^{3+} and the crystalline environment. IV. Aluminates and simple oxides.* Journal of Luminescence **99** (3), 283 (2002).

[Dor04] P. Dorenbos. *Locating lanthanide impurity levels in the forbidden band of host crystals.* Journal of Luminescence **108** (1-4), 301 (2004).

[Efr88] V. A. Efremov, N. G. Chernaya, V. K. Trunov, and V. F. Pisarenko. *Crystal structure of lanthanum magnesium hexaaluminate.* Kristallografiya **33**, 38 (1988).

[Ein16] A. Einstein. *Zur Quantentheorie der Srahlung.* Physikalische Gesellschaft Zürich **16**, 47 (1916).

[Eis13] U. Eismann, A. Bergschneider, F. Sievers, N. Kretzschmar, C. Salomon, and F. Chevy. *2.1-watts intracavity-frequency-doubled all-solid-state light source at 671 nm for laser cooling of lithium.* Opt. Express **21** (7), 9091 (2013).

[Fec09] M. Fechner, A. Richter, N.-O. Hansen, A. Petrosyan, K. Petermann, and G. Huber. *Continuous wave Pr^{3+}:$LuAlO_3$ laser in the visible range.* In: *The European Conference on Lasers and Electro-Optics (CLEO/Europe) 201 paper: CA6.3 , OSA Technical Digest, 2009* (Optical Society of America, 2009).

[Fec10] M. Fechner, F. Reichert, N.-O. Hansen, K. Petermann, and G. Huber. *Spectroscopic and Laser Characteristics of Pr^{3+}:$SrAl_{12}O_{19}$.* In: *4th EPS-QEOD EUROPHOTON Conference 2010, Hamburg, Germany* (2010).

[Fec11] M. Fechner, F. Reichert, N.-O. Hansen, K. Petermann, and G. Huber. *Crystal growth, spectroscopy, and diode pumped laser performance of Pr,Mg:$SrAl_{12}O_{19}$.* Applied Physics B **102**, 731 (2011).

[Fec12] M. Fechner. *Seltenerd-dotierte Oxidkristalle für Festkörperlaser im sichtbaren Spektralbereich*. Ph.D. thesis, University of Hamburg (2012).

[Fib09] M. Fibrich, H. Jelínková, J. Sulc, K. Nejezchleb, and V. Skoda. *Visible cw laser emission of GaN-diode pumped Pr:$YAlO_3$*. Applied Physics B: Lasers and Optics **97**, 363 (2009).

[För48] T. Förster. *Zwischenmolekulare Energiewanderung und Fluoreszenz*. Annalen der Physik **437** (1-2), 55 (1948).

[Fu11] X. Fu, Y. Li, and H. Jiang. *Diode-pumped Pr^{3+}:$YAlO_3$/LBO violet laser at 374 nm*. Laser Physics **21** (5), 864 (2011).

[Gan79] F. Ganits, T. Y. Chemkova, and Y. P. Udalov. *SrO-Al_2O_3 System*. Russian Journal of Inorganic Chemistry **24**, 260 (1979).

[Gie94] A. Giesen, H. Hügel, A. Voss, K. Wittig, U. Brauch, and H. Opower. *Scalable concept for diode-pumped high-power solid-state lasers*. Applied Physics B **58** (5), 365 (1994).

[Gün11a] T. Gün. *Dauerstrich-Festkörperlaser im tief-ultravioletten Spektralbereich*. Ph.D. thesis, University of Hamburg (2011).

[Gün11b] T. Gün, P. Metz, and G. Huber. *Efficient continuous wave deep ultraviolet Pr^{3+}:$LiYF_4$ laser at 261.3 nm*. Applied Physics Letters **99** (18), 181103 (2011).

[Gün11c] T. Gün, P. Metz, and G. Huber. *Power scaling of laser diode pumped Pr^{3+}:$LiYF_4$ cw lasers: efficient laser operation at 522.6 nm, 545.9 nm, 607.2 nm, and 639.5 nm*. Optics Letters **36**, 1002 (2011).

[Gom96] L. Gomes, L. C. Courrol, L. V. G. Tarelho, and I. M. Ranieri. *Cross-relaxation process between +3 rare-earth ions in $LiYF_4$ crystals*. Physical Review B **54**, 3825 (1996).

[Gri05] G. G. Grigoryan, Y. V. Orlov, E. A. Petrenko, A. Y. Shashkov, and N. V. Znamenskiy. *The Features of Coherent Stimulated Emission of Pr^{3+} Doped into a LaF_3 Matrix*. Laser Physics **15**, 602 (2005).

[Gru91] J. B. Gruber, M. E. Hills, M. D. Seltzer, S. B. Stevens, C. A. Morrison, G. A. Turner, and M. R. Kokta. *Energy levels and crystal quantum states of trivalent holmium in yttrium aluminum garnet*. Journal of Applied Physics **69** (12), 8183 (1991).

[Had99] C. Z. Hadad and S. O. Vàsquez. *Energy-transfer processes induced by exchange interactions*. Physcal Review B **60**, 8586 (1999).

[Hal71] B. Halperin and R. Englman. *Cooperative Dynamic Jahn-Teller Effect. II. Crystal Distortion in Perovskites*. Physcal Review B **3**, 1698 (1971).

[Han10] N.-O. Hansen, A.-R. Bellancourt, U. Weichmann, and G. Huber. *Efficient green continuous-wave lasing of blue-diode-pumped solid-state lasers based on praseodymium-doped $LiYF_4$.* Applied Optics **49** (20), 3864 (2010).

[Han12] N.-O. Hansen. *Praseodym-dotierte Fluoride für kompakte Festkörperlaser im sichtbaren Spektralbereich.* Ph.D. thesis, University of Hamburg (2012).

[Har83] I. R. Harris, H. Safi, N. A. Smith, M. Altunbas, B. Cockayne, and J. Plant. *The relationship between crystal growth behaviour and constitution in the systems LiF-LuF_3, LiF-ErF_3, and LiF-YF_3.* Journal of Materials Science **18**, 1235 (1983).

[Heg82] J. Hegarty, D. L. Huber, and W. M. Yen. *Fluorescence quenching by cross relaxation in LaF_3:Pr^{3+}.* Physical Review B **25**, 5638 (1982).

[Hel10] O. Hellmig, S. Salewski, A. Stark, J. Schwenke, P. E. Toschek, K. Sengstock, and V. M. Baev. *Multicolor diode-pumped upconversion fiber laser.* Optics Letters **35** (13), 2263 (2010).

[Hen89] B. Henderson and G. Imbusch. *Optical Spectroscopy of Inorganic Solids* (Clarendon Press, Oxford, United Kingdom, 1989).

[Hin95] Y. Hinatsu. *Magnetic properties of tetravalent praseodymium perovskites $BaPrO_3$, $BaCeyPr_{1-y}O_3$, and $SryBa_{1-y}PrO_3$.* Journal of Solid State Chemistry **119** (2), 405 (1995).

[Hub75] G. Huber, W. W. Kruhler, W. Bludau, and H. G. Danielmeyer. *Anisotropy in the laser performance of NdP_5O_{14}.* Journal of Applied Physics **46** (8), 3580 (1975).

[Ino65] M. Inokuti and F. Hirayama. *Influence of Energy Transfer by the Exchange Mechanism on Donor Luminescence.* The Journal of Chemical Physics **43** (6), 1978 (1965).

[Jer01] D. Jerebtsov and G. Mikhailov. *Phase diagram of CaO - Al_2O_3 system.* Ceramics International **27** (1), 25 (2001).

[Joh71] L. F. Johnson and H. J. Guggenheim. *Infrared-Pumped Visible Laser.* Applied Physics Letters **19**, 44 (1971).

[Jon68] D. Jones and W. Shand. *Crystal growth of flourides in the lanthanide series.* Journal of Crystal Growth **2** (6), 361 (1968). Evaporation.

[Jud62] B. R. Judd. *Optical Absorption Intensities of Rare-Earth Ions.* Physical Review **127**, 750 (1962).

[Kam86] A. A. Kaminskii, V. M. Garmash, G. E. Ermakov, V. A. Akkerman, A. A. Filimonov, and K. Kurbanov. *Luminescence and stimulated emission of orthorhombic crystal of $YAlO$-Ho^{3+}.* Inorganic Materials **22**, 1576 (1986).

[Kam90] A. A. Kaminski. *Laser Crystals* (Springer Berlin / Heidelberg, Heidelberg, New York, 1990).

[Kam93] A. A. Kaminskii, K. Ueda, and N. Uehara. *New Laser-Diode-Pumped CW Laser Based on Nd^{3+}-Ion-Doped Tetragonal $LiLuF_4$ Crystal.* Japanese Journal of Applied Physics **32** (Part 2, No. 4B), L586 (1993).

[Küh07] H. Kühn, S. T. Fredrich-Thornton, C. Kränkel, R. Peters, and K. Petermann. *Model for the calculation of radiation trapping and description of the pinhole method.* Optics Letters **32** (13), 1908 (2007).

[Kim90] K. Kimura, M. Ohgaki, K. Tanaka, H. Morikawa, and F. Marumo. *Study of the bipyramidal site in magnetoplumbite-like compounds, $SrM_{12}O_{19}$ (M = Al, Fe, Ga).* Journal of Solid State Chemistry **87** (1), 186 (1990).

[Kle60] P. G. Klemens. *Thermal Resistance due to Point Defects at High Temperatures.* Physical Review **119**, 507 (1960).

[Kle67] P. H. Klein and W. J. Croft. *Thermal Conductivity, Diffusivity, and Expansion of Y_2O_3, $Y_3Al_5O_{12}$, and LaF_3 in the Range 77 K - 300 K.* Journal of Applied Physics **38** (4), 1603 (1967).

[Koe95] J. Koetke and G. Huber. *Infrared excited-state absorption and stimulated-emission cross sections of Er^{3+}-doped crystals.* Applied Physics B **61** (2), 151 (1995).

[Koo11] P. Koopmann, S. Lamrini, K. Scholle, M. Schäfer, P. Fuhrberg, and G. Huber. *Multi-watt laser operation and laser parameters of Ho-doped Ho^{3+}:Lu_2O_3 at 2.12 µm.* Optics Materials Express **1** (8), 1447 (2011).

[Koo12] P. Koopmann. *Thulium- and Holmium-Doped Sesquioxides for 2 µm Lasers.* Ph.D. thesis, University of Hamburg (2012).

[Krä08] C. Kränkel. *Ytterbium-dotierte Borate und Vanadate mit großer Verstärkungsbandbreite als aktive Materialien im Scheibenlaser.* Ph.D. thesis, University of Hamburg (2008).

[Kru66] W. F. Krupke. *Optical Absorption and Fluorescence Intensities in Several Rare-Earth-Doped Y_2O_3 and LaF_3 Single Crystals.* Physical Review **145**, 325 (1966).

[Kum77] U. V. Kumar, D. R. Rao, and P. Venkateswarlu. *Optical absorption and laser excited fluorescence spectra of LaF_3:Eu^{3+}.* The Journal of Chemical Physics **66** (5), 2019 (1977).

[Kuz97] M. Kuznetsov, F. Hakimi, R. Sprague, and A. Mooradian. *High-power (>0.5 W CW) diode-pumped vertical-external-cavity surface-emitting semiconductor lasers with circular TEM_{00} beams.* Photonics Technology Letters, IEEE **9** (8), 1063 (1997).

[Lam12] S. Lamrini, P. Koopmann, M. Schäfer, K. Scholle, and P. Fuhrberg. *Efficient high-power Ho:YAG laser directly in-band pumped by a GaSb-based laser diode stack at 1.9µm.* Applied Physics B **106** (2), 315 (2012).

[Lap25] O. Laporte and W. F. Meggers. *Some rules of spectral structure.* Journal of the Optical Society of America **11** (5), 459 (1925).

[LeF92] Y. LeFur, N. M. Khaidukov, and S. Aléonard. *Structure of KYF_4.* Acta Crystallographica Section C **48** (6), 978 (1992).

[Lev69] P. M. Levy. *Anisotropy in Two-Center Exchange Interactions.* Physical Review **177**, 509 (1969).

[Mar12] D.-T. Marzahl. *Herstellung und spektroskopische Charakterisierung von Praseodym-dotiertem Hexaaluminaten.* Diploma thesis, University of Hamburg (2012).

[McC64] D. E. McCumber. *Einstein Relations Connecting Broadband Emission and Absorption Spectra.* Physical Review **136** (4A) (1964).

[McI03] J. G. McInerney, A. Mooradian, A. Lewis, A. V. Shchegrov, E. M. Strzelecka, D. Lee, J. P. Watson, M. K. Liebman, G. P. Carey, A. Umbrasas, C. A. Amsden, B. D. Cantos, W. R. Hitchens, D. L. Heald, and V. Doan. *Novel 980-nm and 490-nm light sources using vertical-cavity lasers with extended coupled cavities* 21–31 (2003).

[Mel95] C. Mello-Donega, A. Meijerink, and G. Blasse. *Non-radiative relaxation processes of the Pr^{3+}-ion.* Journal of Applied Spectroscopy **62** (4), 664 (1995).

[Mer96] L. D. Merkle, B. Zandi, R. Moncorgé, Y. Guyot, H. R. Verdun, and B. McIntosh. *Spectroscopy and laser operation of Pr,Mg:$SrAl_{12}O_{19}$.* Journal of Applied Physics **79**, 1849 (1996).

[Met12] P. Metz, F. Reichert, S. Müller, D.-T. Marzahl, N.-O. Hansen, M. Fechner, C. Kränkel, and G. Huber. *Highly effcient Pr:$LiYF_4$-lasers.* In: *EPS-QEOD Europhoton Conference 2012, Stockholm, Sweden, FrA.4* (2012).

[Mir96] V. S. Mironov. *Superexchange interaction between lanthanide f^1 ions. Spin-Hamiltonian calculations for the 90° and 180° superexchange.* Journal of Physics: Condensed Matter **8** (49), 10551 (1996).

[Mog12] F. Moglia, S. Müller, T. Calmano, and G. Huber. *Er:$LiLuF_4$ upconversion waveguide laser fabricated by femtosecond-laser writing.* In: *5th EPS-QEOD EUROPHOTON Conference paper TuP.25, Stockholm, Sweden* (2012).

[Moh01] J. Mohr. *Lasereigenschaften und Spektroskopie Holmium-dotierter Sesquioxide.* Diploma thesis, University of Hamburg (2001).

[Moo70] H. W. Moos. *Spectroscopic relaxation processes of rare earth ions in crystals.* Journal of Luminescence **1,2** (0), 106 (1970).

[Mor75] A. M. Morozow, I. G. Podkolzina, A. M. Tkachuk, V. A. Fedorov, and P. P. Feofilov. *Luminescence and induced emission lithium-erbium and lithium-holmium binary fluorides.* Opt. Spectrosc. **39**, 338 (1975).

[Mor80] C. A. Morrison. *Host dependence of the rare-earth ion energy separation $4f^N$ - $4f^{N-1}$ nl.* The Journal of Chemical Physics **72** (2), 1001 (1980).

[Mor98] J. Morikawa and T. Hashimoto. *Analysis of High-Order Harmonics of Temperature Wave for Fourier Transform Thermal Analysis.* Japanese Journal of Applied Physics **37** (Part 2, No. 12A), L1484 (1998).

[Mor08] J. Morikawa, C. Leong, T. Hashimoto, T. Ogawa, Y. Urata, S. Wada, M. Higuchi, and J. Takahashi. *Thermal conductivity/diffusivity of Nd^{3+} doped $GdVO_4$, YVO_4, $LuVO_4$, and $Y_3Al_5O_{12}$ by temperature wave analysis.* Journal of Applied Physics **103** (6), 063522 (2008).

[Mou86] P. F. Moulton. *Spectroscopic and laser characteristics of Ti:Al_2O_3.* Journal of the Optical Society of America B **3** (1), 125 (1986).

[Nak96] S. Nakamura, M. Senoh, S. Nagahama, N. Iwasa, T. Yamada, T. Matsushita, H. Kiyoku, and Y. Sugimoto. *InGaN-Based Multi-Quantum-Well-Structure Laser Diodes.* Japanese Journal of Applied Physics **35** (Part 2, No. 1B), L74 (1996).

[Nak09] S. Nakamura. *Current Status of GaN-Based Solid-State Lighting.* MRS Bulletin **34**, 101 (2009).

[New13] Newport. *Data Sheet F-SM Series* (2013).

[Nic13a] Nichia. *http://www.nichia.co.jp/en/product/laser.html* (2013).

[Nic13b] Nichia. *http://www.nichia.co.jp/specification/en/product/ld/NDB7875.pdf, 01.07.2013* (2013).

[Nur65] R. W. Nurse, J. H. Welch, and A. J. Majumdar. Transactions and Journal of the British Ceramic Society **64**, 416 (1965).

[Ofe62] G. S. Ofelt. *Intensities of Crystal Spectra of Rare-Earth Ions.* The Journal of Chemical Physics **37** (3), 511 (1962).

[Osi04] E. Osiac, E. Heumann, A. Richter, G. Huber, A. Diening, and W. Seelert. *Red Pr^{3+}:$YLiF_4$ laser excited by 480 nm optically pumped semiconductor laser.* In: *Conference on Lasers and Electro-Optics/International Quantum Electronics Conference and Photonic Applications Systems Technologies*, CFE2 (Optical Society of America, 2004).

[Ost08] V. Ostroumov and W. Seelert. *1 W of 261 nm cw generation in a Pr^{3+}:$LiYF_4$ laser pumped by an optically pumped semiconductor laser at 479 nm* 68711K–68711K–4 (2008).

[Pab11] D. Pabœuf, O. Mhibik, F. Bretenaker, P. Goldner, D. Parisi, and M. Tonelli. *Diode-pumped Pr:BaY_2F_8 continuous-wave orange laser*. Optics Letters **36** (2), 280 (2011).

[Par97] J.-G. Park and A. N. Cormack. *Defect Energetics and Nonstoichiometry in Lanthanum Magnesium Hexaaluminate*. Journal of Solid State Chemistry **130** (2), 199 (1997).

[Pas76] R. Pastor and M. Robinson. *Crystal growth of alkaline earth fluorides in a reactive atmosphere: Part III*. Materials Research Bulletin **11** (10), 1327 (1976). Crucible degradation.

[Pay91] S. A. Payne, J. A. Caird, L. L. Chase, L. K. Smith, N. D. Nielsen, and W. F. Krupke. *Spectroscopy and gain measurements of Nd^{3+} in SrF_2 and other fluorite-structure hosts*. Journal of the Optical Society of America B **8** (4), 726 (1991).

[Pet09] R. Peters. *Ytterbium-dotierte Sesquioxide als hocheffiziente Lasermaterialien*. Ph.D. thesis, University of Hamburg (2009).

[Pod76] I. G. Podkolzina, A. M. Tkachul, V. A. Fedorov, and P. P. Feofilov. *Multifrequency generation of stimulated emission of Ho^{3+} ion in $LiYF_4$ crystals*. Opt. Spectrsosc. **40**, 111 (1976).

[Pop12] P. Popov, N. Moiseev, A. Filimonova, P. Fedorov, V. Konyushkin, V. Osiko, A. Papashvili, A. Smirnov, and I. Mironov. *Thermal conductivity of LaF_3-based single crystals and ceramics*. Inorganic Materials **48**, 304 (2012).

[Pra98] M. Praeger, V. Vuletic, T. Fischer, T. W. Hänsch, and C. Zimmermann. *A broad emitter diode laser system for lithium spectroscopy*. Applied Physics B **67** (2), 163 (1998).

[Ran02] I. M. Ranieri, S. P. Morato, A. H. A. Bressiani, L. C. Courrol, E. P. Maldonado, N. U. Wetter, S. L. Baldochi, N. D. V. Jr., K. Shimamura, and T. Fukuda. *Growth of $LiY_{1-x}Lu_xF_4$ crystals under CF_4 atmosphere*. Journal of Alloys and Compounds **344** (1-2), 203 (2002).

[Rei10] F. Reichert. *Herstellung und Charakterisierung von Ce^{3+}- und Pr^{3+}-dotierten Oxiden mit Emission im grünen Spektralbereich*. Diploma thesis, University of Hamburg (2010).

[Ric04] A. Richter, E. Heumann, E. Osiac, G. Huber, W. Seelert, and A. Diening. *Diode pumping of a continuous-wave Pr^{3+}-doped $LiYF_4$ laser*. Optics Letters **29** (22), 2638 (2004).

[Ric06] A. Richter, N. Pavel, E. Heumann, G. Huber, D. Parisi, A. Toncelli, M. Tonelli, A. Diening, and W. Seelert. *Continuous-wave ultraviolet generation at 320 nm by intracavity frequency doubling of red-emitting Praseodymium lasers*. Optics Express **14** (8), 3282 (2006).

[Ric07] A. Richter, E. Heumann, G. Huber, V. Ostroumov, and W. Seelert. *Power scaling of semiconductor laser pumped Praseodymium-lasers.* Optics Express **15** (8), 5172 (2007).

[Ric08] A. Richter. *Laser parameters and performance of Pr^{3+}-doped fluorides operating in the visible spectral region.* Ph.D. thesis, University of Hamburg (2008).

[Ris68] L. A. Riseberg and H. W. Moos. *Multiphonon Orbit-Lattice Relaxation of Excited States of Rare-Earth Ions in Crystals.* Physical Review **174**, 429 (1968).

[Rod02] P. A. Rodnyi, A. N. Mishin, and A. S. Potapov. *Luminescence of trivalent praseodymium in oxides and fluorides.* Optics and Spectroscopy **93**, 714 (2002).

[San94] T. Sandrock, T. Danger, E. Heumann, G. Huber, and B. H. T. Chai. *Efficient Continuous Wave-Laser Emission of Pr^{3+}-Doped Fluorides at Room Temperature.* Applied Physics B: Lasers and Optics **58**, 149 (1994). 10.1007/BF01082350.

[Sch67] H. L. Schläfer and G. Gliemann. *Einführung in die Ligandenfeldtheorie* (Akademische Verlagsanstalt, Wiesbaden, Germany, 1967).

[Sch73] P. Schuster. *Ligandenfeldtheorie* (Verlag Chemie, Weinheim, Germany, 1973).

[Sch00] H. J. Scheel. *Historical aspects of crystal growth technology.* Journal of Crystal Growth **211**, 1 (2000).

[Sch04] H. Scheife, G. Huber, E. Heumann, S. Bär, and E. Osiac. *Advances in upconversion lasers based on Er^{3+} and Pr^{3+}.* Optical Materials **26** (4), 365 (2004).

[Sha69] W. Shand. *Single crystal growth and some properties of $LiYF_4$.* Journal of Crystal Growth **5** (2), 143 (1969).

[Sie09] J. Siebenmorgen, K. Petermann, G. Huber, K. Rademaker, S. Nolte, and A. Tünnermann. *Femtosecond laser written stress-induced $Nd:Y_3Al_5O_{12}$ (Nd:YAG) channel waveguide laser.* Applied Physics B **97**, 251 (2009).

[Sie10] J. Siebenmorgen. *Herstellung von Wellenleiterlasern mittels Femtosekunden-Laserstrukturierung in Nd- und Yb-dotierten YAG-Kristallen.* Ph.D. thesis, University of Hamburg (2010).

[Sob02] B. P. Sobolev. *Chemical aspects of crystal growth of multicomponent fluoride materials from the melt.* Crystallography Reports **47**, 63 (2002).

[Sol63] R. Solomon and L. Mueller. *Stimulated emission at 5985 Åfrom Pr^{+3} in LaF_3.* Applied Physics Letters **3**, 135 (1963).

[Sta00] S. Stankus, R. Khairulin, and K. Lyapunov. *Thermal properties and phase transitions of heavy rare-earth fluorides.* High Temperatures - High Pressures **32**, 467 (2000).

[Str85] D. Strickland and G. Mourou. *Compression of amplified chirped optical pulses.* Optics Communications **56** (3), 219 (1985).

[Stu96] B. C. Stuart, M. D. Feit, S. Herman, A. M. Rubenchik, B. W. Shore, and M. D. Perry. *Nanosecond-to-femtosecond laser-induced breakdown in dielectrics.* Physical Review B **53**, 1749 (1996).

[Sve98] O. Svelto. *Principles of Lasers* (Springer Science + Business Media, Inc, New York, USA, 1998), 4. edition.

[Syt91] J. Sytsma, S. J. Kroes, G. Blasse, and N. M. Khaidukov. *Spectroscopy of Gd^{3+} in KYF_4: a system with several luminescent sites.* Journal of Physics: Condensed Matter **3** (45), 8959 (1991).

[Tan10] Y. Tan, A. Rodenas, F. Chen, R. R. Thomson, A. K. Kar, D. Jaque, and Q. Lu. *70% slope efficiency from an ultrafast laser-written Nd:$GdVO_4$ channel waveguide laser.* Optics Express **18** (24), 24994 (2010).

[Thi08] N. Thielmann. *Spektroskopie von Pr^{3+}-dotierten oxidischen Kristallen.* Diploma thesis, University of Hamburg (2008).

[Tro04] A. C. Tropper, H. D. Foreman, A. Garnache, K. G. Wilcox, and S. H. Hoogland. *Vertical-external-cavity semiconductor lasers.* Journal of Physics D: Applied Physics **37** (9), R75 (2004).

[Udo08] T. J. Udovic, Q. Huang, A. Santoro, and J. J. Rush. *The nature of deuterium arrangements in YD_3 and other rare-earth trideuterides.* Zeitschrift für Kristallographie - Crystalline Materials **223**, 697 (2008).

[Uts88] A. Utsunomiya, K. Tanaka, H. Morikawa, F. Marumo, and H. Kojima. *Structure refinement of $CaO \cdot 6Al_2O_3$.* Journal of Solid State Chemistry **75** (1), 197 (1988).

[Ver12] S. Veronesi, Y. Zhang, M. Tonelli, and M. Schellhorn. *Efficient laser emission in Ho^{3+}:$LiLuF_4$ grown by micro-Pulling Down method.* Optics Express **20** (17), 18723 (2012).

[Vor65] Y. K. Voron'ko, A. A. Kaminski, V. V. Osiko, and A. M. Prokhorov. *Stimulated Emission of Ho^{3+} in CaF_2 at $\lambda = 5512$ Å.* JETP Letters **1** (1), 3 (1965).

[Vor66] Y. K. Voron'ko, A. Kaminskii, and V. Osiko. *Optical Relaxation of Ho^{3+} and Er^{3+} Ions in the CaF_2 Lattice (Type I) in the Visible Wavelength Region.* Journal of Experimental and Theoretical Physics **49**, 710 (1966).

[Vor82] Y. K. Voron'ko, A. A. Kaminski, V. V. Osiko, and A. M. Prokhorov. *Luminescence of Laser Crystals.* Izvestiya Akademii Nauk SSSR. Seriya Fizicheskaya **46**, 970 (1982).

[Wal98] B. M. Walsh, N. P. Barnes, and B. D. Bartolo. *Branching ratios, cross sections, and radiative lifetimes of rare earth ions in solids: Application to Tm^{3+} and Ho^{3+} ions in $LiYF_4$.* Journal of Applied Physics **83**, 2772 (1998).

[Wal05] B. Walsh, G. Grew, and N. P. Barnes. *Energy levels and intensity parameters of Ho^{3+} ions in $LiGdF_4$,$LiYF_4$, and $LiLuF_4$.* Journal of Physics: Condensed Matter **17**, 7643 (2005).

[Web75] M. J. Weber. *Handbook of optical materials* (Plenum Press, New York, USA, 1975).

[Wei88] J. Weidlein, U. Müller, and K. Dehnicke. *Schwingungsspektroskopie* (Georg Thieme Verlag, Stuttgart, Germany, 1988).

[Wem70] S. H. Wemple and M. DiDomenico. *Theory of the Elasto-Optic Effect in Nonmetallic Crystals.* Physical Review B **1**, 193 (1970).

[Wis55] L. G. Wisnyi. *The high alumina phases in the system lime-alumina.* Ph.D. thesis, Rutgers University, New Brunswick, NJ, USA (1955).

[Wyo90] C. Wyon, J. Aubert, and Y. Grange. *Crystal growth of $LaMgAl_{11}O_{19}$: Nd.* Journal of Crystal Growth **99** (1-4, Part 2), 845 (1990).

[Xu11] B. Xu, P. Camy, J.-L. Doualan, Z. Cai, and R. Moncorgé. *Visible laser operation of Pr^{3+}-doped fluoride crystals pumped by a 469 nm blue laser.* Optics Express **19** (2), 1191 (2011).

[Xu13] B. Xu, F. Starecki, D. Pabœuf, P. Camy, J. L. Doualan, Z. P. Cai, A. Braud, R. Moncorgé, P. Goldner, and F. Bretenaker. *Red and orange laser operation of Pr:KYF_4 pumped by a Nd:YAG/LBO laser at 469.1 nm and a InGaN laser diode at 444 nm.* Optics Express **21** (5), 5567 (2013).

[Yar62] A. Yariv, S. P. S. Porto, and K. Nassau. *Optical Maser Emission from Trivalent Praseodymium in Calcium Tungstate.* Journal of Applied Physics **33** (8), 2519 (1962).

[Yen64] W. M. Yen, W. C. Scott, and A. L. Schawlow. *Phonon-Induced Relaxation in Excited Optical States of Trivalent Praseodymium in LaF_3.* Physical Review **136**, A271 (1964).

[Zan97] B. Zandi, L. D. Merkle, J. B. Gruber, D. E. Wortman, and C. A. Morrison. *Optical spectra and analysis for Pr^{3+}:$SrAl_{12}O_{19}$.* Journal of Applied Physics **81** (3), 1047 (1997).

[Zha94] X. Zhang, A. Schulte, and B. Chai. *Raman spectroscopic evidence for isomorphous structure of $LiGdF_4$ and $LiYF_4$ laser crystals.* Solid State Communications **89** (2), 181 (1994).

List of Publications

Publications in Scientific Journals

- T.T. Basiev, V.A. Konyushkin, D.V. Konyushkin, M.E. Doroshenko, G. Huber, F. Reichert, N.-O. Hansen, and M. Fechner. *First ceramic laser in the visible spectral range.* Optical Materials Express **1** (8), 1511 - 1514 (2011).

- T. Calmano, J. Siebenmorgen, F. Reichert, M. Fechner, A.-G. Paschke, N.-O. Hansen, K. Petermann, and G. Huber. *Crystalline Pr,Mg:$SrAl_{12}O_{19}$ waveguide laser in the visible spectral region.* Optics Letters **36** (23), 4620 - 4622 (2011).

- M. Fechner, F. Reichert, N.-O. Hansen, K. Petermann, and G. Huber. *Crystal growth, spectroscopy, and diode pumped laser performance of Pr,Mg:$SrAl_{12}O_{19}$.* Applied Physics B **102** (4), 731 - 735 (2011).

- F. Reichert, M. Fechner, P. Koopmann, C. Brandt, K. Petermann, and G. Huber. *Spectroscopy and laser operation of Nd-doped mixed sesquioxides ($Lu_{1-x}Sc_x)_2O_3$.* Applied Physics B **108** (3), 475 - 478 (2012).

- F. Reichert, F. Moglia, D.-T. Marzahl, P. Metz, M. Fechner, N.-O. Hansen, and G. Huber. *Diode pumped laser operation and spectroscopy of Pr^{3+}:LaF_3.* Optics Express **20** (18), 20387 - 20395 (2012).

- F. Reichert, D.-T. Marzahl, P. Metz, M. Fechner, N.-O. Hansen, and G. Huber. *Efficient Laser Operation of Pr^{3+},Mg^{2+}:$SrAl_{12}O_{19}$.* Optics Letters **37** (23), 4889-4891 (2012).

- F. Reichert, T. Calmano, S. Müller, D.-T. Marzahl, M. Fechner, and G. Huber. *Efficient visible laser operation of Pr,Mg:$SrAl_{12}O_{19}$ channel waveguides.* Optics Letters **38** (15), 2698-2701 (2013).

- D.-T. Marzahl, F. Reichert, P. Metz, M. Fechner, N.-O. Hansen, and G. Huber. *Laser Operation of Pr^{3+},Mg^{2+}:$SrAl_{12}O_{19}$ Pumped by Polarization Coupled InGaN Laser Diodes .* Applied Physics B, DOI: 10.1007/s00340-013-5655-3

- Philip W. Metz, Sebastian Müller, Fabian Reichert, Daniel-Timo Marzahl, Francesca Moglia, Christian Kränkel, and Günter Huber. *Wide Wavelength Tunability and Green Laser Operation of Diode-pumped Pr^{3+}:KY_3F_{10}.* Opt. Express **21** (25), 31274-31281 (2013).

- Fabian Reichert, Daniel-Timo Marzahl, and Günter Huber. *Spectroscopic Characterization and Laser Performance of Pr,Mg:$CaAl_{12}O_{19}$.* J. Opt. Soc. Am. B **31** (2), (2014).

International Conferences

- M. Fechner, F. Reichert, N.-O. Hansen, K. Petermann, and G. Huber. *Spectroscopic and Laser Characteristics of Pr^{3+}:$SrAl_{12}O_{19}$.* 4th EPS-QEOD EUROPHOTON Conference 2010, Hamburg, Germany, talk XX00.0 (2010).

- T.T. Basiev, V.A. Konyushkin, D.V. Konyushkin, M.E. Doroshenko, G. Huber, F. Reichert, N.-O. Hansen, and M. Fechner. *New Visible SrF_2:Pr^{3+} Ceramic Laser at 639 nm.* Advanced Solid-State Photonics (ASSP) 2011, Istanbul, Turkey, paper: AMF1 (2011).

- M. Fechner, F. Reichert, K. Petermann, and G. Huber. *Crystal growth and Spectroscopy of Cerium doped $CaSc_2O_4$.* Advances in Optical Materials (AIOM) 2011, Istanbul, Turkey, paper: AIThC4 (2011).

- F. Reichert, P. Koopmann, M. Fechner, C. Brandt, K. Petermann, and G. Huber. *Spectroscopy and Laser Action of the Nd-Doped Mixed Sesquioxide $Lu_{2-x}Sc_xO_3$.* Advanced Solid-State Photonics (ASSP) 2011, Istanbul, Turkey, paper: AMB19 (2011).

- T.T. Basiev, V.A. Konyushkin, D.V. Konyushkin, M.E. Doroshenko, G. Huber, F. Reichert, N.-O. Hansen, and M. Fechner. *First Visible 639 nm SrF_2:Pr^{3+} Ceramic Laser.* Conference on Lasers and Electro-Optics (CLEO/Europe - EQEC) 2011, Munich, Germany paper: CA2_2, (2011).

- T. Calmano, J. Siebenmorgen, F. Reichert, M. Fechner, A.-G. Paschke, N.-O.Hansen, K. Petermann, and G. Huber. *Femtosecond laser written Pr,Mg:$SrAl_{12}O_{19}$ channel-waveguide laser in the visible spectral range.* Conference on Lasers and Electro-Optics (CLEO/Europe - EQEC) 2011, Munich, Germany paper: CJ8_1, (2011).

- M. Fechner, F. Reichert, P. Koopmann, K. Petermann, and G. Huber. *Spectroscopy of Ho:Lu_2O_3 with Respect to the Realization of a Visible Laser.* Conference on Lasers and Electro-Optics (CLEO/Europe - EQEC) 2011, Munich, Germany paper: CA8_4, (2011).

- C. Kränkel, K. Beil, C. Brandt, F. Reichert, P. Koopmann, K. Petermann, and G. Huber. *Tailored Gain Spectra in Rare Earth Doped Mixed Oxide Crystals.* 20th INTERNATIONAL LASER PHYSICS WORKSHOP, Sarajevo, Bosnia, (2011).

- M. Doroshenko, T. T. Basiev, V. Konyushkin, A. Papashvili, O. Alimov, V. Osiko, P. Popov, G. Huber, F. Reichert, and M. Fechner. *Spectroscopic and oscillation properties of Pr^{3+} ions in CaF_2-SrF_2-LaF_3 solid solutions.* Advanced Solid-State Photonics (ASSP) 2012, San Diego, CA, USA, paper: AT4A.21 (2012).

- F. Moglia, F. Reichert and G. Huber. *Er^{3+}:LaF_3 as Potential Material for Upconversion Lasers.* Advances in Optical Materials (AIOM) 2012, San Diego, CA, USA, paper: IW5D.6 (2012).

- F. Reichert, F. Moglia, M. Fechner, P. Koopmann, and G. Huber. *Diode Pumped Laser Oscillation at 750 nm and Excited State Absorption Measurements of Ho^{3+}:$LiLuF_4$.* Advances in Optical Materials (AIOM) 2012, San Diego, CA, USA, paper: IW3D.2 (2012).

- F. Reichert, F. Moglia, M. Fechner, N.-O. Hansen, D.-T. Marzahl, and G. Huber. *Diode Pumped Laser Oscillation and Spectroscopy of Pr^{3+}:LaF_3.* Conference on Lasers and Electro-Optics (CLEO/QELS) 2012, San José, CA, USA, paper: CM2D.2 (2012).

- T. Calmano, S. Müller, F. Reichert, M. Fechner, N-O Hansen, and G. Huber. *Dual Wavelength and Switchable Laser Operation of Visible Pr,Mg:$SrAl_{12}O_{19}$ Waveguide Lasers.* 5th EPS-QEOD EUROPHOTON Conference 2012, Stockholm, Sweden, paper FrB.2 (2012).

- D.-T. Marzahl, F. Reichert, M. Fechner, N.-O. Hansen, and G. Huber. *Laser Operation and Spectroscopy of Pr:$LaMgAl_{11}O_{19}$.* 5th EPS-QEOD EUROPHOTON Conference 2012, Stockholm, Sweden, paper ThP.3 (2012).

- P. Metz, F. Reichert, S. Müller, D.-T. Marzahl, N.-O. Hansen, M. Fechner, C. Kränkel, and G. Huber. *Highly efficient Pr:$LiYF_4$-lasers.* 5th EPS-QEOD EUROPHOTON Conference 2012, Stockholm, Sweden, paper FrA.4 (2012).

- F. Reichert, D.-T. Marzahl, P. Metz, M. Fechner, N.-O. Hansen, and G. Huber. *OPSL-Pumped Laser Operation of Pr^{3+},Mg^{2+}:$SrAl_{12}O_{19}$.* 5th EPS-QEOD EUROPHOTON Conference 2012, Stockholm, Sweden, paper WeP.7 (2012).

- F. Reichert, F. Moglia, D.-T. Marzahl, P. Metz, M. Fechner, N.-O. Hansen, and G. Huber. *Tunable Laser Operation of Pr:LaF_3.* 5th EPS-QEOD EUROPHOTON Conference 2012, Stockholm, Sweden, paper ThP.14 (2012).

- S. Müller, T. Calmano, F. Reichert, M. Fechner, C. Kränkel, and G. Huber. *Advances in visible and near infrared fs-laser written waveguide lasers.* Photonics West 2013, San Francisco, CA, USA, paper 8599-5 (invited) (2013).

- F. Reichert, T. Calmano, S. Müller, D.-T. Marzahl, and G. Huber. *Visible laser operation of Pr,Mg:$SrAl_{12}O_{19}$ waveguides.* Conference on Lasers and Electro-Optics (CLEO/Europe - EQEC) 2013, Munich, Germany, paper: CJ-12.5, (2013).

- D.-T. Marzahl, F. Reichert, P. W. Metz, N.-O. Hansen, and G. Huber. *Efficient Pr^{3+}:$SrAl_{12}O_{19}$ laser pumped with four diode lasers.* Conference on Lasers and Electro-Optics (CLEO/Europe - EQEC) 2013, Munich, Germany, paper: CA-P.3, (2013).

- P. W. Metz, F. Moglia, F. Reichert, S. Müller, D.-T. Marzahl, N.-O. Hansen, C. Kränkel, and G. Huber. *Novel Rare Earth Solid State Lasers with Emission Wavelengths in the Visible Spectral Range.* Conference on Lasers and Electro-Optics (CLEO/Europe - EQEC) 2013, Munich, Germany, paper: CA-2.5, (2013).

- F. Reichert, D.-T. Marzahl, and G. Huber. *Spectroscopic Properties and Laser Operation of Pr,Mg:$CaAl_{12}O_{19}$.* Advances in Solid-State Lasers (ASSL) 2013, Paris, France, paper: AW1A.9 (2013).

National Conferences

- M. Fechner, F. Reichert, K. Petermann, and G. Huber. *Kristallzüchtung und spektroskopische Untersuchungen von Ce:$CaSc_2O_4$.* Frühjahrstagung der Deutschen Physikalischen Gesellschaft 2012, Stuttgart, Germany, paper Q54.14 (2012).

- D.-T. Marzahl, F. Reichert, M. Fechner, and G. Huber. *Polarisationsgekoppeltes InGaN-Diodenpumpen von Pr,Mg:$SrAl_{12}O_{19}$.* Frühjahrstagung der Deutschen Physikalischen Gesellschaft 2012, Stuttgart, Germany, paper Q18.8 (2012).

- D.-T. Marzahl, F. Reichert, M. Fechner, and G. Huber. *Spektroskopische Eigenschaften von Dy^{3+}:$SrAl_{12}O_{19}$ im sichtbaren Spektralbereich.* Frühjahrstagung der Deutschen Physikalischen Gesellschaft 2013, Hannover, Germany, paper Q44.4 (2013).

- Philip Werner Metz, Francesca Moglia, Sebastian Müller, Fabian Reichert, Daniel-Timo Marzahl, Nils-Owe Hansen, Matthias Fechner, Christian Kränkel. and G. Huber. *Spectroscopy and self-pulsed red and orange laser operation of Sm^{3+} doped $LiLuF_4$ crstals.* Frühjahrstagung der Deutschen Physikalischen Gesellschaft 2013, Hannover, Germany, paper Q43.3 (2013)

- Philip Werner Metz, Sebastian Müller, Fabian Reichert, Daniel-Timo Marzahl, Christian Kränkel, and Günter Huber. *Wavelength Tuning of Praseodymium Lasers in Different Fluoride Hosts.* Frühjahrstagung der Deutschen Physikalischen Gesellschaft 2014, Berlin, Germany, paper Q1.5 (2014).

- Benedikt Niklas Stumpf, Daniel-Timo Marzahl, Fabian Reichert, Christian Kränkel und Günter Huber. *Spektroskopische Eigenschaften von Sm^{3+}:$Y_3Al_5O_{12}$ im sichtbaren Spektralbereich.* Frühjahrstagung der Deutschen Physikalischen Gesellschaft 2014, Berlin, Germany, paper Q30.38 (2014).

Talks at Seminars and Workshops

- F. Reichert. *Ce^{3+}-doped Crystals.* 1st Las-F Workshop, Lintrup, Denmark (2009).

- F. Reichert. *Optimization of Crystal Growth of $CaSc_2O_4$ and $SrAl_{12}O_{19}$.* 2nd Las-F Workshop, Vorbasse, Denmark (2010).

- F. Reichert. *A possible pump source for a green Pr^{3+},Mg^{2+}:$SrAl_{12}O_{19}$ continuous wave laser.* GrK Workshop, Lüneburg, Germany (2010).

- F. Reichert. *Pr- and Ho-doped materials for lasers in the visible spectral range.* 3rd Las-F Workshop, Lonborg, Denmark (2011).

- F. Reichert. *Project A3: Pr- and Ho-doped materials for lasers in the visible spectral range.* GrK 1355 Workshop 2011, Amrum, Germany (2011).
- F. Reichert, C. Brandt, K. Beil, C. Kränkel, K. Petermann, and G. Huber. *Crystal Field Tuning and Laser Action of RE-doped Mixed Sesquioxides.* 1st French-German Oxidecrystal-/Dielectrics-Lasercrystal-Workshop, Idar-Oberstein, Germany (2011).
- F. Reichert. *Laser Operation of Pr:LaF_3.* 4$^{\text{th}}$ Las-F Workshop, Lavensby, Denmark (2012).
- F. Reichert, K. Beil, and F. Moglia. *Short-Wwavelength Solid-State Lasers (VIS and UV)).* GrK 1355 Workshop 2012, Amrum, Germany (2012).
- C. Kränkel, D.-T. Marzahl, F. Reichert, P. Metz, M. Fechner, N.-O. Hansen, and G. Huber. *Oxide host materials for visible lasers.* 2$^{\text{nd}}$ French-German Oxidecrystal-/Dielectrics-Lasercrystal-Workshop, Saint-Louis, France (2012).
- D.-T. Marzahl, F. Reichert, C. Kränkel, and G. Huber. *Oxidische Wirtsmaterialien für Laser im sichtbaren Spektralbereich.* Deutsche Kristallzüchtungtagung DKT-2013, Erlangen, Germany (2013).
- D. Marzahl, P. Metz, F. Reichert, C. Kränkel, and G. Huber. *Visible Laser Materials.* GrK 1355 Workshop 2013, Amrum, Germany (2013).
- F. Reichert. *Spectroscopy and Laser Operation of Ho:LaF_3.* 5$^{\text{th}}$ Las-F Workshop, Assentoft, Denmark (2012).

Patents

- Cerium doped $CaSc_2O_4$ crystals with improved pump light absorption for laser and LED applications. *EP10193793.6.*
- Ausnutzen der polarisationsabh. Absorption aus angeregten Zust. zur Realisierung eines Cer-Lasers. *EP10166783.0.*

Further Written Publications

- F. Reichert. *Herstellung und Charakterisierung von Ce^{3+}- und Pr^{3+}-dotierten Oxiden mit Emission im grünen Spektralbereich.* Diploma thesis, University of Hamburg (2010).

Acknowledgements

The work presented in this thesis was carried out from 2010 until 2013 in the group "Festkörperlaser" of Prof. Dr. Günter Huber at the Institute of Laser-Physics of the University of Hamburg. It was conducted within the framework of the graduate school 1355 "Physics with new advanced coherent radiation sources". During this work I received support from numerous people and I would like to use the following section to express my gratitude to them.

First of all I would like to thank Prof. Huber for giving me the opportunity to conduct this research in his group. A constant source of support, he was always available to discuss problems that arose within the course of this thesis and to provide advice on how to tackle them. At the same time he always let me work independently which is something I value very much.

Next I'd like to thank Prof. Mauro Tonelli for refereeing this thesis, for providing several of the crystals, and also for giving me the chance to work with his group in Pisa in the fall of 2012. I really enjoyed my time there and it was a very fruitful and productive collaboration without which several parts of this thesis would not have been possible.

Prof. Klaus Sengstock I'd like to thank for refereeing the defense of this thesis.

My secondary supervisor Dr. Becker I would like to thank for our numerous discussions. As someone from another field of physics he often provided know-how and a perspective that I otherwise would not have had access to.

I heavily benefitted from Dr. Petermann knowledge on all things related to crystal growth and from his numerous contacts he would readily (and often instantaneously) bother to help me.

Dr. Christian Kränkel I would like to thank for our various discussions and for proof-reading this thesis even though he was on vaccation.

The whole group "Festkörperlaser" I would like to thank for the highly motivated atmosphere and for the constant support. Help was almost always only a small way away. This goes in particular for the members of office 103, Dr. Philipp Koopmann, Dr. Thomas Calmano, and Sebastian Müller. The mood and atmosphere in this office often made sure that a bleak day in the lab was very much compensated for. Special thanks go to Thomas and Sebastian for proofreading and especially for introducing me to fs-laser structuring and to Philipp for his assistance concerning Tm-lasers.

My former supervisor Dr. Matthias "Red Igel" Fechner I would like to thank for introducing me to this field in the first place and for teaching me all those tricks about crystal growth, spectroscopy, and lasers that you won't find in any textbook ("ESA-spectra HAVE to be noisy!").

A big thank you is due to my diploma student Daniel-Timo Marzahl whithout whom a good part of the work on the hexaluminates would not have been possible. The discussions we had on all things praseodymium related were always insightful and the level of

motivation he showed in the lab was outstanding. Also thank you for proofreading this thesis.

A very heartily thank you I owe to my fellow PhD students Francesca Moglia and Philip Metz, first for proofreading this thesis but mostly for all our discussions on developing and improving our methods of crystal growth (and how to call them), tackling spectroscopic problems (Inokuti-Hirayama ...), and lasers in general. A special thank you goes to Francesca for sharing 1513 espresso with me (oh yes, I counted) often while listening to me when I needed to rant.

Dr. Sebastian Heinrich, Kolja Beil, Ulrike Wolters, and Sven Waeselmann I would like to thank for proofreading this thesis. Special thanks go to Sebastian for introducing me to the PLD and to Ulrike for her sometimes brutal but nevertheless welcomed honesty.

Much thanks I owe to Dr. Andrea "Generale" Arcangeli from Prof. Tonellis group for organizing a big part of my stay in Pisa and for much fun inside and outside of the lab during my stay there and his stays here in Hamburg. From Pisa I would also like to thank Dr. Stefano Veronesi and Daniela Parisi for introducing me to the labs and for our joint experiments.

I would like to thank Prof. Fredrik Laurell and Dr. Kai Seger of the KTH Stockholm for the collaboration on frequency-doubled Nd-lasers which unfortunately did not make it into this thesis.

For the cooperation on thin-disk-lasers I would like to thank Dr. Andreas Voß, Dr. Uwe Brauch, and Dr. Marwan Abdou-Ahmed of the Institut für Strahlwerkzeuge in Stuttgart.

Of the IKZ Berlin I'd like to thank Dr. Reinhard Uecker for providing crystals and Dr. habil. Detlef Klimm for simulating various Ellingham diagrams as well as for measuring the specific heat of several systems. Thanks also go to Benjamin Herden of the FH Münster for performing the various IR-absorption and XRD measurements and to Dr. Heinz-Jürgen Bernhardt of the Ruhr-Universität in Bochum for performing the microprobe analysis. LISA Laser Products I would like thank for providing a much needed and crucial pump diode.

Dr. Friedjof Tellkamp, Robert Fischer, and Stefan Garbers deserve a big "thank you" for all the technical support. The same also goes for the late Silke Frömmig for the administration and for ensuring a sufficient caffeine level which allowed to accomplish this work.

In terms of proofreading I also want to thank Madeleine Carter who took it upon herself to correct my English.

Last but not least I want to thank all those people outside of the ILP who supported me throughout the last four years. First and foremost these were my mother and my brothers but I am also particularly grateful to all friends who were always there no matter what.